ALMA MATER STUDIORUM
UNIVERSITÀ DI BOLOGNA

DOTTORATO DI RICERCA IN

SCIENZE BIOMEDICHE E NEUROMOTORIE

Ciclo 38

Settore Concorsuale: 06/D3 - MALATTIE DEL SANGUE, ONCOLOGIA E REUMATOLOGIA

Settore Scientifico Disciplinare: MED/15 - MALATTIE DEL SANGUE

DEVELOPMENT OF RADIO CELL THERANOSTICS IN ONCOLOGY

Presentata da: Anna Gaimari

Coordinatore Dottorato

Matilde Yung Follo

Supervisore

Lucia Catani

Co-supervisore

Massimiliano Mazza

Esame finale anno 2026

TABLE OF CONTENTS

Abstract 4
Goal of the Project 4
1. Introduction 5
1.1 Theranostics in Oncology 5
1.2 Immunotherapy and cancer 7
2. Experimental Plan 27
2.1 Modular Radiotracer Localisation 27
2.2 Inducible Platforms for Targeted Imaging and Therapy 28
3. Materials and Methods 31
3.1 Plasmid acquisition and preparation 34
3.2 Cloning strategies and construct design 36
3.3 Plasmid Backbones and General Strategy 38
3.4 Cloning verification through plasmid digestion and gel electrophoresis 39
3.5 Viral Vector Production 40
3.6 Cell Isolation, Culture Conditions and Transduction 41
3.7 Preliminary Evaluation of Constitutive hNIS Expression (pCONTROL vector) 43
3.8 Transduction and Detection of Constitutive 001_pCCL_EF1a Vectors 44
3.9 Evaluation of inducibility in target cells expressing the 8xNFAT-ZsG-hCD8 construct 45
3.10 Co-transduction With Anti-BCMA CAR 46
3.11 Inducible Expression Systems: pBULLET (NFAT) and pHR_5xGAL4 (synNotch) 46
4. Results 48
4.1 pCONTROL lentiviral vector testing 48
4.2 Inducible and constitutive expression vectors cloning strategy 58
4.3 Cloning and constructs' validation: constitutive expression systems 62
4.3.1 Surface Expression Analysis on Transfected HEK293T cells 62
4.3.2 Evaluation of Transduction Performance in Jurkat and Pan-T Cells 66
4.4 Evaluation of 8xNFAT-ZsG-hCD8 (Nakayama vector) 77
4.5 Evaluation of pBULLET (NFAT) based constructs 88
4.6 Evaluation of pHR_5xGAL4 (synNotch) 108
4.6.1 Co-culture of synNotch-HER2 Jurkat Cells with SKBR3 HER2+ Target Cells 116
4.6.2 Co-culture of synNotch-CD19 Jurkat Cells with NALM-6 CD19+ Target Cells ... 129

5. Discussion..... 134
6. Conclusions 145
ADDENDUM 1...... 146
ADDENDUM 2...... 149
7. BIBLIOGRAPHY 151

Abstract

This research project aims to develop a modular radio-cell theranostic platform that integrates molecular imaging with adoptive cell immunotherapy. We engineered viral vectors to endow human effector cells with dual functions: non-invasive in vivo tracking and antigen-driven recruitment of therapeutic radionuclides. Two inducible circuits were implemented: NFAT-responsive transcription and SynNotch-GAL4, and an EF1a-driven constitutive expression; both inducible and constitutive systems focused on the human sodium iodide symporter (hNIS) and avidin/monodin (biotin-binding) receptors. The project goal was to enable imaging of activated cells and localised radiation delivery through radionuclide uptake.

Lentiviral and retroviral backbones were designed to express hNIS, CD8TM-avidin, or CD8TM-monodin genes and those constructs were validated in Jurkat and primary Pan-T cells. Constitutive systems established feasibility across cell contexts, revealing cell-type-dependent receptor display (e.g., higher monodin surface signal in Jurkat versus relatively better avidin detection in primary T cells). In contrast, the inducible NFAT and SynNotch architectures provided stimulus-dependent control but showed suboptimal induction and context-dependent leakiness in Jurkat cells, highlighting the need to refine promoter/enhancer design and chromatin accessibility to maximise on/off ratios.

Collectively, the data deliver a proof-of-concept for dual-function immune cells capable of diagnostic imaging and targeted radiotherapy, while delineating clear engineering priorities, stronger inducible promoters, signal amplification, AND-gate logic, and safety switches, to progress toward clinically viable, programmable cell therapies.

Goal of the Project

This project aims to develop viral vectors for the engineering of human effector cells, such as chimeric antigen receptor T (CAR-T) cells or chimeric antigen receptor Natural Killer cells (CAR-NK), with the dual purpose of enabling non-invasive in vivo tracking and of promoting a localised antigen-driven accumulation of therapeutic radiation. This dual-function platform is designed to integrate imaging and therapy, offering a new level of precision in adoptive immunotherapy.

1. Introduction

1.1 Theranostics in Oncology

The word “Theranostics” derives from the combination of "therapy" and "diagnostics," and reflects the ability to detect, monitor, and treat human diseases simultaneously. A theranostic platform represents a transformative paradigm for managing oncological patients. This approach is particularly critical in the era of precision medicine, where the biological complexity of tumours demands nuanced and multifactorial strategies. The field of radio-cell theranostics, which synergistically combines radiopharmaceutical targeting and cellular therapies, offers a promising frontier in this domain[1].

While modern in terminology, the concept of theranostics has historical roots. In 1946, Seidlin and colleagues pioneered the use of radioactive iodine (I-131) to treat metastatic thyroid cancer, demonstrating both the diagnostic localisation and therapeutic eradication of disease using a single radiopharmaceutical agent[2]. This work laid the foundation for modern approaches that integrate functional imaging with molecularly targeted therapies.

A notable example is the targeting of Prostate-Specific Membrane Antigen (PSMA), a transmembrane protein overexpressed in prostate cancer. Maresca and colleagues synthesised halogenated heterodimeric inhibitors that bind PSMA with high affinity, enabling precise imaging and therapeutic applications[3]. Building on this chemistry, Zechmann and colleagues developed MIP-1095, a PSMA-targeting molecule labelled with iodine isotopes for both diagnostic (I-124) and therapeutic (I-131) use[4]. Clinical implementation of these agents has yielded promising results, notably in the LuPSMA trial (Australian New Zealand Clinical Trials Registry, number 12615000912583), where [177Lu]-PSMA-617 demonstrated significant efficacy in patients with metastatic castration-resistant prostate cancer[5]. These advances exemplify the theranostic principle, which leverages a single molecular target across multiple clinical applications.

Beyond prostate cancer, theranostic strategies are being extended to various malignancies through the engineering of nanomaterials and smart drug delivery systems. Sneider and colleagues proposed remotely triggered nano-theranostics

capable of delivering payloads in response to specific external stimuli, such as heat or ultrasound, thereby enhancing spatiotemporal control over drug release[6]. This level of control is critical for minimising off-target effects and improving therapeutic indices, particularly in solid tumours characterised by complex microenvironments.

Increasingly, theranostics is expanding beyond the molecular level to include cellular modalities. The confluence of advanced molecular imaging and adoptive cell therapies has led to the emergence of radio-cell theranostics. This innovative approach leverages genetically engineered immune cells, such as CAR-T cells, in conjunction with radiolabeled probes to enable real-time tracking, biodistribution analysis, and targeted cytotoxic activity[7].

Among the theranostic platforms, peptide receptor radionuclide therapy (PRRT) with radiolabelled somatostatin analogues represents one of the most established examples of a clinically validated theranostic platform[8]. Neuroendocrine tumours frequently overexpress somatostatin receptors, enabling patient selection through ^{68}Ga-DOTATATE PET/CT imaging followed by targeted therapy using ^{177}Lu-DOTATATE or ^{177}Lu-DOTATOC. This diagnostic–therapeutic pair has demonstrated significant clinical benefit, as shown in the pivotal NETTER-1 phase III trial, where ^{177}Lu-DOTATATE markedly improved progression-free survival and overall response rates compared with high-dose octreotide in patients with advanced midgut neuroendocrine tumours. Because of its strong translational impact, PRRT is now considered a prototypical theranostic model and is relevant when discussing image-guided targeted therapies and emerging approaches such as CAR-T cell tracking[9].

In recent years, immunotherapy, a treatment approach that stimulates the immune system in patients, has shown significant progress, boosting the success rate of therapies for several types of cancer. This is especially advantageous for haematological tumours, as it effectively targets widespread diseases.

The following examples are used to illustrate how immunotherapy has transformed the prognosis of several advanced cancers and to motivate the development of novel cell-based immunotherapies such as CAR-T cells.

For metastatic melanoma, a recent comparative meta-analysis of >5,000 patients showed that combination nivolumab + ipilimumab achieves a higher overall response

rate (≈52% vs ≈32%) and improved 5-year overall survival (≈56% vs ≈34%) compared with ICI monotherapy, at the cost of increased immune-related adverse events[10].

Furthermore, to summarise other data from recent meta-analyses in non-small cell lung cancer (NSCLC), we report significant improvements in overall survival and progression-free survival for first-line ICI-based regimens compared with chemotherapy, both in squamous and non-squamous histologies. More in detail, pembrolizumab+chemotherapy, atezolizumab+bevacizumab+chemotherapy, and nivolumab were superior to other treatments in NSCLC patients with liver metastases. These new findings may help clinicians better select therapeutic strategies for NSCLC patients with liver metastases[11,12].

1.2 Immunotherapy and cancer

The immune system is traditionally categorised into two major branches: the innate and the adaptive (or acquired) immunity. The innate immune response acts rapidly but lacks specificity; it includes physical and chemical defences such as the skin and mucosal barriers, circulating proteins like complement, various phagocytic cells (including macrophages, neutrophils, dendritic cells [DCs], and natural killer [NK] cells), as well as cytokines that orchestrate and modulate these immune components. In contrast, the adaptive immune system is slower to activate, highly specific, able to generate immunological memory, recognise self-versus non-self-molecules, and boost stronger responses upon repeated antigen exposures. This adaptive arm is composed primarily of T and B lymphocytes. T cells comprise $CD8^+$ cytotoxic T lymphocytes, which interact with MHC class I molecules, $CD4^+$ helper T cells, which interact with MHC class II receptors, as well as memory and regulatory T cells. B lymphocytes are central to the humoral immune response, producing antibodies that can activate complement, promote phagocytosis of opsonised targets, and mediate antibody-dependent cellular cytotoxicity. While T cell responses are often considered more critical in anti-tumour immunity, the contribution of B cells is still under investigation, and definitive conclusions remain elusive. It is important to note that the innate and adaptive immune systems are interdependent: innate responses shape the nature and intensity of adaptive immunity, and many effector mechanisms are shared. Immune responses are also distinguished by whether they are active, elicited through direct exposure to foreign antigens, or passive, whereby immunity is conferred by

transferring immune components (such as antibodies or lymphocytes) from a previously immunised host. Both strategies can target specific antigens, but only active responses are typically capable of inducing long-lasting immunological memory. The key players in active/adaptive responses include lymphocytes, antigen-presenting cells, and effector cells. Furthermore, immune responses can be characterised based on their specificity: antigen-specific responses target a defined antigen, while non-specific approaches aim to broadly activate the immune system without antigen selectivity. This framework enables more nuanced classifications, such as “active-specific” or “passive-nonspecific,” depending on the immune mechanism involved[13].

Immune surveillance refers to the concept that the immune system may naturally limit or prevent tumour development. Several lines of evidence support this hypothesis including: (1) interferon-gamma (IFN-γ) has been shown to inhibit tumor growth in mice; (2) mice deficient in IFN-γ receptors exhibit heightened susceptibility to chemically induced sarcomas and spontaneous tumors; (3) animals lacking functional T and B lymphocytes have an increased frequency of spontaneous malignancies; and (4) mice with combined deficits in IFN-γ signaling and adaptive immunity tend to develop tumors at an earlier age[14–17].

However, tumour immune evasion presents major challenges to effective anti-cancer immunity. Despite having competent immune systems, many individuals develop and succumb to cancer, illustrating the ability of tumours to escape immunological control. Tumors achieve this through several mechanisms, including: (1) secretion of immunosuppressive cytokines such as transforming growth factor-beta (TGF-β) and interleukin-10 (IL-10)[18,19], (2) impairment of dendritic cell (DC) function, either by inducing anergy or by blocking DC maturation via deregulation of cytokines like IL-6, IL-10, VEGF, or GM-CSF[20], (3) induction of regulatory T cells (Tregs), a subset of $CD4^+/CD25^+$ cells expressing markers such as CTLA-4, GITR, and Foxp3, that inhibit $CD4^+$ and $CD8^+$ T cell responses; (4) loss of MHC class I expression, due to structural mutations, defects in β2-microglobulin synthesis, impaired antigen processing via TAP proteins, or deletion of MHC alleles/loci; and (5) disruption of MHC I antigen presentation, even when MHC molecules are present, through downregulation of co-stimulatory molecules such as B7-1, which is crucial for CD28-mediated T cell activation[13].

Immunotherapy regimens include monoclonal antibodies (mAbs), checkpoint inhibitors, anti-cancer vaccines, cytokine therapy, oncolytic virus therapy, and adoptive cell therapy (ACT)[21–23]. On the contrary, conventional treatments based on radiotherapy, chemotherapy and surgery are seldom associated with disease eradication, especially for diseases at advanced stages, yet with significant side effects[24,25]. Therefore, novel strategies with higher efficacy and fewer complications have been developed, and immunotherapy is one of them. More in detail, immunotherapy is the modification and enhancement of the host immune system to tackle different pathologies, such as cancer; actually, cancer immunotherapy has dramatically changed the landscape of treatment for this complex condition. Conventional chemotherapy affects all tissues of the body systemically, while targeted therapies are more restricted to tissues expressing the specific target[26]. The aim of targeting the immune system to recognise and destroy cancer cells has afforded many patients the prospect of achieving deep, long-term remission and potential cure. However, many challenges remain to be addressed for achieving the goal of effective immunotherapy for all cancer patients[27]. In this regard, ACT plays a major role; it is a type of breakthrough immunotherapy, in which patient-derived T-cells are genetically engineered ex vivo and are subsequently delivered back into the patient to target and kill cancer cells. Such cells are modified to express synthetic tumour-targeting receptors - typically either a chimeric antigen receptor (CAR) or a T-cell receptor (TCR) - which trigger a cytotoxic response, upon binding to specific antigens on the surface of cancer cells[28].

1.3 CAR-T cells

The CAR is a recombinant receptor composed of the antigen-binding domain, typically a single-chain variable fragment (scFv) derived from a monoclonal antibody (mAb), which is molecularly fused to intracellular signalling domains that activate immune cells. The antigens recognised by the CAR are either tumour-specific or tumour-associated antigens. The spacer or hinge is the flexible portion of the CAR that links the extracellular domain to the intracellular domain and is responsible for receptor flexibility in antigen recognition and, to some extent, for the modulation of downstream signalling[29]. The intracellular domain is the functional portion of the receptor, consisting of both signalling and co-stimulatory domains. CD3 is the most used signalling domain that, upon antigen engagement by the CAR, triggers a nuclear factor

of the activated T cell (NFAT)-dependent transcriptional pathway. This activation is crucial for eliciting T cell cytotoxicity. Signalling domains can be combined with costimulatory molecules, such as CD28, 4-1BB, CD27, and OX40, among others. These costimulatory molecules determine efficient receptor activation, influencing the cytotoxicity rate and the development of an immunological memory phenotype[29] (Figure 1).

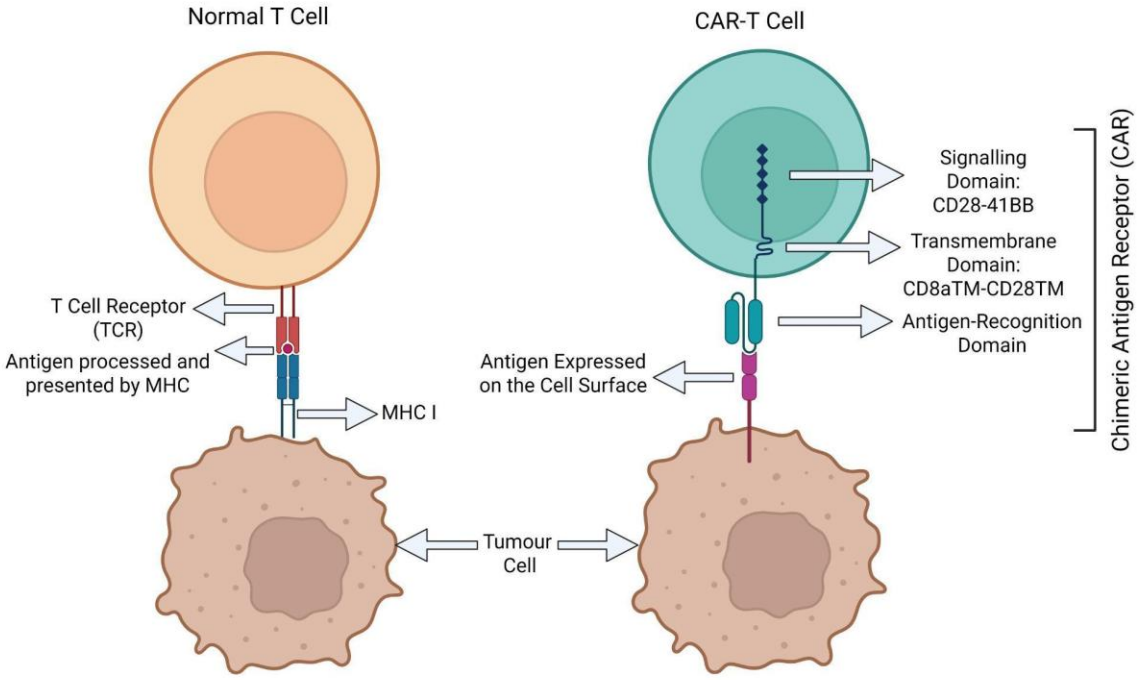

Figure 1. Comparison of antigen recognition by normal T cells and CAR-T cells. The figure illustrates how normal T cells rely on the T Cell Receptor (TCR) to recognise peptide antigens presented by MHC molecules on tumour cells, a process that is MHC-restricted and susceptible to tumour immune evasion. In contrast, CAR-T cells are engineered to express a chimeric antigen receptor (CAR) composed of an antibody-derived antigen-recognition domain, a transmembrane region, and intracellular signalling domains (e.g., CD28, 4-1BB). This allows them to recognise antigens directly on the tumour cell surface, enabling potent, MHC-independent activation and cytotoxicity. Created on BioRender.

Leukapheresis of the patient is often the first step in producing autologous CAR-T cells, while some researchers have explored the use of non-separated whole peripheral blood (Figure 2). The T cells are then stimulated and co-stimulated ex vivo in the presence of a cytokine cocktail. In addition, stimulating antibodies can be expressed on artificial antigen-presenting cells, chemically attached to beads, or supplied in soluble form[30]. Before apheresis, patients must abstain from all medications for two weeks to guarantee enough cell counts and quality viability for the production process, which typically lasts two to four weeks according to the different protocols[31]. CAR-T cells are genetically modified by introducing a CAR gene into autologous T cells using a retro-/lentivirus or via transposable elements[32]. Several clinical trials have shown substantial efficacy with both viral and non-viral vectors[33]. However, safety concerns have recently been raised regarding the use of transposons, such as PiggyBack (PB) based transposons, which have been associated with the development of CAR-T cell lymphomas in treated patients[34].

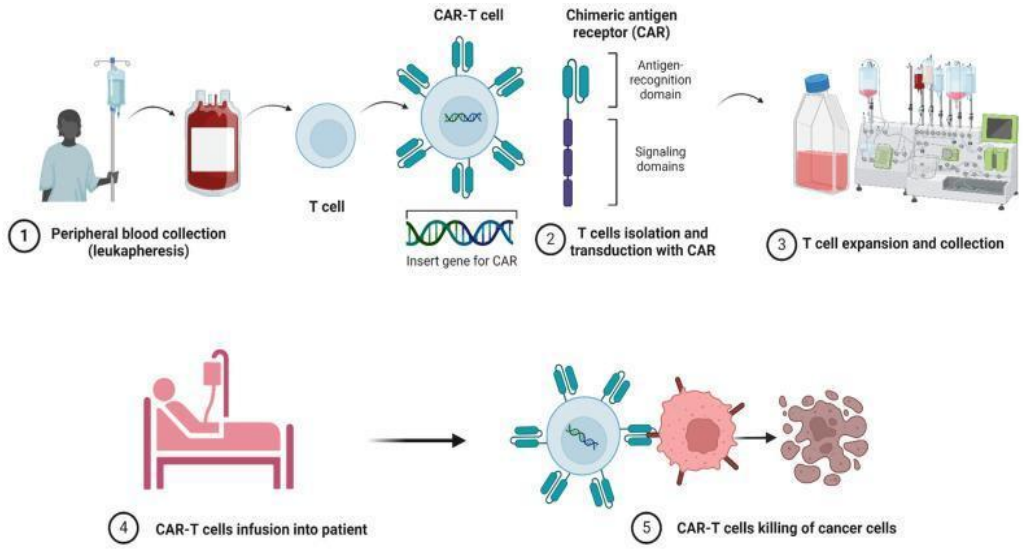

Figure 2. **Schematic representation of the CAR-T cell production process.** The currently approved autologous CAR-T cell treatment modifies a patient's T cells ex vivo before redistributing them to the same individual. Multiple quality assessments monitor the production process, which is conducted in compliance with Good Manufacturing Practice (GMP) norms. Isolating T cells from the patient's peripheral blood is the first stage in the creation of autologous CAR-T cells. Viral transduction is then used to activate and genetically modify isolated T cells so they can express the CAR molecule. After that, CAR-T cells are grown in culture to reach billions of cells. To precisely target and eradicate cancer cells, the altered

CAR-T cells are usually cryopreserved and then reinfused into the patient. Created on BioRender, from Gaimari, A. (2022)[35].

To date, six CAR-T cell therapies have been approved by the Food and Drug Administration (FDA), with the first approval dating back to 2017[36]. All have received approval for treating patients with refractory and relapsed (r/r) haematological malignancies, namely acute B lymphoblastic leukaemia (B-ALL), B-cell lymphoma (DLBCL, PMBCL), follicular lymphoma (FL), and mantle cell lymphoma (MCL), as well as multiple myeloma (MM) patients. These include (i) tisagenlecleucel (Kymriah™, tisa-cel), an anti-CD19 CAR-T therapy with 4-1BB-CD3 domains; (ii) axicabtagene ciloleucel (Yescarta™, axi-cel), an anti-CD19 CAR-T construct with CD28-CD3 domains; (iii) brexucabtagene autoleucel (Tecartus™, brex-cel), also anti-CD19 with CD28-CD3 domains; (iv) lisocabtagene maraleucel (Breyanzi™, liso-cel), an anti-CD19 CAR-T with 4-1BB-CD3 domains; (v) idecabtagene vicleucel (Abecma®, ide-cel), an anti- B-cell maturation antigen (BCMA) with 41BB-CD3 domains; and (vi) ciltacabtagene autoleucel (Carvykti®), designed for r/r MM, which targets two unique BCMA epitopes using dual nanobody domains[37–39].

Conventionally, five CAR vector generations are recognised in the field of immunotherapy, each representing a distinct evolution of CAR design and engineering. These generations encompass improvements in terms of CAR structure, signalling domains, and targeting capabilities, aiming to enhance the specificity, efficacy, and safety of CAR-T cell therapies according to the number and type of co-stimulatory modules and the possibility of expressing specific cytokines[40].

The first generation of CAR-T consists of an extracellular scFv domain connected to an intracellular CD3 signalling domain. The first clinical trials showed low survival rates and short-lived immunological responses[40,41]. Therefore, second-generation CAR molecules have been developed by adding costimulatory domains (i.e., CD28 or 4-1BB) to the CD3z signalling domain. The third-generation CAR design included two such co-stimulatory domains and showed enhanced efficacy, notable proliferation, and improved durability when targeting tumour cells[40,41].

However, third-generation CAR-T therapies, while more advanced than their predecessors, still face significant obstacles. Manufacturing these cells remains a complex, resource-intensive process, which limits scalability and accessibility. Moreover, their clinical effectiveness has not consistently surpassed second-generation CAR-T cells, especially in solid tumours, where the tumour microenvironment further hampers their performance[42]. These limitations underscore the ongoing need for innovation to enhance both their efficiency and therapeutic impact[43].

The fourth generation, also known as TRUCK cells (T Redirected Universal Cytokine Killer cells), is engineered to produce cytokines, enzymes, and other biochemical substances[44]. Common cytokines used in TRUCKs include interleukin (IL)-2, IL-15, and IL-18, which enhance the immune response against solid tumours and extend the persistence of CAR-T cells within the tumour microenvironment[45,46]. Finally, fifth-generation CARs are designed with additional elements into the standard CAR design, enabling them to detect multiple antigens or targets, even in cases of low antigen density, further improving their therapeutic potential[47].

Specific CAR designs and strategies have also emerged to boost specificity, efficacy, and lower immune evasion by tumour cells. Some of those strategies comprise logic-gated constructs[48].

Examples of this kind are as follows:

- “OR logic”: modular T cells can eliminate different malignant cells with various switching modules that target different antigens on cancer cells. Tandem CAR-T cells, for example, contain two bispecific ligand-binding domains. T cells are activated when one or the other antigen-binding domain binds the antigen on the target cell’s surface.
- “AND logic”: T cells express two different CARs, activating the immune response only when both antigens are expressed on the target cell. Dual CARs are a practical example of this logic.
- “NOT logic”: This is used when a specific antigen is expressed both by normal and cancerous cells, and a certain one is expressed only by normal

cells/healthy tissues. Two complementary modules, targeting the antigen present only on normal cells, are used so they can inactivate each other.

An example of a promising, customisable, multi-targeted “AND-GATE” CAR-T cell is the synthetic Notch receptor (SynNotch)-CAR, which enables multimodal tumour antigen targeting[49]. SynNotch receptors are composed of several key components, including (i) synthetic external recognition domains (such as single-chain antibodies), (ii) a synthetic intracellular GAL4VP64 transcription transcriptional domain, called the Notch intracellular domain (NICD), with a regulatory role in gene transcription, and (iii) the central core domain, which plays central role in the Notch signalling pathway and helps regulate the cleavage and activation of the SynNotch-CAR after binding to antigens[50,51]. The engagement with a specific antigen triggers a controlled transmembrane cleavage of the SynNotch receptor, mimicking a physiological Notch activation process. The intracellular transcriptional domain is released and transported to the nucleus, where it activates the expression of target genes under the control of the corresponding upstream cis-activating promoter[49]. Such an activation pathway differs from conventional CAR activation by scFv antigen recognition[52]. The SynNotch receptor is designed to produce responses in programmable pathways, in contrast to traditional CARs that lack any controlled mechanism. Moreover, because of the distinctive structure of the SynNotch receptor, it is possible to employ a synthetic transcription factor rather than the intracellular domain of Notch, and instead of the extracellular part, other substitutes can be introduced into the receptor structure[41]. This design (Figure 3) enables precise control over transgene expression and has been integrated into CAR-T platforms to improve tumour specificity and reduce toxicity[53,54].

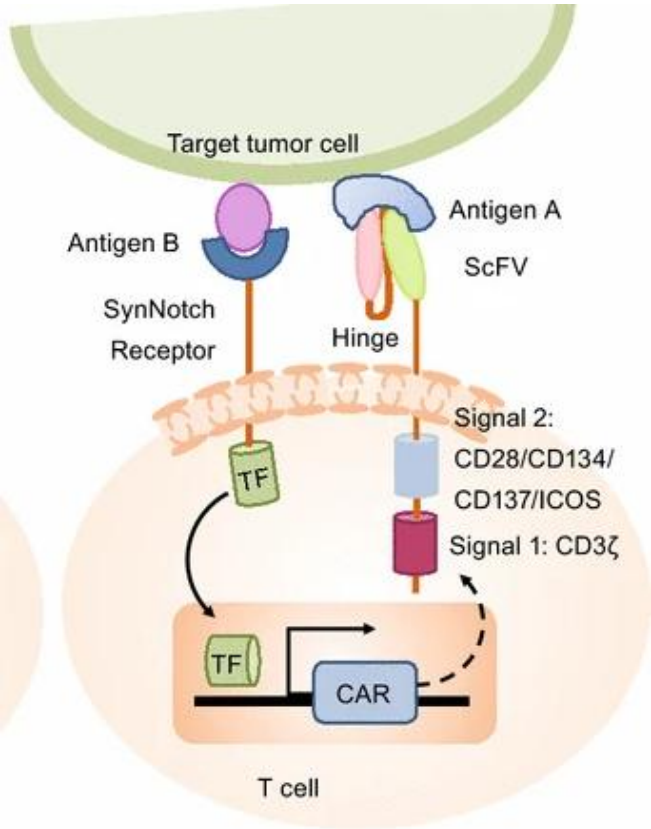

Figure 3. SynNotch AND-Gate Activation Mechanism. The synNotch system is designed as a sequential, antigen-dependent activation strategy. It starts with the synNotch receptor detecting antigen B on a target cell. Upon recognition, the receptor undergoes cleavage, releasing a transcriptional activator that translocates into the nucleus. This event triggers the expression of a chimeric antigen receptor (CAR) that is specific for antigen A. Once the CAR is expressed and binds to antigen A, the T cell becomes fully activated. In this way, T cell activation occurs only when both antigens are present, implementing an AND-gate logic. Adapted from Li H. et al. (2017)[55].

Unlike conventional CARs, AND-gate T cells are designed to be activated only when two target antigens are present, while being inactive in the presence of a single antigen only. The subsequent expression of the CAR occurs following the activation of the SynNotch receptor. Since this controllable mechanism is not present in conventional CAR-T cells, the likelihood of side effects in the latter is increased compared to Syn-Notch CAR-expressing T cells. This class of CAR-T cells has the potential to produce a wide range of cytokines[50]. In addition, previous studies have reported the possibility of employing a SynNotch receptor system able to activate the expression of a secondary CAR upon binding to a specific antigen via the SynNotch receptor[56,57].

Furthermore, T cells with multiple synNotch receptors serving as versatile regulatory adapters have recently been developed. These cells are capable of precisely targeting cancers by incorporating up to three distinct antigens while avoiding the recognition of tumours associated with only two antigens[58].

The synNotch-CAR has demonstrated superior tumour elimination compared to conventional CAR-T cells. This increased performance is achieved by preventing tonic signalling and exhaustion and maintaining a larger proportion of T cells in a naive/stem cell memory state[59,60].

The use of synNotch CARs has been reported and described by several authors. Choe and colleagues tested a SynNotch-CAR to target specific antigens for glioblastoma, such as the variable but tumour-specific glioblastoma neoantigen epidermal growth factor receptor variant III (EGFRvIII), the tissue-specific antigen for the central nervous system (CNS), and the myelin oligodendrocyte glycoprotein (MOG)[60]. Administering a single intravenous infusion of EGFRvIII synNotch-CAR-T cells in immunodeficient mice bearing intracerebral patient-derived xenografts (PDXs), with a heterogeneous expression of EGFRvIII resulted in higher anti-tumour efficacy, improved T cell survival, more stem-like phenotypes, less exhaustion, and enhanced in vivo persistence compared to traditional CARs[60]. In a second study, Hyrenius-Wittsten and colleagues identified the tumour-specific antigen Alkaline Phosphatase Placental-like 2 (ALPPL2) as a target expressed in various solid malignancies, including mesothelioma and ovarian cancer. By testing the activity of SynNotch CAR-T cells in mice models of human mesothelioma and ovarian cancer, they observed greater control of tumour progression as compared to conventional CARs[48]. Additionally, the SynNotch-controlled expression helped prevent CAR-mediated tonic signalling, allowing T cells to preserve a long-lasting memory and active state[61].

Another regulatory platform that can be exploited for precise control in engineered T cell therapies is the NFAT promoter, which enables inducible gene expression in response to CAR/TCR activation. This platform exploits endogenous T-cell signalling. TCR activation increases intracellular calcium, activating calcineurin, which dephosphorylates NFAT transcription factors (primarily NFAT1, NFAT2, and NFAT4), allowing their nuclear translocation and initiation of gene transcription (Figure 4). NFAT often cooperates with AP1 at composite binding sites to regulate cytokine gene expression, but can also function independently or with other partners. This dynamic

regulation allows nuanced control of T-cell activation, differentiation, and tolerance mechanisms. Importantly, this system can be activated by physiological stimuli or pharmacologic agents (e.g., PHA, PMA/Ionomycin) and is well-suited for CAR-T cell applications[62].

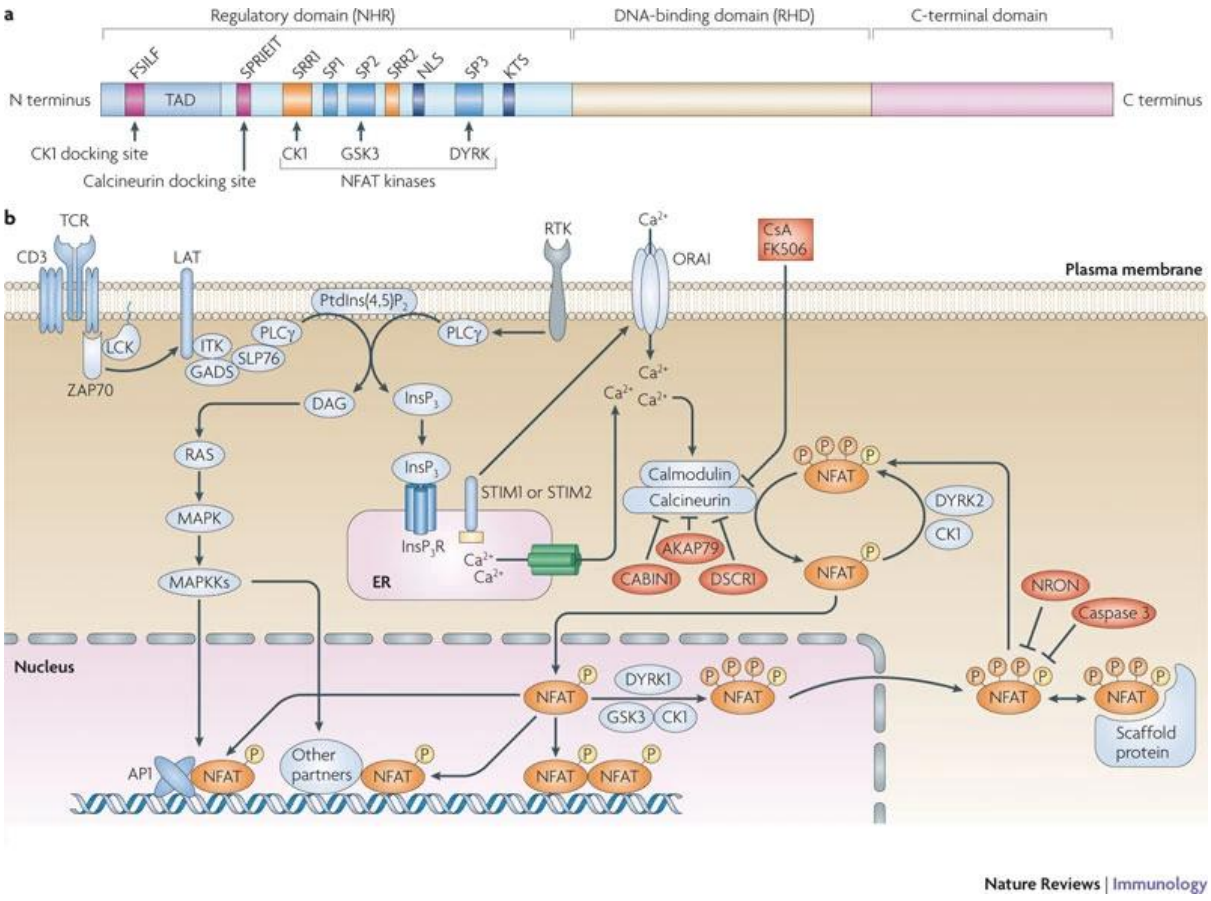

Figure 4. General structure of NFAT transcription factors. NFAT transcription factors have a modular structure comprising an N-terminal regulatory domain (NHR), a DNA-binding REL-homology domain (RHD), and a C-terminal region. The regulatory domain includes transactivation motifs, serine-rich regions, and binding sites for key regulators like calcineurin and CK1. Upon receptor stimulation, PLCγ activation leads to calcium release from the ER via InsP3 signalling. The drop in ER Ca^{2+} activates STIM1/2 and the CRAC channel ORAI, enabling extracellular Ca^{2+} influx. Ca^{2+}-bound calmodulin activates calcineurin, which dephosphorylates NFAT, promoting its nuclear translocation. In the nucleus, NFAT partners with AP-1 and others to drive gene expression. NFAT is re-inactivated via phosphorylation by kinases such as GSK3 and DYRK. Regulatory proteins like CABIN1, AKAP79, and NRON, as well as drugs like cyclosporin A and FK506, modulate NFAT activity. NFAT transcription factors have a modular structure comprising an N-terminal regulatory domain (NHR), a DNA-binding REL-homology domain (RHD), and a C-terminal region. The regulatory domain

includes transactivation motifs, serine-rich regions, and binding sites for key regulators like calcineurin and CK1. Upon receptor stimulation, PLCγ activation leads to calcium release from the ER via InsP3 signalling. The drop in ER Ca^{2+} activates STIM1/2 and the CRAC channel ORAI, enabling extracellular Ca^{2+} influx. Ca^{2+}-bound calmodulin activates calcineurin, which dephosphorylates NFAT, promoting its nuclear translocation. In the nucleus, NFAT partners with AP-1 and others to drive gene expression. NFAT is re-inactivated via phosphorylation by kinases such as GSK3 and DYRK. Regulatory proteins like CABIN1, AKAP79, and NRON, as well as drugs like cyclosporin A and FK506, modulate NFAT activity. From Müller MR. et al., 2010[63].

ACT has proven quite effective for patients affected by haematological tumours, such as acute lymphoid leukaemia and multiple myeloma[64]. However, despite the remarkable success of adoptive T-cell therapy in haematological malignancies, its application in solid tumours has remained considerably limited. This discrepancy stems from the inherent complexity of the solid tumour microenvironment and the biological heterogeneity characteristic of most epithelial cancers, which together pose a significant barrier to T-cell-based immunotherapies[65].

Solid tumours, for example, present various biological and structural challenges that considerably impair the effectiveness of CAR-T cells. First, the high degree of antigenic heterogeneity across tumour cells represents a major mechanism of immune escape. Most current CAR-T constructs are designed to recognise a single tumour-associated antigen (TAA) and therefore fail to eliminate tumour cells that downregulate or lack the targeted antigen. To address this issue, dual- or multi-antigen targeting strategies have been explored, such as tandem CARs and pooled CAR-T cell products, aiming to broaden antigen recognition and improve tumour cell coverage. However, increasing CAR specificity across multiple antigens also raises the risk of on-target, off-tumour toxicity, particularly when low-level antigen expression is present on healthy tissues[65].

Second, physical barriers characteristic of solid tumours severely limit T-cell access. The dense extracellular matrix (ECM), often rich in fibrillar collagens and hyaluronic acid, forms a stiff, fibrotic architecture that physically obstructs immune cell infiltration. This barrier is compounded by the presence of cancer-associated fibroblasts (CAFs), which actively remodel the stroma and secrete suppressive cytokines, further impeding CAR-T cell migration and persistence[66].

Third, even when CAR-T cells successfully infiltrate tumour masses, they must operate within a highly immunosuppressive tumour microenvironment (TME). The TME comprises a complex network of suppressive signals, including regulatory immune cells such as Tregs and myeloid-derived suppressor cells (MDSCs), immunosuppressive cytokines (e.g., IL-10, TGF-β), and metabolic constraints such as hypoxia, low glucose, and high lactate levels[67]. Collectively, these factors induce T-cell exhaustion, metabolic dysfunction, and reduced cytolytic potential[65,68]. Additionally, aberrant tumour vasculature, marked by irregular vessel structure and dysfunctional endothelial cells, hinders CAR-T cell extravasation due to altered expression of adhesion molecules such as ICAM-1 and VCAM-1[69,70]. Therefore, strategies aimed at preserving the functional cytotoxicity of T cells and enhancing their trafficking within the tumour mass are essential and of utmost importance for the success of CAR-T cell therapy against solid tumours. Recent clinical results have indeed highlighted that non-responsive patients accumulate T cells with an early memory and exhausted phenotype after CAR-T cell therapy, in contrast to responders[61].TRUCKs have been developed to tackle a variety of malignancies, including glioblastoma, breast cancer, and other solid tumours, employing several cytokines such as IL-2, IL-12, IL-15, and IL-18[29,71]. For instance, sustaining the function of cytolytic CD8+ T cells relies on a network of transcription factors, with FoxO1 playing a key role. The balance between FoxO1 and T-bet transcription factors affects T cell function. By inducing FoxO1-low and T-bet-high T cells, the cytolytic CD8+ T cell attack can be maintained, offering prolonged immune responses to advanced tumours. IL-18 has been identified as a potent cytokine capable of inducing this desired T cell phenotype. These observations have been supported by recent findings in which CAR-T cell activity was enhanced by IL-18 release from engineered cells, promoting acute inflammation, reduced numbers of exhausted cells within the tumour and resulting in a more effective immune response against established tumours[61].

In a study by Krenciute and colleagues, IL-15 expression and secretion in IL13R2-CAR-T cells showed enhanced cytotoxic activity of transduced T cells towards glioma tumour cells[72]. Previous investigations have also reported that IL-12 induces immune-boosting properties in addition to IL-15, which can be achieved by reconfiguring

suppressor cells in the TME and stimulating the innate immune system's anticancer defences, including NK cells[72]. Moreover, TRUCK T cells increase the anti-tumour effectiveness of CAR-T cells by destroying target cells that are inaccessible to CAR-T cells and by boosting the levels of IFN-γ, IL-6, and IL-27 cytokines. TRUCK T cells' expression of IL-12 can also modify the tumour stroma to enhance its suitability for the function and persistence of the engineered T cells[71,73].

Additionally, alternative CAR-engineered effector cells derived from healthy donors may help address these current limitations in cell therapy approaches[74–76]. Among these, cytokine-induced killer (CIK) cells have shown both clinical efficacy and a favourable safety profile despite being HLA-mismatched in allogeneic settings[77–79]. CIK cells display strong anti-tumour activity against a wide range of haematological and solid tumours[78,80]. They represent a heterogeneous T cell population that exhibits features of both adaptive T cells and innate immune cells, particularly MHC-unrestricted cytotoxicity characteristic of NK cells. Within this population, the $CD3^+CD56^+$ subset, often referred to as "T-NK" cells, shares some phenotypic similarities with invariant NKT (iNKT) cells[80–83] and γδ T cells[84,85], though they remain a distinct group that primarily expresses variable αβ T cell receptors, derived from conventional $CD3^+$ T cells[86,87]. Importantly, CIK cells can be efficiently generated from peripheral blood mononuclear cells (PBMCs) through in vitro expansion using cytokines and are amenable to genetic modification with CAR constructs[88–90].

However, these multifactorial barriers have led to the notion that CAR-T cells alone are probably insufficient to effectively tackle solid tumours. A consensus is emerging in the field that combinatorial strategies, pairing CAR-T cells with immune checkpoint inhibitors (ICIs), chemotherapy, radiotherapy, or oncolytic viruses, may be required to modulate the TME, promote endogenous immunity, and potentiate CAR-T activity in patients. Beyond therapeutic limitations, an important unmet need in current CAR-T cell strategies is the inability to track the spatial and functional dynamics of engineered T cells in vivo. It remains largely unclear where these cells traffic after infusion, whether and for how long they are activated upon tumour encounter, and to what extent they infiltrate and persist within primary or metastatic lesions. This gap represents a major obstacle to optimising treatment schedules, understanding failure modes, and tailoring individualised therapies[91].

In response to this need, molecular imaging-based strategies have gained interest. A notable advance came from Emami-Shahri and colleagues, who introduced the human sodium iodide symporter (hNIS) as a reporter gene in CAR-T cells[91]. hNIS enables non-invasive imaging using clinically available radiotracers such as Technetium-99m pertechnetate [99mTc], which allows for the longitudinal tracking of T cells in vivo. This approach qualifies as a cell-based theranostic, as it can both visualise and potentially deliver therapeutic radiation (e.g., iodine-131) to the tumour site, provided the CAR-T cells remain viable and engaged with the tumour. The advantage of this system lies in its compatibility with nuclear medicine procedures already in clinical use, leveraging well-established safety profiles. The NIS (or SLC5A5) is an integral membrane protein primarily responsible for transporting iodide into thyroid follicular cells, where it plays a central role in thyroid hormone synthesis and metabolic regulation[92,93]. Positioned at the basolateral membrane, NIS co-transports one iodide ion with two sodium ions using the inward sodium gradient established by the Na^+/K^+-ATPase pump[94,95]. This mechanism is critical not only for physiological iodine uptake, but also for the diagnosis and radioiodine-based treatment of thyroid disorders, both benign and malignant[96,97]. Because of its selective and active transport function, NIS has emerged as a powerful theranostic and reporter gene, combining diagnostic imaging capabilities with therapeutic potential[98]. It is naturally expressed, non-toxic, and non-immunogenic, making it well-suited for gene transfer applications. Crucially, iodide uptake occurs only in viable cells, so radiotracer accumulation via NIS directly reflects cell viability and metabolic activity[99]. Its ability to concentrate substrates rather than binding them stoichiometrically results in enhanced detection sensitivity[100]. NIS can transport various clinically relevant radiotracers such as ^{123}I, ^{125}I, ^{131}I, ^{99m}Tc, and ^{188}Re, enabling gamma scintigraphy and SPECT-based imaging. Moreover, ^{131}I and ^{188}Re are β-emitting isotopes with therapeutic applications. Although SPECT and planar scintigraphy remain standard imaging modalities for NIS, positron emission tomography (PET) using ^{124}I offers better spatial resolution and quantitative capability[101]. However, ^{124}I poses several clinical limitations: a long half-life (4.2 days), low positron yield (23%), high-energy emissions, and limited commercial availability, all of which restrict its widespread diagnostic use[102,103]. To address these drawbacks, [^{18}F]tetrafluoroborate (TFB) has been introduced as a promising alternative PET tracer. As a fluorinated anion structurally like pertechnetate and a recognised NIS substrate, [^{18}F]TFB offers improved pharmacokinetics and image quality. It has a

shorter half-life (110 min), higher positron yield (97%), and lower positron energy, resulting in clearer PET images with superior signal-to-noise ratio compared to ^{124}I[101,102,104,105]. Importantly, unlike iodide, [^{18}F]TFB is not organified in the thyroid, avoiding long-term sequestration and improving availability for non-thyroidal tissues. Its biodistribution resembles that of ^{99m}Tc-pertechnetate, with uptake in the thyroid, salivary glands, stomach, and kidneys, but it remains pharmacologically safe in humans[102,106,107].

Preclinical studies have shown that [^{18}F]TFB exhibits higher tumoral uptake and faster clearance from blood compared to iodine-based tracers, leading to improved target-to-background ratios and enabling the detection of small NIS-expressing metastases not visualised with [^{18}F]FDG-PET[108]. This makes [^{18}F]TFB especially attractive for low-volume tumour models and applications such as glioblastoma or disseminated cancer lesions. Despite its clinical promise, broader adoption of [^{18}F]TFB has been limited due to production constraints and differences in pharmacokinetics that prevent reliable extrapolation for dosimetry in radioiodine therapy[101,102,104,107,109]. Overall, NIS represents a uniquely valuable tool in molecular imaging and gene therapy, with growing interest in its application for non-thyroidal tumours, provided that high-efficiency gene delivery and membrane localisation are achieved[110,111]. Additionally, Volpe and colleagues demonstrated that the PET probe ^{18}F-BF4^{-} reaffirms the role of the NIS reporter system in trafficking CAR-T cells[112]. They constructed T4NT CAR-T cells that express the NIS reporter and can target the pan-ErbB family. The cell uptake assay showed that the CAR-T cells had significantly higher *in vitro* uptake of SPECT radiotracer ^{99m}TcO4^{-} and PET radiotracer ^{18}F-BF4^{-} in comparison to NIS-negative T cells[112].

Another strategy relies on the avidin–biotin system, which exploits the exceptionally high affinity between the two molecules to achieve selective delivery of therapeutic or imaging agents to the tumour site. Avidin is a 66 kDa, highly glycosylated, positively charged tetrameric protein derived from egg white, with an extremely high affinity for biotin (Kd ≈ 10^{-15})[113–115]. The avidin–biotin interaction is so strong that it is considered effectively irreversible, making it attractive for biomedical applications such as tumour-targeted radionuclide delivery. One notable approach is the pretargeting strategy, in which monoclonal antibodies (MoAbs) and radionuclides are administered in separate

steps. This technique optimises tumour-to-background ratios by delaying radiolabeled molecule delivery until MoAbs have selectively accumulated in tumour tissue. Two primary pretargeting strategies have been explored: a two-step protocol, in which biotinylated antitumor MoAbs are first injected and followed by radiolabeled avidin and a three-step protocol involving (1) injection of biotinylated MoAbs, (2) cold avidin to bind tumour-localised antibodies and clear circulating ones, and (3) a final dose of radiolabeled biotin[116]. These approaches have been tested clinically in various cancers, including gliomas and breast tumours. In an early study, Paganelli et al.[117] demonstrated the feasibility of the three-step protocol in patients with carcinoembryonic antigen (CEA)-expressing tumours, highlighting reduced background signal and preserved MoAb function. However, the technique required multiple injections and was limited by the immunogenicity of avidin or streptavidin. Cremonesi et al.[118] later characterised the pharmacokinetics of this protocol, showing that although kidneys, liver, and bladder absorbed the most radioactivity, toxicity remained low. Paganelli et al.[116] also applied the two-step protocol in patients with ovarian carcinoma, reporting favourable tumour targeting but again noting the drawbacks of repeated administrations and immunogenicity. In the context of high-grade gliomas, Paganelli and colleagues[119] reported that their three-step protocol achieved up to 15-fold greater tumour targeting compared to other organs. The treatment was well tolerated, and disease stabilisation or regression was observed in most patients. PEGylated avidin was recommended to reduce immune responses. Grana et al.[120] also showed promising results using this strategy in glioma patients, particularly when combined with surgery, chemotherapy, or radiotherapy. In a separate study, Paganelli et al.[121] established the maximum tolerated dose (1.11 GBq) and documented therapeutic responses and overall survival benefits. Building on these findings, Paganelli and coworkers developed the IART (Intraoperative Avidination for Radionuclide Therapy) technique, initially for breast cancer. This two-step method involves avidin application to the tumour bed immediately after surgical resection, followed the next day by intravenous injection of radiolabeled biotin. Circulating avidin is first neutralised by biotinylated albumin (20 mg). The post-surgical inflammatory microenvironment supports avidin retention at the tumour site[113,114,122]. Clinical trials showed that ^{111}In-labeled biotin (via DOTA) was rapidly and stably taken up at the surgical site, with favourable clearance and low toxicity. In a phase II study, Paganelli et al.[114] showed that administration of 3.7 GBq of ^{90}Y-DOTA-biotin delivered

a biologically effective dose (BED) of 21 Gy to the tumour bed. The authors concluded that IART could serve as a boost to conventional radiotherapy, and that the method might apply to other solid tumours beyond breast cancer, including bladder, prostate, and brain malignancies.

On the other hand, monomeric streptavidin possesses distinct structural and functional features that make it advantageous for certain biological applications compared to its natural tetrameric form. Its ability to bind biotin without inducing multivalent crosslinking is particularly useful in live-cell imaging and tracking, as it avoids unintended clustering of biotinylated targets, an effect that can alter biological activity. Moreover, monomeric streptavidin is well-suited as a genetically encoded biotin-binding tag, since it does not disrupt the oligomeric state of fusion partners, which is often a limitation with the tetramer. Despite having a lower affinity than the native form (which binds biotin with femtomolar strength), this weaker interaction can be beneficial in cellular assays, reducing saturation by endogenous biotin and allowing for controlled, reversible binding under mild conditions[123].

Historically, most engineered streptavidin monomers and dimers have suffered from low biotin affinity, poor stability, and aggregation[124–127]. These limitations were largely attributed to the absence of inter-subunit interactions, particularly the “hydrophobic lid” that stabilises biotin binding in the tetramer[126,128]. Structural studies confirmed that in tetrameric streptavidin, residues from multiple subunits contribute to the biotin-binding pocket[129,130]. However, more recent work by Lim et al.[131] introduced an A/D dimer, which preserves the tetramer-like binding site via covalent linkage of two subunits. Although this construct showed improved properties compared to a monomer (Kd = 17 nM vs. 38 nM), its affinity remained vastly lower than the tetramer’s (Kd ≈ 10^{-14} M), suggesting that additional factors beyond subunit organisation influence high-affinity biotin binding.

A significant breakthrough came with the study of rhizavidin, a natural streptavidin homolog from *Rhizobium etli* that forms a dimer instead of a tetramer due to key structural differences[132.] Surprisingly, rhizavidin still displays high-affinity biotin binding, even though its binding pocket is formed entirely within a single subunit[132]. This demonstrated that high affinity does not require inter-subunit contributions and

inspired efforts to redesign monomeric streptavidin using rhizavidin-based architecture. By grafting rhizavidin binding residues into a streptavidin monomer and introducing stabilising mutations through rational design, researchers achieved a 13-fold improvement in binding affinity and a significant increase in thermal stability. This optimised monomer is now the most stable variant reported to date, enabling its use in diverse molecular applications such as controlled ligand capture, biotin-based imaging, and affinity purification systems where reversible binding is required[123].

To exploit the avidin–biotin system in the context of cellular therapies and CAR-T cell platforms, Nagy et al. engineered Universal CAR-T (UniCAR-T) cells expressing a monomeric streptavidin variant (mSA2), which binds biotinylated trastuzumab as a modular targeting linker. These UniCAR-T cells showed efficient tumour infiltration and cytotoxicity in HER2-positive spheroids and xenograft models otherwise resistant to trastuzumab-mediated ADCC[133]. Central to this strategy is the use of antigen-dependent transcriptional control systems such as synNotch, which enable programmable gene expression in response to target cell recognition[51,134–136].

Finally, to mention another relevant pretargeting approach, the Dock-and-Lock (DNL) method by Goldemberg and colleagues is a modular engineering platform that generates multivalent, multifunctional molecules for improved cancer imaging and therapy. It exploits the natural interaction between the DDD domain of protein kinase A and the AD domain of AKAPs: when these domains are fused to different biological components, they form a stable and well-defined complex that preserves each component’s activity. This strategy enables the production of trivalent, bispecific constructs, such as two anti-CEA Fab fragments linked to a third Fab that binds a radionuclide-bearing hapten peptide. Used in a two-step pretargeting approach, these constructs first localise to the tumour and subsequently capture the radiolabelled hapten, achieving highly sensitive and specific tumour targeting for immunoSPECT/PET and demonstrating improved therapeutic efficacy in preclinical radioimmunotherapy models[137].

Monitoring the behaviour of CAR-T cells in vivo remains a critical challenge. Understanding whether these cells successfully home in on the tumour, infiltrate the tissue, and persist long enough to exert a therapeutic effect is essential for developing future optimised schedules and strategies.

Several imaging strategies have been developed to monitor CAR-T cell biodistribution and persistence in vivo using radionuclides. These approaches can be broadly divided into direct radiolabelling and indirect reporter-gene–based imaging, each offering specific advantages and limitations in terms of sensitivity, labelling stability, and feasibility for clinical translation. Table 1 summarises the main methodologies used for CAR-T cell imaging with PET and SPECT, including representative radionuclides and key considerations for preclinical and clinical applications.

Approach	Principle	Radionuclide (s)	Imaging Modality	Advantages	Limits	References
Direct radiolabelling (ex vivo)	CAR-T cells are labelled directly with a radionuclide before infusion	^{89}Zr-oxine, ^{89}Zr-DFO, ^{111}In-oxine	PET / SPECT	Simple; no genetic modification; high initial sensitivity	Label dilution as cells divide; potential impact on viability; no long-term tracking	*Kurebayashi et al.*[138]; *Lee et al.*[139]
Indirect imaging (reporter gene: NIS)	CAR-T cells are engineered to express the human sodium-iodide symporter (NIS)	^{124}I, ^{99m}Tc-pertechnetate, ^{18}F-TFB	PET / SPECT	Clinically approved reporter; good sensitivity; unlimited longitudinal imaging	Requires genetic modification; potential immunogenicity or altered biology	*Day et al.* [140]
Indirect imaging (reporter gene: HSV1-tk)	CAR-T cells express viral thymidine kinase, which traps specific radiotracers	^{18}F-FHBG, ^{124}I-FIAU	PET	High sensitivity; well-characterised reporter system	Viral genes may raise safety concerns; requires gene integration	*Semenova et al.*[141]
SPECT-based direct labelling	Radiolabelling of cells with γ-emitters	^{111}In-oxine	SPECT	Widely available; relatively simple	Lower spatial resolution; limited duration;	*Helfer et al.*[142]

					radiation burden	
PET reporter gene (e.g., hNET, eDHFR)	CAR-T cells express PET-compatible reporters	^{18}F-MFBG (hNET)	PET	High sensitivity; modular	Not clinically validated yet; genetic engineering required	*Sellmyer et al.*[143]

Table 1. Summary of currently available direct and indirect nuclear imaging approaches for *in vivo* tracking of CAR-T cells using radionuclides. For each strategy, the principle of labelling or reporter gene expression, the radionuclides and imaging modalities used, as well as key advantages, limitations and representative references are reported.

2. Experimental Plan

2.1 Modular Radiotracer Localisation

To enhance the precision of immune cell tracking and restrain off-target toxicities of radionuclide-based therapy, we have designed a series of viral vectors harbouring artificial receptors whose transcription should be active only upon tumour antigen engagement. The receptors are under the control of either the NFAT-responsive promoter, applicable to both CAR and TCR-based strategies, or the SynNotch-based transcriptional system, offering a highly modular and orthogonal design. Inducibility is thought to tightly regulate transgene expression, mirroring physiological immune activation, minimising off-target effects and enhancing safety.

A central component of this platform is the inclusion of the human sodium/iodide symporter (hNIS), which supports non-invasive imaging via PET or SPECT, as well as selective radionuclide uptake within the tumour microenvironment. hNIS expression, limited to tumour-engaged cells, ensures that only activated immune cells accumulate the radiotracer, thereby improving signal specificity and therapeutic precision.

In addition to hNIS, we engineered inducible expression of surface-displayed artificial receptors such as avidin and the monomeric variant monodin. Avidins can bind

biotinylated molecules, enabling a wide range of downstream applications, including cell labelling, diagnostic probe delivery, or ligand-mediated activation. Their expression exclusively in activated cells adds another layer of functional specificity. We explored the adaptation of the classical avidin–biotin pretargeting strategy, widely used in localised oncology settings for systemic disease[144,145]. This approach, termed Intraoperative Avidination for Radionuclide Therapy (IART®), has been developed and tested in breast cancer patients. This proof-of-principle study demonstrates that the intraoperative injection of avidin into the tumour bed after quadrantectomy enables the selective accumulation of intravenously administered radiolabelled biotin at the surgical site. The procedure is carried out in two sequential phases: first, the surgeon injects avidin into and around the tumour bed, thereby "marking" the local tissue, and subsequently, radiolabelled biotin is administered intravenously, allowing rapid and specific homing to the avidin-pretreated area. Scintigraphic imaging confirmed a fast and stable retention of labelled biotin in the operated breast quadrant. Dosimetric evaluation indicated that the local radiation dose exceeded 5 Gy/GBq, which corresponds to a therapeutic boost of approximately 20 Gy with the administration of 3.7 GBq (100 mCi) of ^90Y-biotin. These findings demonstrate the feasibility of IART® and strongly support the rationale for larger clinical trials assessing its integration with reduced-dose external beam radiotherapy[113]. However, such methods are inherently limited to locally advanced disease settings and not applicable to disseminated tumours.

To overcome this limitation, we propose a novel system in which avidin-based receptors are expressed in effector cells in an inducible manner, allowing them to recruit radiolabeled biotin only upon activation. This strategy enables targeted irradiation of disseminated tumours, as only immune cells that have successfully infiltrated and have been activated within the tumour microenvironment will retain the therapeutic agent. This reversible and highly specific platform broadens the application of pretargeting beyond local delivery, offering a powerful new avenue for systemically administered, cell-directed radiotherapy.

2.2 Inducible Platforms for Targeted Imaging and Therapy

To support this theranostic strategy, we designed twelve inducible vectors combining tumour-activated promoters with radionuclide-recruiting genes such as hNIS[38],

CD8TM-avidin, or CD8TM-monodin[64,65.] These genes are induced only in response to immune cell engagement, thereby improving spatiotemporal precision and reducing off-target toxicity.

The inducible platforms implemented are:

1. the synNotch system,

2. NFAT-responsive system

both described in the introduction section.

The vector backbones used include both retroviral and lentiviral systems. Specifically:

- pBULLET, a retroviral vector, was used for several constructs requiring efficient transduction of dividing T cells. It is an "all-in-one" vector with a constitutive CAR expression cassette and the NFAT-inducible cassette for a protein of interest, kindly provided by Professor Hinrich Abken (University of Leibniz).
- pCCL_EF1a, a third-generation lentiviral vector, offers stable integration and high transgene expression in a wide range of cell types, including primary T lymphocytes.
- The pHR_5xGAL4 UAS element was used to drive inducible expression downstream of the synNotch receptor, ensuring compatibility with the GAL4VP64 transcriptional module.

Table 2 summarises the constructs designed and the plasmid backbones functionally characterised in vitro for inducibility, dynamic range, leakiness, and radionuclide uptake. This design lays the foundation for an integrated immuno-radionuclide theranostic platform with unprecedented precision and control.

As previously reported, the receptors cloned downstream of these inducible elements include:

- hNIS (human sodium iodide symporter), enabling in vivo imaging and radionuclide-based therapy through accumulation of clinically approved radiotracers[91].

- monomeric CD8TM-avidin and CD8TM-monodin (monomeric Rhizavidin), which bind with high affinity to biotinylated compounds, thereby supporting a pretargeting strategy for localised delivery of radionuclides, as previously described[144,145].

Receptor/Marker	Host vector	Novel Vector name
Monodin/EGFP	pBULLET	pIND_Monodin EGFP
	ARI-001_pCCL_EF1a	pCOST_Monodin_EGFP
	pHR_5x Gal4 UAS sequence	pSYN_Monodin_EGFP
hNIS/EGFP	pBULLET	pIND_hNIS_EGFP
	ARI-001_pCCL_EF1a	pCOST_hNIS_EGFP
	pHR_5x Gal4 UAS sequence	pSYN_hNIS_EGFP
Avidin/EGFP	pBULLET	pIND_Avidin_EGFP
	ARI-001_pCCL_EF1a	pCOST_Avidin_EGFP
	pHR_5x Gal4 UAS sequence	pSYN_Avidin_EGFP
Empty-Control EGFP	pBULLET	pIND_EGFP
	ARI-001_pCCL_EF1a	pCOST_EGFP
	pHR_5x Gal4 UAS sequence	pSYN_EGFP

Table 2. Summary of final genetic constructs indicating the inserted gene and the corresponding host vectors. Each insert (monodin, hNIS, avidin, or "empty"-control EGFP) was cloned into three different backbones to enable either inducible or constitutive expression. Inducible vectors included the NFAT-responsive pBULLET retrovirus and the GAL4-UAS-based pHR_5x lentiviral system, while constitutive expression was achieved using the ARI-001_pCCL_EF1a vector.

3. Materials and Methods

Reagents and Resources

Material / Reagent	**Company**	**Catalog #**	**Notes / Application**
8xNFAT-ZsG-hCD8 plasmid	Addgene (Nakayama Lab)	153417	NFAT-driven reporter plasmid (ZsGreen, hCD8αβ)
[99mTc]NaTcO4	-	-	Radionuclide uptake assay
Agarose	Biorad	1613101	Gel electrophoresis
Anti-FLAG M2 antibody	Sigma-Aldrich	F1804	Detection of FLAG-tagged constructs
Anti-hNIS Alexa Fluor 647 (Clone 90232)	R&D Systems	FAB7720R	Flow cytometry detection of hNIS
Anti-Myc-PE antibody	Cell Signalling	9B11	Detection of Myc-tag (SynNotch)
ARP-1 cells	-	-	Multiple myeloma BCMA+ cells
BCPAP	-	-	Papillary thyroid carcinoma cell line
Biotin-Atto 655	Sigma-Aldrich	77633	Detection of avidin/monodin receptors
Biotin-PE	Sigma-Aldrich	B3497	Detection of avidin/monodin receptors
CD137-PE antibody	Miltenyi Biotec	130-110-900	T cell activation marker
DMEM High Glucose	Euroclone	ECB7501L	Cell culture medium
Dynabeads CD3/CD28	Miltenyi Biotec	11131D	T cell activation

EcoRI-HF restriction enzyme	New England Biolabs	R3101S	Restriction digestion
FACS Melody cell sorter	BD Biosciences	-	Cell sorting system
Fetal Bovine Serum (FBS)	Thermo Fisher Scientific	17974731	Cell culture supplement
Flow cytometer Attune NxT	Thermo Fisher Scientific	-	Flow cytometry analyses
FlowJo software	BD Biosciences	-	Flow cytometry data analysis
Goat anti-Mouse IgG (H&L) Alexa Fluor 488	Thermo Fisher Scientific	A11001	Secondary antibody for FLAG detection
HEK293T	Takara Bio	632180	Lentiviral production
Human PBMCs (from buffy coats)	-	-	Primary T cell source
IL-15	Miltenyi Biotec	170-076-114	Cytokine supplement
IL-7	Miltenyi Biotec	170-076-111	Cytokine supplement
Jurkat cells	-	-	Human T-cell line
K562 cells	-	-	Lymphoblast BCMA- cells
L-Glutamine	Thermo Fisher Scientific	25030081	Cell culture supplement
Lenti-X Concentrator	Takara Bio	631232	Concentration of viral particles
MACS buffer (PBS + EDTA + BSA)	Miltenyi Biotec	130-091-221	FACS buffer/separation buffer
NALM-6 cells	-	-	CD19+ acute lymphoblastic leukemia

NEB Stable Competent E. coli	New England Biolabs	C3040H	Bacterial strain for plasmid propagation
Nthy-ori	-	-	Immortalised thyroid follicular epithelial cells
Pan T Cell Isolation Kit	Miltenyi Biotec	130-096-535	Negative selection of Pan-T cells
pBullet vector	Prof. Hinrich Abken	N/A	NFAT-inducible retroviral vector (backbone)
pCCL_EF1a_BCMAh	Custom / ARI-001 backbone	N/A	Constitutive lentiviral backbone
pCL-ECO packaging plasmid	Addgene	12371	Retroviral packaging
Penicillin/Streptomycin	Euroclone	ECB3001D	Cell culture supplement
Phoenix-Ampho cells	-	CRL-3213	Retroviral production
pHR_5xGAL4 UAS	Addgene	79119	GAL4 UAS-inducible vector
pHR_PGK_antiCD19_synNotch_Gal4VP64	Addgene	79125	SynNotch anti-CD19 receptor
pHR_PGK_antiHer24D5-3_synNotch_Gal4VP64	Addgene	85422	SynNotch anti-Her2 receptor
Phytohaemagglutinin (PHA)	InvivoGen	00-4970-93	NFAT stimulation
Polybrene	Sigma-Aldrich	TR-1003	Lentiviral transduction enhancer
Polyethylenimine, (PEI) Linear, MW 25000, Transfection Grade (PEI 25K™)	Polysciences	23966	DNA transfection reagent
Qiagen EndoFree Plasmid Maxi Kit	Qiagen	12362	Plasmid DNA extraction with endotoxin removal

rCutSmart Buffer	New England Biolabs	B6004S	Reaction buffer for digestions
Retro-X Concentrator	Takara Bio	631455	Concentration of retroviral particles
RetroNectin reagent	Takara Bio	T100A/B	Virus coating for transduction
RPMI 1640 medium	Euroclone	ECB9006L	Cell culture medium
SK-BR-3 cells	-	-	HER2+ breast cancer cell line
Sodium perchlorate (NaClO4)	-	-	Competitive inhibitor of NIS
Sodium rhenate (NaReO4)	-	-	Competitive inhibitor of NIS
TAE buffer	Biorad	1610743	Electrophoresis

Table 3. Comprehensive list of reagents and resources employed. The table provides a complete overview of the plasmid backbones, cell lines, kits, reagents, antibodies, and buffers utilised in the present study. For each material, the corresponding supplier and catalog number (when available) are indicated, in order to facilitate traceability, reproducibility, and potential replication of the experimental procedures.

3.1 Plasmid acquisition and preparation

To initiate the development of our expression constructs, several plasmids were acquired via Addgene with their respective identifiers:

- 8xNFAT-ZsG-hCD8 (Addgene Plasmid #153417)[135]: this served as the initial inducible system before transitioning to the pBullet vector. This construct enables conditional expression of genes placed under the control of eight tandem NFAT DNA-binding consensus sequences, followed by a TATA box, which provides tight regulation of transcriptional activation. In its original form, the plasmid includes ZsGreen as a fluorescent reporter, allowing for real-time

monitoring of NFAT pathway activation via fluorescence microscopy and flow cytometry (Figure 5).

- pHR_PGK_antiHer24D5-3_synNotch_Gal4VP64 (Addgene Plasmid #85422): a synNotch antiHer2 receptor expression vector.
- pHR_PGK_antiCD19_synNotch_Gal4VP64 (Addgene Plasmid #79125): a synNotch antiCD19 receptor expression vector.
- pHR_5x Gal4 UAS (Addgene Plasmid #79119): containing upstream activation sequences for inducible expression[50].

The plasmid vector developed by Prof. Hinrich Abken (pBullet) was provided directly on spotted filter paper and served as the backbone for NFAT-inducible expression.

The final twelve constructs used throughout the project were cloned as detailed in the section below.

To generate bacterial glycerol stocks for long-term storage and plasmid propagation, all vectors were transformed into NEB® Stable Competent *E. coli* (*New England Biolabs*) cells, using standard transformation protocols to minimise recombination.

Plasmid DNA was extracted using the Qiagen EndoFree Plasmid Maxi Kit, following the manufacturer's instructions and centrifugation at maximum speed for 25 minutes. This kit includes specific endotoxin-removal steps that are critical for downstream applications involving mammalian cell transduction.

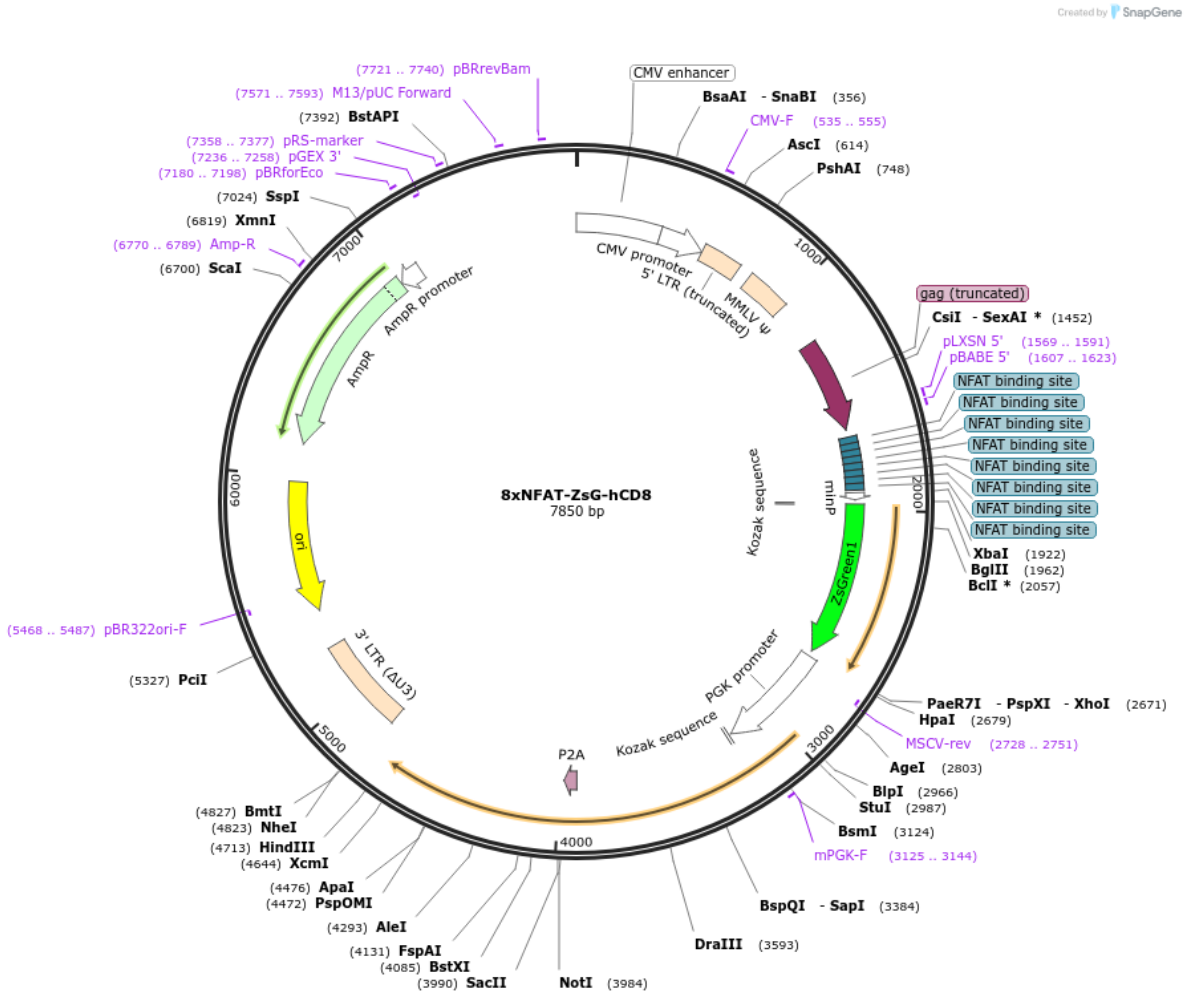

Figure 5. Schematic representation of the 8xNFAT-ZsGreen1-hCD8 plasmid (Addgene #153417). This retroviral plasmid contains a synthetic promoter composed of eight tandem NFAT response elements (8xNFAT) upstream of a minimal TATA box, allowing inducible transcription in response to NFAT pathway activation. Downstream of the promoter, the expression cassette includes the ZsGreen1 fluorescent protein, followed by an IRES (internal ribosome entry site) enabling bicistronic expression of the human CD8α and CD8β chains. The vector is based on an MSCV-derived retroviral backbone and includes long terminal repeats (LTRs) for retroviral integration, a packaging signal, and an ampicillin resistance gene for bacterial selection.

3.2 Cloning strategies and construct design

The design and generation of synthetic constructs were based on a detailed cloning plan developed collaboratively to support both inducible and constitutive expression of engineered receptors in effector cells. This cloning strategy aimed to allow modular insertion of receptors (e.g., hNIS, avidin, monodin) into vectors suitable for

downstream functional studies in T cells, including CAR-T models. The cloning strategy was designed to generate both inducible and constitutive constructs for those receptors, with EGFP used as a control.

All receptors were codon-optimised for mammalian expression and included a CD8α leader peptide for ER targeting, an optional FLAG tag (for avidin and monodin), the receptor sequence, a CD8α hinge and transmembrane domain for membrane localisation, and a stop codon. Detection of hNIS was performed using a specific antibody; no FLAG tag was added.

Inducible constructs were generated in two backbones:

- pBullet retroviral vector, carrying an NFAT-responsive promoter, where receptor sequences were cloned between HindIII–NcoI sites.

- pHR_5xGAL4 UAS lentiviral vector, optimised for SynNotch systems, where receptor sequences were cloned between BamHI–NotI sites.

In both systems, the receptor genes were placed in the sense orientation, while the CMV–T2A–eGFP cassette was positioned on the opposite strand to allow simultaneous inducible receptor expression and constitutive GFP expression to track transduced cells. Final constructs included:

- Inducible NIS Construct

- Inducible Avidin Construct

- Inducible Monodin Construct

- Vector-only control CMV–T2A–eGFP (no receptor).

Constitutive constructs were generated using the pCCL_EF1a lentiviral vector. Receptor sequences were cloned between BamHI–BspEI sites under the control of the CMV promoter (full-length, to ensure robust expression). As in the inducible

vectors, the CMV–T2A–eGFP cassette was retained in the antisense orientation, functioning as a constitutive marker. All sequences were designed and annotated in Serial Cloner, and the final expression cassettes were synthesised and prepared for external cloning (Figure 6).

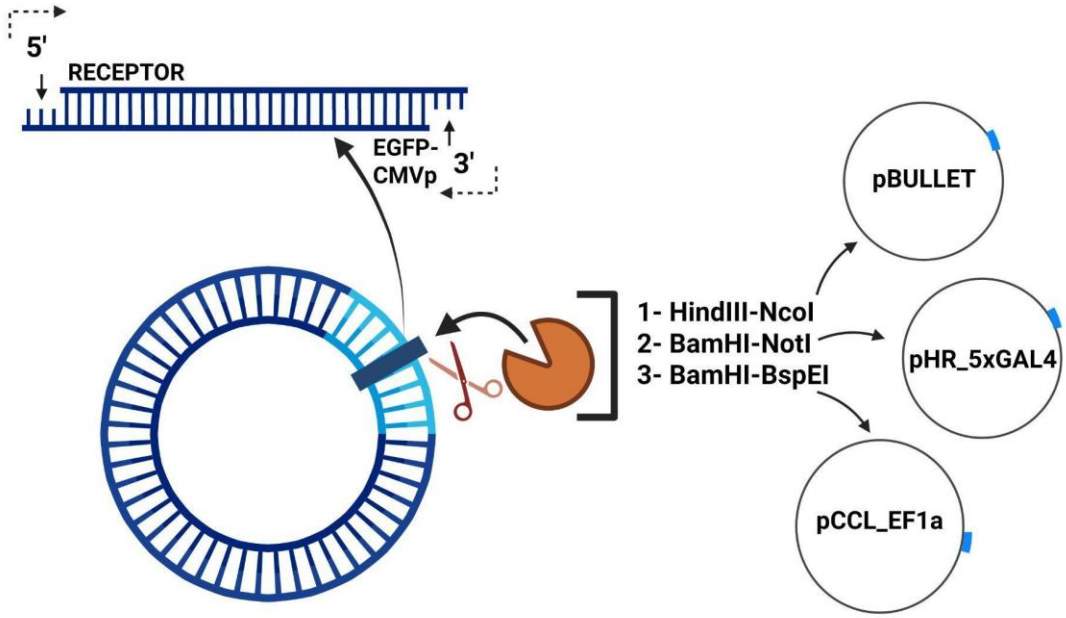

Figure 6. Schematic representation of the cloning workflow for engineered receptor genes (hNIS, avidin, monodin, or EGFP as control) into different retroviral and lentiviral vectors. Inserts were excised from the donor plasmid with diverse combinations of endonucleases, specifically HindIII–NcoI for pBULLET inducible retroviral vector, BamHI–NotI for pHR_5xGAL4 lentiviral vectors, and BamHI–BspEI for pCCL_EF1a constitutive lentiviral vector. EGFP constitutive expression under the control of CMV promoter (CMVp–EGFP) was achieved by cloning into the antisense strand. Created on Biorender.

3.3 Plasmid Backbones and General Strategy

Three main plasmid vectors were used to subclone the inserts described in 3.2:

1. The pBullet retroviral vector is designed for an NFAT-driven inducible expression in an MMLV-based system. Inserts were cloned as HindIII / NcoI fragments with the inducible receptor genes and the constitutively expressed EGFP marker on opposite strands to reduce potential transcriptional interference. In this vector, EGFP is under the control of the original CMV promoter to function as a constitutive marker of transduction, allowing fluorescence-based tracking of infected cells regardless of receptor activation.
2. pHR_5xGAL4 UAS lentiviral vector (Addgene #79119) is used in association with SynNotch-based inducible systems. Inserts were cloned as BamHI / NotI fragments, while GFP was expressed from the opposite strand under CMV.
3. pCCL_EF1a lentiviral vector was used to drive constitutive expression of the receptors. In this vector, inserts were cloned as BamHI / BspEI[146].

In all vectors, EGFP constitutive expression functions as a marker of effective transduction.

3.4 Cloning verification through plasmid digestion and gel electrophoresis

To verify the correct insertion of target sequences into the plasmid backbones, analytical restriction digests were performed on both inducible and constitutive constructs. Each plasmid sample was prepared for digestion by combining 1 µg of plasmid DNA with 5 µL of rCutSmart® Buffer (New England Biolabs) and 1 µL of EcoRI-HF® restriction enzyme (NEB #R3101), in a final volume of 50 µL adjusted with nuclease-free water. Digestion reactions were incubated overnight in a thermal block using a pre-set program: 15 minutes at 37 °C for enzymatic activity, followed by 20 minutes at 65 °C for enzyme heat inactivation, and then held at 4 °C overnight.

For gel electrophoresis, 200 ng of DNA was loaded per well, both for digested and undigested (control) samples. In the case of digested plasmids, 10 µL of the digestion mixture was mixed with 2 µL of loading buffer. Undigested samples were prepared by adjusting the appropriate volume of plasmid DNA to reach 200 ng, then bringing the total volume to 12 µL with nuclease-free water and 2 µL of loading dye. All samples were run on a 1% agarose gel in TAE buffer along with a molecular weight marker (1.5 µL per lane) loaded at regular intervals for size comparison.

3.5 Viral Vector Production

Lentiviral particles were produced in HEK293T cells cultured in RPMI 1640 supplemented with 10% fetal bovine serum (FBS), 1% L-glutamine, and penicillin/streptomycin. This medium was selected due to its relatively low biotin content, which minimises avidin/monodin saturation and facilitates downstream detection. Retroviral particles were produced in Phoenix-Ampho cells cultured in DMEM high glucose + 10% FBS, 1% L-glutamine, and penicillin/streptomycin.

Cells were plated the day before transfection at a density of 3×10^6 cells per 10 cm dish. The following day, the transfection was performed using third-generation lentiviral packaging vectors with the quantities indicated as follows:

- VSV-G (1.5 µg)
- pRRE (2.5 µg)
- pRSV-REV (1.25 µg)

Within the same transfection solution, 5 µg of plasmid/plate for the single receptor constructs were added, all diluted in 500 µL of 150 mM NaCl. Separately, polyethylenimine (PEI) was diluted in 150 mM NaCl to 500 µL (30 µg per plate, 3:1 PEI:DNA ratio). The PEI mix was added dropwise to the DNA solution, vortexed, and incubated for 15 minutes at room temperature. The 1 mL transfection mix was then added dropwise to the cells. As a transfection control, a separate dish was transfected with 5 µg of a constitutive GFP-expressing plasmid (pcDNA3.1+P2A-eGFP/6.2kb).

After 24 hours, the medium was replaced. Viral supernatants were collected at 48- and 72-hours post-transfection, each time replacing the medium with 10ml fresh medium. Supernatants were centrifuged at 2000 rpm for 5 minutes to remove cell debris, filtered through a 0.45 µm filter, and stored at 4 °C. The two harvests were pooled.

Retroviral production was performed following the same procedure but using the packaging plasmid pCL-ECO (5 µg) instead of the lentiviral packaging mix. Virus titers were later assessed by transduction-based titration assays.

To increase viral transduction efficiency, both lentiviral and retroviral particles were concentrated using the Lenti-X/Retro-X Concentrator reagent (Takara Bio), following the manufacturer's protocol.

3.6 Cell Isolation, Culture Conditions and Transduction

Peripheral blood mononuclear cells (PBMCs) were isolated from healthy donor buffy coats using standard Ficoll density gradient centrifugation (LymphoSep). Pan-T cells were then enriched by negative selection using the Pan T Cell Isolation Kit (Miltenyi Biotec), according to the manufacturer's protocol. Isolated T cells were activated for 3 days using anti-CD3/CD28 Dynabeads (Miltenyi Biotec), following bead-to-cell ratios as recommended. After removing the beads using a magnet, cells were cultured in RPMI medium supplemented with 10% FBS, 10 ng/mL IL-7 and 5 ng/mL IL-15 before proceeding to transduction.

Jurkat cells were maintained in RPMI 1640 with 10% FBS and used as an additional target cell line for transduction experiments.

Nthy-ori and BCPAP thyroid lines were used for specific uptake and blocking assays and cultured on gelatin-coated flasks in specialised thyroid medium.

Cell viability was routinely assessed using trypan blue exclusion, and surface marker expression was verified via flow cytometry.

Jurkat and activated Pan-T cells were transduced using a RetroNectin®-based protocol (Takara Bio), suitable for both lentiviral and retroviral particles. Non-treated 24- or 6-well plates were coated with RetroNectin at a concentration of 20–100 µg/mL in PBS and incubated for 2 hours at room temperature. After blocking with 2% BSA and washing, viral supernatant was added to the coated plates and centrifuged at 1900g for 2 hours at 4 °C to promote virus binding. The viral supernatant was then removed, and target cells (either Jurkat or previously activated Pan-T cells), were added at a density of $0.5–2.5\times10^4$ cells/cm². Cultures were maintained for 48–72 hours at 37 °C, 5% CO_2, before downstream analysis.

Additionally, lentiviral transduction of Jurkat cells was performed using polybrene (8 µg/mL) to enhance viral entry. In this alternative approach, cells in suspension were

exposed to viral supernatant supplemented with polybrene and centrifuged at 800g for 90 minutes at room temperature (spinfection), followed by incubation for 48–72 hours.

Transduced cells were then expanded, and to purify transduced cell populations, fluorescence-activated cell sorting was performed using a BD FACSMelody. On the day before sorting, collection tubes were filled with MACS buffer (PBS, 2 mM EDTA, 0.5% BSA) and stored overnight at 4 °C to allow BSA coating of the tube surface, thereby promoting cell recovery. Starting with the protocol, cells were harvested, counted, and resuspended at a density of 10 million cells/mL in MACS buffer. A small aliquot (50 µL) was diluted to 1 mL with MACS buffer for compensation and unstained controls. Cells were stained using appropriate antibodies in MACS buffer, washed with PBS, and filtered through a 40 µm cell strainer to prevent clogging.

Collection tubes were pre-filled with 300 µL of culture medium to preserve cell viability upon sorting. After sorting, the collected cells were centrifuged shortly and resuspended in a minimal volume of fresh medium, considering typical cell losses during the procedure. Cells were then seeded at the desired density for expansion and further experimental use.

When multiple vectors were introduced, sequential infections followed by ATTUNE flow cytometer-based enrichment were performed to ensure the purity of the engineered cell populations.

All flow cytometry experiments were performed with the number of independent biological replicates indicated in the corresponding figure legends. For experiments conducted with multiple biological replicates ($n \geq 2$), data are reported as mean ± standard deviation (or SEM). Experiments shown as representative technical validations of multi-step workflows (including lentiviral vector production, transfection/transduction, and downstream flow cytometry analyses) were, in some cases, performed with a single biological replicate ($n = 1$); in these instances, error bars are not shown, as variability cannot be calculated from a single measurement.

3.7 Preliminary Evaluation of Constitutive hNIS Expression (pCONTROL vector)

To evaluate the constitutive expression and functional activity of the hNIS, Jurkat and HEK293T cells were transduced with a pCONTROL lentiviral vector encoding hNIS under a constitutive promoter. It also included additional functional elements: HSV-TK (herpes simplex virus thymidine kinase) as a suicide gene, and FGFR1 FKBP12-FLAG, which enables drug-inducible dimerisation and downstream signalling activation. The three elements HSV-TK, FGFR1-FKBP12-FLAG, and hNIS were separated by self-cleaving peptides T2A and P2A, ensuring equimolar expression from a single promoter (Figure 7).

HEK293T cells were cultured in DMEM High Glucose supplemented with 10% fetal bovine serum (FBS), 1% penicillin/streptomycin, and 2% L-glutamine (twice the standard concentration) to support robust growth and protein expression, while Jurkat cells were cultured in RPMI 1640 as previously reported.

Forty-eight to seventy-two hours post-transduction, NIS expression on the cell surface was monitored by flow cytometry (Attune NxT system) using the Human SLC5A5 Alexa Fluor® 647-conjugated antibody (Clone 90232, R&D Systems). Transduced, NIS-positive populations were then purified by FACS based on Alexa Fluor 647 signal.

Sorted Jurkat and HEK293T cell populations were shipped to the CNR of Padua for functional validation via radionuclide uptake assays. 1×10^6 NIS-positive cells/not positive cells as control were resuspended in 500 µL serum-free medium and incubated with 5–10 µCi of [^{99m}Tc]$NaTcO_4$ at 37 °C or 4 °C. Uptake kinetics were evaluated at multiple time points (5, 15, 30, 60 minutes, and up to 6 hours for retention studies). Post-incubation, cells were washed with either ice-cold PBS or an acidic buffer (0.1 M acetic acid, 0.15 M NaCl, pH 5.5) to eliminate non-specific surface-bound radioisotopes. Pellets and supernatants were collected separately, and radioactivity was quantified using a gamma counter. Total uptake was calculated as the percentage of total counts in the cell pellet.

To assess transport specificity, parallel conditions included competitive inhibition with sodium perchlorate ($NaClO_4$, 100 µM) or sodium rhenate ($NaReO_4$, 100 µM), added 15 minutes before [^{99m}Tc]$NaTcO_4$ exposure.

As a physiological control, the same [^{99m}Tc]$NaTcO_4$ uptake assay was performed on two well-characterised thyroid-derived cell lines: BCPAP (a papillary thyroid carcinoma line) and NTHY-ORI (an immortalised non-tumoral human thyroid follicular epithelial cell line). These served as positive and baseline controls, respectively, to validate NIS-mediated radiotracer uptake in cells endogenously expressing the symporter.

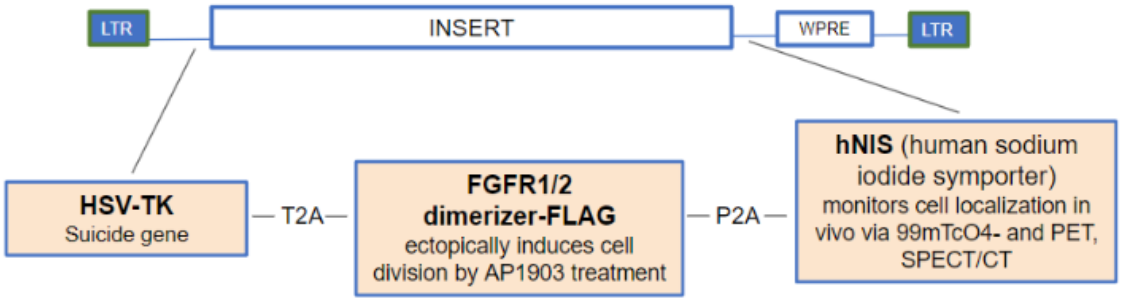

Figure 7. Structure and organisation of the individual modules that constitute the pCONTROL vector.

3.8 Transduction and Detection of Constitutive 001_pCCL_EF1a Vectors

Jurkat and Pan-T cells were transduced with lentiviral vectors derived from the ARI-001_pCCL_EF1a backbone, encoding constitutively expressed surface receptors, hNIS, avidin, and monodin, as previously described using a RetroNectin®-based transduction protocol. Following 48–72 hours of incubation post-transduction, infection efficiency and surface expression of the receptors were assessed by flow cytometry using the Attune NxT cytometer.

To detect hNIS expression, cells were stained with Human SLC5A5 Alexa Fluor® 647-conjugated antibody (Clone 90232, R&D Systems).

For the detection of avidin-based receptors, cells were analysed using multiple strategies:

- Biotin-Phycoerythrin (PE) (Merck) and biotin-Atto 655 (Sigma-Aldrich) were used as fluorophore-conjugated ligands to detect cell surface expression via high-affinity binding to avidin or monodin.

- Receptors were also detected with Anti-FLAG M2 mouse monoclonal antibody (Sigma-Aldrich), followed by Goat anti-Mouse IgG (H&L) Alexa Fluor® 488-conjugated secondary antibody (Thermo Fisher Scientific). Analyses were carried out using FlowJo software.

3.9 Evaluation of inducibility in target cells expressing the 8xNFAT-ZsG-hCD8 construct

Jurkat T cells and primary human Pan-T cells were transduced with retroviral particles encoding the 8xNFAT-ZsG-hCD8 reporter construct (Addgene #153417, Nakayama lab), produced in Phoenix-Ampho packaging cells as previously described. After 48–72 hours, NFAT pathway activation was induced using phytohaemagglutinin (PHA, InvivoGen) at various concentrations (0.125 µg/mL, 0.25 µg/mL, 0.625 µg/mL, 1.25 µg/mL, 2.5 µg/mL) for 2, 4, 6, or 24 hours, depending on the experiment.

Following PHA stimulation, cells were washed in PBS and resuspended in fresh complete medium. GFP fluorescence (ZsGreen) was analysed by flow cytometry (Attune NxT) to determine the extent of NFAT activation. Based on the percentage of GFP^+ cells observed, GFP^+ Jurkat cells were sorted using a FACS Melody BD cell sorter. Cells were collected into tubes pre-filled with 300 µL of RPMI medium supplemented with 10% FBS, penicillin/streptomycin, and glutamine, and subsequently expanded in 24-well plates.

Approximately 40,000 sorted GFP^+ Jurkat cells were expanded and maintained in culture for subsequent assays. A time-course experiment was performed to evaluate signal persistence: cells were stimulated with 1.25 µg/mL PHA for 4 hours, then extensively washed and cultured in fresh medium. ZsGreen signal was monitored at 2-hour intervals over 24 hours. A restimulation assay was also conducted after signal decay, by re-exposing the cells to PHA to assess NFAT re-inducibility.

3.10 Co-transduction With Anti-BCMA CAR

Sorted NFAT^{+} Jurkat cells were co-transduced with a lentiviral vector encoding a constitutively expressed anti-BCMA CAR and analysed for dual expression and functional response. Activation assays included:

- PHA stimulation (1,25 µg/mL to 2,5 µg/mL for 6–24 hours);
- Stimulation with soluble BCMA-Fc fusion protein (ENZO Life Sciences);
- Co-culture with ARP-1 cells (multiple myeloma cells BCMA^{+}) and K562 (lymphoblast cells BCMA^{-}) target cells (1:1 E:T ratio);
- Dynabeads CD3/CD28 (Miltenyi Biotec) stimulation at 25 µL per 1×10^{6} cells for up to 72 hours.

ZsGreen expression was used as a direct readout of NFAT activation. CAR expression was detected via anti-human Fab2-Alexa Fluor 647 staining. Additional activation markers, such as CD137-PE, were assessed to monitor early T cell activation. All samples were analysed by flow cytometry, with gating on live, single-cell lymphocyte populations.

3.11 Inducible Expression Systems: pBULLET (NFAT) and pHR_5xGAL4 (synNotch)

To evaluate the inducible expression of engineered receptors (hNIS, avidin and monodin), Jurkat cells were transduced with retroviral or lentiviral particles encoding each construct cloned into either the pBULLET (NFAT-inducible) or pHR_5xGAL4 (GAL4-inducible) vectors, respectively. Viral production and transduction were performed as previously described using Retronectin-coated plates.

NFAT-Inducible System (pBULLET):
Following transduction, Jurkat cells were stimulated with either PHA (1,25 µg/mL, InvivoGen) or Dynabeads CD3/CD28 (25 µL per 1×10^{6} cells, Miltenyi) to activate the NFAT pathway. Stimulations were performed for either 4 or 24 hours. After stimulation, cells were stained with the appropriate reagents to detect surface expression of inducible proteins:

- Anti-hNIS Alexa Fluor 647 (Clone 90232)
- Biotin-PE (Sigma) or Biotin-Atto655 (Sigma) for avidin/monodin

- Anti-FLAG M2 (Sigma) followed by Goat anti-Mouse Alexa Fluor 488 secondary antibody (Thermo Fisher)

Flow cytometric analysis was carried out using the Attune NxT cytometer. Activation-induced expression of inducible receptors was compared with control vector–transduced cells lacking any receptor insert (“empty vector”). Only upon stimulation did the transduced cells express the respective receptors, validating NFAT-dependent inducibility.

SynNotch Inducible System (pHR_5xGAL4):

In parallel, Jurkat cells were transduced with pHR_5xGAL4 inducible constructs and stimulated through co-culture with SK-BR-3 $HER2^+$ or CD19+ (NALM-6) target cells. For this purpose, effector Jurkat cells had been previously transduced with the pHR_PGK_antiHer24D5-3_synNotch_Gal4VP64 or pHR_PGK_antiCD19_synNotch_Gal4VP64 vector and sorted for Myc-tag expression using anti-Myc-PE staining. These SynNotch-positive Jurkat lines served as the effector platform for subsequent co-transductions with GAL4-responsive vectors encoding NIS and the avidin variants. These engineered cells will express GAL4-inducible receptors (hNIS, avidin, or monodin) only upon HER2/CD19 recognition.

SynNotch-expressing Jurkat cells were co-cultured with $HER2^+$ SKBR3 breast cancer cells or CD19+ NALM-6 acute lymphoblastic leukaemia cells, at different effector-to-target (E:T) ratios (1:1, 1:5, and 1:10) for either 2 or 3 days. Following co-culture, cells were harvested and stained as above for receptor detection. Only co-culture with $HER2^+$/$CD19^+$ targets would trigger GAL4-dependent receptor expression, confirming inducibility in the synNotch context.

All experiments included unstimulated controls and “empty vector” controls to verify the specificity and inducibility of expression.

4. Results

4.1 pCONTROL lentiviral vector testing

In order to test if the sequence for the hNIS to be cloned in the inducible vectors was correct, we relied on the pCONTROL lentiviral vector available in the lab (above, Figure 7), where hNIS is constitutively expressed under the EF1a promoter.

Experiments on Jurkat and HEK293T transduced as described in the Methods section led to successful expression and functional validation of hNIS. Specifically, successful expression of both FLAG and hNIS proteins was first confirmed by Western blot analysis (Figure 8, panel A). Additionally, the correct localisation and folding of hNIS at the plasma membrane was verified by flow cytometry using a specific anti-hNIS antibody that recognises an extracellular epitope, suggesting that the protein is correctly folded and topologically functionally accessible on the cell surface (Figure 8, panel B). These results confirm that the pCONTROL is capable of efficiently transducing Jurkat and HEK293T human cell lines and is expressed at the plasma membrane.

Western Blot and Flow Cytometry Results

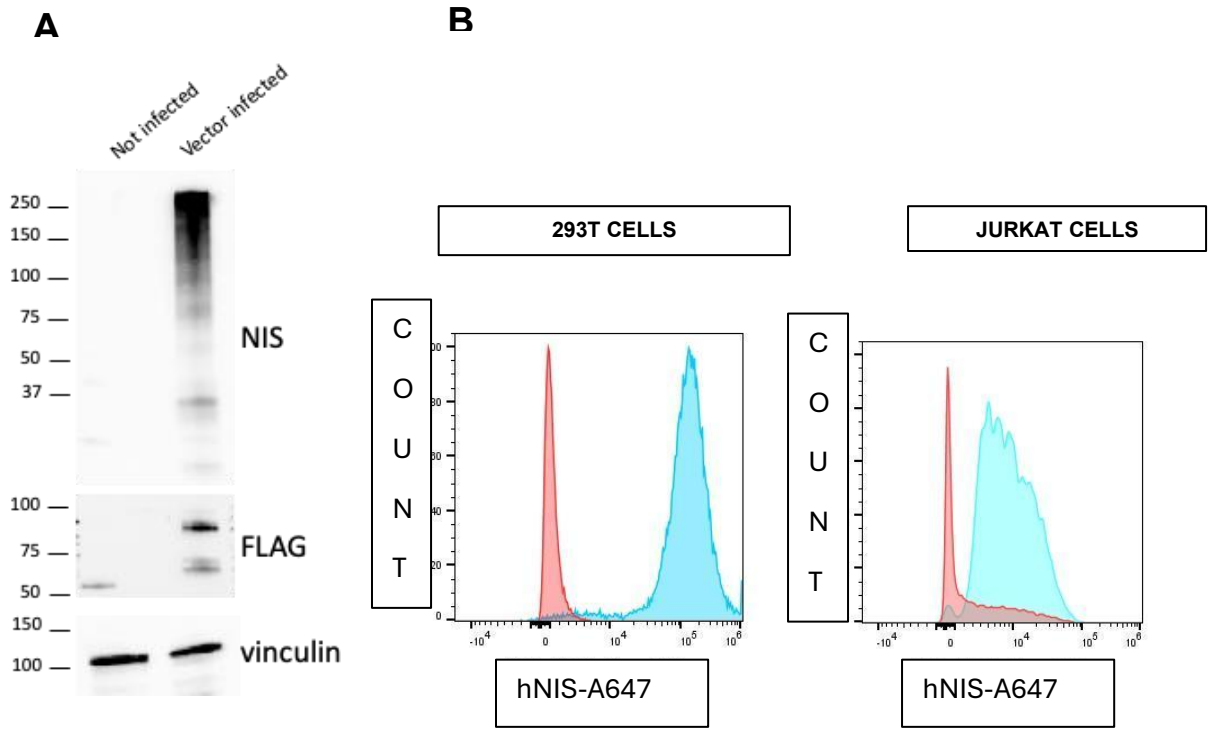

Figure 8. Western blot and flow cytometry analysis of hNIS expression and plasma-membrane localisation in cells not infected/infected with the pCONTROL vector.

Panel (A): Western blot of hNIS expression. Two lanes are shown: Not infected and Vector infected. In the NIS blot, the *Vector-infected* lane displays a strong, broad signal spanning high molecular weights (≈150–250 kDa), while the *Not infected* lane shows no detectable band. In the FLAG blot, a distinct band is present only in the *Vector-infected* lane (≈100 kDa); no signal is observed in the *Not infected* lane. Vinculin (~100–120 kDa) appears as a band of comparable intensity in both lanes (loading control).

Panel (B): Flow cytometry assessment of surface hNIS and proper folding on HEK292T and Jurkat cells. Live cells were stained with an anti-hNIS antibody and analysed by flow cytometry. Anti-hNIS fluorescence is plotted on the x-axis and side scatter (SSC) on the y-axis. A positive shift in anti-hNIS signal relative to the appropriate control indicates that hNIS is correctly localised at the plasma membrane, properly folded, and functionally accessible on the cell surface.

To functionally validate hNIS activity, sorted hNIS-positive and negative cells were subjected to radionuclide uptake assays using technetium-99m pertechnetate ($[^{99m}Tc]NaTcO_4$). The workflow and the setup of the uptake experiments, performed in collaboration with the CNR of Padua, are shown in Figure 9.

Cell uptake protocol

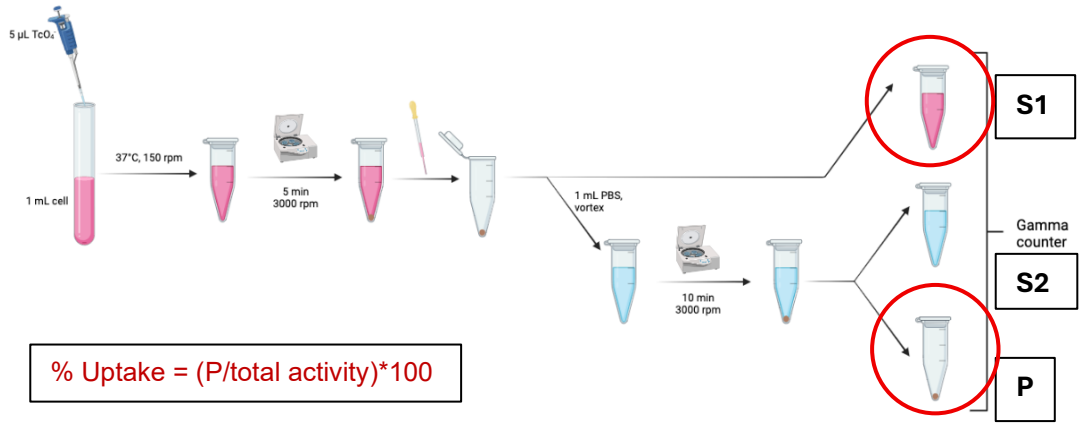

Figure 9. Schematic representation of [^{99m}Tc]pertechnetate uptake experiment. Cells (1 × 10^6 cells mL^{-1}) were incubated with 5 µL (≈ 5 µCi) of [^{99m}Tc]pertechnetate in 1 mL of medium at 37 °C with gentle agitation (150 rpm). After incubation, cells were pelleted by centrifugation (5 min, 3000 rpm), and the first supernatant (S1) was collected. Cell pellets were washed with 1 mL PBS, vortexed, and re-centrifuged (10 min, 3000 rpm); the second supernatant (S2) was then collected to account for residual unbound radiotracer. The final pellet (P), corresponding to intracellular and membrane-associated tracer, was recovered. All three fractions (S1, S2, P) were analysed separately using a gamma counter to quantify radiotracer distribution and calculate specific uptake.

The experiments were mainly articulated into four categories: time-course experiments (rotation, culture media, Figure 10); temperature dependence assays, 37°C vs 4°C uptake (Figure 11) and competitive inhibition (block studies) with NaReO4 and NaClO4 (Figure 12). Flow cytometric analysis revealed higher levels of hNIS expression in HEK293T cells, which correlate with improved tracer uptake. Quantitative analysis of tracer uptake over time (Figure 10) demonstrated a rapid increase within 15–30 minutes post-incubation, with signal saturation observed by 3 hours. Notably, the uptake percentage at 30 minutes in HEK293T cells was approximately tenfold higher than in Jurkat cells, consistent with their superior transduction efficiency and hNIS expression levels (MFI signal).

Time course experiment

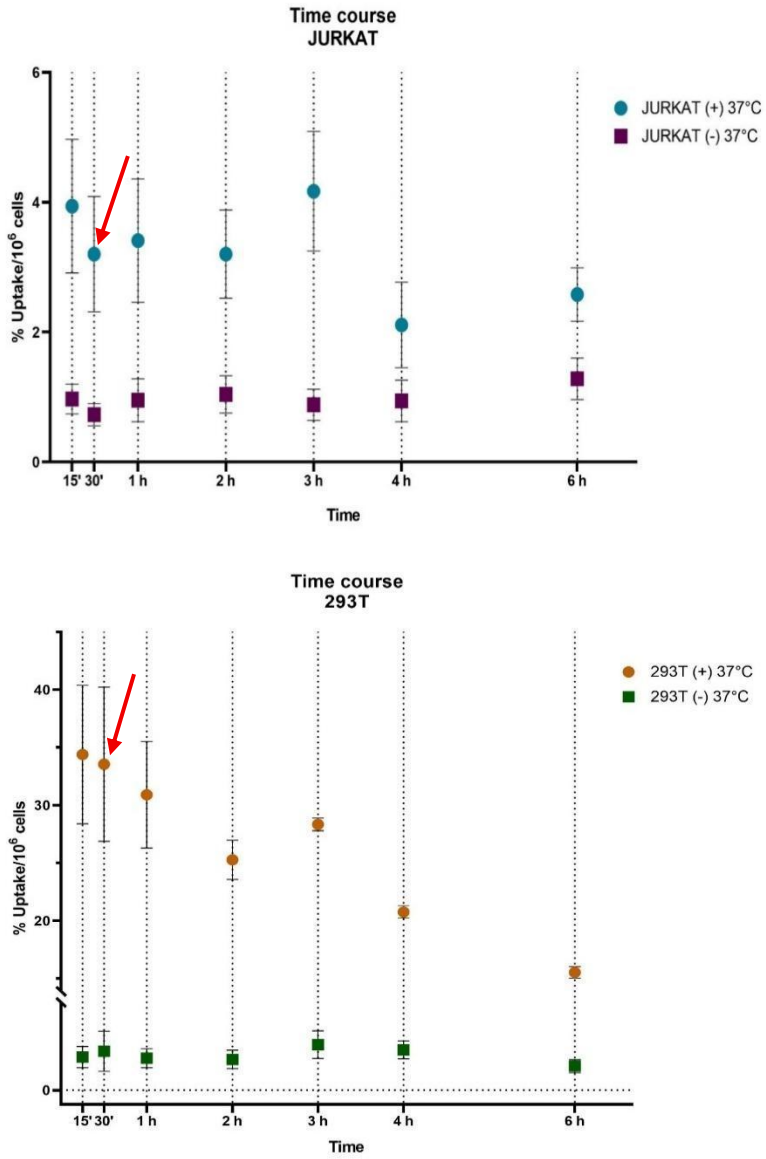

Figure 10. Time course experiment: Jurkat and 293T cells infected/not infected with pCONTROL were tested at multiple time points (15 min, 30 min, 1 h, 2 h, 3 h, 4 h, 6 h) at 37 °C to assess uptake kinetics, expressed as % uptake per 1 × 10^6 cells. Rotational speeds during incubation ranged from 0 rpm to 170 rpm (0, 100, 130, 150, 170 rpm), but no significant differences were observed between static and agitated conditions. Similarly, medium composition (RPMI vs DMEM) did not affect Jurkat uptake. In contrast, HEK293T cells showed markedly higher uptake than Jurkat cells, and "fresh" HEK293T cultures consistently outperformed older passages. Uptake increased rapidly within the first 15–30 min, reached a plateau by 3 h, and declined thereafter, consistent with reduced cell viability under prolonged assay conditions.

Further confirmation of functional membrane-localised hNIS was obtained through temperature-dependent uptake experiments (Figure 11). Uptake of [^{99m}Tc]pertechnetate was markedly higher at 37 °C compared to 4 °C, indicating an energy-dependent active transport process.

Uptake 37°C vs 4°C

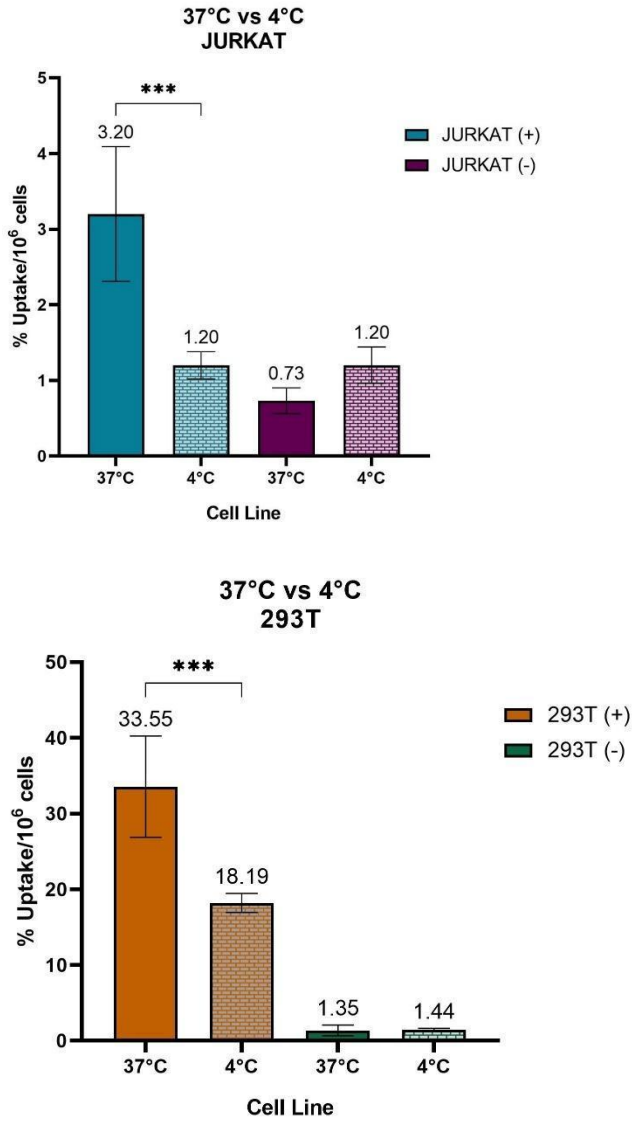

Figure 11. Temperature assays 37°C vs 4°C: Jurkat and 293T infected/not infected with pCONTROL were incubated with $Na^{99m}TcO_4$ (5 µL/5 µCi) for 30 min, 150 rpm, at different temperatures, to assess whether uptake performance could be defined as temperature-dependent.

Finally, blocking assays with known hNIS inhibitors ($NaClO_4$ and $NaReO_4$) demonstrated complete inhibition of radiotracer uptake following 20-minute pre-incubation (Figure 12), confirming that the observed uptake was explicitly mediated by the hNIS transporter encoded in the hNIS construct.

Block Studies

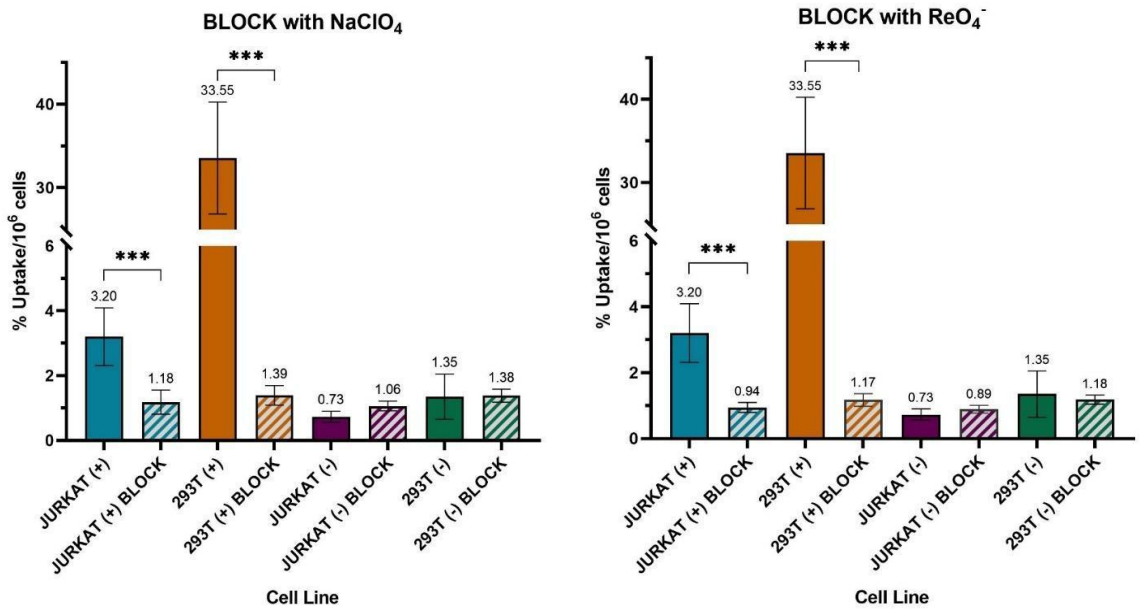

Figure 12. Block studies: Jurkat and 293T transduced/non-transduced with pCONTROL were pre-incubated for 20 minutes, 150 rpm, with NIS blocking agents ($NaClO_4$ and $NaReO_4$ 10 mM; 25 µL/1 mL cell followed by incubation with $Na^{99m}TcO_4$ (5 µL/5 µCi) for 30 min, 150 rpm, to determine whether $Na^{99m}TcO_4$ uptake was hNIS-dependent and specific.

To validate the specificity and physiological relevance of the NIS-mediated uptake assay, we performed control experiments using two thyroid-derived cell lines: BCPAP, a papillary thyroid carcinoma cell line, and NTHY-ORI, an immortalised non-tumorigenic human thyroid follicular cell line. Despite being physiologically competent for NIS expression, both lines displayed remarkably limited radiotracer uptake, with overall values about 1% across the time course (Figure 13).

Time course experiment BCPAP vs NTHY-ORI

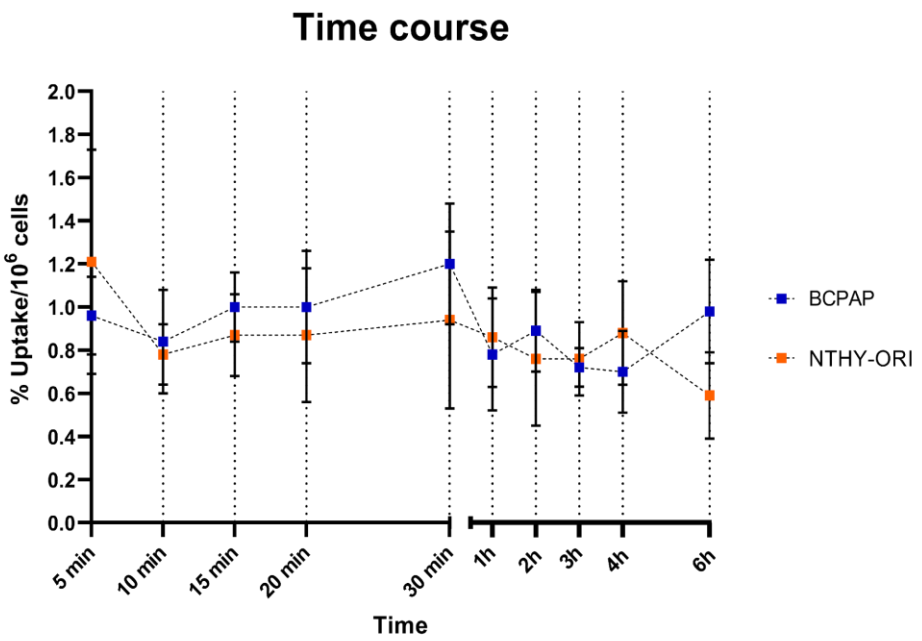

Figure 13. Time course of [^{99m}Tc]pertechnetate uptake in BCPAP and NTHY-ORI cells over 6 hours. BCPAP and NTHY-ORI cells were incubated with 5 µL [^{99m}Tc]pertechnetate (≈5 µCi) in 1 mL of medium (1 × 10^6 cells mL^{-1}) at 37 °C under gentle agitation (150 rpm). Uptake was measured at 5 min, 10 min, 15 min, 20 min, 30 min, 1 h, 2 h, 3 h, 4 h, and 6 h. Both cell lines consistently exhibited very low uptake levels (≤1% of total activity), indicating limited functional NIS activity despite detectable surface expression.

This low uptake is consistent with NIS downregulation in BCPAP cells due to their tumoral origin, and with low receptor surface expression in NTHY-ORI, as further supported by flow cytometry data (Figure 14). Specifically, flow cytometry quantification showed that only 4.9% of NTHY-ORI cells and 13.9% of BCPAP cells were positive for surface hNIS, confirming that both populations express limited levels of accessible transporter protein.

Flow Cytometry Results

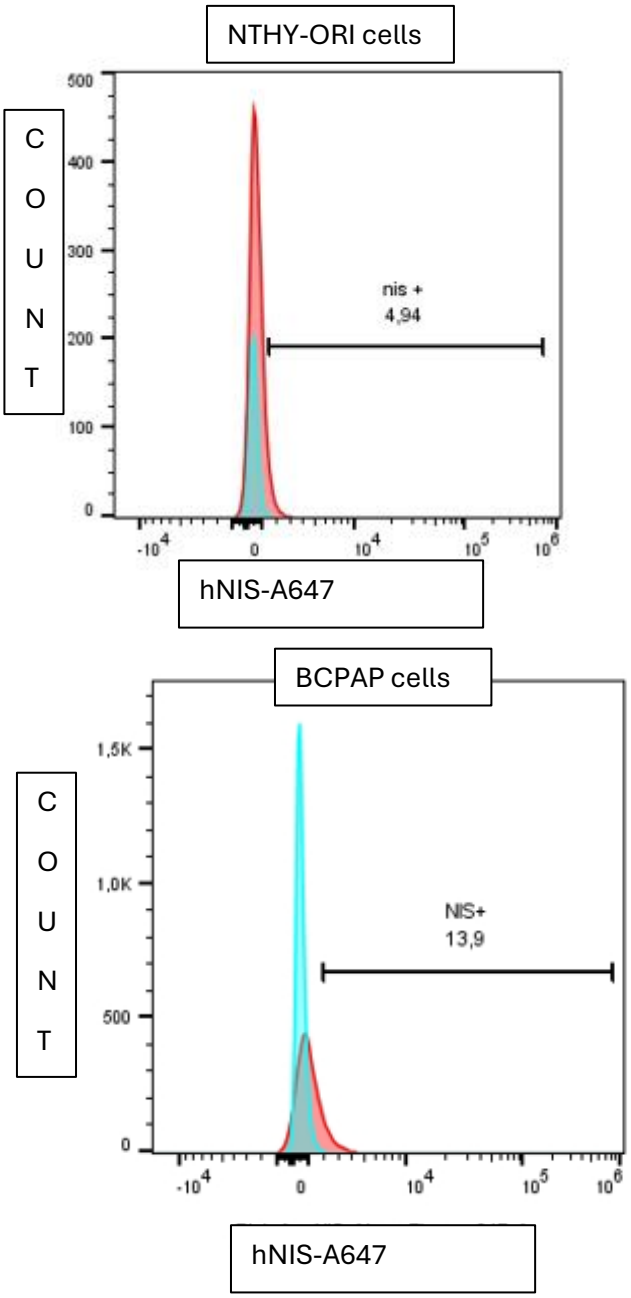

Figure 14. Surface hNIS detection by flow cytometry in NTHY-ORI (above) and BCPAP (below) cells using anti-hNIS-Alexa Fluor 647. Low percentages of positive cells were detected: 4.94% in NTHY-ORI and 13.9% in BCPAP.

To further dissect the mechanism of TcO_4^- uptake and validate NIS-specificity, blocking experiments using $NaClO_4$ as a competitor were performed. Pre-incubation with $NaClO_4$ for 15 minutes before radiotracer exposure reduced the small yet

significant ($p < 0.01$) uptake of TcO_4^- in BCPAP cells (Figure 15A), suggesting that the signal was largely dependent on functional NIS. In contrast, the uptake levels in NTHY-ORI cells were modest and not significantly affected by pre-blocking of the receptor, likely due to the low NIS expression.

Block Studies Pre Incubation

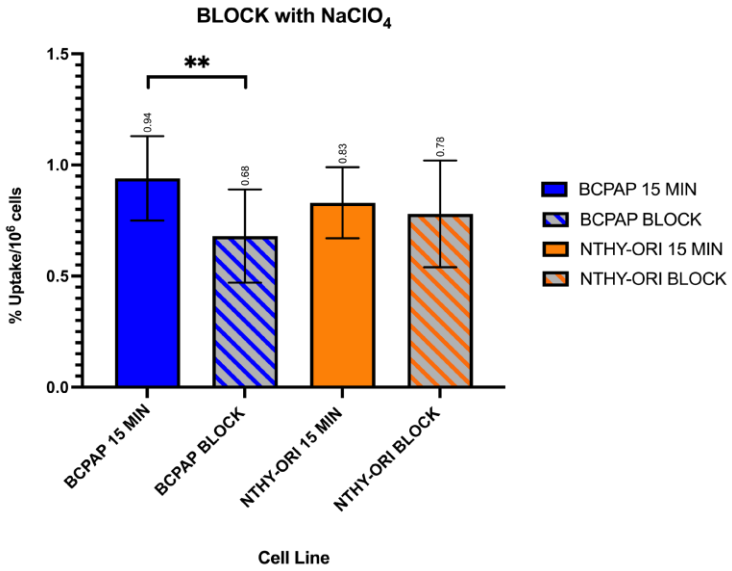

Figure 15A. Inhibition of [^{99m}Tc] pertechnetate uptake by $NaClO_4$. BCPAP and NTHY-ORI cells (1×10^6 cells mL^{-1}) were pre-incubated for 15 min at 37 °C under gentle agitation (150 rpm) with 25 µL of 10 mM $NaClO_4$ in 1 mL of medium, followed by incubation with 5 µL [^{99m}Tc]pertechnetate (≈5 µCi) for 30 min under the same conditions. Pre-treatment with $NaClO_4$ significantly reduced radiotracer uptake in BCPAP cells ($p < 0.01$), confirming that the observed uptake is mediated by hNIS. In contrast, NTHY-ORI cells showed minimal changes due to their already low baseline NIS activity.

In a complementary setup, post-blocking studies were conducted by reversing the incubation order: cells were first exposed to TcO_4^-, followed by a 15-minute post-incubation with $NaClO_4$ (Figure 15B). In this configuration, a modest increase in uptake was observed in NTHY-ORI cells, particularly at the 30-minute time point, suggesting that competitive displacement of the blocking agent by TcO_4^- may enhance signal detection under certain conditions. Conversely, BCPAP cells did not show a significant

difference between pre- and post-blocking, reinforcing that NIS-dependent uptake is saturable and competitively inhibited.

Block Studies Post-Incubation

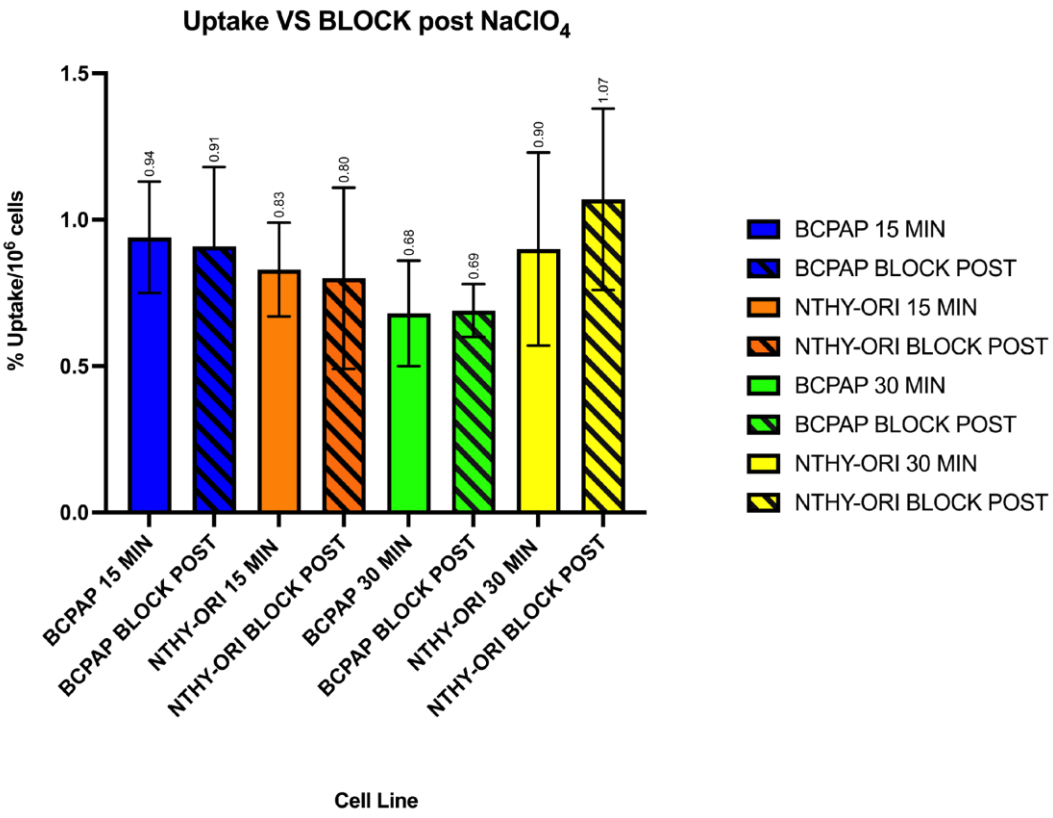

Figure 15B. Post-blocking assay with $NaClO_4$. Cells (1×10^6 cells mL^{-1}) were first incubated with 5 µL [^{99m}Tc]pertechnetate (≈5 µCi) in 1 mL of medium for 30 min at 37 °C under gentle agitation (150 rpm). After tracer exposure, a 15-min post-incubation with 25 µL of 10 mM $NaClO_4$ (1 mL cell suspension) was performed under the same conditions. Radiotracer uptake increased modestly in NTHY-ORI cells at the 30-min time point, possibly due to displacement of the inhibitor by TcO_4^-. In contrast, BCPAP cells showed no significant differences compared to pre-blocking conditions, consistent with saturable and competitively inhibited NIS-mediated uptake.

Together, these results support the specificity of radiotracer uptake via NIS in both physiological and cancer-derived thyroid models and underscore the limited transporter availability as the primary limiting factor. This validation supports the robustness of our functional assay and provides a comparative physiological benchmark for engineered NIS-expressing cells.

4.2 Inducible and constitutive expression vectors cloning strategy

To confirm the identity and correctness of the selected clones, mini-DNA preps and following analytical digestions of plasmid DNA were performed using EcoRI enzyme on both GAL4- and pBULLET-based vectors carrying inducible genes. Upon gel electroforesis undigested plasmids displayed the typical supercoiled and relaxed forms, while digested samples revealed clear linearised or two-band patterns corresponding to the expected backbone and diagnostic fragment sizes.

For GAL4-based constructs, digestion of pSYN_Avidin_EGFP yielded fragments of ~9000 bp and ~1700 bp, while pSYN_hNIS_EGFP showed fragments of ~9000 bp and ~2980 bp, consistent with theoretical predictions. Similar profiles were observed for monodin and GFP constructs. Digestion of the original empty GAL4 vector yielded a single linearised band at ~8700 bp, as expected. In pBULLET-based vectors, digestion of pIND_Avidin_EGFP and pIND_Monodin_EGFP produced bands at ~4124 bp and ~2920–2950 bp. pIND_hNIS_EGFP and pIND_EGFP showed insert bands of 2728 bp and 795 bp, respectively. All profiles were consistent with successful cloning and insert orientation (Figure 16).

Restriction Digest Summary – Inducible Constructs

Construct Name	Backbone	Restriction Enzyme(s)	Expected Vector Band (bp)	Expected Insert Band (bp)	Cloning Verified
pSYN_Avidin_EGFP	pHR_5xGAL4	EcoRI	9003	1709	Yes
pSYN_Monodin_EGFP	pHR_5xGAL4	EcoRI	9003	1730	Yes
pSYN_hNIS_EGFP	pHR_5xGAL4	EcoRI	9003	2981	Yes
pSYN_EGFP	pHR_5xGAL4	EcoRI	9003	1048	Yes
pIND_Avidin_EGFP	pBULLET	EcoRI	4124	2920	Yes
pIND_Monodin_EGFP	pBULLET	EcoRI	4124	2935	Yes
pIND_hNIS_EGFP	pBULLET	EcoRI	4124	4192	Yes
pIND_EGFP	pBULLET	EcoRI	4124	2259	Yes

A

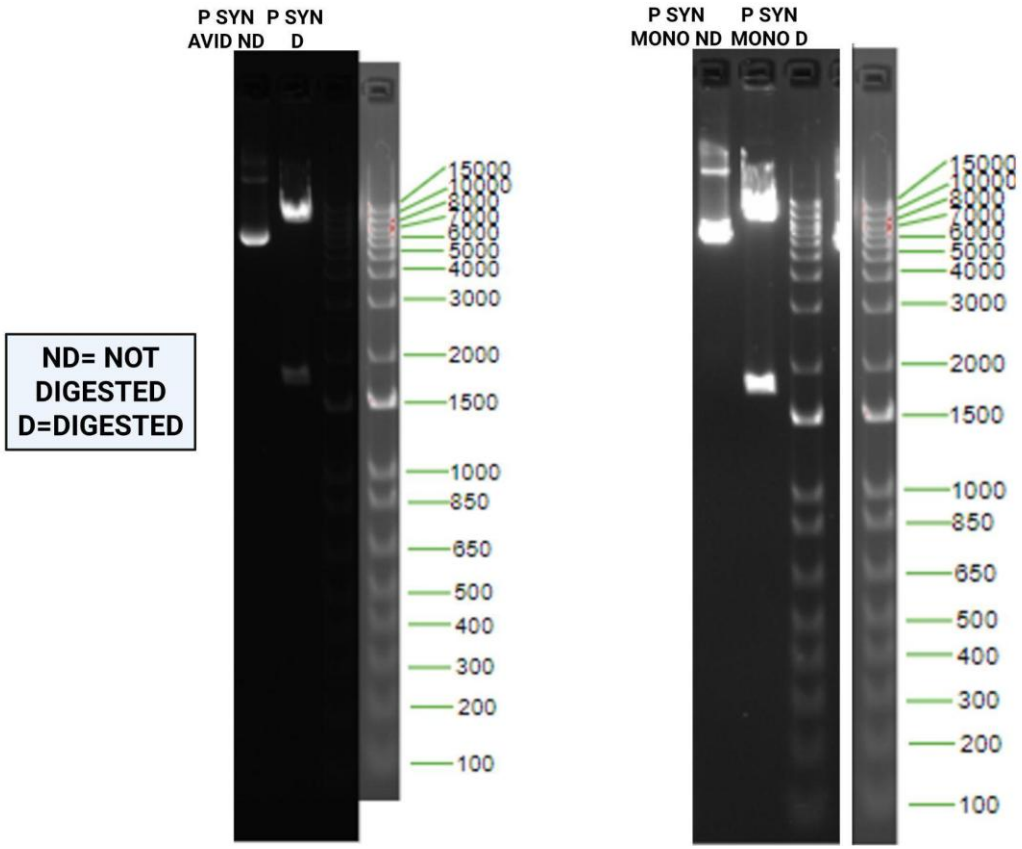

B

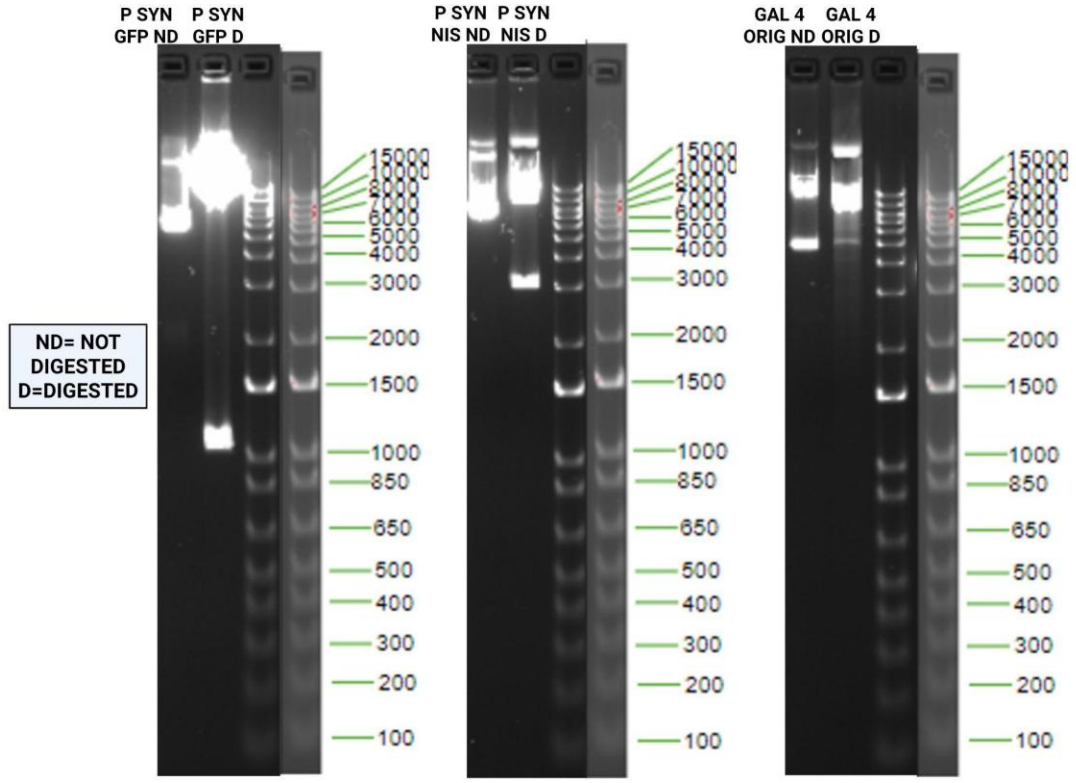
P SYN GFP ND
P SYN GFP D
P SYN NIS ND
P SYN NIS D
GAL 4 ORIG ND
GAL 4 ORIG D
ND= NOT DIGESTED
D=DIGESTED
15000
10000
8000
7000
6000
5000
4000
3000
2000
1500
1000
850
650
500
400
300
200
100

C

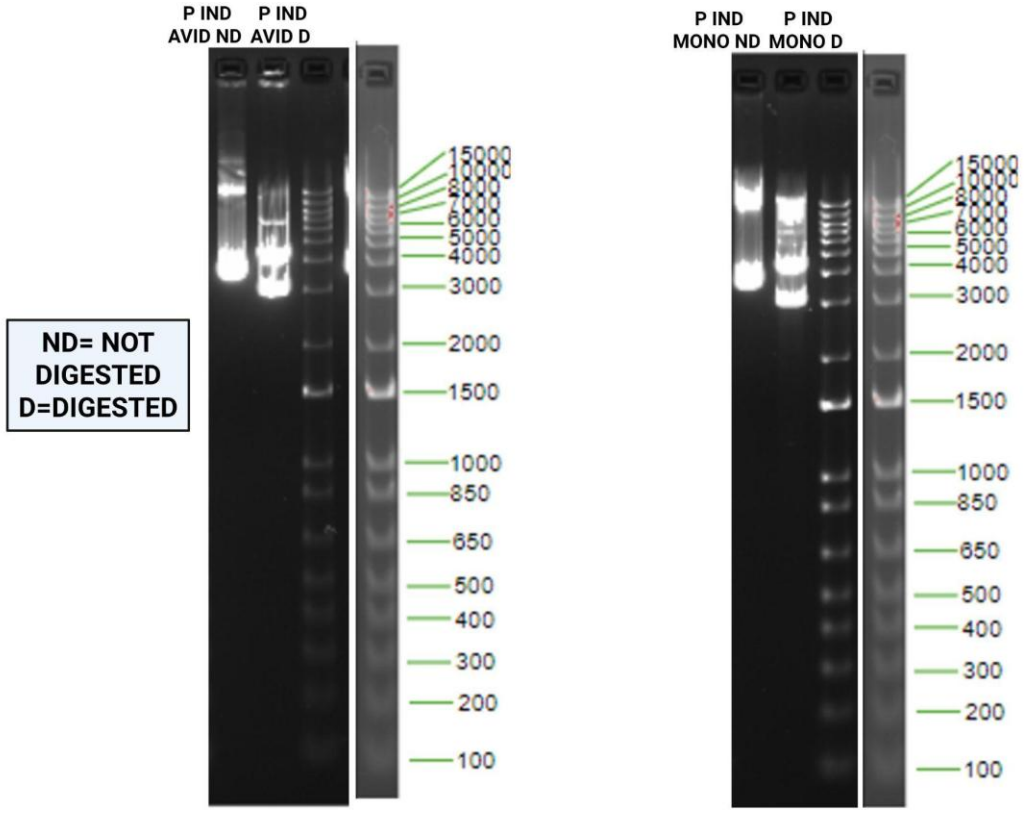
P IND AVID ND
P IND AVID D
P IND MONO ND
P IND MONO D
ND= NOT DIGESTED
D=DIGESTED
15000
10000
8000
7000
6000
5000
4000
3000
2000
1500
1000
850
650
500
400
300
200
100

D

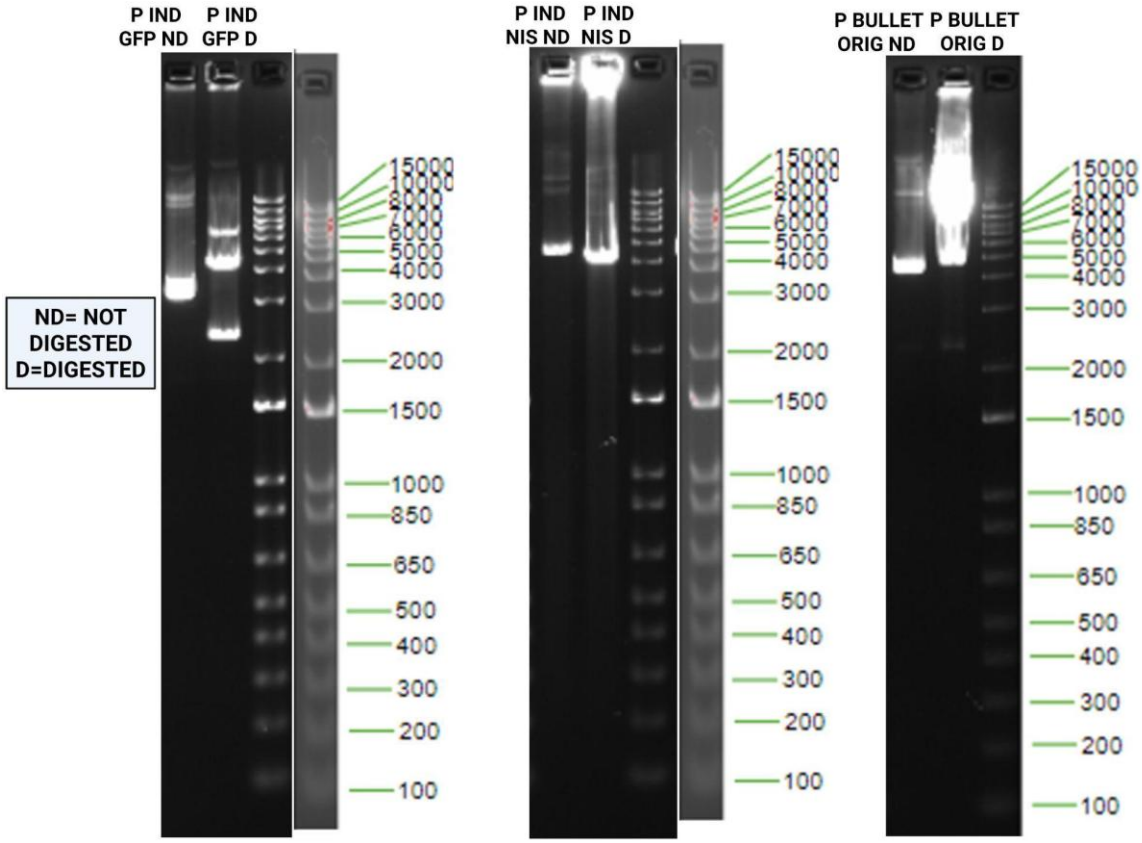

Figure 16. Agarose gel electrophoresis of plasmid digestion products confirms successful cloning of inducible constructs into GAL4- and pBULLET-based backbones. For each plasmid, the undigested (nd) and digested (d) forms were analysed. Constructs include pSYN_Avidin_EGFP (**A**) pSYN_Monodin_EGFP, (**A**) pSYN_hNIS_EGFP **(B)**, pSYN_EGFP **(B);** GAL4- **(B)** pInd_Avidin_EGFP (**C**), pInd_Monodin_EGFP **(C**), pInd_EGFP (**D**), pInd_hNIS_EGFP (**D**), pBULLET (**D**). Digestions were carried out using EcoRI-HF and expected fragment sizes were based on *in silico* plasmid maps. All digested samples exhibit a shift from supercoiled to linearised or fragmented bands, corresponding to the predicted sizes: ~9000/4000 bp (vector backbone) and ~1000–4100 bp (insert fragments), depending on the construct. The presence of distinct bands at expected positions supports the correct insertion of each transgene. A molecular weight marker (1,5 µL/lane) was used as a molecular weight reference.

4.3 Cloning and constructs' validation: constitutive expression systems

4.3.1 Surface Expression Analysis on Transfected HEK293T cells

To evaluate the expression of constitutively encoded receptors in the viral producer cells, HEK293T cells were transfected with ARI-001 lentiviral vectors harbouring the different receptors, hNIS, avidin, and monodin. Expression of the surface receptors was assessed by flow cytometry at 48- and 72-hours post-transfection.

For the detection of hNIS, cells were stained with an Alexa Fluor® 647-conjugated anti-NIS antibody. Non-transfected HEK293T displayed a negligible background signal (0.06% positive cells; MFI: 2022), confirming the specificity of the staining. MFI (median fluorescence intensity) represents the median fluorescence signal detected within the analysed cell population and is commonly used to quantify receptor expression levels. Unstained HEK293T transfected with the ARI-001 NIS construct showed minimal background (0.43% positive cells; MFI: 2423). In contrast, HEK293T transfected with the ARI-001 NIS vector and stained with anti-NIS-647 exhibited robust expression, with 85.8% of NIS+ cells and a corresponding marked increase in MFI (11374) (Figure 17).

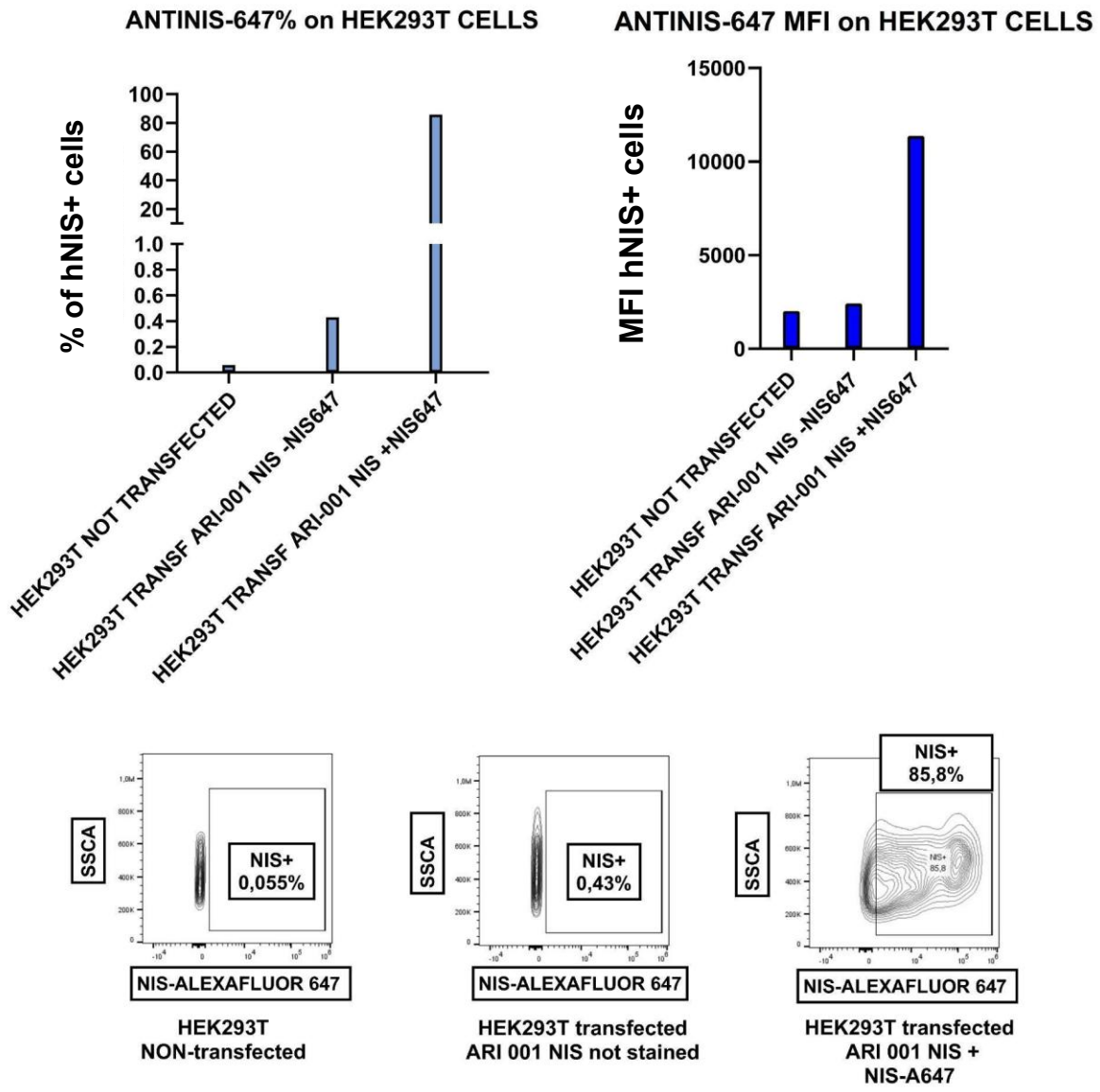

Figure 17. Surface expression of hNIS on transfected HEK293T cells. HEK293T cells were transfected with the ARI-001 NIS vector. Seventy-two hours post-transfection, cells were stained with an Alexa Fluor® 647-conjugated anti-NIS antibody and analysed by flow cytometry. A clear increase in NIS-positive cells and fluorescence intensity is observed only in transfected and stained samples compared to non-transfected and unstained controls. Data are shown as a representative experiment (n = 1).

The expression of avidin- and monodin-based receptors was assessed using an anti-FLAG antibody, followed by Alexa Fluor® 488-conjugated secondary antibody, to detect the FLAG-tagged receptors. Non-transfected HEK293T showed no significant

background staining (0.14% positive cells; MFI 2091). Cells transfected with the ARI-001 avidin construct but not stained with the anti-FLAG antibody showed low background levels (6.02% positive cells; MFI 5899), whereas those stained with anti-FLAG exhibited 37.4%, MFI 10346 positivity, confirming successful receptor expression.

Similarly, HEK293T transfected with the ARI-001 monodin construct showed 4.89% MFI 5665 positivity in the absence of FLAG staining, and 43.5% MFI 11462 positivity upon FLAG detection, indicating surface expression of monodin (Figure 18).

These results demonstrate efficient expression of hNIS, avidin, and monodin in transfected HEK293T, validating the production of functional viral particles for downstream transduction of Jurkat and Pan-T effector cells.

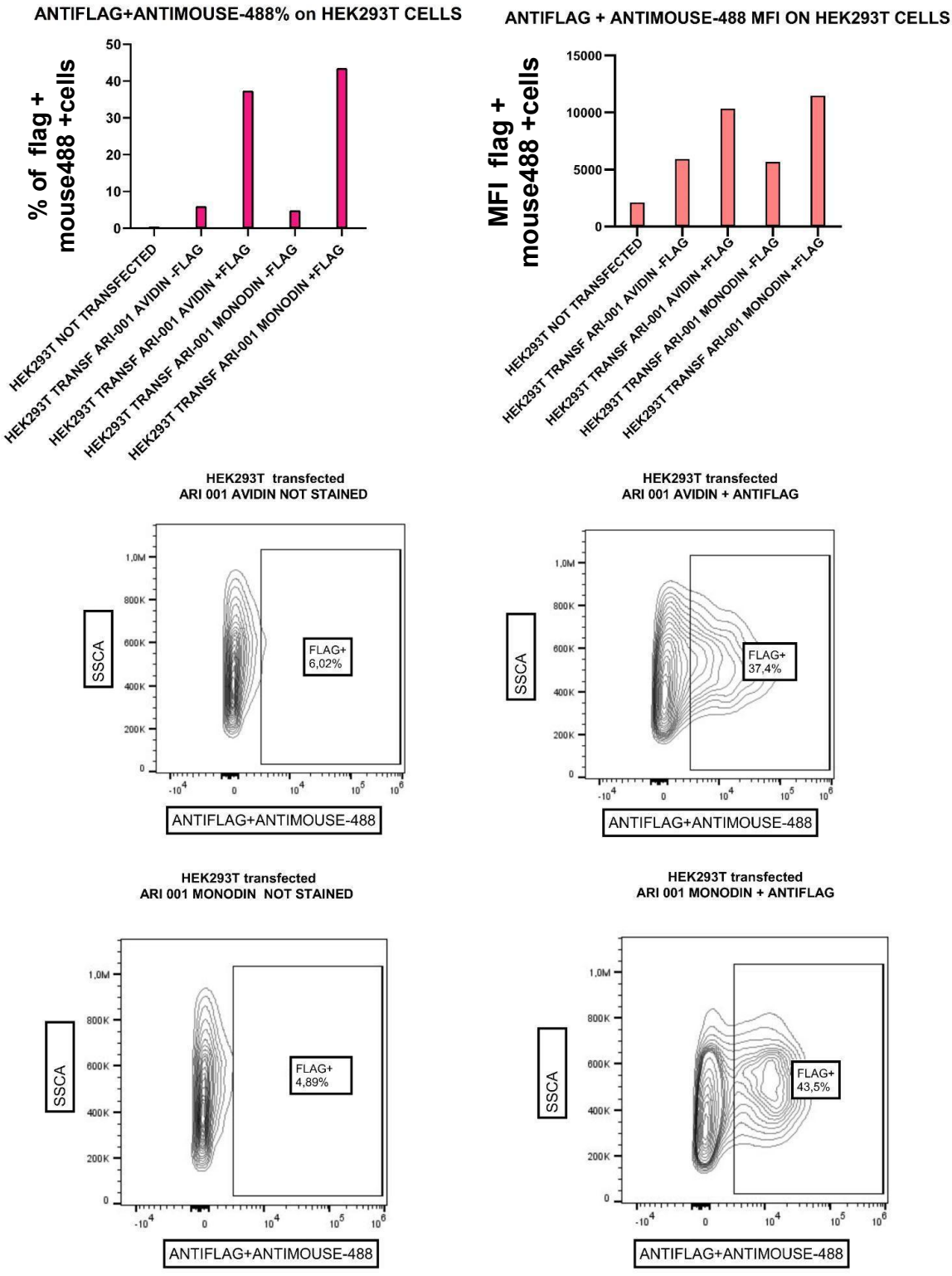

Figure 18. Expression of FLAG-tagged avidin and monodin in transfected HEK293T cells was evaluated by flow cytometry. HEK293T cells were transfected with ARI-001 constructs encoding FLAG-tagged avidin or monodin. After 72 hours, cells were stained with an anti-FLAG primary antibody followed by Alexa Fluor® 488-conjugated secondary antibody.

Flow cytometry analysis shows an increase in FLAG-positive cells in both conditions compared to unstained and non-transfected controls. Data are shown as a representative experiment (n = 1).

4.3.2 Evaluation of Transduction Performance in Jurkat and Pan-T Cells

To assess the efficiency of lentiviral transduction, surface expression of engineered receptors and their functional activity, all constructs derived from the ARI-001_pCCL_EF1a backbone encoding hNIS, avidin, and monodin under a constitutive EF1α promoter, were systematically tested in two cellular models.

As a first step, Jurkat cells were used as a standardised lymphoid model to evaluate transgene expression levels, membrane localisation, and ligand-binding capacity via flow cytometry. This allowed direct comparison of vector performance under uniform and controlled conditions.

In parallel, the same lentiviral vectors were tested in primary human Pan-T cells (activated peripheral blood-derived T lymphocytes) to validate receptors expression and functionality in a more physiological and clinically relevant context. This two-tiered approach ensured that each construct was evaluated both in terms of its technical performance in vitro and its potential translational applicability in primary human immune cells.

Jurkat cells transduced with the ARI-001 monodin vector exhibited strong surface expression of the receptor, as shown by biotin-PE staining. In this condition, 77.10% of cells tested positive for biotin binding, with a median fluorescence intensity (MFI) of 1355, while unstained cells showed only 1.16% positivity, confirming the staining's specificity. Additionally, Jurkat cells transduced with the ARI-001 GFP control vector and stained with biotin-PE showed a very low background signal, with 3.51% positive cells. Jurkat cells transduced with the ARI-001 avidin vector showed detectable surface expression of the receptor, with 33.20% of cells positive for biotin binding and a median fluorescence intensity (MFI) of 333. In contrast, non-stained transduced cells showed only 0.65% positive events, confirming the specificity of the detection method (Figure 19A).

JURKAT CELLS

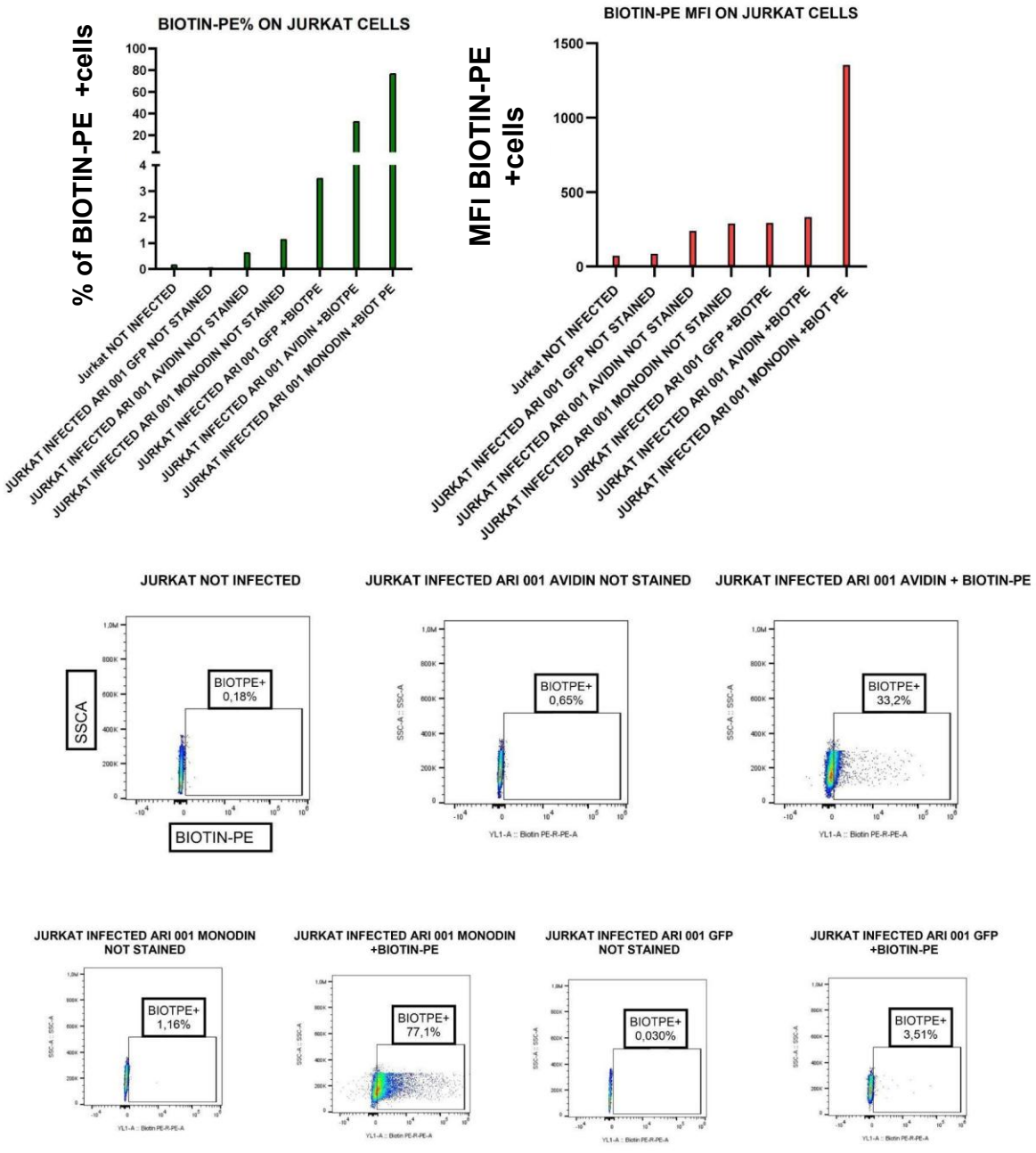

Figure 19A. Flow cytometry analysis of Biotin-PE binding in Jurkat cells transduced with constitutive ARI-001 vectors encoding avidin or monodin receptors. Forty-eight to seventy-two hours post-transduction, Jurkat cells were stained with Biotin-PE, a fluorophore-conjugated ligand used to detect surface-expressed avidin and monodin via their high-affinity biotin-binding domains. Cells transduced with the avidin construct showed 33.20% Biotin-PE^{+} events, while those transduced with monodin exhibited 77.3% Biotin-PE^{+}. Non-infected (NI)

and GFP-only transduced controls showed negligible signal. These results confirm the functional surface expression of both receptors, with substantially higher efficiency observed for monodin in the Jurkat model. Data are shown as a representative experiment (n = 1).

In Figure 19B, Jurkat cells are represented as a dot plot based on GFP expression (horizontal axis) and biotin-PE staining (vertical axis). In the first plot, the ARI-001 monodin-transduced but unstained cells, the vast majority of events (>99%) are confined to the lower-left quadrant, indicating the absence of both GFP and biotin signal. Only 0.007% of double-positive events are detected. In the right plot, corresponding to ARI-001 monodin-transduced cells stained with biotin-PE, a clear population of double-positive cells is observed in the upper-right quadrant (12.5%), indicating co-expression of the constitutive GFP marker and surface monodin, as detected through biotin binding. On the contrary, when comparing the expression profiles of avidin- and monodin-transduced Jurkat cells, a lower percentage of double-positive events is observed in avidin-positive cells. Specifically, only 1.10% of GFP^+/biotin-PE^+ cells were detected in avidin-transduced and stained samples, compared to 12.5% in monodin-transduced cells. This suggests that, under the same experimental conditions, the surface expression of monodin is more efficient than that of avidin, resulting in a higher proportion of cells simultaneously expressing the constitutive GFP marker and displaying biotin-binding capacity. The specificity of these signals is further confirmed by the control using ARI-001 GFP transduced Jurkat cells stained with biotin-PE, where a double-positive population is absent, demonstrating that biotin binding occurs exclusively in the presence of the monodin or avidin receptors.

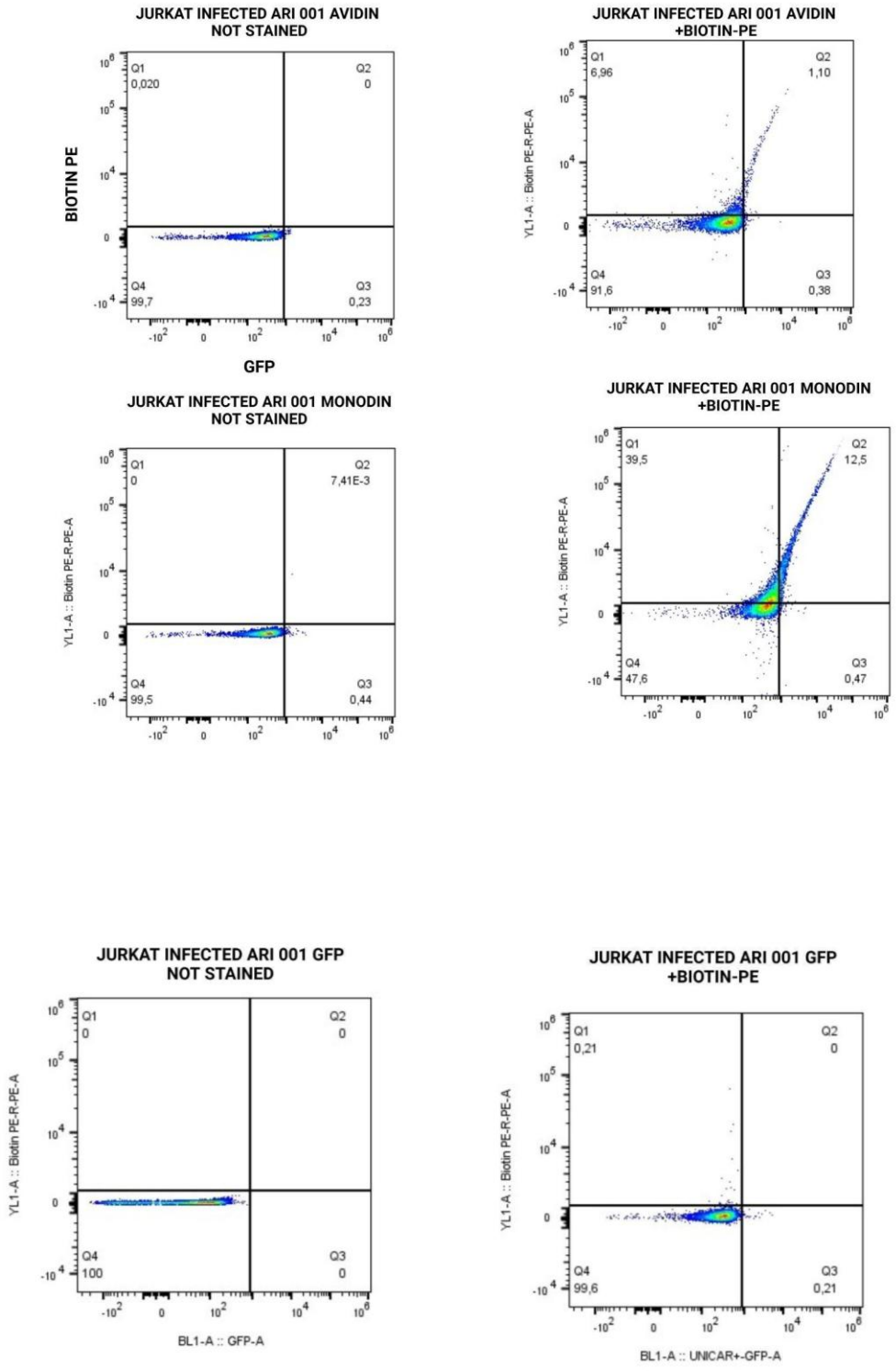

Figure 19B. Detection of double-positive cells for GFP (empty control) and Monodin/Avidin expression in ARI-001-transduced Jurkat cells. Jurkat cells were infected with the ARI-001 vector encoding Monodin-Avidin-GFP (empty control) and analysed by flow cytometry 48–72 hours post-infection. Cells were stained with biotin-PE to detect surface expression of the monodin/avidin receptor. In this Figure, dot plots display the GFP signal

(constitutive marker of infection) on the x-axis and biotin-PE staining on the y-axis. In the left plot (unstained control), no double-positive population is detected. In the right plot (biotin-PE stained sample), a clear population of double-positive cells is visible in the upper-right quadrant (Q2), indicating co-expression of GFP and surface monodin/avidin, compared to the empty GFP-control.

Regarding hNIS expression, Jurkat cells transduced with the constitutive ARI-001 hNIS vector were stained with an Alexa Fluor® 647-conjugated anti-hNIS antibody specifically targeting the extracellular domain of the symporter. Flow cytometry analysis revealed a distinct $hNIS^{+}$ population corresponding to 3.59% of total cells. This confirms the membrane localisation and surface accessibility of the hNIS protein in a subset of transduced Jurkat cells. Although the overall percentage was lower compared to cells expressing avidin-based receptors, the clear separation from background in non-infected and control cells supports the specificity and proper folding of the hNIS construct (Figure 20).

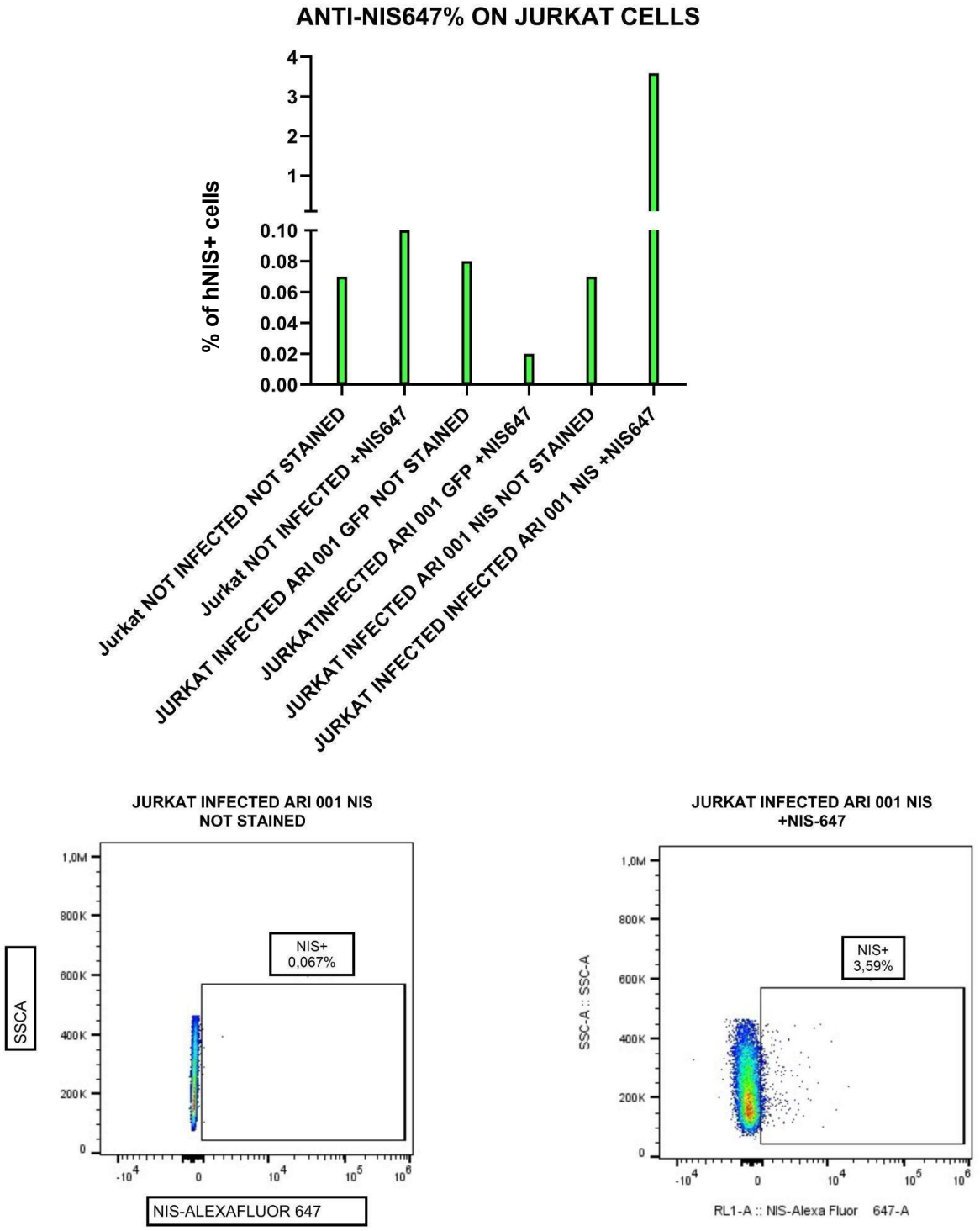

Figure 20. Flow cytometry analysis of Jurkat cells transduced with the ARI-001 vector encoding hNIS. Surface expression of hNIS was detected with Alexa Fluor 647-conjugated antibody. $hNIS^{+}$ cells represent 3.59% of the total population. Data are shown as a representative experiment (n = 1).

ARI-001 Avidin-transduced Pan-T cells showed robust Biotin-PE staining, with 3.7% of cells positive, compared to 0% in the non-infected control and 0.01% in GFP-only transduced cells. Similarly, monodin-transduced Pan-T cells showed an intermediate level of Biotin-PE positivity at 1.31% (Figure 21).

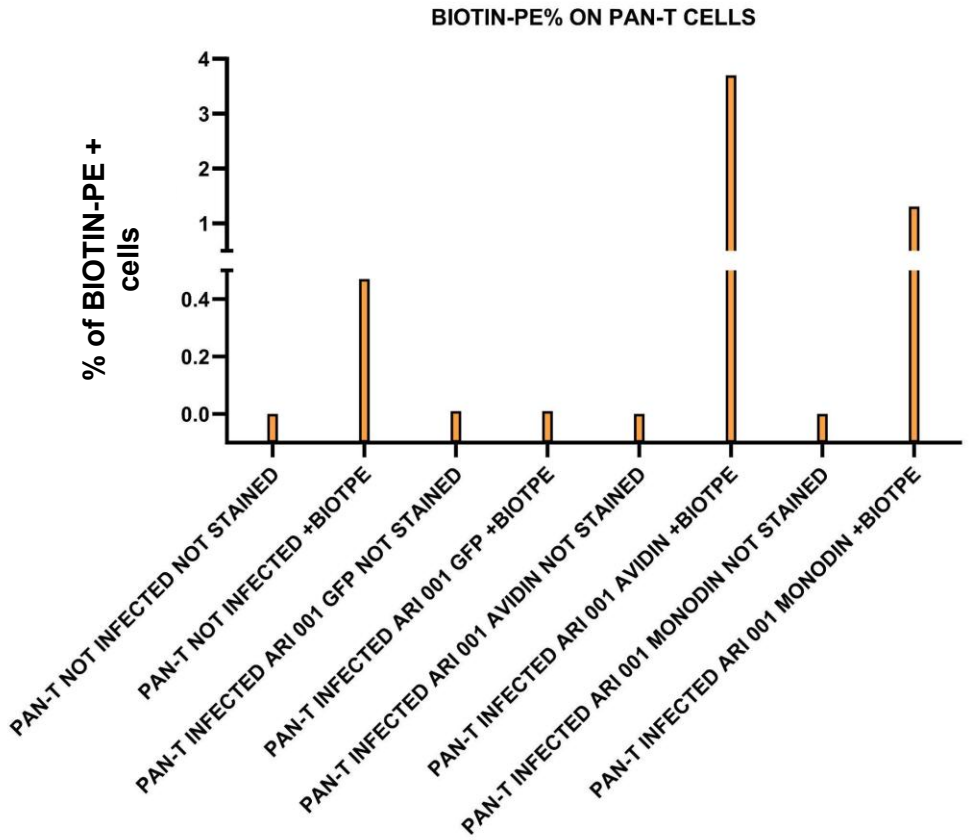

PAN-T NOT INFECTED
NOT STAINED

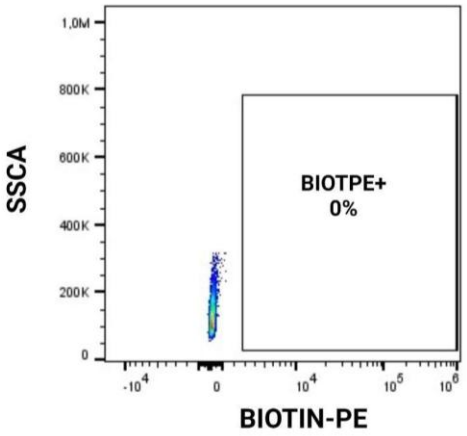

PAN-T NOT INFECTED
+BIOTIN-PE

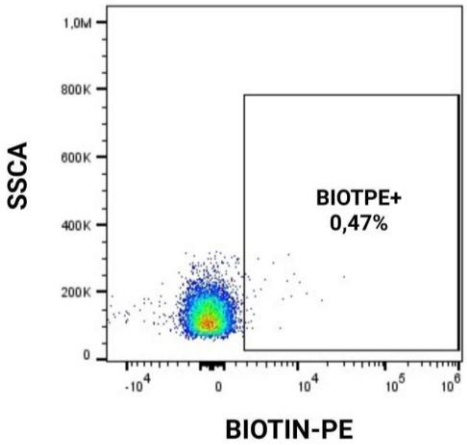

PAN-T INFECTED
ARI 001 AVIDIN NOT STAINED

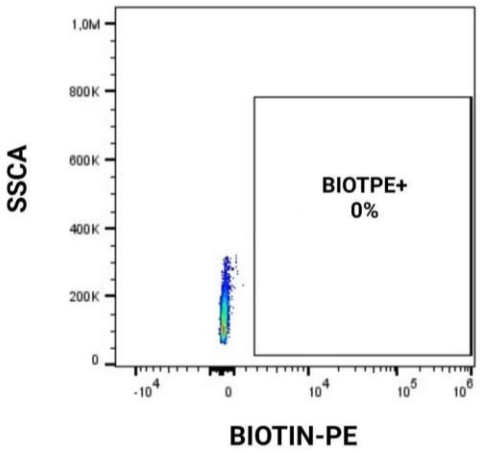

PAN-T INFECTED
ARI 001 AVIDIN + BIOTIN-PE

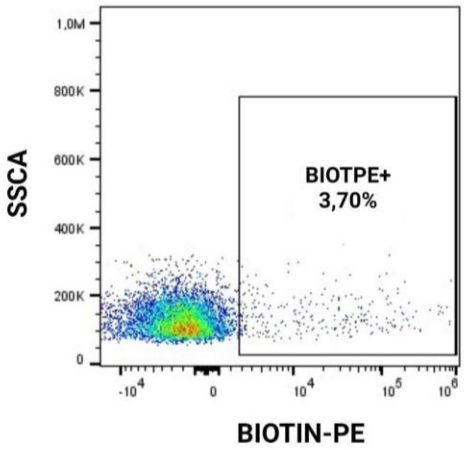

PAN-T INFECTED
ARI 001 MONODIN NOT STAINED

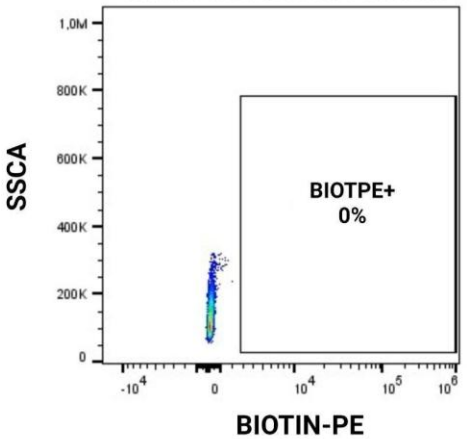

PAN-T INFECTED
ARI 001 MONODIN +BIOTIN-PE

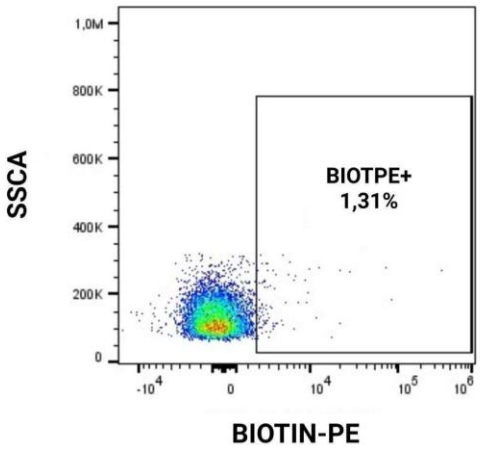

Figure 21. Flow cytometry analysis of Pan-T cells transduced with ARI-001_Avidin/Monodin vectors. Avidin/Monodin-transduced PAN-T cells displayed strong surface biotin binding, with 3.7%/1,31% Biotin-PE^{+} cells, respectively. In contrast, both non-infected and GFP-transduced controls showed no appreciable signal. Data are shown as a representative experiment (n = 1).

The corresponding fold changes in Biotin-PE positivity were for Avidin-transduced PAN-T cells ~7.9-fold versus non-infected and ~370-fold versus GFP-transduced control, while Monodin-transduced PAN-T cells exhibit a ~2.8-fold and ~131-fold increase relative to the two respective controls. While still significant, the lower percentage compared to avidin suggests reduced biotin-binding capacity or surface display for monodin under identical conditions (Figure 22).

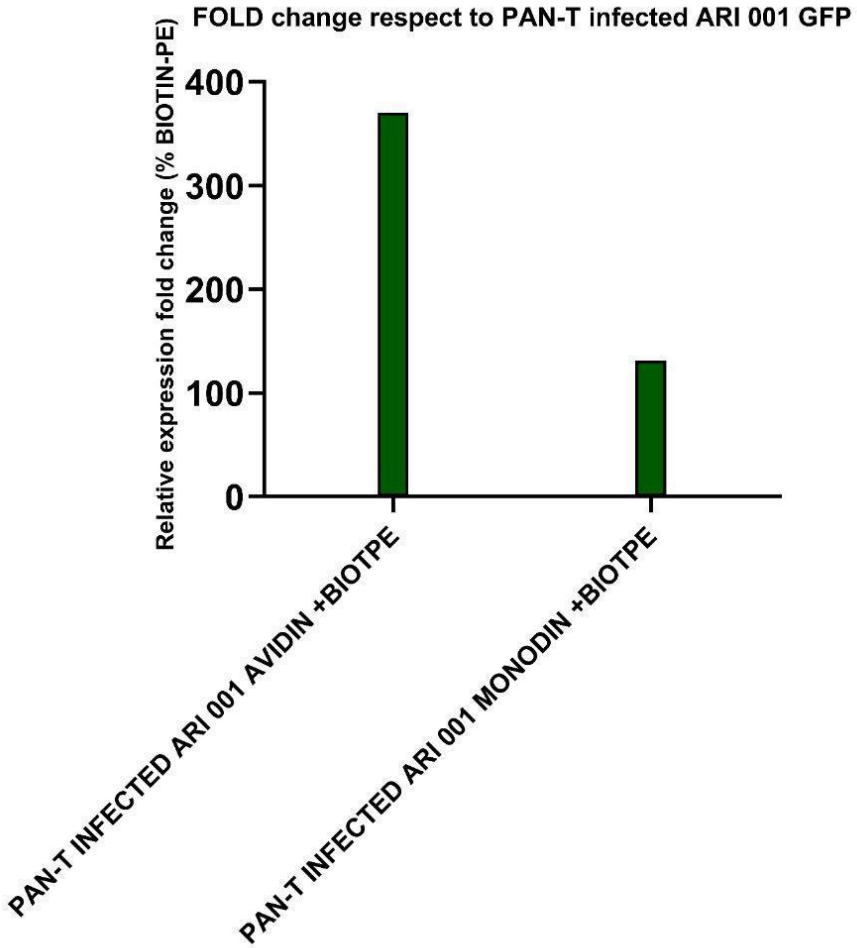
FOLD change respect to PAN-T infected ARI 001 GFP
Relative expression fold change (% BIOTIN-PE)
400
300
200
100
0
PAN-T INFECTED ARI 001 AVIDIN +BIOTPE
PAN-T INFECTED ARI 001 MONODIN +BIOTPE

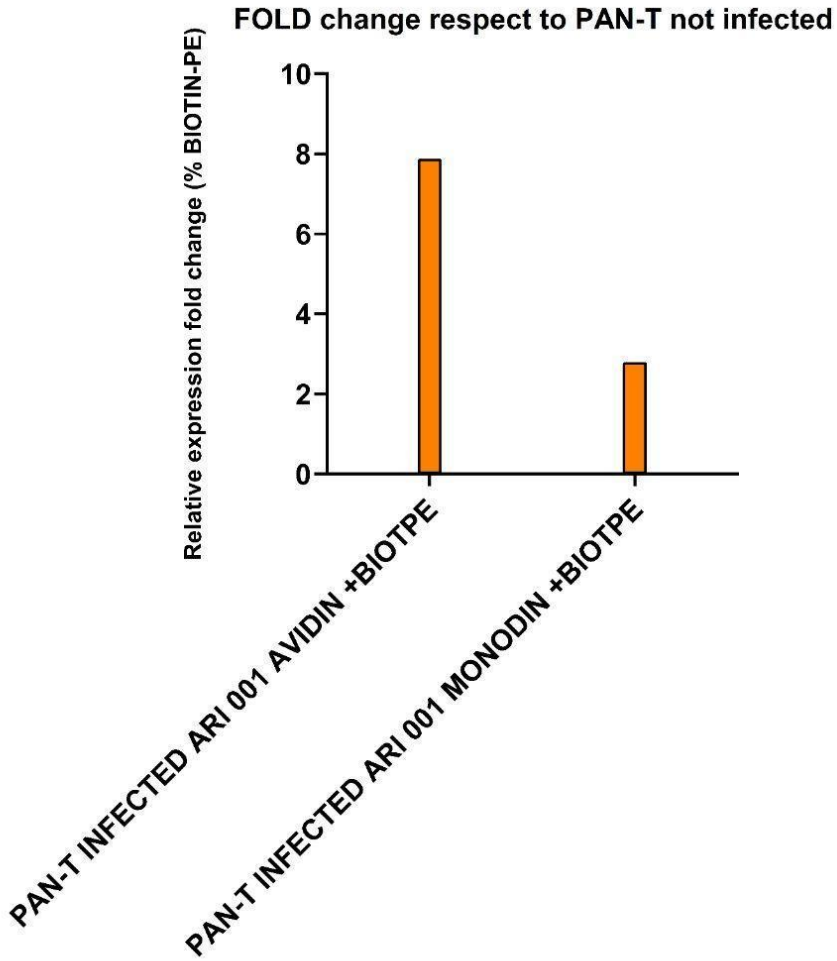
FOLD change respect to PAN-T not infected
Relative expression fold change (% BIOTIN-PE)
10
8
6
4
2
0
PAN-T INFECTED ARI 001 AVIDIN +BIOTPE
PAN-T INFECTED ARI 001 MONODIN +BIOTPE

Figure 22. Fold change (%) in Biotin-PE$^+$ cell population following constitutive expression of avidin or monodin receptors. Fold change was calculated relative to two independent controls: ARI-001 GFP-transduced cells (above figure, green bars) and non-infected cells (below figure, orange bars), both incubated with Biotin-PE. ARI-001 Avidin-transduced PAN-T cells exhibited a ~7.9-fold increase vs Not Infected and ~370-fold increase vs GFP controls, while ARI-001 monodin-expressing cells showed ~2.8- and ~131-fold increases, respectively. Data support the effective localisation of membrane-bound avidin and its biotin-binding capacity, with comparatively reduced performance of monodin under identical conditions. Data are shown as a representative experiment (n = 1).

These findings indicate that both avidin and monodin are functionally displayed on the surface of primary T cells following lentiviral transduction, with avidin exhibiting a superior binding profile as evidenced by a higher detectable Biotin-PE signal. The observed differences may reflect intrinsic differences in structure, expression efficiency, or membrane presentation between the two constructs.

Interestingly, avidin and monodin displayed opposite trends in receptor surface expression between Jurkat and Pan-T cells. In Jurkat cells, monodin showed markedly higher expression, with ~77% Biotin-PE$^+$ cells, compared to ~33% in avidin-expressing cells. Conversely, in Pan-T cells, avidin outperformed monodin, with Biotin-PE$^+$ populations of 3.7% and 1.31%, respectively. These findings suggest that the efficiency of surface localisation and/or stability of the two receptors is strongly influenced by the cellular context.

Inducible Expression Systems

4.4 Evaluation of 8xNFAT-ZsG-hCD8 (Nakayama vector)

To evaluate the inducible expression profile driven by NFAT activation, Jurkat T cells and primary human Pan-T cells were transduced with retroviral vectors encoding the 8xNFAT-ZsGreen-hCD8 reporter construct (Addgene #153417, Nakayama lab). Retroviral particles were produced in Phoenix-Ampho packaging cells and used to transduce target cells via a retronectin-transduction protocol, as described above in the methods section. Forty-eight to seventy-two hours post-transduction, cells were stimulated to activate the NFAT signalling pathway using either phytohaemagglutinin (PHA) at concentrations ranging from 0,125µg/mL to 2,5 µg/mL or anti-CD3/CD28 Dynabeads® (25 µL per 10^6 cells). Stimulation times varied depending on the experiment (2, 4, 6, or 24/48/72 hours), and NFAT-driven transcriptional activation was monitored by ZsGreen fluorescence, serving as a direct reporter of inducible promoter activity.

Jurkat cells that were not infected did not show any detectable ZsGreen expression (GFP^+ cells ~0%), regardless of whether they were left unstimulated or treated with PHA or Dynabeads®. This confirmed the absence of background fluorescence, which remained transcriptionally inactive without viral integration and NFAT pathway engagement (Figure 23, panel A).

In cells transduced with unconcentrated viral supernatant, stimulation for 3 days with anti-CD3/CD28 beads induced a modest 3.43% GFP^+ cells, indicating reporter gene activation. In contrast, aspecific PHA stimulation led to a more robust response, with 20% GFP^+ cells, indicating higher efficacy of PHA in triggering NFAT activation in this context (Figure 23, panel B).

When a tenfold concentrated viral preparation was used, a further increase in reporter expression was observed. Dynabead-stimulated cells showed 10.5% GFP positivity, while PHA stimulation induced the highest activation level, with 25.1% of the population expressing ZsGreen. These results indicate that both the method of stimulation and the efficiency of transduction, enhanced by viral concentration, directly influence the magnitude of NFAT-driven transcription. In particular, PHA

consistently outperformed CD3/CD28 beads in activating the reporter, suggesting that it may trigger stronger or more sustained NFAT pathway activation in Jurkat cells (Figure 23, panel C).

A

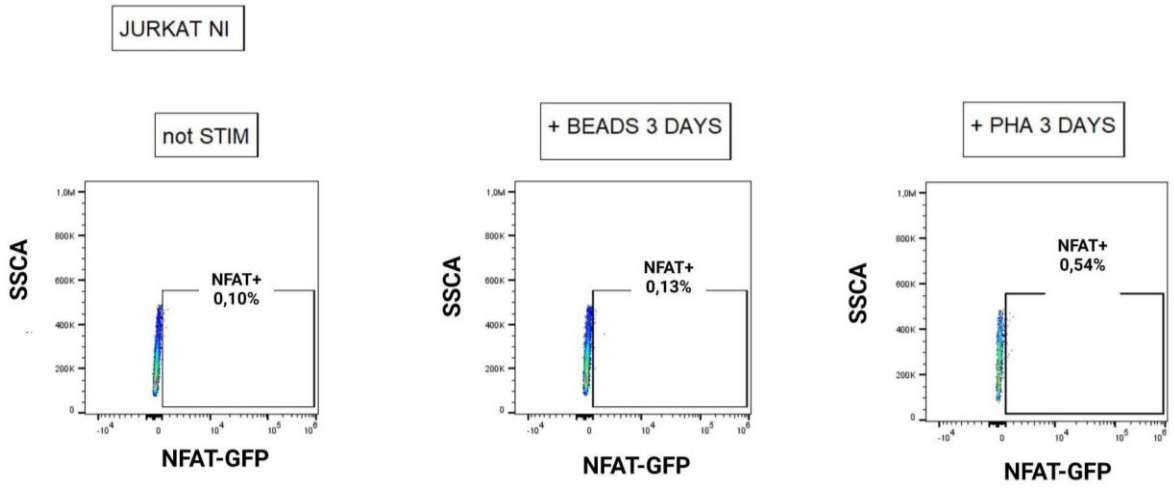

B

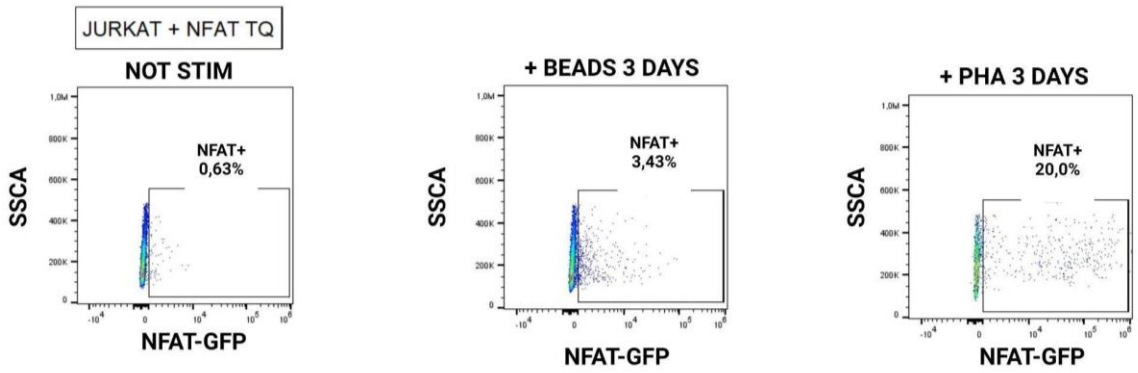

C

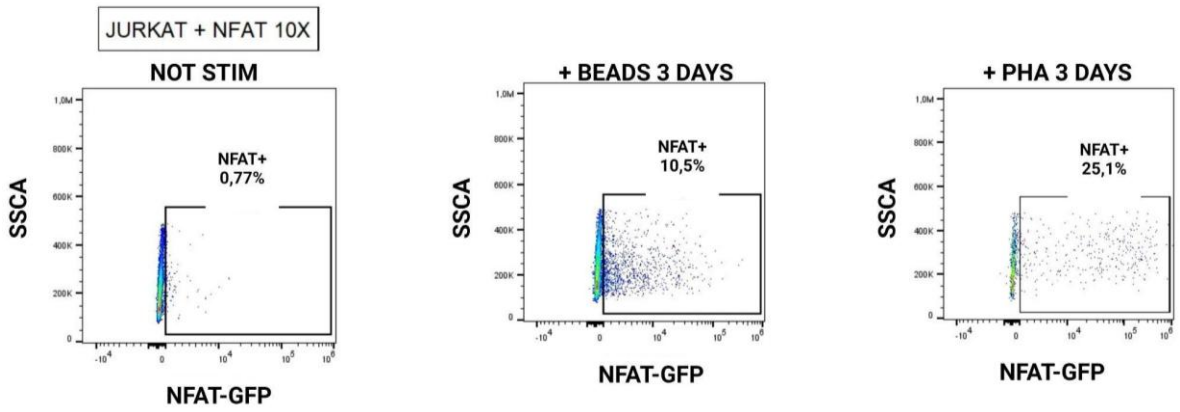

Figure 23. FACS analysis of NFAT reporter activation in Jurkat cells transduced with NFAT-ZsGreen and stimulated with anti-CD3/CD28 Dynabeads or PHA.

Panel **(A)** No reporter activation in non-transduced Jurkat cells. Jurkat cells not transduced with the NFAT-ZsGreen reporter were either left unstimulated or treated with anti-CD3/CD28 Dynabeads or PHA for 3 days. Flow cytometry plots show NFAT–GFP$^+$ cells at 0.10% (unstimulated), 0.13% (Dynabeads), and 0.54% (PHA).

Panel **(B)** NFAT activation in Jurkat cells transduced with unconcentrated virus. Jurkat cells were transduced with unconcentrated NFAT-ZsGreen retroviral supernatant and stimulated for 72 hours. Representative plots show 0.16% GFP$^+$ cells in unstimulated controls, 3.43% after anti-CD3/CD28 Dynabeads, and 20.0% after PHA.

Panel **(C)** Enhanced NFAT activation with concentrated viral transduction. Jurkat cells were transduced with 10× concentrated NFAT-ZsGreen virus and stimulated for 72 hours. Representative plots show 0.27% GFP$^+$ cells in unstimulated controls, 10.5% after anti-CD3/CD28 Dynabeads, and 25.1% after PHA.

To confirm the reproducibility of NFAT-driven ZsGreen activation in Jurkat cells, a second experiment was performed using the most effective condition identified previously: stimulation with PHA following transduction with ten-fold concentrated

viruses. As expected, uninfected Jurkat cells stimulated with PHA again showed negligible activation (GFP^+ cells ~0%), confirming the absence of background signal. In contrast, infected cells displayed a consistent reporter response, with 19.2% GFP-positive cells, closely matching the ~25% observed in the initial experiment. This reproducibility supports the robustness of the PHA-induced NFAT activation in this cellular context and confirms the sensitivity and stability of the reporter system (Figure 24).

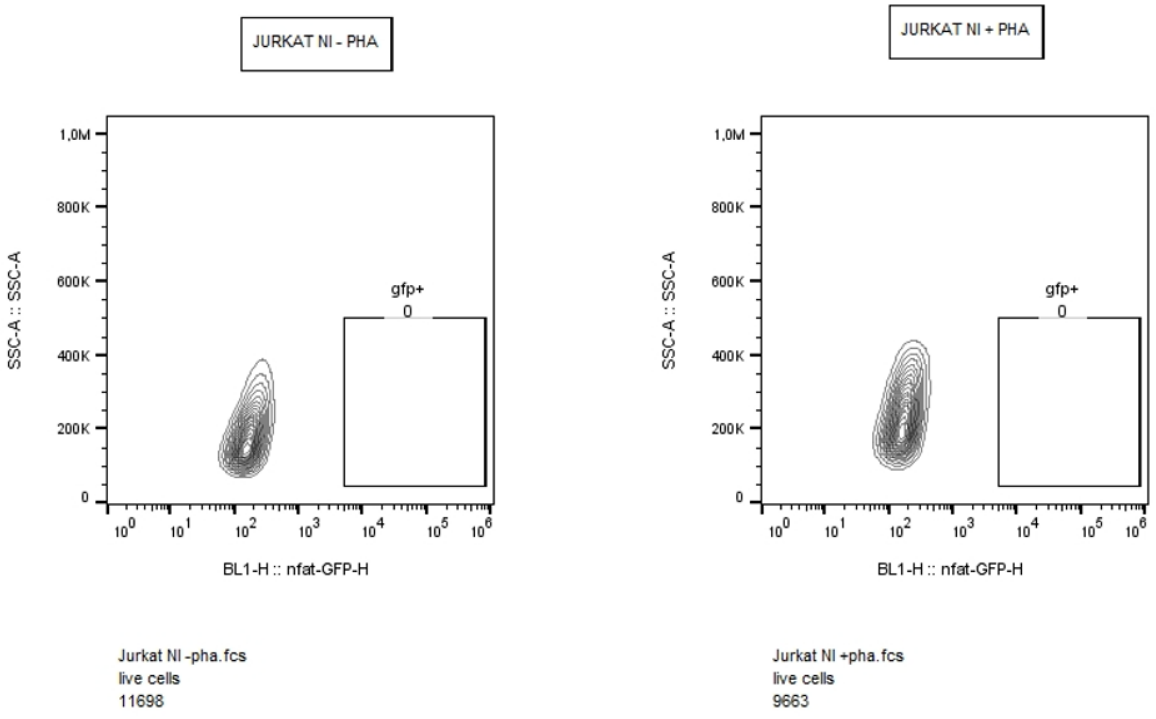

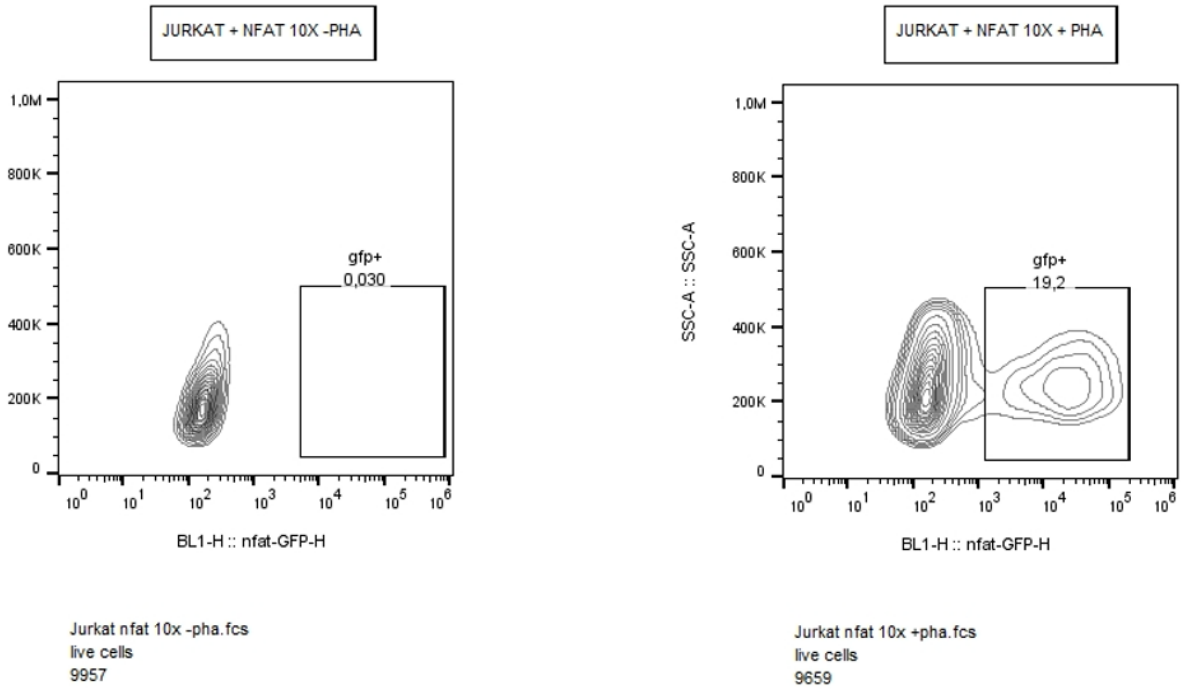

Figure 24. FACS analysis of NFAT reporter activation in Jurkat cells transduced/not transduced with 10× concentrated NFAT-ZsGreen and stimulated with PHA for 72 hours. Flow cytometry plots display NFAT–GFP fluorescence on the x-axis and side scatter (SSC-A) on the y-axis. In the PHA-stimulated Jurkat transduced cells, the GFP^+ gate shows 19.2% of events. The uninfected control shows no GFP^+ population under the same acquisition settings.

In primary Pan-T cells, preliminary tests using PHA revealed a high level of toxicity, resulting in extensive cell death. Therefore, for subsequent analyses, stimulation was performed using anti-CD3/CD28 Dynabeads®, which represent a more physiological and less cytotoxic method of T cell activation. Under these conditions, ZsGreen expression was successfully induced, confirming that the reporter system is also functional in primary human T cells. Notably, as observed in Jurkat cells, non-transduced Pan-T cells stimulated with Dynabeads® remained GFP-negative, highlighting the inducibility and specificity of the system.

In particular, NFAT activation in Pan-T cells following stimulation with anti-CD3/CD28 beads and CD137 co-staining was evaluated through GFP expression as a readout of NFAT pathway activation. Upon retroviral transduction with the NFAT-ZsGreen reporter vector and stimulation with Dynabeads in combination

with a CD137 agonist, Pan-T cells displayed a progressive increase in GFP-positive cells. In unstimulated conditions, the $NFAT^+$ population was limited to 1.20–1.51%. Following stimulation, the proportion of GFP^+ cells rose to 10.3% and 11.3% across two independent replicates, indicating robust activation of the NFAT pathway under these conditions (Figure 25A).

PAN-T NFAT 10X NOT STIM
NOT STAINED WITH CD137

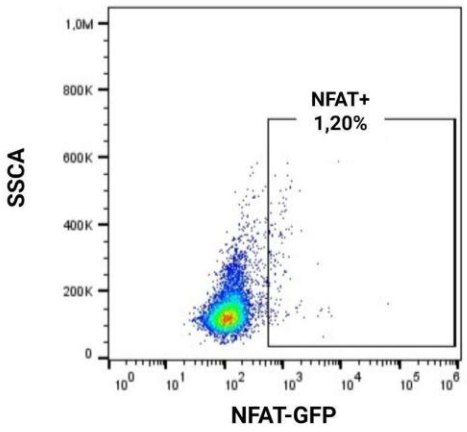

PAN-T NFAT 10X NOT STIM
STAINED WITH CD137

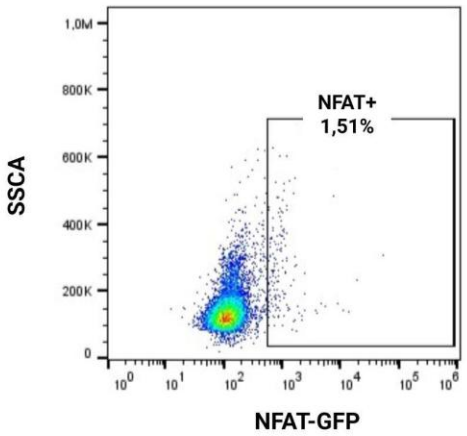

PAN-T NFAT 10X +BEADS
NOT STAINED WITH CD137

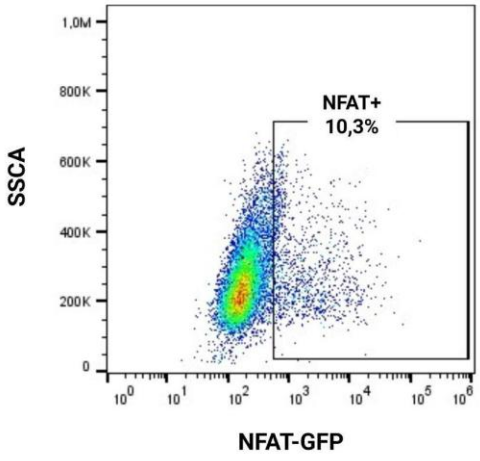

PAN-T NFAT 10X +BEADS
NOT STAINED WITH CD137

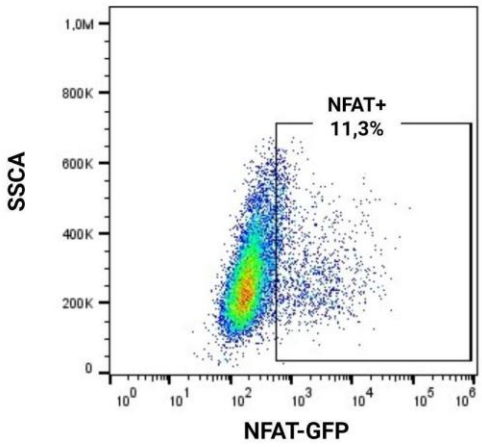

Figure 25A. Quantification of NFAT pathway activation via GFP expression in transduced Pan-T cells.

Dot plots depict the NFAT-GFP signal in Pan-T cells transduced with the 8xNFAT-ZsGreen reporter vector. Unstimulated cells show baseline GFP expression levels of 1.20–1.51%. Upon stimulation with anti-CD3/CD28 beads, GFP^+ cells increase to 10.3% and 11.3%, confirming activation of the NFAT signalling cascade.

In Figure 25B, the same cells were represented as flow-cytometry double dot plot: on the left plot, a weak NFAT response is observed: only 2.58% of cells fall into the double-positive quadrant (Q2), co-expressing GFP and CD137, while 0.41% are GFP^+ only (Q3), and the majority of cells remain $CD137^+$ only (Q1: 70.3%) or negative for both markers (Q4: 26.8%). In the right plot, a stronger activation is evident, with 22.0% of cells in the $GFP^+/CD137^+$ double-positive quadrant and 1.17% expressing only the GFP reporter. The increase in NFAT-GFP signal (from 2.58% to 22.0%) following bead stimulation suggests efficient T cell activation, correlating with CD137 upregulation. These results demonstrate that the NFAT reporter construct is responsive to T cell activation and that ZsGreen fluorescence correlates with CD137 expression.

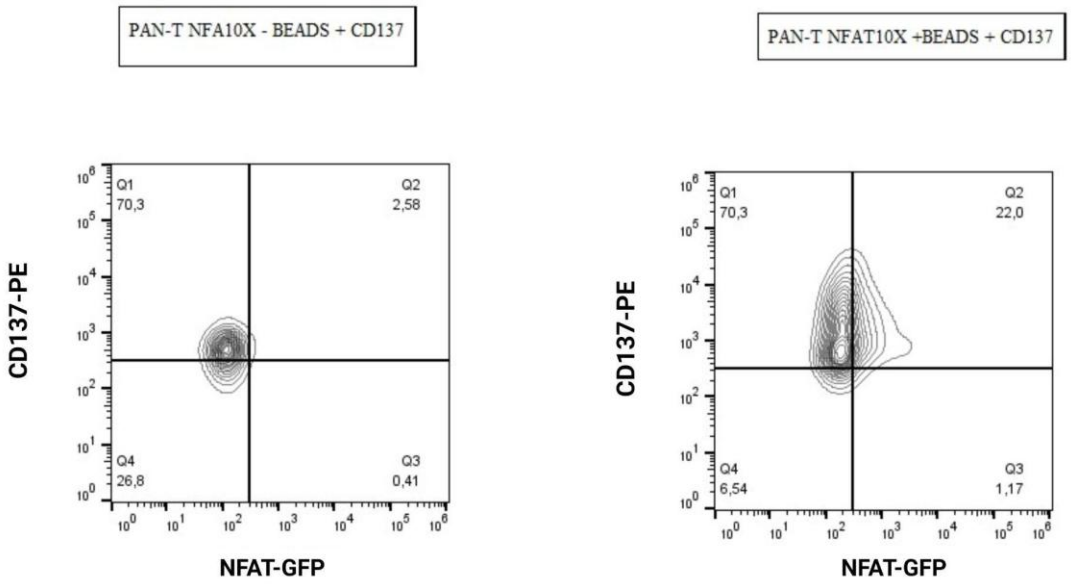

Figure 25B. Flow cytometry analysis of NFAT reporter activation and CD137 co-stimulatory marker expression in primary Pan-T cells following anti-CD3/CD28 bead stimulation. Flow cytometry dot plots show the co-expression of ZsGreen (NFAT-driven GFP reporter, x-axis) and CD137 (activation-induced surface marker, y-axis) in Pan-T cells transduced with the 8xNFAT-ZsGreen reporter vector and stimulated with anti-CD3/CD28 Dynabeads.

Overall, these findings collectively demonstrate that while both Jurkat and Pan-T cells can be engineered to express NFAT-inducible reporters, the optimal stimulation strategy is context-dependent, with PHA being effective in Jurkat cells and CD3/CD28 engagement being required in Pan-T cells to prevent activation-associated cytotoxicity.

To investigate the functional responsiveness and antigen specificity of NFAT activation in engineered T cells, Jurkat cells previously sorted for ZsGreen^{+} expression (indicating functional NFAT reporter activity) were co-transduced with a constitutively expressed anti-BCMA CAR. These dual-modified cells were then subjected to various activation conditions, such as co-culturing with BCMA^{+} (ARP-1) or BCMA^{-} (K562) target cells.

Specifically, when cultured with ARP-1 multiple myeloma cells, which endogenously express the BCMA antigen, approximately 15% of Jurkat cells became GFP-positive, indicating reporter activation via the NFAT pathway. In contrast, co-culture with K562 cells, which lack BCMA expression, failed to induce any detectable ZsGreen signal, confirming the absence of off-target or tonic signalling from the CAR construct (Figure 26).

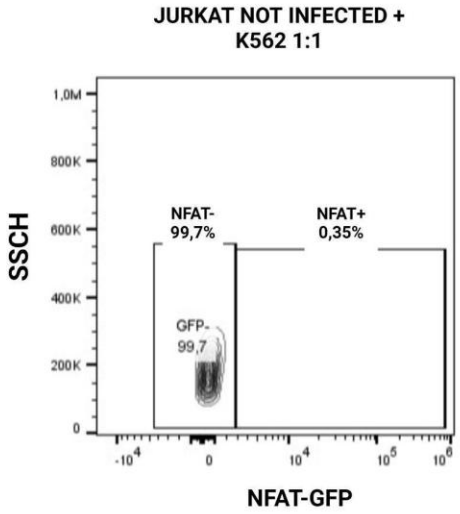
JURKAT NOT INFECTED +
K562 1:1
SSCH
NFAT-GFP
NFAT-
99,7%
NFAT+
0,35%
GFP-
99,7

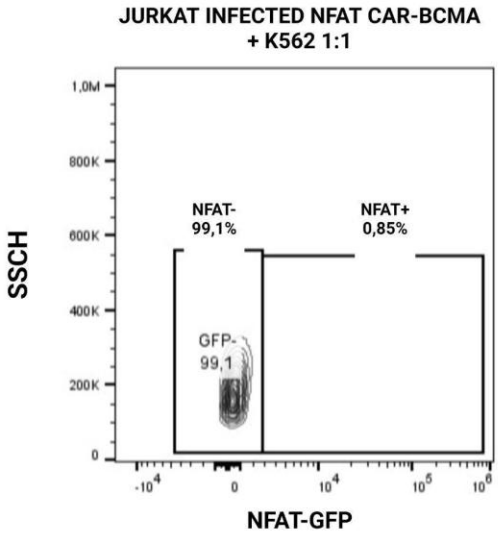
JURKAT INFECTED NFAT CAR-BCMA
+ K562 1:1
SSCH
NFAT-GFP
NFAT-
99,1%
NFAT+
0,85%
GFP-
99,1

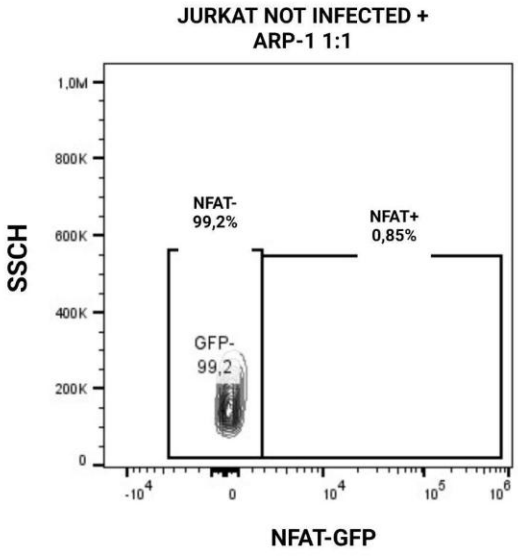
JURKAT NOT INFECTED +
ARP-1 1:1
SSCH
NFAT-GFP
NFAT-
99,2%
NFAT+
0,85%
GFP-
99,2

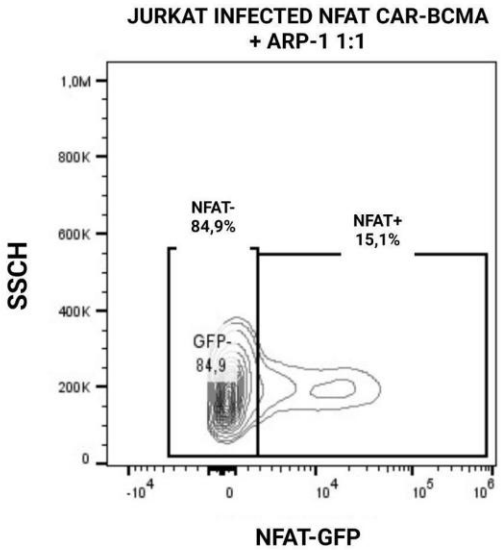
JURKAT INFECTED NFAT CAR-BCMA
+ ARP-1 1:1
SSCH
NFAT-GFP
NFAT-
84,9%
NFAT+
15,1%
GFP-
84,9

Figure 26. Antigen-specific NFAT activation in Jurkat cells co-transduced with 8xNFAT-ZsGreen-hCD8 and anti-BCMA CAR. Flow cytometry analysis after 72 h of co-culture shows robust NFAT activation (15% GFP^+) only in the presence of $BCMA^+$ ARP-1 myeloma cells. At the same time, no signal is detected upon co-culture with $BCMA^-$ K562 control cells, confirming antigen specificity and absence of tonic signalling.

These findings validate the functional integration and cooperation of the CAR and NFAT reporter modules and demonstrate that NFAT activation in this system is strictly dependent on the presence of the specific antigen (BCMA). The absence of activation in the K562 condition further supports the specificity and safety of the construct, with no evidence of ligand-independent CAR signalling per se or in the presence of BCMA-negative target cells.

4.5 Evaluation of pBULLET (NFAT) based constructs

To assess the NFAT-dependent inducibility of engineered surface receptors, Jurkat cells were transduced with retroviral particles encoding either hNIS, avidin, monodin, or a control GFP-only construct cloned into the pBULLET vector. Following stimulation with PHA (1,25 µg/mL) for either 4 or 24 hours, expression of the inducible receptors was assessed via flow cytometry.

Jurkat cells transduced with pBULLET vectors encoding GFP, hNIS, avidin, or monodin showed comparable basal GFP expression levels (range:12,9%–55,7%), confirming successful transduction with all constructs. The pBULLET_Avidin vector showed 14,3% GFP^+ cells, pBULLET_Monodin 12,9%, pBULLET_NIS 55,7%, while the control “empty” vector showed 46.9% GFP^+ cells, compared to 0,051% of not infected Jurkat cells (Figure 27A).

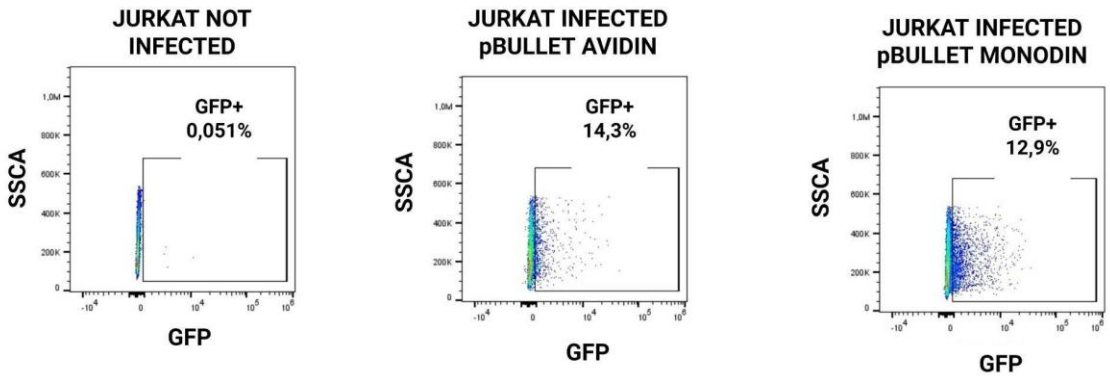

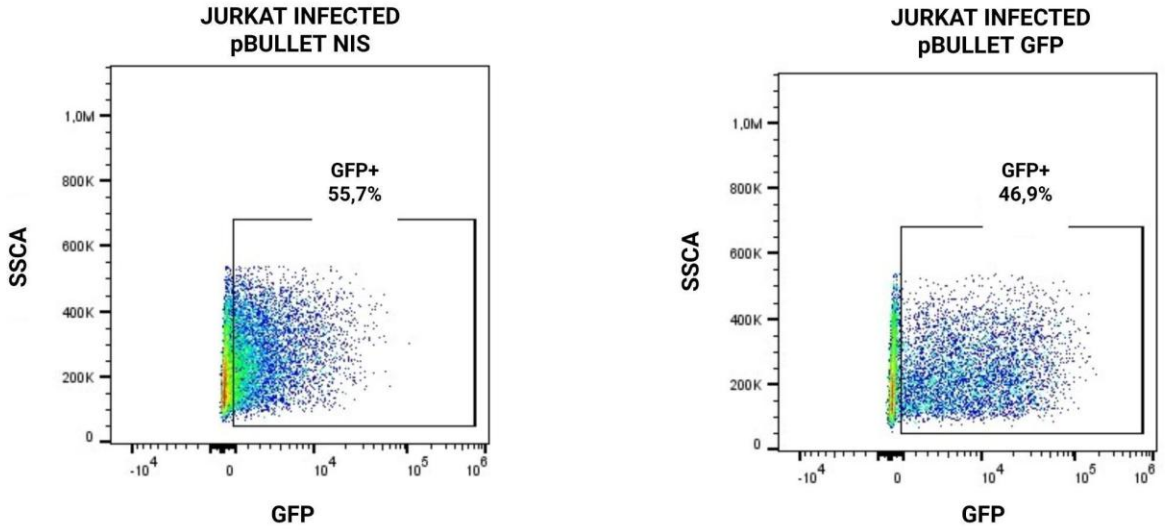

Figure 27A. Flow cytometry analysis of transduction efficiency in Jurkat cells transduced with pBULLET vectors. Flow cytometry plots display GFP fluorescence (x-axis) vs SSC-A (y-axis). In transduced Jurkat cells, the GFP^+ gate ranges from 12.9% to 55.7% of events. The non-infected control shows 0.051% GFP^+ events under identical acquisition settings.

Jurkat cells infected with the 8xNFAT-ZsGreen-hCD8 reporter construct and sorted to purity were used as a positive control to validate PHA-induced NFAT activation. As expected, this population showed high GFP expression (34,9%) after 4 hours of PHA stimulation (Figure 27B).

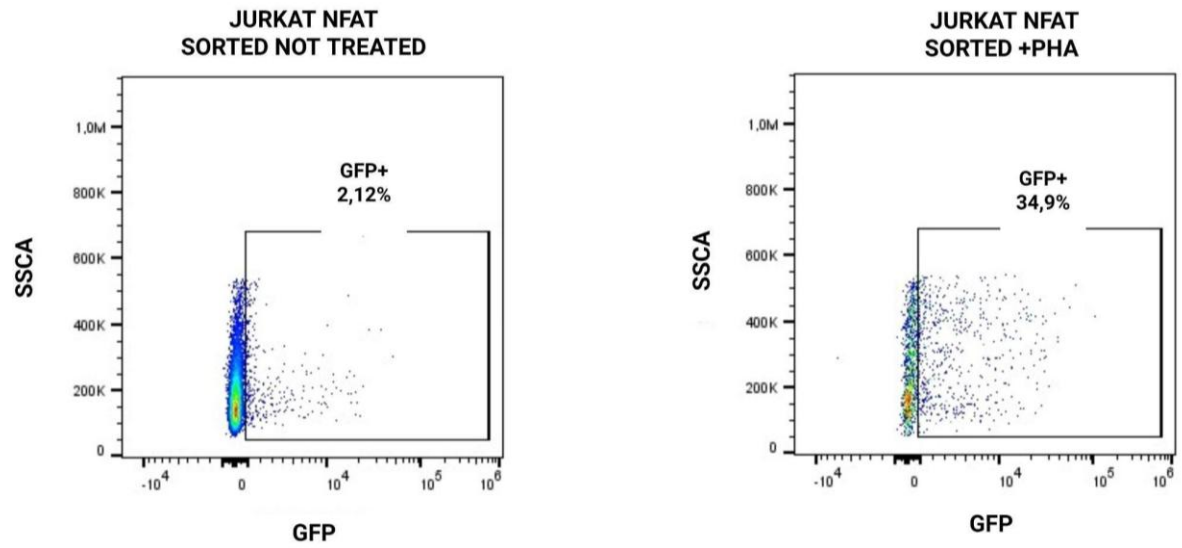

Figure 27B. Flow cytometry analysis of PHA-induced NFAT–GFP signal in sorted Jurkat NFAT–GFP⁺ control cells. Flow cytometry plots display GFP (x-axis) vs SSC-A (y-axis). In the PHA-stimulated Jurkat NFAT-GFP⁺ sorted cells (4 hours), the GFP⁺ gate exhibits 34.9% of events, compared to 2.12 % in the unstimulated control, validating NFAT pathway activation.

Jurkat cells transduced with pBULLET_avidin or pBULLET_monodin vectors were stimulated for 4 hours with PHA and then stained with biotin-PE to detect surface expression of the biotin-binding receptors. However, the biotin-PE signal did not appear to be specifically inducible under these conditions. In pBULLET_monodin-transduced cells, an elevated biotin-PE signal was observed even in the absence of PHA, suggesting basal expression or non-specific staining. In pBULLET_avidin-transduced cells, a modest increase was observed upon PHA stimulation, but a similar signal was also detected in the GFP-only control. These findings suggest that the biotin-PE signal in this experimental setup is not specifically associated with inducible expression of avidin or monodin, and may result from non-specific binding or background fluorescence, independent of NFAT pathway activation (Figure 28).

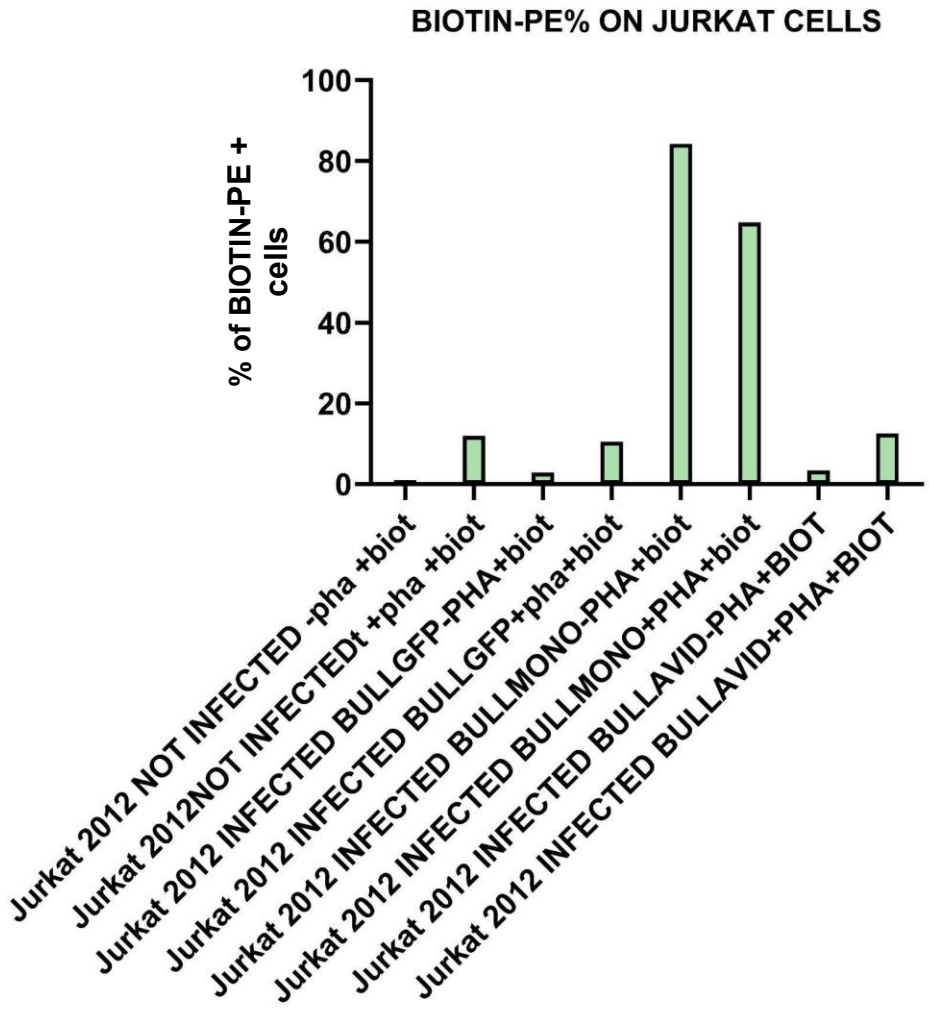

Figure 28. Quantification of Biotin-PE$^+$ Jurkat cells after 4 hours of PHA stimulation. The column chart shows the percentage of Biotin-PE$^+$ cells across different experimental conditions, including non-infected controls, GFP-only controls, and cells transduced with avidin or monodin constructs. Biotin-PE staining shows similar percentages in unstimulated and control samples, with no specific increase in Biotin-PE signal upon PHA stimulation. Data are shown as a representative experiment (n = 1).

Flow cytometry analysis using an anti-hNIS antibody was performed on Jurkat cells transduced with pBULLET_NIS and stimulated with PHA for 4 hours. While a signal (36,4%) was observed in the hNIS-transduced cells, a comparable level of fluorescence was also detected in the GFP-only control, which does not contain the hNIS insert (Figure 29). This suggests that the observed anti-hNIS staining is not specifically associated with inducible receptor expression and may reflect non-specific

antibody binding or background signal. Therefore, these data do not support specific or inducible surface expression of hNIS under PHA stimulation conditions.

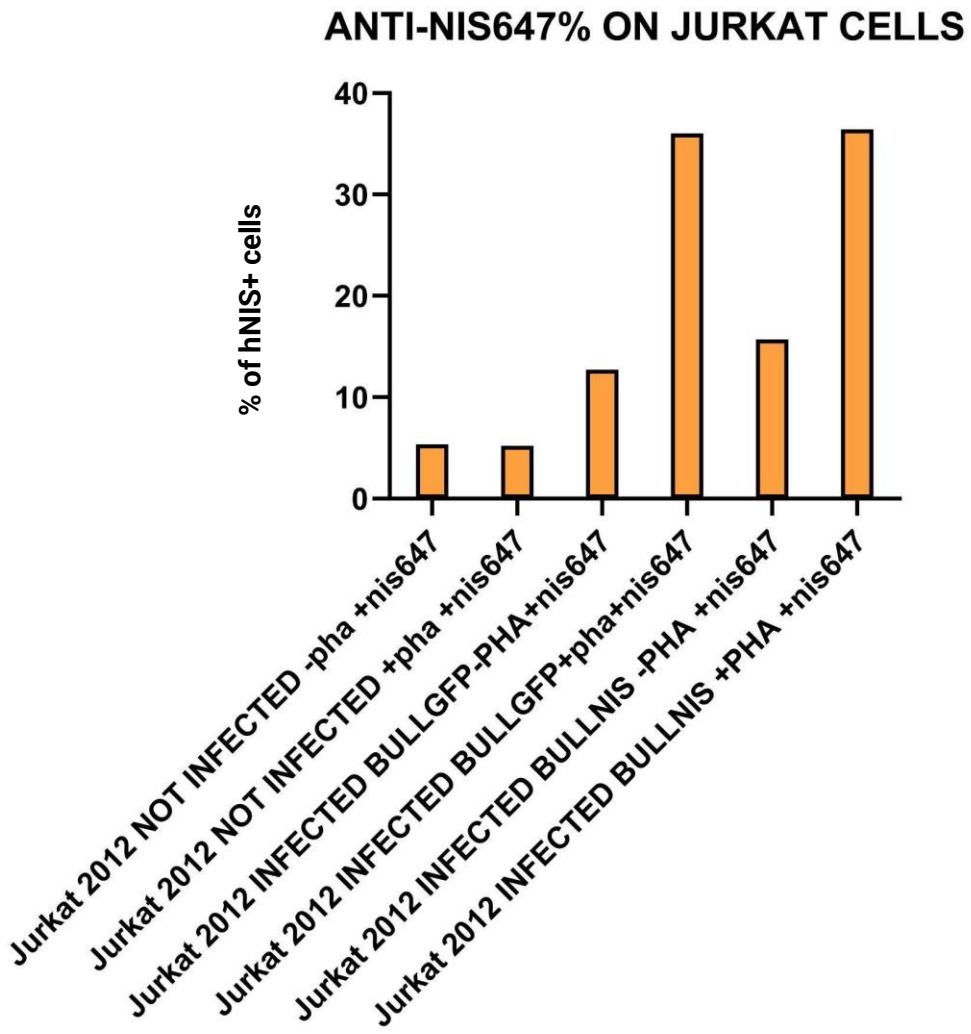

Figure 29. Quantification of hNIS$^+$ Jurkat cells after 4 hours of PHA stimulation. Column chart showing the percentage of anti-hNIS$^+$ cells in pBULLET_NIS–transduced Jurkat cells and GFP-only controls. Anti-hNIS staining shows 36.4% positive events in pBULLET_NIS cells, with a comparable signal in GFP-only controls, indicating non-specific antibody binding. Data are shown as a representative experiment (n = 1).

Following 24-hour stimulation with PHA, Jurkat cells transduced with pBULLET vectors encoding hNIS, avidin, monodin, or GFP-only were analysed by flow

cytometry. All constructs maintained measurable GFP expressions, with positivity ranging from approximately 7% to 42,5%, confirming successful transduction in each condition (Figure 30A).

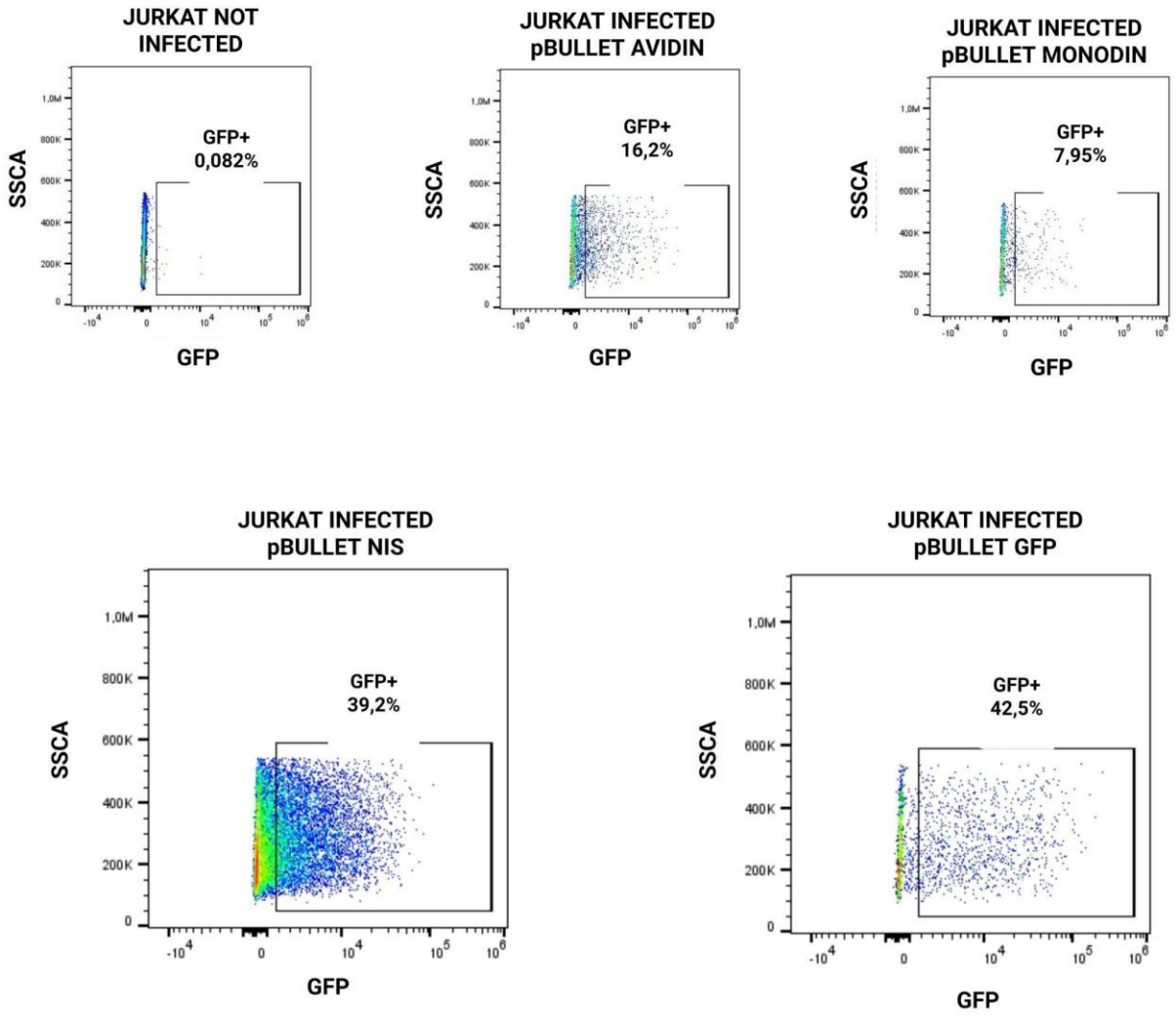

Figure 30A. Flow cytometric analysis of GFP expression in Jurkat cells transduced with pBULLET vectors following 24 hours of PHA stimulation. Jurkat T cells transduced with pBULLET retroviral vectors encoding hNIS, avidin, monodin, or GFP-only and subsequently stimulated for 24 hours with PHA. GFP expression was assessed by flow cytometry as a reporter of successful transduction. All constructs maintained measurable GFP expressions, with positivity ranging from approximately 7% to 42.5%, indicating efficient transduction across conditions. Representative flow cytometry histograms/plots are shown for each construct.

Positive control cells again showed robust GFP expression (49,8%) after 24-hour PHA stimulation, confirming the NFAT pathway (Figure 30B).

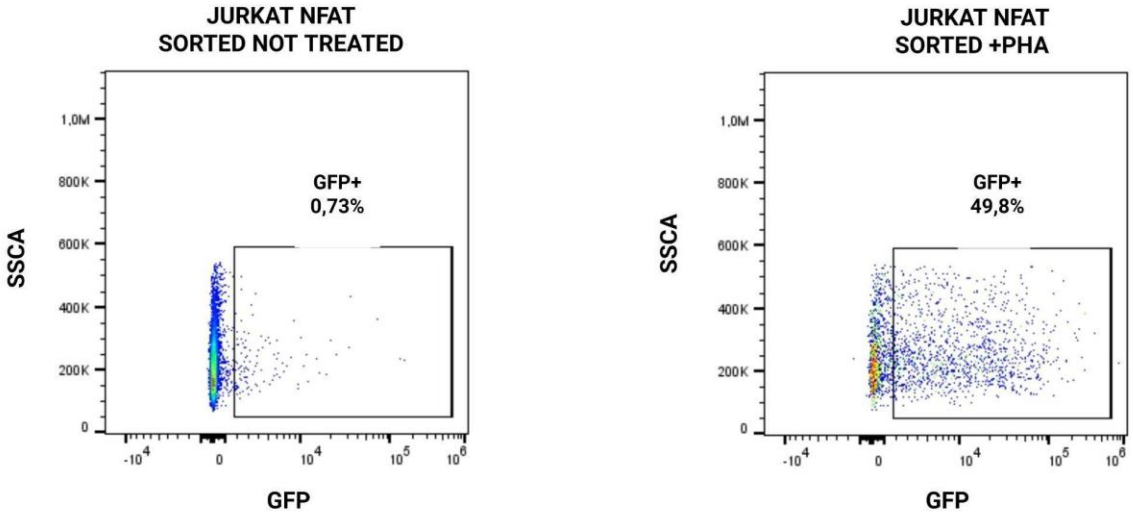

Figure 30B. Flow cytometry analysis of PHA-induced NFAT–GFP signal in sorted Jurkat NFAT–GFP$^+$ control cells. Flow cytometry plots display GFP (x-axis) vs SSC-A (y-axis). In the PHA-stimulated Jurkat NFAT-sorted cells (24 hours), the GFP$^+$ gate shows 49.8% of events, compared to 0.73% in the unstimulated control.

Jurkat cells transduced with pBULLET_avidin, pBULLET_monodin, or pBULLET_GFP were analysed by flow cytometry after 24-hour stimulation with PHA, followed by staining with biotin-PE to detect the surface expression of biotin-binding receptors. However, no specific upregulation of avidin or monodin expression was observed in the respective transduced populations. The biotin-PE signal remained low or comparable to non-stimulated and non-infected controls, suggesting that NFAT-driven expression was not effectively induced under these conditions.

In addition, a notably elevated PE signal was detected in cells transduced with the pBULLET_GFP construct, which lacks any biotin-binding domain. This signal was present even in the absence of PHA stimulation, indicating substantial non-specific

background staining. These findings suggest that, even after 24 hours of stimulation, the biotin-PE probe does not detect receptor expression in this context and may be unsuitable as a reliable readout of inducible avidin or monodin expression in Jurkat cells (Figure 31).

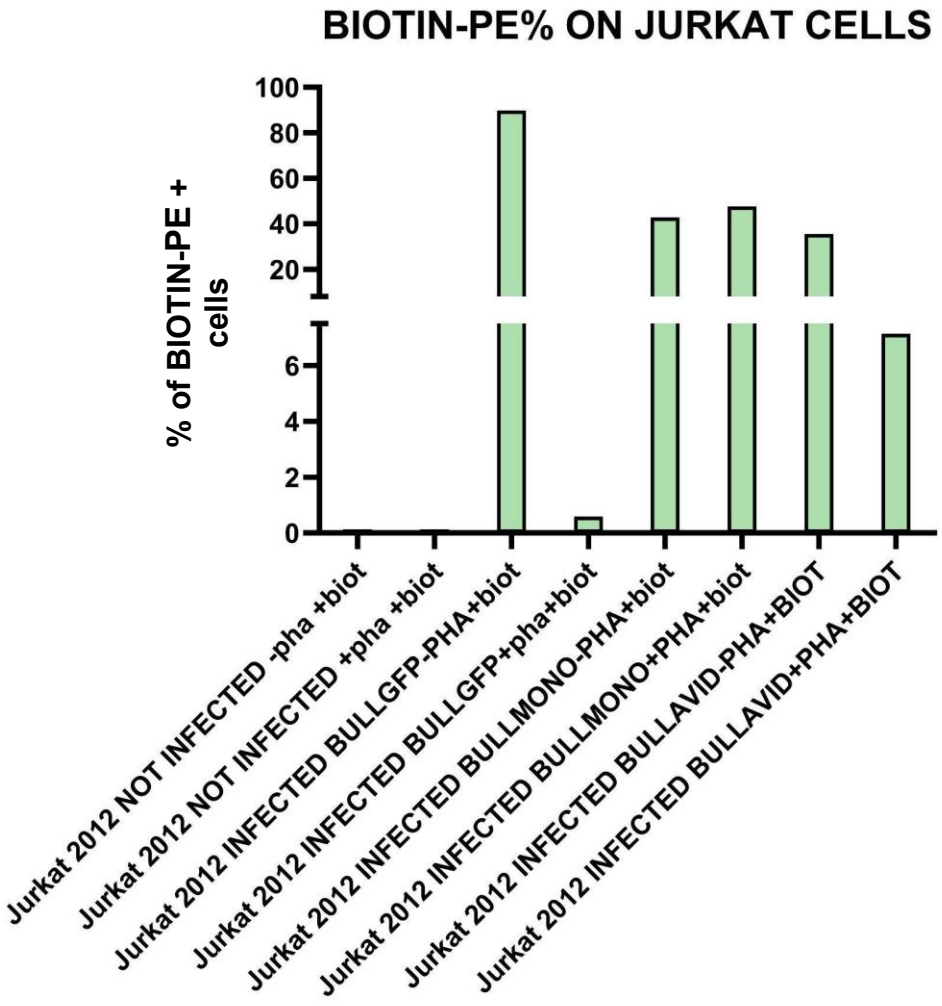

Figure 31. Quantification of Biotin-PE$^+$ in pBULLET transduced/not transduced Jurkat cells after 24 h of PHA stimulation. The column chart shows the percentage of Biotin-PE$^+$ cells across different experimental conditions, including non-infected controls, GFP-only controls, and cells transduced with avidin or monodin constructs. No specific increase in Biotin-PE signal is observed in avidin- or monodin-expressing cells, while an elevated

background signal is detected in pBULLET_GFP controls. Data are shown as a representative experiment (n = 1).

Jurkat cells transduced with pBULLET_NIS did not exhibit any detectable surface staining using anti-NIS antibody compared to the GFP-control vector, confirming the lack of inducible expression again after 24 hours of PHA treatment (Figure 32). In particular, flow cytometry analysis revealed a slight increase in anti-NIS fluorescence in the pBULLET_NIS-transduced population compared to the pBULLET_GFP control (approximately 1% difference). However, given the low absolute intensity of the signal and the presence of comparable background staining in control samples, this variation is not sufficient to indicate specific or inducible expression of hNIS. These results confirm that, under the tested conditions, the NFAT-inducible vector does not mediate detectable hNIS surface expression in Jurkat cells.

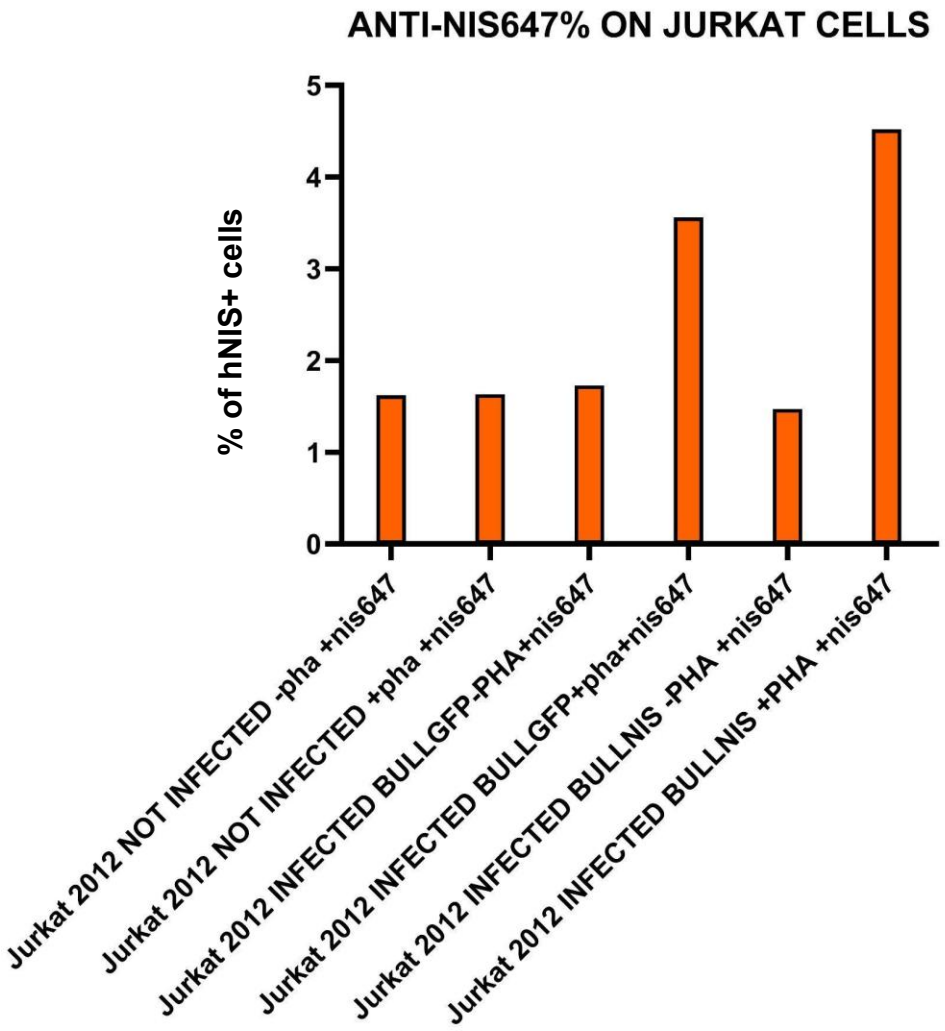

Figure 32. Quantification of hNIS expression in pBULLET transduced/not transduced Jurkat cells stained with anti-hNIS-647 after 24 hours of PHA stimulation. Column chart showing the percentage of anti-hNIS^{+} cells across different experimental conditions, including non-infected controls, GFP-only controls, and pBULLET_NIS–transduced cells. The difference between pBULLET_NIS and GFP controls is approximately 1%, indicating low and non-specific signal and no detectable inducible hNIS expression. Data are shown as a representative experiment (n = 1).

Jurkat cells transduced with pBULLET_GFP and pBULLET_NIS vectors were selected for biotin titration experiments, as these two constructs had shown the highest GFP expression levels among the conditions, confirming efficient transduction. The goal was to evaluate whether modifying the quantity of PHA during staining could enhance the detection of potential surface expression of NIS or uncover low-level background in GFP controls.

Cells were stained at 4 hours (Figure 33) and 24 hours (Figure 34) after PHA stimulation, using a PHA range from 0,625µg/mL to 1,25µg/mL. However, no significant increase in the specific signal for hNIS was observed across the titration curve in any condition. Both pBULLET_GFP and pBULLET_NIS populations exhibited overlapping fluorescence profiles, confirming that PHA level did not impact detection, and no NFAT-induced hNIS expression was measurable under these conditions.

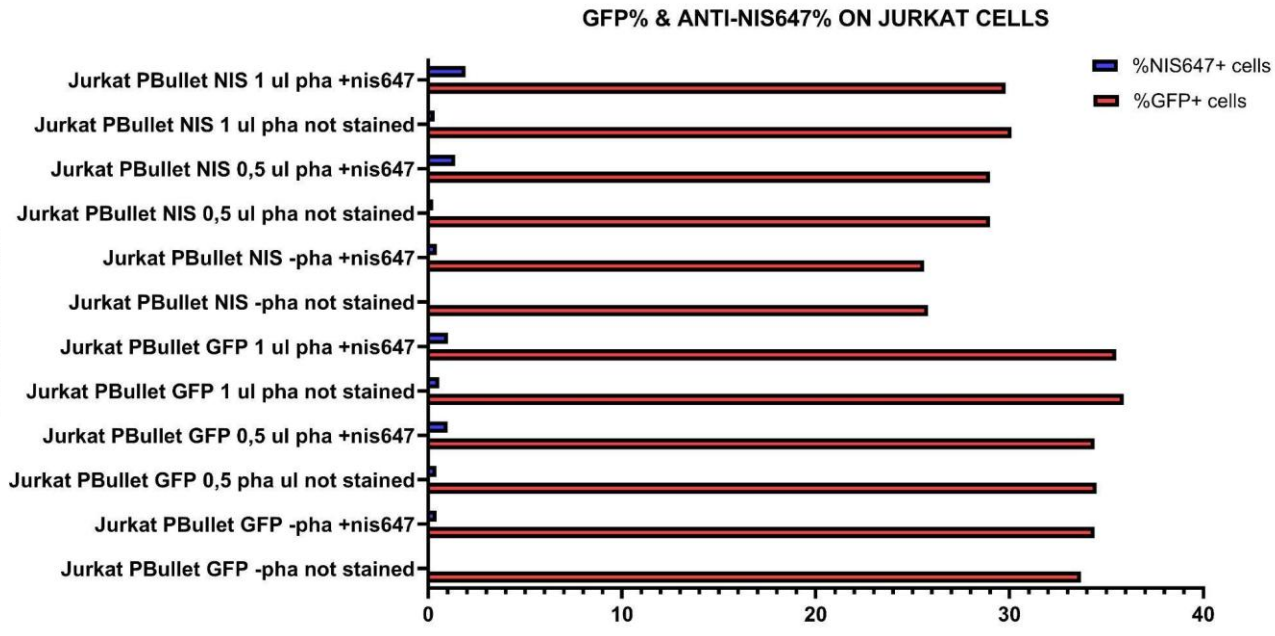

Figure 33. Quantification of GFP and hNIS expression in Jurkat pBULLET_NIS and pBULLET_GFP cells stained with anti-hNIS-647 after 4 hours of PHA stimulation at different concentrations. Horizontal bar chart shows the percentage of GFP^+ (red bars) and anti-$hNIS^+$ (blue bars) cells in Jurkat pBULLET_NIS and Jurkat pBULLET_GFP cells stimulated with different volumes of PHA. GFP^+ percentages remain stable across all conditions, while anti-hNIS-647 staining shows no increase in signal at any PHA concentration tested, indicating a lack of inducible hNIS surface expression after 4 hours. Data are shown as a representative experiment (n = 1).

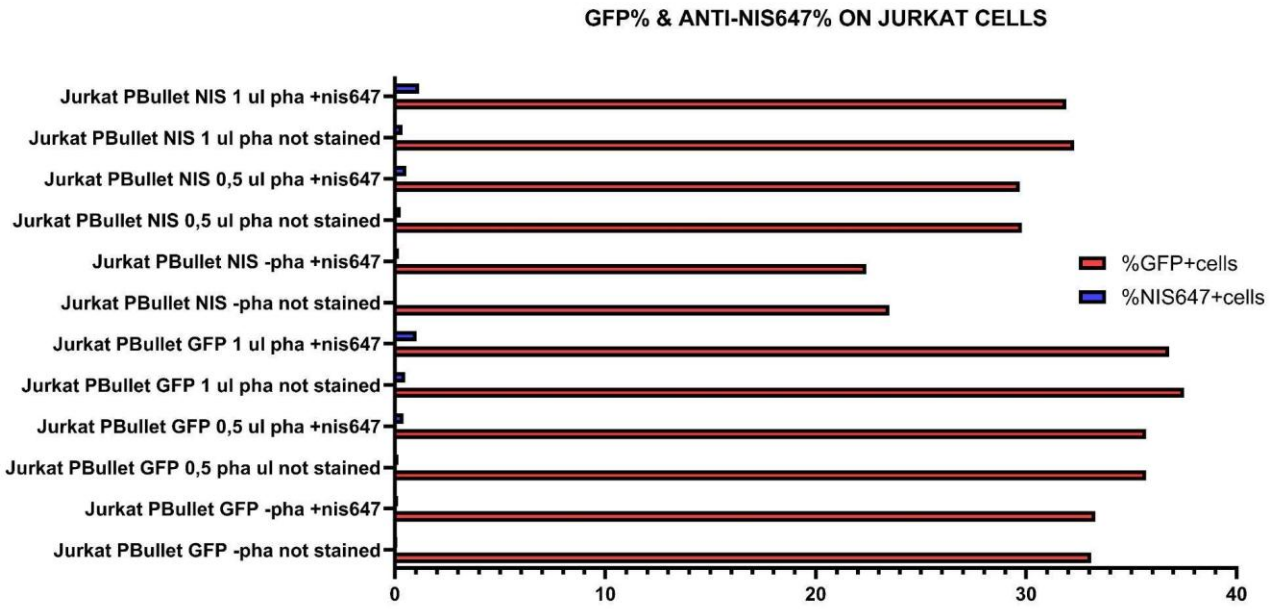

Figure 34. Quantification of GFP and hNIS expression in Jurkat pBULLET_NIS and pBULLET_GFP cells stained with anti-hNIS-647 after 24 hours of PHA stimulation at different concentrations. Horizontal bar chart shows the percentage of GFP^+ (red bars) and anti-$hNIS^+$ (blue bars) cells in Jurkat pBULLET_NIS and Jurkat pBULLET_GFP cells stimulated with different volumes of PHA. GFP^+ percentages remain stable across all conditions, while anti-hNIS-647 staining shows no measurable increase in signal at any PHA concentration tested, indicating no inducible hNIS surface expression after 24 hours. Data are shown as a representative experiment (n = 1).

A second round of Jurkat transduction (N=2) was performed using the same viral batches previously tested for pBULLET_NIS and pBULLET_GFP. Flow cytometry confirmed comparable transduction efficiency, with GFP^+ populations ranging from 12,5% to 53,45%, confirming the reproducibility of the infection protocol across independent experiments.

Following stimulation with PHA for either 4 hours (Figure 35) or 24 hours, Jurkat cells transduced with pBULLET_NIS were analysed by flow cytometry to assess surface expression of the hNIS receptor. Despite confirmed transduction, no hNIS expression was detected at the cell surface, consistent with the results from the first experiment. Furthermore, a low but persistent anti-NIS signal was again observed in the pBULLET_GFP control, indicating ongoing non-specific background staining. Data for 24 hours are not shown.

Biotin-based staining was also performed but yielded 0% signal across all conditions and was therefore excluded from graphical representation. These findings reinforce that NFAT-dependent inducible expression of hNIS was not achieved, and that the system continues to exhibit background in both experimental replicates.

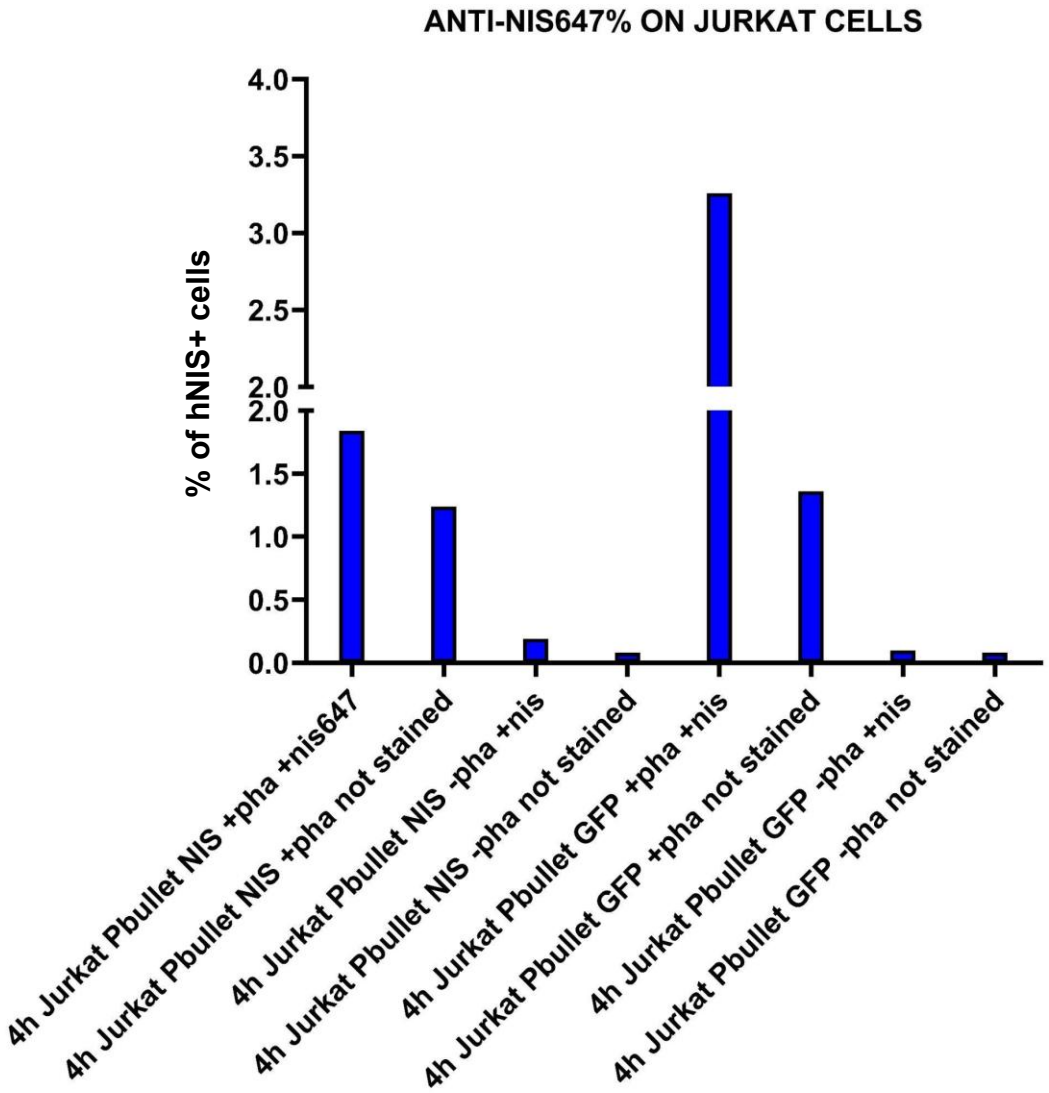

Figure 35. Quantification of hNIS expression in Jurkat pBULLET_NIS and pBULLET_GFP cells stained with anti-hNIS-647 after 4 hours of PHA stimulation (second transduction). The column chart shows the percentage of anti-hNIS^{+} cells in Jurkat pBULLET_NIS and Jurkat pBULLET_GFP populations under different stimulation and staining conditions. Surface hNIS expression remains undetectable in pBULLET_NIS cells. A background signal of 3.26% anti-hNIS^{+} cells is observed in the pBULLET_GFP control. Data are shown as a representative experiment (n = 1).

To assess whether alternative T cell activation stimuli could improve inducible receptor expression, Jurkat cells transduced with pBULLET_NIS, pBULLET_Avidin, pBULLET_Monodin, and pBULLET_GFP (N=2) were stimulated with anti-CD3/CD28 Dynabeads for either 4 hours or 48 hours and analysed by flow cytometry. However, the results from these experiments confirmed the absence of induction seen in previous experiments (data not shown).

In order to monitor persistence of transduced cells and potential silencing of pBULLET vectors over time, the percentage of GFP^+ Jurkat cells was quantified at four time points: day 0 (7 days post-transduction), day 1 (8 days), day 14 (21 days), and day 16 (23 days). All constructs showed a progressive decline in GFP expression over time (Figure 36). At day 0, pBULLET_NIS-transduced cells exhibited the highest GFP^+ percentage (approximately 44%), followed by pBULLET_GFP (40%), pBULLET_Avidin (19%), and pBULLET_Monodin (12%). By day 1, GFP levels slightly increased in pBULLET_NIS (to ~54%) and remained stable in pBULLET_GFP (41%), while modest increases were also observed in pBULLET_Avidin (23%) and pBULLET_Monodin (14%). However, from day 14 onward, all constructs showed a marked reduction in GFP^+ cells. By day 16, pBULLET_NIS dropped to 23%, pBULLET_GFP to 30%, pBULLET_Avidin to 9%, and pBULLET_Monodin to 4,5%, indicating potential vector silencing, cellular selection against transduced populations, or instability of the integration over time.

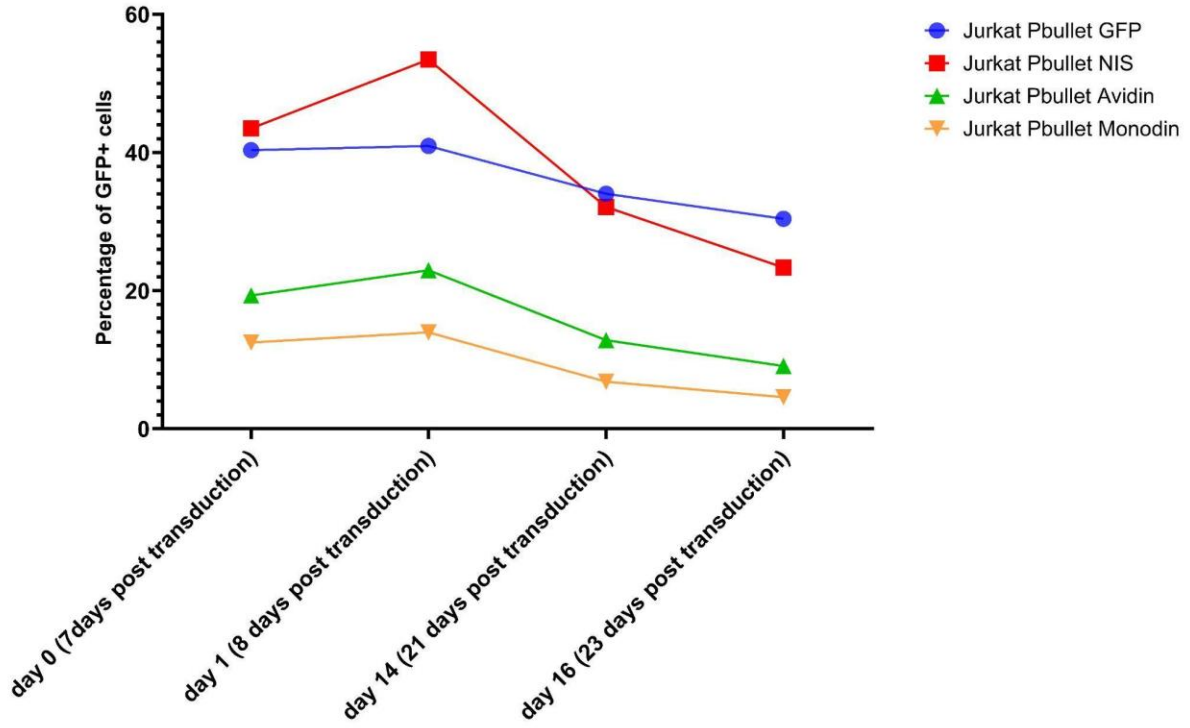

Figure 36. Percentage of GFP-positive Jurkat cells transduced with pBULLET-based vectors over time. Jurkat cells were transduced with pBULLET vectors encoding GFP, hNIS, avidin, or monodin. GFP expression was measured by flow cytometry at four time points: day 7, day 8, day 21, and day 23 post-transduction. Data are shown as a representative experiment (n = 1).

Similar experiments were performed on Pan-T cells derived from healthy donor PBMCs. Following isolation, Pan-T cells were activated for 3 days using anti-CD3/CD28 Dynabeads and subsequently transduced with pBULLET vectors encoding GFP, hNIS, avidin, or monodin, using the RetroNectin-based protocol described in the Materials and Methods section. Since primary Pan-T cells require the activation phase before transduction and a subsequent recovery/expansion period, transduction efficiency was evaluated at time points defined relative to T-cell stimulation rather than absolute days post-transduction. Accordingly, transduction efficiency was evaluated by monitoring GFP expression at 6- and 8-day post-transduction (designated as day 0 and day 2 after stimulation, respectively). At day 0, the frequency of GFP^+ cells was 32.9% for pBULLET_GFP, 24.3% for pBULLET_NIS, 10.7% for pBULLET_Avidin, and 7.7% for pBULLET_Monodin (Figure 37).

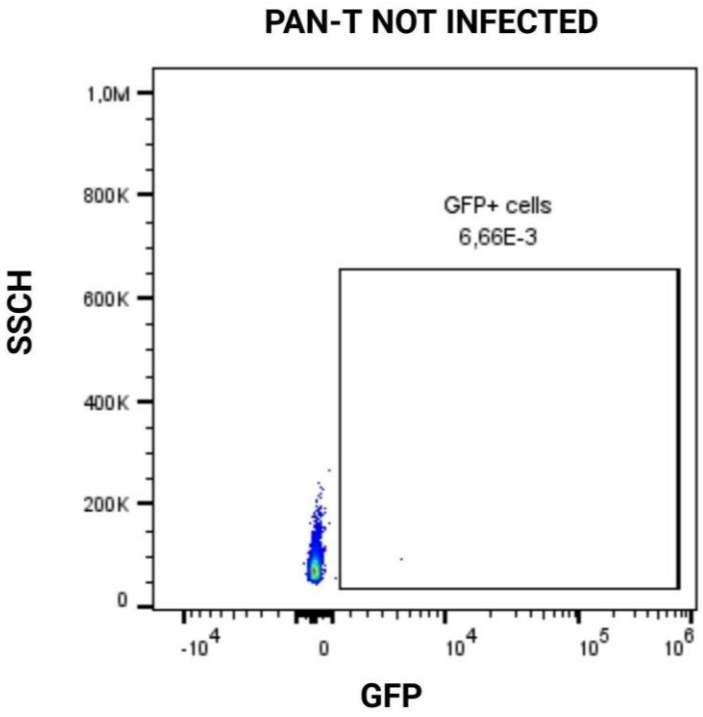
PAN-T NOT INFECTED
1,0M
800K
600K
400K
200K
0
SSCH
GFP+ cells
6,66E-3
-10^4
0
10^4
10^5
10^6
GFP

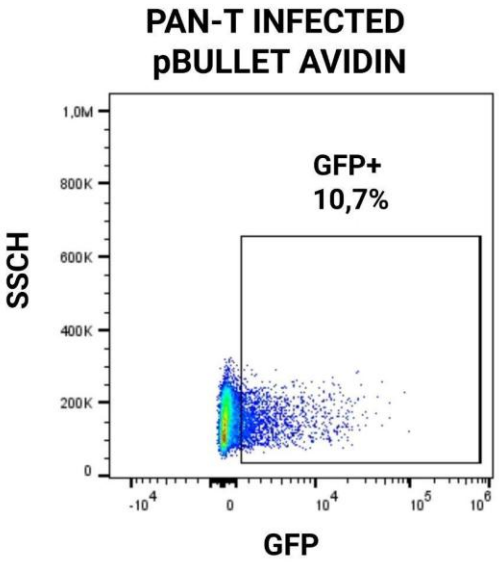
PAN-T INFECTED
pBULLET AVIDIN
1,0M
800K
600K
400K
200K
0
SSCH
GFP+
10,7%
-10^4
0
10^4
10^5
10^6
GFP

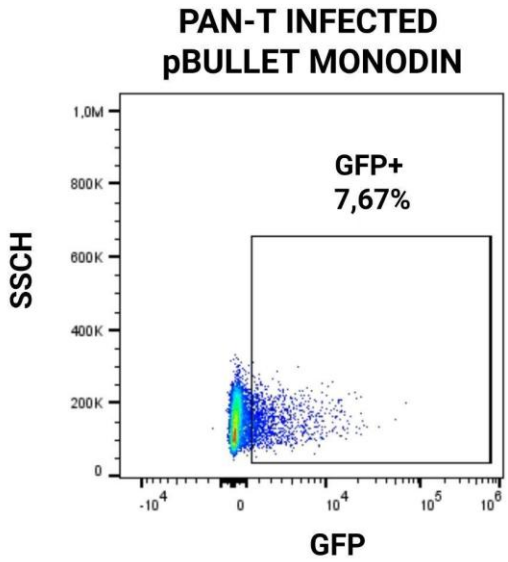
PAN-T INFECTED
pBULLET MONODIN
1,0M
800K
600K
400K
200K
0
SSCH
GFP+
7,67%
-10^4
0
10^4
10^5
10^6
GFP

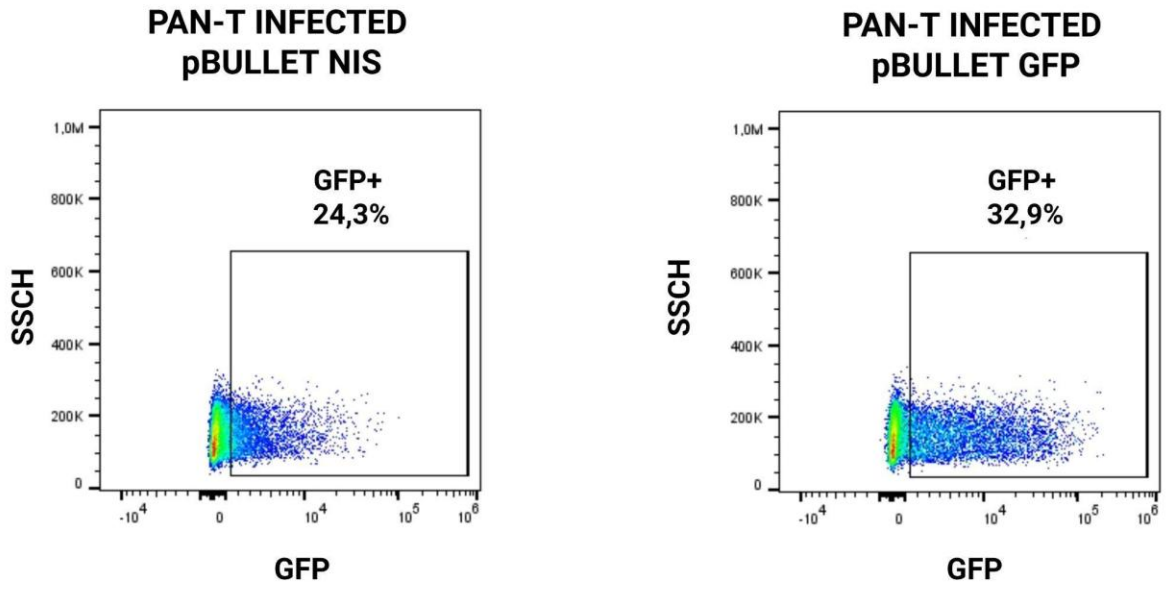

Figure 37. Flow cytometry plots showing GFP⁺ Pan-T cells 6 days after transduction with pBULLET constructs (GFP, NIS, Avidin, Monodin) vs PAN-T Not Infected. Flow cytometry plots display GFP (x-axis) vs SSC-A (y-axis). Pan-T cells not infected show a GFP⁺ gate of 0.0066%, indicating negligible background fluorescence. In transduced cells, the GFP⁺ population corresponds to 10.7% for pBULLET_Avidin, 7.67% for pBULLET_Monodin, 24.3% for pBULLET_NIS, and 32.9% for pBULLET_GFP, reflecting the transduction efficiency achieved with each construct.

These values showed minimal decline by day 2 (31.4%, 20.1%, 8.91%, and 5.86%, respectively), confirming consistent transgene expression across timepoints and constructs (Figure 38).

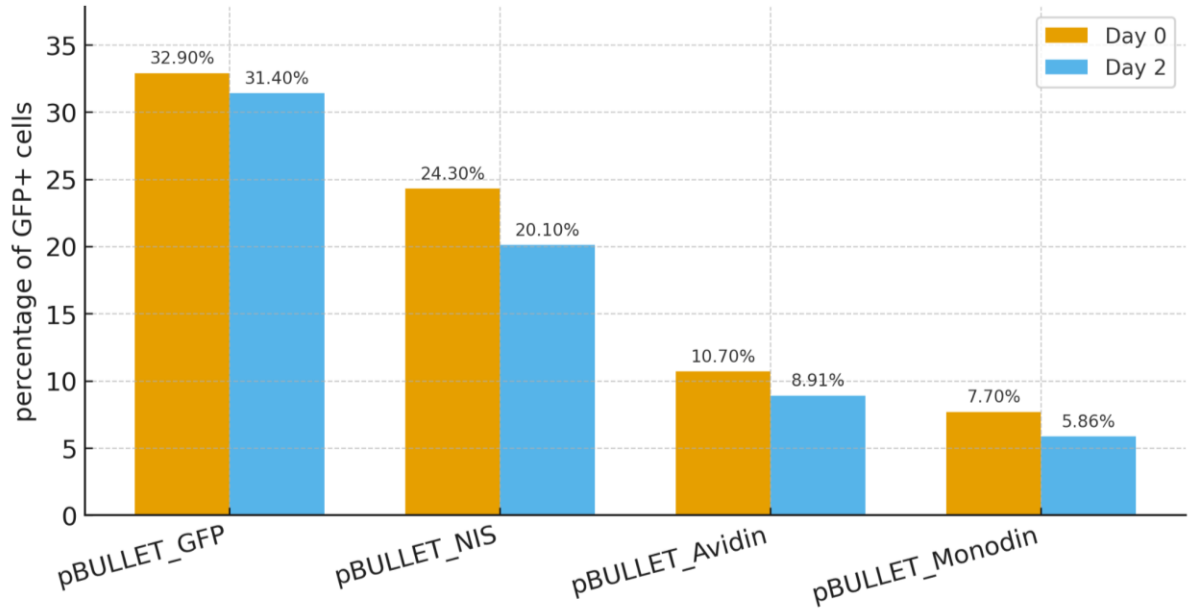

Figure 38. Column chart of transduction efficiency at two timepoints in PAN-T cells transduced with pBULLET constructs. PAN-T cells were monitored for GFP expression at 6 and 8 days post-transduction (designated as day 0 and day 2 after stimulation, respectively). Bars show the percentage of GFP⁺ cells for each construct at both timepoints: pBULLET_GFP—32.9% (day 0) and 31.4% (day 2); pBULLET_NIS—24.3% (day 0) and 20.1% (day 2); pBULLET_Avidin—10.7% (day 0) and 8.91% (day 2); pBULLET_Monodin—7.7% (day 0) and 5.86% (day 2). The plot reports all values as "percentage of GFP+ cells" on the y-axis, with constructs on the x-axis. Data are shown as a representative experiment (n = 1).

Based on preliminary results obtained with NFAT (Nakayama vector)-transduced PBMCs (section 4.4), in which Dynabeads proved to be the most effective activation stimulus, we chose to test this condition directly on the transduced Pan-T cells using pBULLET vectors. To assess potential receptor activation, Dynabeads were used as a stimulus at two time points: 4 hours and 48 hours. Surface expression of the inducible receptors was then evaluated by flow cytometry to determine whether CD3/CD28 stimulation could trigger their activation in this cellular context. However, flow cytometry analysis confirmed previous negative results, even after 48 hours of stimulation (Figures 39-40).

Taken together, these data suggest that although the retroviral constructs successfully transduce and express GFP in Pan-T cells, the inducible promoters in the pBULLET vector fail to trigger receptor expression upon T cell activation, mirroring the results obtained in Jurkat cells.

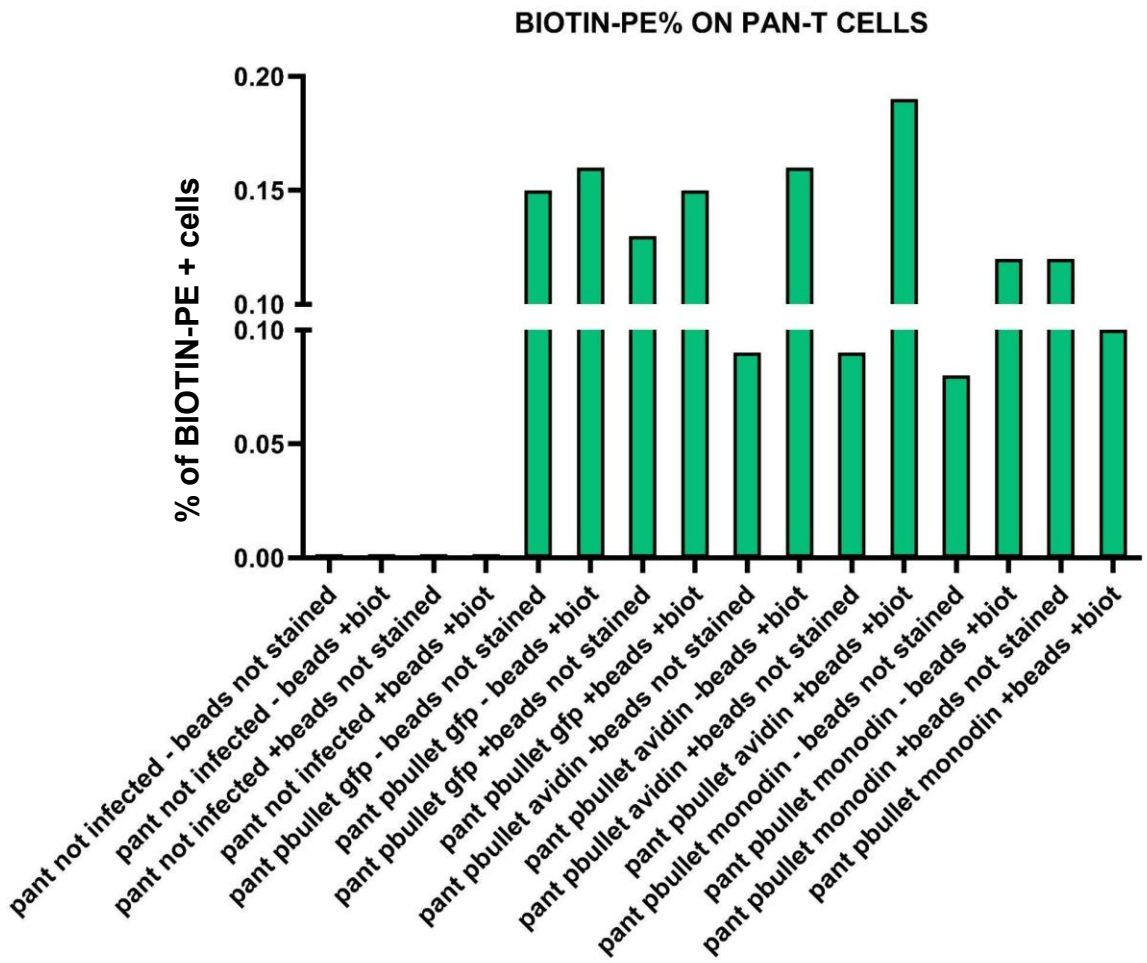

Figure 39. Quantification of Biotin-PE$^+$ PAN-T cells after 48 hours of Dynabeads stimulation. The column chart shows the percentage of Biotin-PE$^+$ cells in PAN-T not infected and in PAN-T infected with pBULLET_GFP, pBULLET_Avidin, or pBULLET_Monodin under different stimulation and staining conditions. All conditions show low Biotin-PE$^+$ percentages, with no detectable increase in avidin- or monodin-transduced cells, indicating the absence of

specific receptors expression after 48 hours of stimulation. Data are shown as a representative experiment (n = 1).

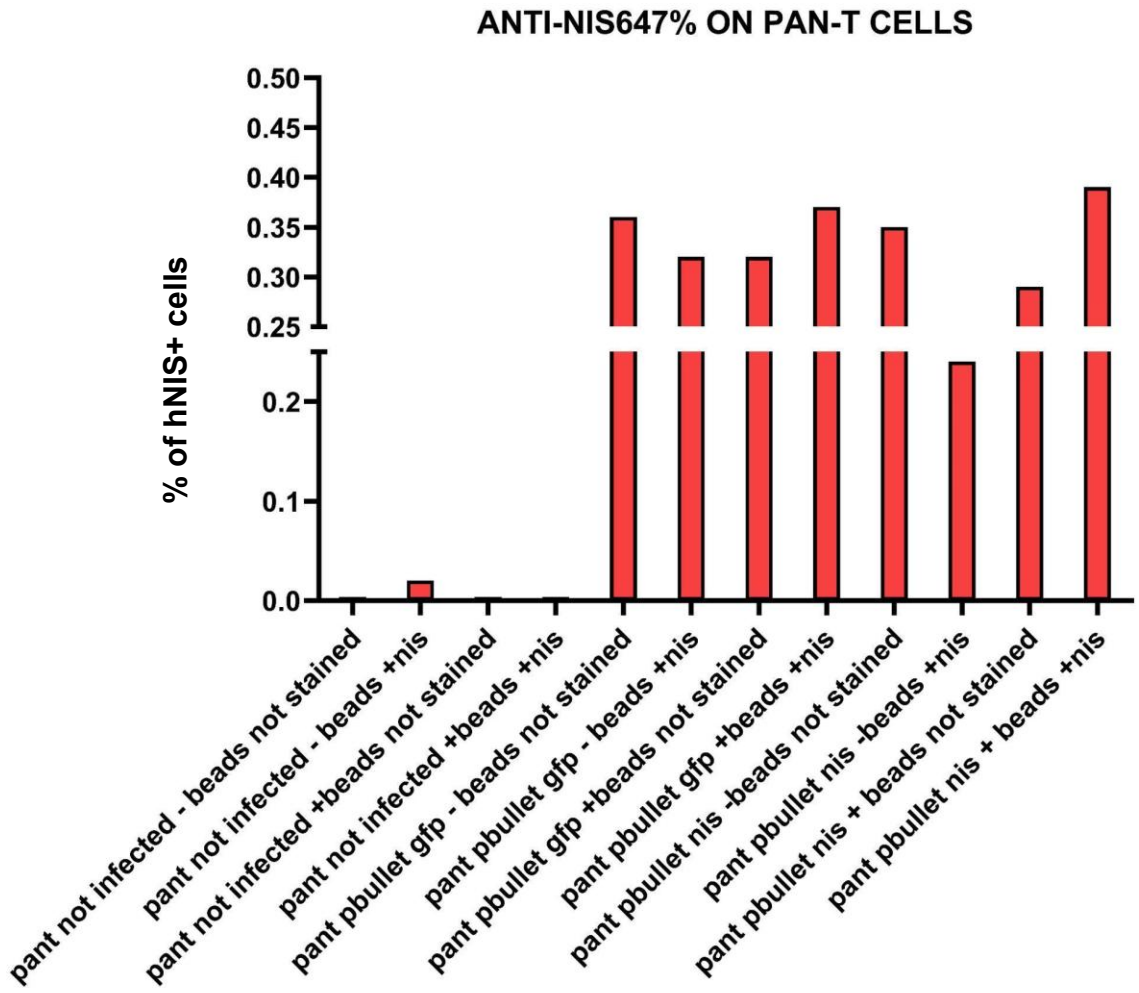

Figure 40. Quantification of hNIS expression in Pan-T cells stained with anti-hNIS-647 after 48 hours of Dynabeads stimulation. The column chart shows the percentage of anti-hNIS^{+} cells in Pan-T not infected, PAN-T infected with pBULLET_GFP, and pBULLET_NIS populations under different stimulation and staining conditions. All conditions display low percentages of hNIS^{+} cells, with no specific increase in pBULLET_NIS-transduced cells, indicating the absence of detectable hNIS surface expression after 48 hours of stimulation. Data are shown as a representative experiment (n = 1).

4.6 Evaluation of pHR_5xGAL4 (synNotch)

This section examines the functionality of the pHR_5xGAL4 inducible expression system in combination with synNotch receptors. These experiments aimed to determine whether antigen-dependent synNotch activation could be used to drive controlled expression of reporters and payload genes in engineered cells. To this end, to evaluate the functionality of synNotch-inducible constructs, Jurkat cells were engineered to express anti-HER2 or anti-CD19 synNotch receptors and subsequently co-transduced with GAL4-responsive vectors encoding hNIS, avidin, or monodin, as described in the materials and methods section. Receptor expression was designed to occur only upon synNotch activation following contact with $HER2^+$ (SK-BR-3) or $CD19^+$ (NALM-6) target cells. After Myc-based selection of $synNotch^+$ Jurkat populations, co-culture experiments were performed at different effector-to-target (E:T) ratios and for different durations. Receptor induction was assessed by flow cytometry following antigen-specific stimulation. Unstimulated and empty-GFP vector controls were included to validate specificity and inducibility. In addition, HEK293T cells were used in parallel experiments as a model system and transduced to express SynNotch-HER2/CD19.

To assess SynNotch-HER2 transduction efficiency, both Jurkat cells and HEK293T were stained with an anti-myc-PE antibody and analysed by flow cytometry. SynNotch-HER2 infected cells showed 83% and 62% positive staining with anti-myc-PE for HEK293T (Figure 41, Panel A) and Jurkat (Figure 41, Panel B), respectively, confirming substantial receptor expression. Following the sorting procedure for Myc-PE^+ cells, the resulting population displayed an enrichment of approximately 86% Myc^+ cells, indicating successful selection of a HER2-synNotch-expressing Jurkat population. This purified population (Figure 41, Panel C) was subsequently transduced with the inducible pHR_5xGAL4 vectors and then used in co-culture assays to test receptor activation in the presence of $HER2^+$ target cells (Section 4.6.1).

HEK293T cells (SynNotch-HER2)

A.

COLOUR	SAMPLE NAME	FREQ. PARENT % POSITIVE CELLS	MFI
	HEK293T cells not infected not stained	0,72	2022
	HEK293T cells not infected mycpe	1,79	2423
	HEK293T cells her2 synnotch infected not stained	2,11	1976
	HEK293T cells HER2 synnotch infected stained mycpe	83,0	7741

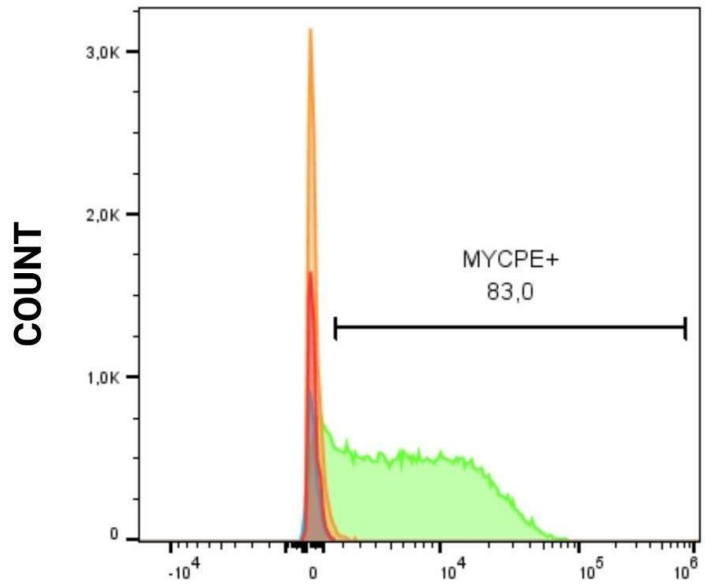

% of MYCPE+ cells

B.

JURKAT CELLS (SynNotch-HER2) BEFORE SORTING

COLOUR	SAMPLE NAME	FREQ. PARENT % POSITIVE CELLS	MFI
	Jurkat not infected not stained	0,26	1340
	Jurkat not infected stained mycpe	0,035	1533
	Jurkat HER2 synnotch infected not stained	0	N/A
	Jurkat HER2 synnotch infected stained mycpe	61,8	4561

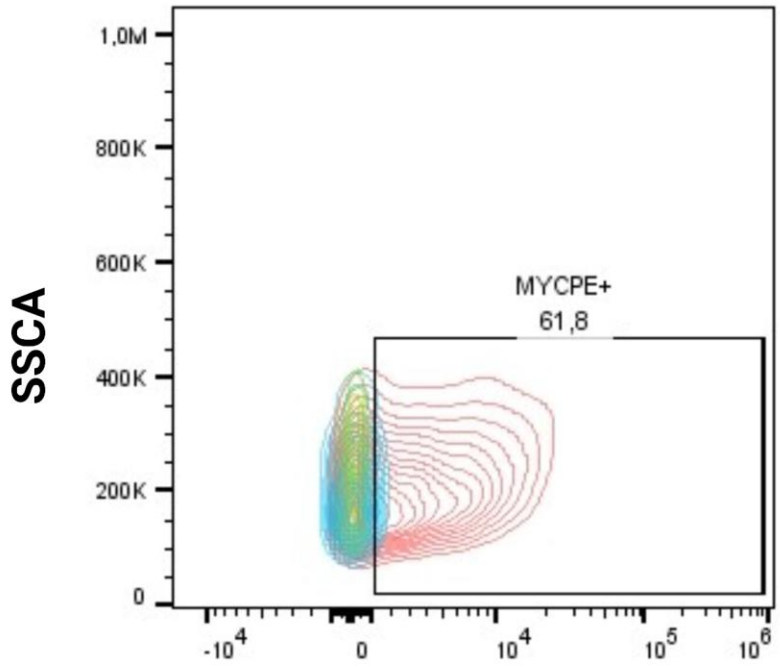

% of MYCPE+ cells

C.

JURKAT CELLS (SynNotch-HER2) SORTED

COLOUR	SAMPLE NAME	FREQ. PARENT % POSITIVE CELLS	MFI
	Jurkat HER2 synnotch sorted not stained	0,70	5,59E5
	Jurkat HER2 synnotch sorted stained mycpe	86,1	4,85E5

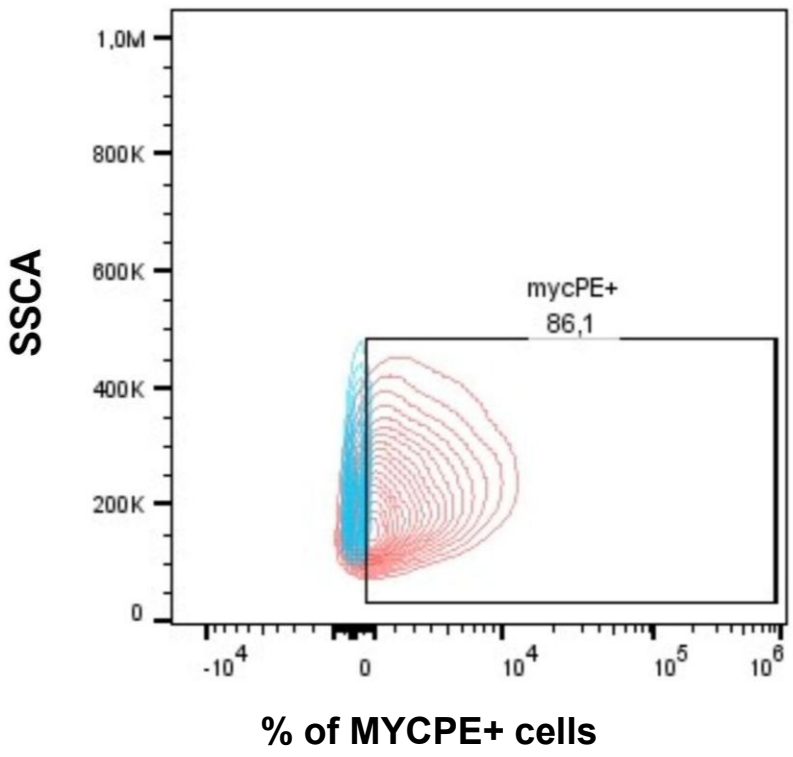

Figure 41. Flow cytometry assessment of SynNotch–HER2 transduction using anti-MYCPE staining in 293T and Jurkat cells, with Jurkat enrichment by sorting. MYC-PE fluorescence is plotted on the x-axis and side scatter (SSC) on the y-axis.

Panel (A): HEK293T cells stained with anti-Myc-PE to assess SynNotch–HER2 expression; 83% of events are Myc-PE$^+$, indicating high transduction efficiency in this model system. **Panel (B):** Jurkat cells (pre-sorted) stained with anti-Myc-PE; 61,8% of events are Myc-PE$^+$, confirming substantial receptor expression before enrichment. **Panel (C):** Jurkat cells (post-sorted) for Myc-PE$^+$ events; the enriched population displays 86,1% Myc$^+$ cells, indicating successful selection of a SynNotch–HER2–expressing Jurkat population.

HEK293T transduced with synNotch-CD19 showed good expression levels, with 57.6% Myc-PE$^+$ cells (Figure 42, Panel A). Even for Jurkat cells transduced with the synNotch receptor specific for CD19, flow cytometry analysis using anti-Myc-PE staining showed that 66.4% of the cells expressed the receptor before sorting,

indicating successful transduction (Figure 42, Panel B). Following Myc-based sorting, the proportion of Jurkat Myc$^+$ cells increased to 95.2%, yielding a highly enriched population of CD19-synNotch$^+$ Jurkat cells. The sorted population (Figure 42, panel C) was transduced with the pHR_5xGAL4 vectors and then subjected to downstream assays to evaluate receptor induction upon CD19 antigen engagement (Section 4.6.2).

A.

HEK293T cells (SynNotch-CD19)

COLOUR	SAMPLE NAME	FREQ. PARENT % POSITIVE CELLS	MFI
	HEK293T cells not infected not stained	0,11	4745
	HEK293T cells not infected mycpe	0,39	4205
	HEK293T cells CD19 synnotch infected not stained	0,90	3827
	HEK293T cells CD19 synnotch infected stained mycpe	57,6	11139

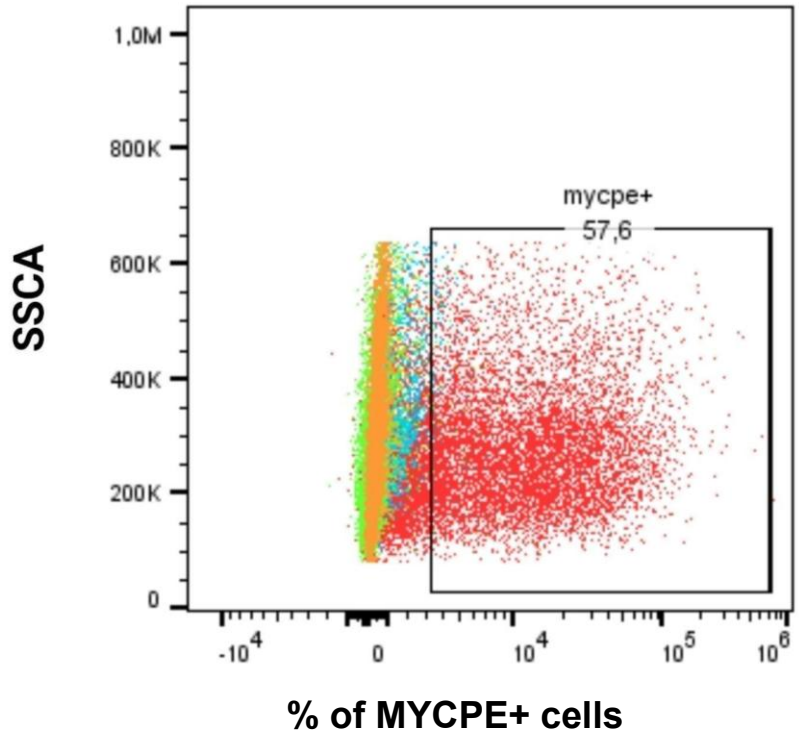

B.

JURKAT CELLS (SynNotch-CD19) BEFORE SORTING

COLOUR	SAMPLE NAME	FREQ. PARENT % POSITIVE CELLS	MFI
	Jurkat not infected not stained	0,27	1340
	Jurkat not infected stained mycpe	0,030	2298
	Jurkat CD19 synnotch infected not stained	0,017	1392
	Jurkat CD19 synnotch infected stained mycpe	66,4	8351

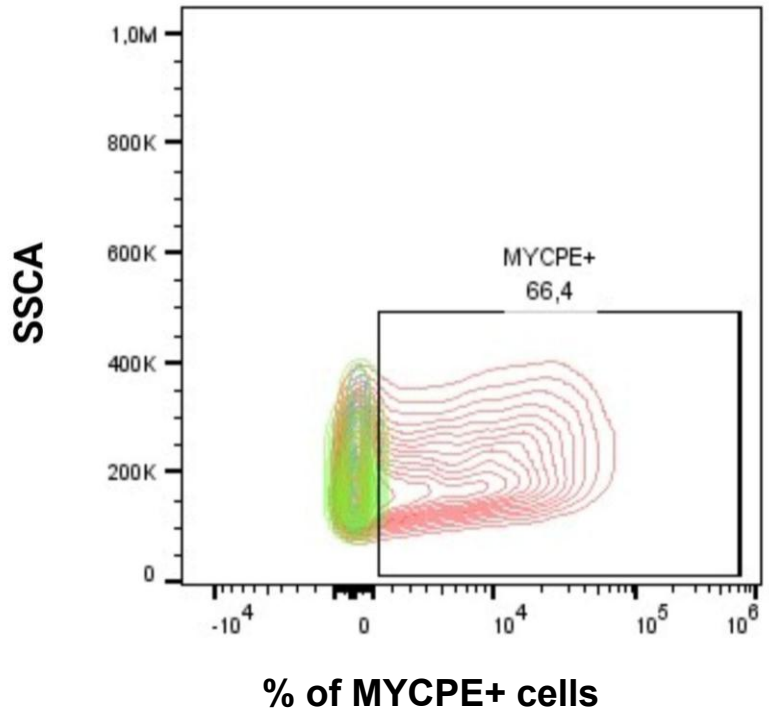

% of MYCPE+ cells

C.

JURKAT CELLS (SynNotch-CD19) SORTED

COLOUR	SAMPLE NAME	FREQ. PARENT % POSITIVE CELLS	MFI
	Jurkat CD19 synnotch sorted not stained	0,64	5,90E5
	Jurkat CD19 synnotch sorted stained mycpe	95,2	4,96E5

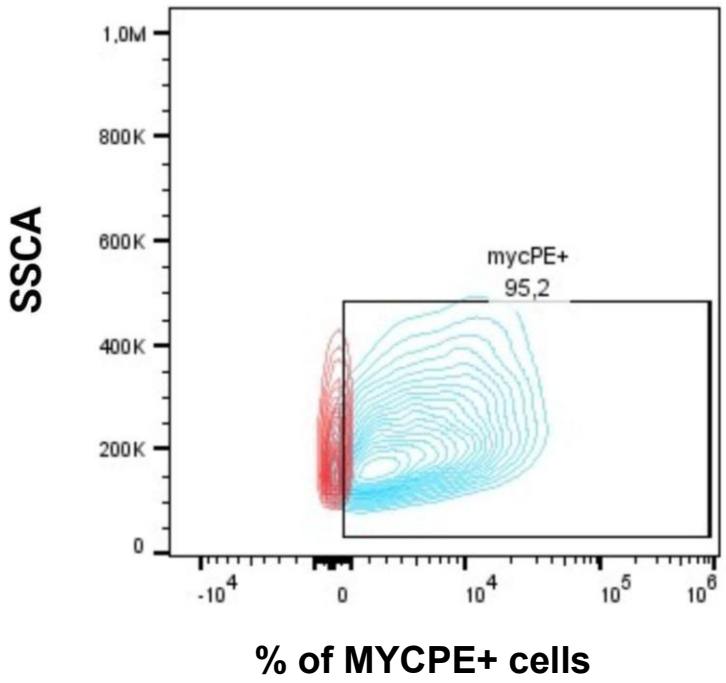

Figure 42. Flow cytometry assessment of SynNotch–CD19 transduction using anti-Myc-PE staining in 293T and Jurkat cells, with Jurkat enrichment by sorting. Anti-Myc-PE fluorescence is plotted on the x-axis and side scatter (SSC) on the y-axis.

Panel (A): HEK293T cells stained with anti-Myc-PE to assess SynNotch–CD19 expression; 57.6% of events are Myc-PE$^+$, indicating efficient receptor expression in this model system. **Panel (B):** Jurkat cells (pre-sorted) stained with anti-Myc-PE; 66.4% of events are Myc-PE$^+$, confirming substantial receptor expression before enrichment. **Panel (C):** Jurkat cells (post-sorted) for Myc-PE$^+$ events; the enriched population displays 95.2% Myc$^+$ cells, indicating successful selection of a SynNotch–CD19–expressing Jurkat population.

4.6.1 Co-culture of synNotch-HER2 Jurkat Cells with SKBR3 HER2+ Target Cells

To evaluate synNotch-dependent induction of engineered receptors, Jurkat cells were transduced with pHR_5xGAL4 lentiviral vectors encoding hNIS, avidin, monodin, or GFP (used as a negative control). Two experimental groups were established: (i) “GAL” Jurkat cells, which were transduced only with the inducible vector and served as controls; and (ii) “SYN” Jurkat cells, which were previously transduced with a

synNotch receptor specific for HER2 (synNotch-HER2^{+}) and sorted for Myc expression, then subsequently transduced with the inducible pHR_5xGAL4 vectors.

To assess synNotch functionality, co-culture assays were performed using SKBR3 cells (HER2^{+} adherent breast cancer cells) as target cells. Effector (Jurkat) to target (SKBR3) ratios of 1:1, 1:5, and 1:10 were tested. After 72 hours of co-culture, Jurkat cells were recovered from the supernatant and analysed by flow cytometry. Receptor expression was assessed using anti-hNIS-Alexa Fluor 647 and biotin-PE staining to detect inducible expression of hNIS and biotin-binding receptors, respectively. Only non-adherent Jurkat cells were collected and analysed, ensuring that only effector cells were evaluated for reporter induction.

In all subsequent Figures, “SYN” refers to Jurkat cells expressing both the synNotch-HER2 receptor and the inducible pHR_5xGAL4 construct, while “GAL” refers to Jurkat cells transduced only with the inducible construct, lacking synNotch expression and thus serving as negative controls.

In the first experiment, in GAL4NIS Jurkat cells (without synNotch), hNIS expression remained low across all conditions (1:1 = 1.25%; 1:5 = 0.71%) except a single spike at 1:10 (21,8%) that is likely nonspecific, since no upstream Notch activation was present. In SYNHER2_NIS Jurkat cells (expressing the HER2-specific synNotch receptor), hNIS expression remained similarly low. The highest expression level was observed specifically in the SYNHER2_NIS 1:5 condition, where 20% of the cells were hNIS^{+}. By contrast, all other synNotch conditions (1:1 and 1:10) showed only minimal expression (≤1.06%) (Figure 43).

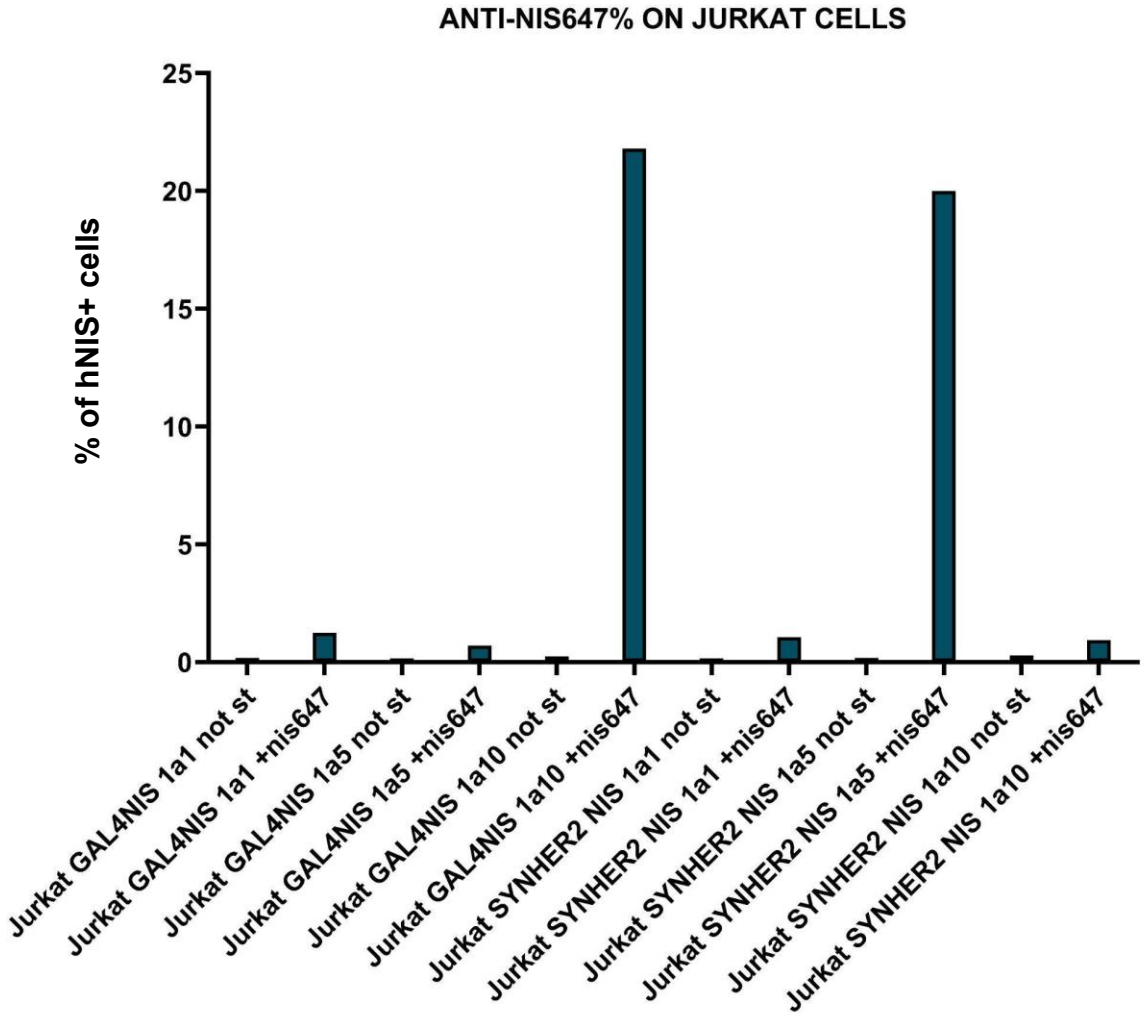

Figure 43. Antigen-dependent hNIS expression in synNotch co-transduced Jurkat cells. hNIS surface expression (anti-NIS-AF647) in GAL4_NIS and SYNHER2_NIS Jurkat cells after 72-hour co-culture with HER2^{+} SKBR3 cells at different effector-to-target (E:T) ratios. Minimal hNIS signal was detected in most conditions (≤1.25%), except for a prominent peak (20%) in the SYNHER2_NIS 1:5 condition, indicating synNotch-driven, antigen-dependent activation. An unexpected non-specific peak was observed in the GAL4_NIS 1:10 group (21.8%), despite the absence of HER2-specific recognition. Data are shown as a representative experiment (n = 1).

Importantly, this activation could be antigen-dependent, as the GAL4-NIS controls, lacking HER2 recognition, failed to show comparable induction, except for an unexpected non-specific peak (21.8%) observed in the GAL4NIS 1:10 condition.

In the control GAL4-GFP groups, minimal NIS staining was present as expected. However, in SYNHER2_GFP co-cultures, a notable signal was detected at the 1:1 (15%) and 1:5 (9.55%) E:T ratios. This again reflects background or nonspecific staining, since the GFP vector does not contain the NIS sequence (Figure 44).

Biotin-based staining (for pHR_5xGAL4_avidin and _monodin constructs) was also performed but yielded 0% signal across all conditions (both GAL and SYN groups) (data not shown).

Overall, the data indicate that despite co-culture with $HER2^{+}$ targets, the inducible system fails to yield a robust functional response, and synNotch-HER2 activation does not reproducibly and specifically drive artificial receptors expression from the pHR_5xGAL4 vector.

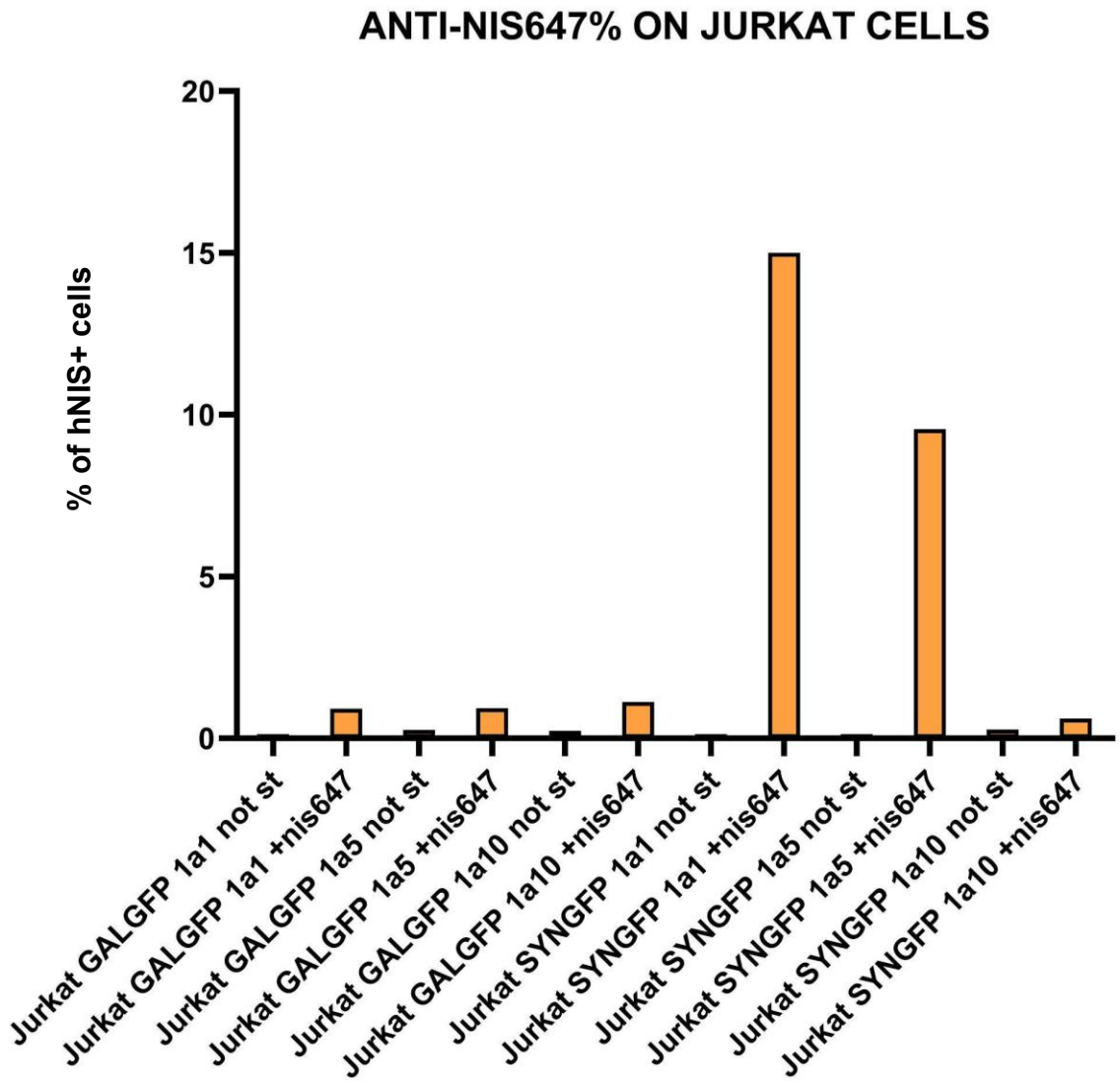

Figure 44. Anti-hNIS staining of control Jurkat cells transduced with pHR_5xGAL4-GFP or SYNHER2_GFP constructs after 72-hour co-culture with SKBR3 cells. No NIS-specific expression was detected in the GAL4-only group. A low, but notable signal was observed in the SYNHER2_GFP co-cultures at E:T 1:1 (15%) and 1:5 (9.55%), likely reflecting non-specific background. Data are shown as a representative experiment (n = 1).

To clarify the previously ambiguous findings regarding antigen-dependent induction of hNIS expression, a second experiment was conducted using freshly thawed SKBR3 cells ($HER2^+$ adherent targets) with Jurkat effector cells previously transduced either with pHR_5xGAL4 vectors encoding GFP or hNIS, or with both the HER2-specific synNotch receptor. In this second experiment, only the previously generated Jurkat

populations were used (no new infections), to validate the reproducibility and specificity of synNotch-mediated receptor expression.

Following a 3-day co-culture at a 1:5 effector-to-target (E:T) ratio, Jurkat cells were recovered from the supernatant and stained for surface hNIS expression using anti-hNIS Alexa Fluor 647 antibody. Biotin staining was not repeated in this experiment, as the previous trial yielded 0% signal in all conditions.

In GAL4_NIS cells, Jurkat cells lacking synNotch but transduced with pHR_5xGAL4_NIS, the highest hNIS expression was detected at a 1:5 ratio, with 36.0% NIS^+ cells, while lower signals were observed at 1:1 (2.87%) and 1:10 (3.77%). However, surprisingly similar expression levels were also found in GAL4_GFP control cells, which do not carry the NIS gene. Specifically, GAL4_GFP cells reached 27.3% NIS^+ at 1:1 and 26.5% at 1:5, strongly suggesting non-specific background staining or unspecific binding of the anti-NIS antibody in this experimental context (Figure 45).

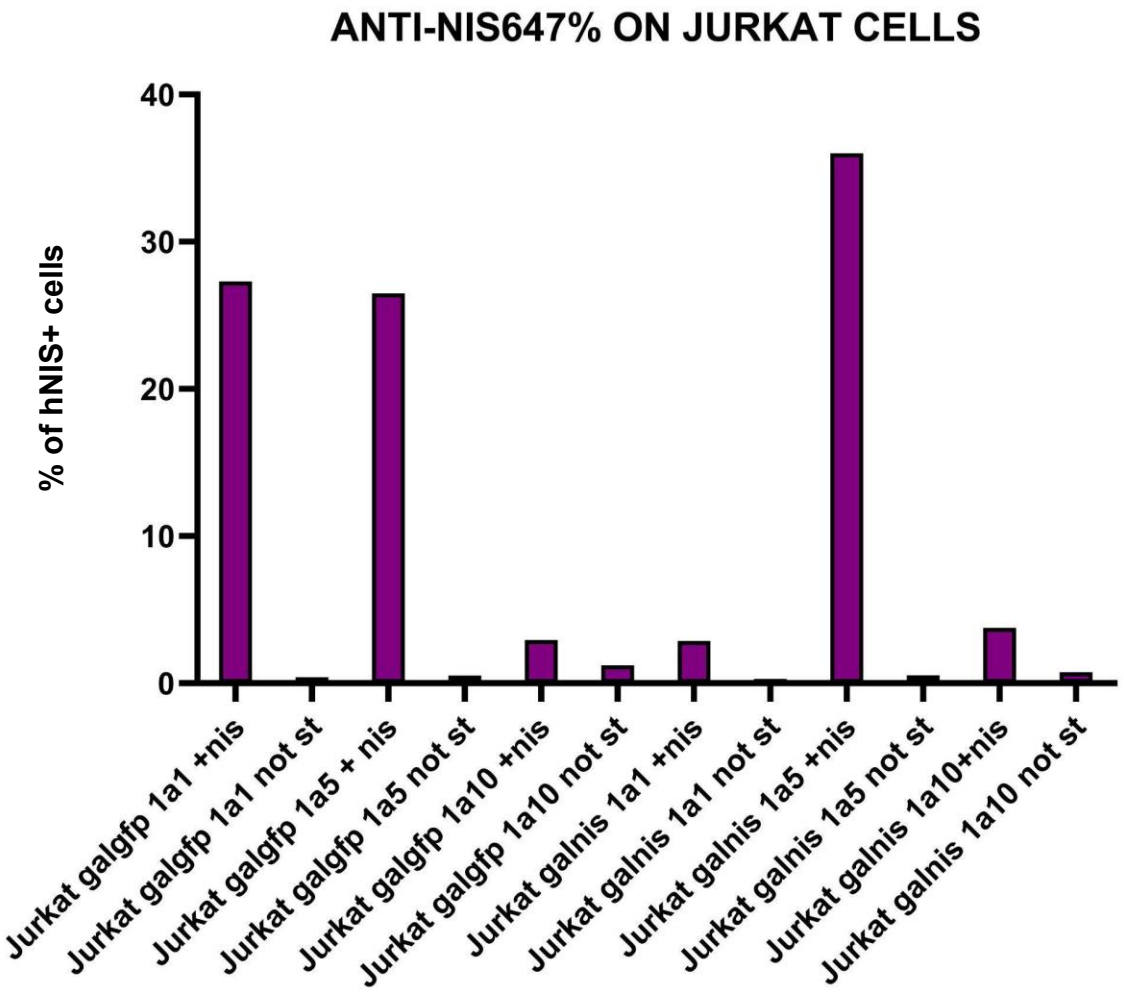

Figure 45. hNIS expression in GAL4-transduced Jurkat cells upon SKBR3 co-culture. Analysis of Jurkat cells transduced with GAL4_GFP or GAL4_NIS vectors and co-cultured with SKBR3 cells at 1:1, 1:5, and 1:10 effector-to-target ratios for 72 hours. Anti-hNIS staining shows the highest signal in GAL4_NIS 1:5 (36.0%), but similarly elevated staining in GAL4_GFP controls (27.3% and 26.5% at 1:1 and 1:5, respectively), suggesting non-specific antibody binding. Data are shown as a representative experiment (n = 1).

Similarly, SYN_GFP cells displayed 24.1% and 13.4% NIS^+ cells at 1:1 and 1:5, respectively, again without containing the NIS gene. In contrast, SYN_NIS cells showed low levels of NIS expression (maximum 3.11% at 1:10) and no clear evidence of synNotch-dependent induction (Figure 46).

These results demonstrate that, even in a repeated assay, the synNotch–GAL4 inducible system did not reliably trigger NIS expression, and that a strong background signal in GFP-only controls compromises the interpretation of inducibility. The observed NIS^+ staining is likely due to non-specific antibody binding or assay interference, and not to true antigen-driven activation.

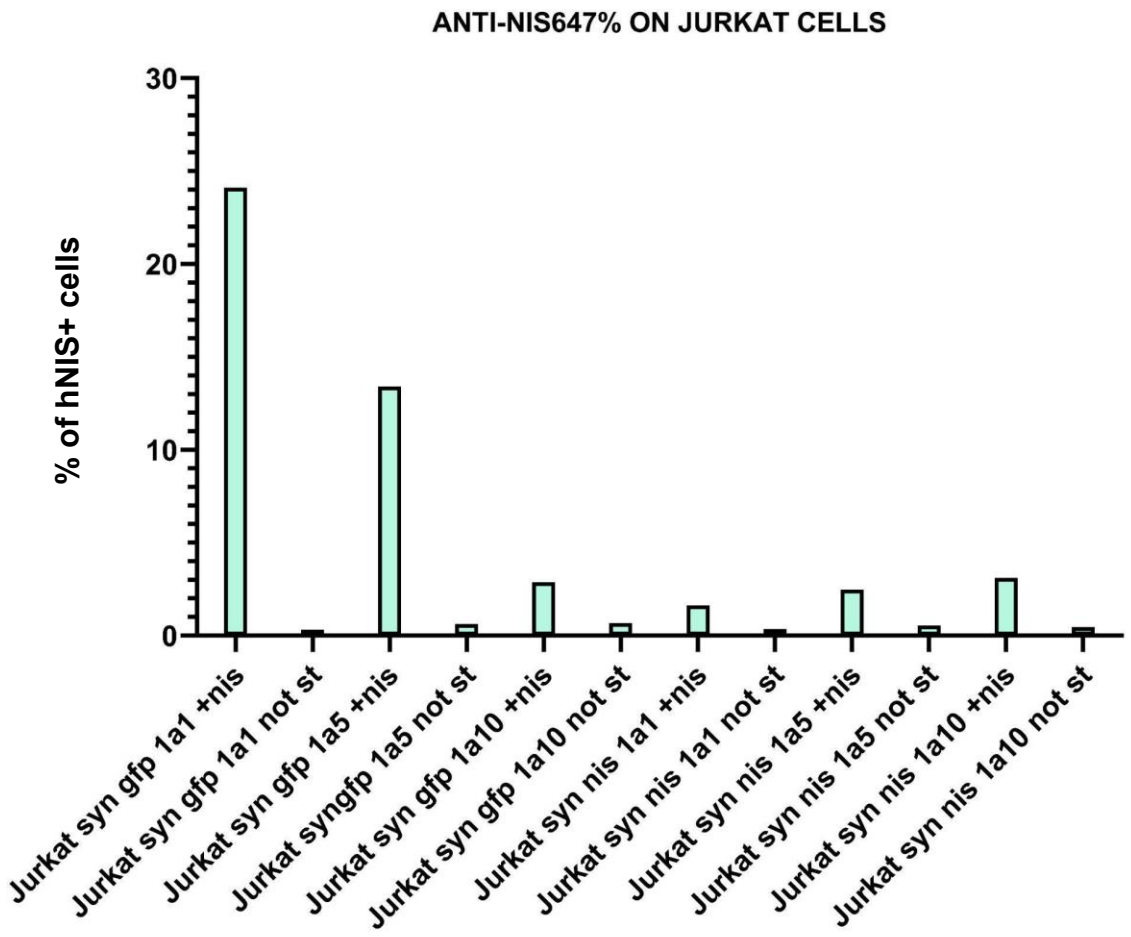

Figure 46. hNIS expression in SYN-transduced Jurkat cells upon SKBR3 co-culture. Jurkat cells transduced with SYN_GFP or SYN_NIS vectors were co-cultured with SKBR3 target cells. SYN_GFP controls showed notable non-specific anti-NIS staining (24.1% at 1:1; 13.4% at 1:5), while SYN_NIS cells displayed low hNIS expression, with a peak of only 3.11% at 1:10, indicating no synNotch-mediated induction. Data are shown as a representative experiment (n = 1).

To validate previous findings and exclude technical variability due to lentiviral production errors, a third experiment was performed using freshly generated 5xUAS-GAL4 lentiviral particles encoding either hNIS, avidin, monodin, or GFP as a control. HEK293T cells used for packaging showed robust GFP expression during transfection, suggesting efficient lentivirus production.

Jurkat cells were then transduced and co-cultured with SKBR3 target cells at different effector-to-target (E:T) ratios (1:1, 1:5, and 1:10) for 72 hours. Following stimulation,

hNIS expression was assessed by anti-NIS-647 staining, and avidin/monodin expression was evaluated using biotin-PE staining.

In GAL4_NIS-transduced Jurkat cells, a moderate aspecific level of NIS^+ cells was detected at E:T 1:5 (4.37%) and 1:10 (2.88%), compared to lower background levels in the respective unstained controls (0.26% and 0%). At 1:1, NIS expression was low (0.51%), similar to the background (0.14%) (Figure 47).

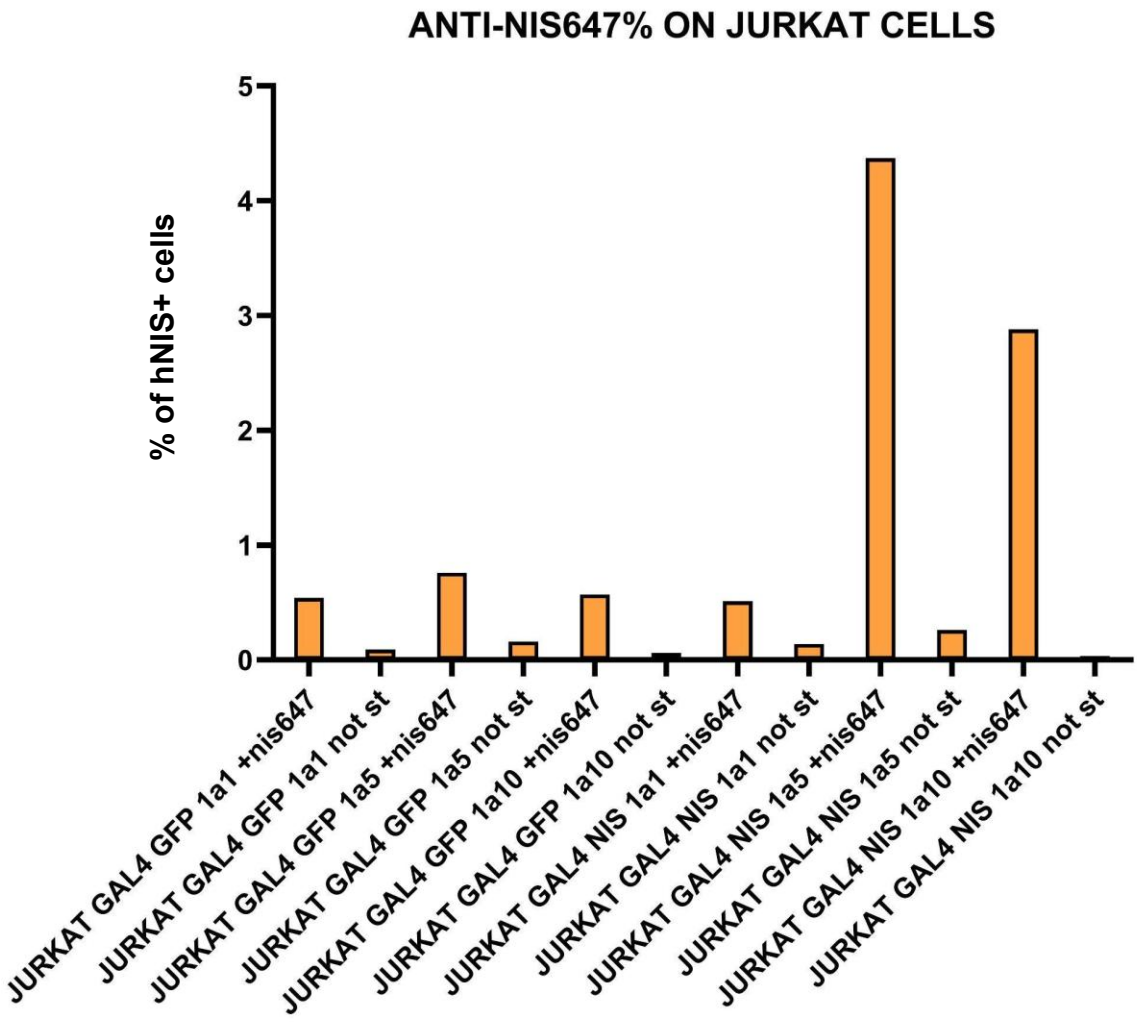

Figure 47. Assessment of hNIS expression in GAL4_NIS/GFP Jurkat cells. Jurkat cells transduced with GAL4_NIS/GFP were co-cultured with $HER2^+$ SKBR3 cells at E:T ratios of 1:1, 1:5, and 1:10. Flow cytometry with anti-NIS-647 staining revealed low to moderate hNIS expression, with the highest signal at 1:5 (4.37%) and 1:10 (2.88%). Unstained controls and GAL4_GFP cells showed low background levels (≤0.76%). Data are shown as a representative experiment (n = 1).

In contrast, SYN_NIS-transduced Jurkat cells exhibited only low-level NIS expression at all ratios: 1.14% (1:1), 0.91% (1:5), and 1.25% (1:10), with minimal background (≤0.08%) (Figure 48).

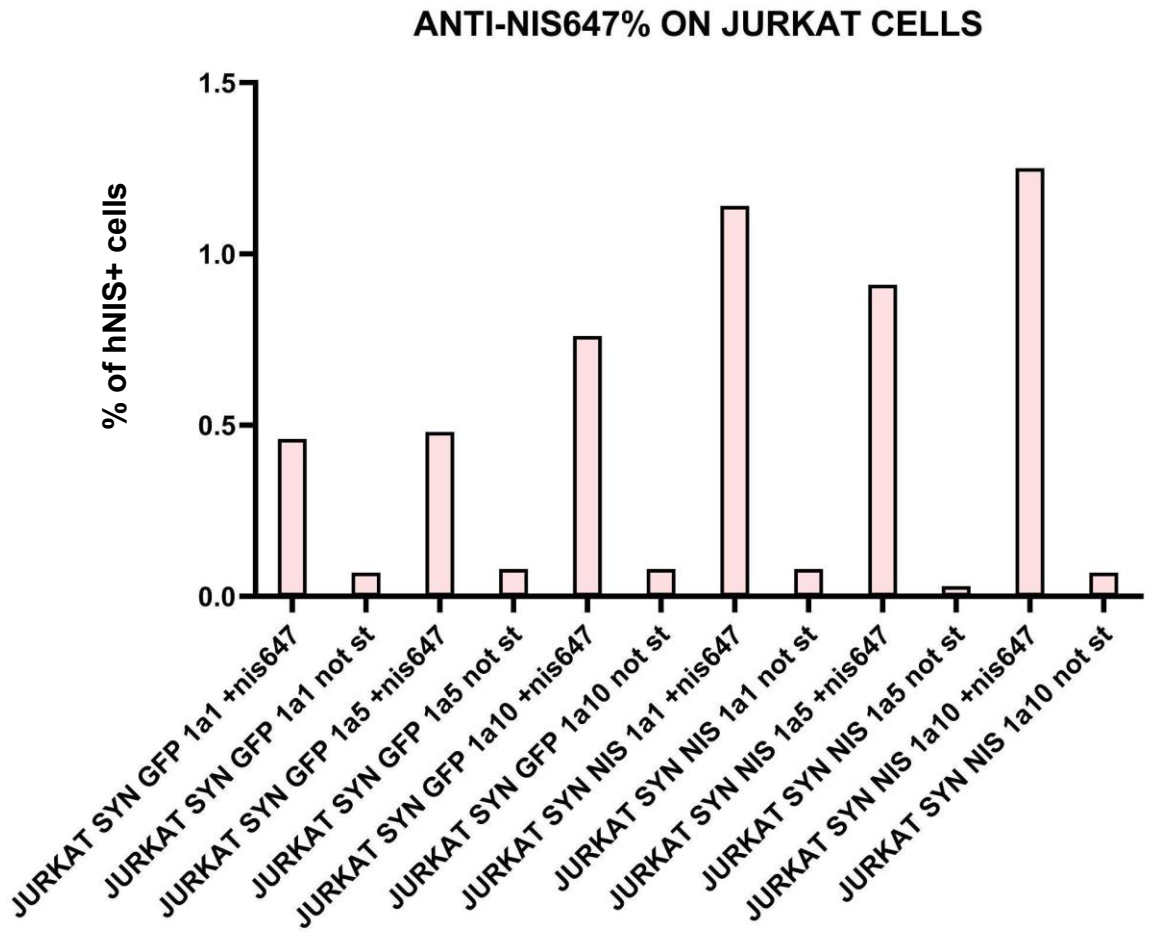

Figure 48. Assessment of hNIS expression in SYN_NIS/GFP Jurkat cells. SYN_NIS-transduced Jurkat cells showed low levels of hNIS$^+$ cells across all conditions: 1.14% at 1:1, 0.91% at 1:5, and 1.25% at 1:10. Background levels in unstained/GFP controls were minimal (≤0.76%). Data are shown as a representative experiment (n = 1).

This indicates that even with a freshly produced virus, no robust synNotch-mediated activation was detected. Nevertheless, despite the low absolute levels of hNIS expression across all conditions, the highest induction was again observed in the 1:10 E:T condition (1.25% NIS$^+$ cells) in SYN_NIS Jurkat cells. This trend is similar to the

previous experiment (Figure 46), where the 1:10 condition also showed the highest activation level (3.11%), suggesting that increasing the density of $HER2^+$ target cells may enhance synNotch-mediated activation, albeit modestly.

Importantly, GAL4_GFP and SYN_GFP control groups, which lack the NIS insert, showed only minimal NIS^+ signal across all conditions (range: 0.46–0.76%), suggesting a significant reduction in non-specific staining compared to prior experiments.

In GAL4-avidin and GAL4-monodin conditions, the highest biotin-binding signal was again observed at the 1:5 ratio, reaching 1.09% and 1.40%, respectively. A moderate signal was detected at 1:10 (0.41% for avidin; 0.68% for monodin), and background was 0% in all unstained controls. In contrast, GAL4_GFP controls showed very low levels of $biotin^+$ cells (≤0.48% across all ratios), suggesting low background sensitivity (Figure 49). However, the biotin-positive signal observed in GAL4-avidin and GAL4-monodin is unexpected, as these constructs lack the synNotch receptor and should not activate UAS-dependent expression. This suggests the presence of background activity or potential leakiness of the system, highlighting once again the challenges in attributing low-level induction specifically to antigen-driven activation.

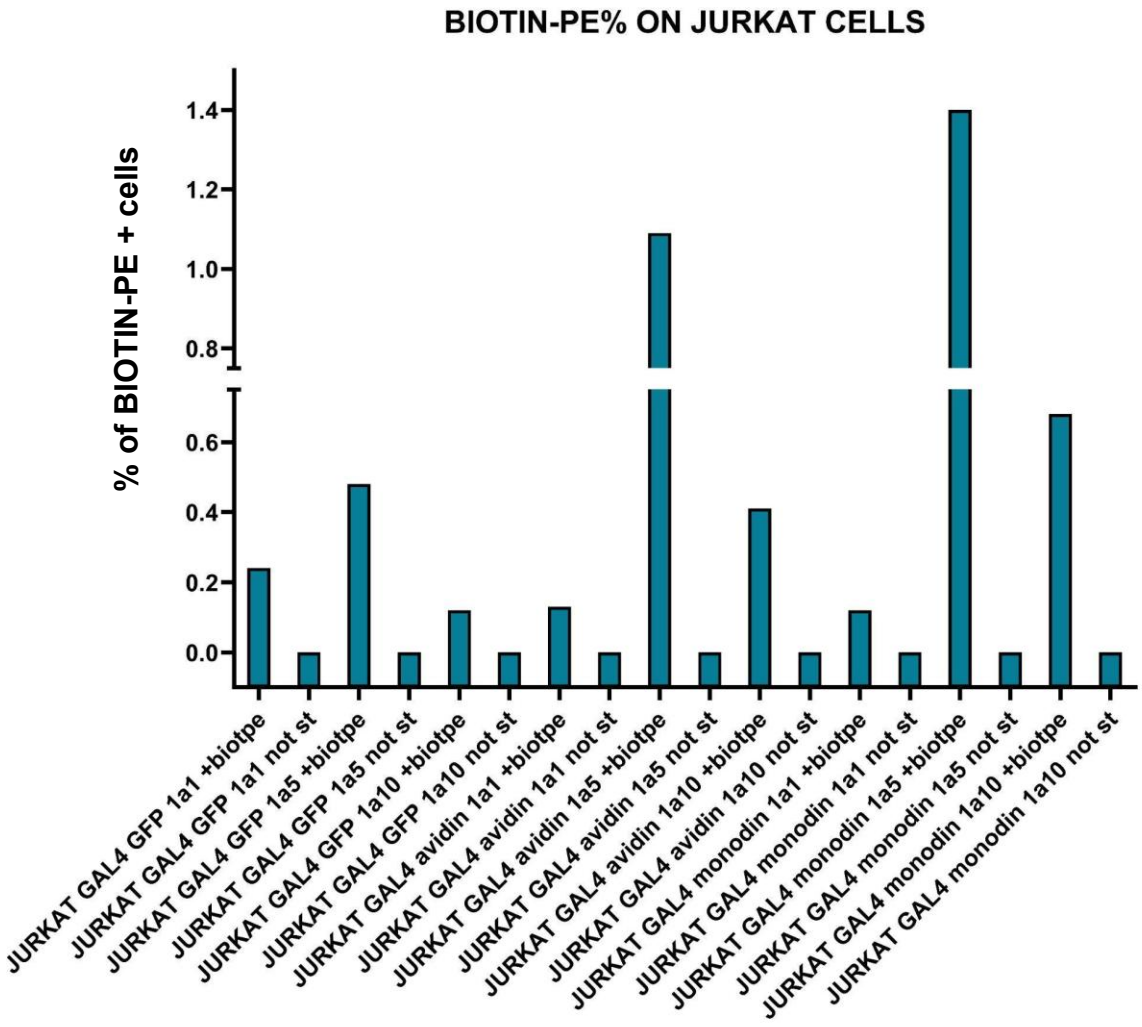

Figure 49. Evaluation of biotin-binding receptor expression in GAL4-transduced Jurkat cells. Jurkat cells transduced with GAL4_avidin or GAL4_monodin were stained with biotin-PE. The highest biotin$^+$ cell percentages were detected at E:T 1:5 (1.09% for avidin, 1.40% for monodin), with lower signal at 1:10 (0.41% and 0.68%, respectively). No biotin signal was detected in unstained controls, while GAL4_GFP controls remained ≤0.48% across all ratios. Data are shown as a representative experiment (n = 1).

In SYN_avidin and SYN_monodin groups, no clear synNotch-dependent induction was observed. While SYN_monodin showed biotin$^+$ cells at 1:5 (2.03%) and 1:10 (1.16%), these levels were close to those seen in SYN_GFP controls (1.34% at 1:5, 0.60% at 1:10), showing no antigen-dependent increase in receptor expression. SYN_avidin showed no induction (0%–0.41% biotin$^+$) (Figure 50).

These findings confirm that the new batch of GAL4 lentivirus reduces background signals compared to earlier experiments; however, no consistent or clear synNotch-dependent activation was observed in SYN-transduced cells.

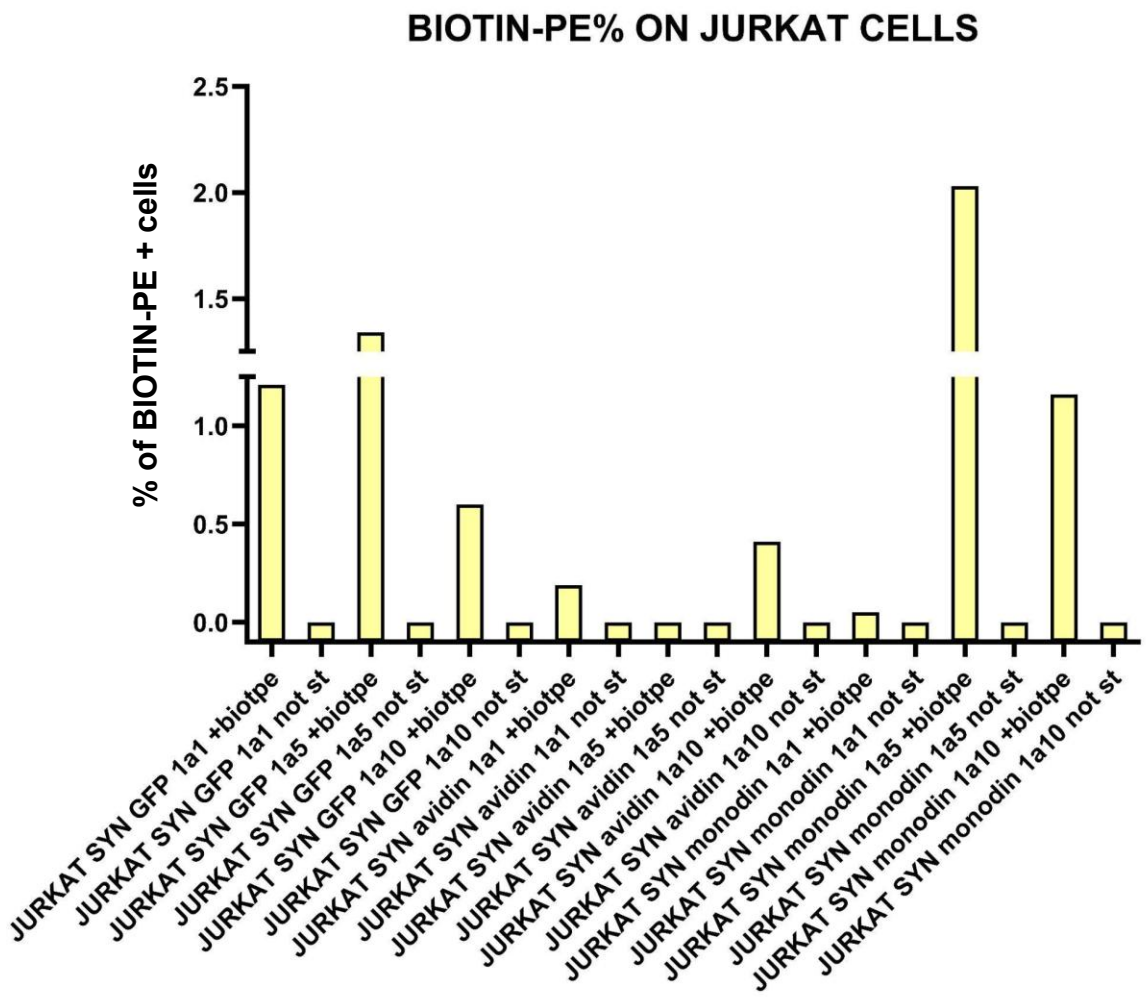

Figure 50. Biotin-binding receptor expression in SYN-transduced Jurkat cells. SYN_monodin Jurkat cells showed low biotin$^+$ signal at 1:5 (2.03%) and 1:10 (1.16%), comparable to SYN_GFP controls. SYN_avidin showed minimal to no biotin$^+$ events (0%–0.41%). Data are shown as a representative experiment (n = 1).

4.6.2 Co-culture of synNotch-CD19 Jurkat Cells with NALM-6 CD19+ Target Cells

A similar experimental setting was applied to Jurkat cells expressing a CD19-specific synNotch receptor to test the inducibility of artificial receptors. Jurkat cells were transduced with pHR_5xGAL4 lentiviral vectors encoding hNIS, avidin, monodin, or GFP as a negative control. As in the HER2 model, two experimental groups were analysed: "GAL" Jurkat cells, transduced only with the pHR_5xGAL4 inducible vectors, lacking synNotch receptor expression and serving as baseline controls; "SYN" Jurkat cells, previously transduced with the synNotch-CD19 construct and sorted for Myc expression, followed by transduction with the pHR_5xGAL4 inducible vectors. To evaluate synNotch activation upon antigen recognition, Jurkat effector cells were co-cultured with NALM-6 ($CD19^+$ lymphoblastic leukaemia) target cells at effector-to-target (E:T) ratios of 1:1, 1:5, and 1:10. After 72 hours, Jurkat and NALM-6 cells, both in suspension, were harvested together from the co-culture. The entire mixed population was stained with a cocktail of anti-hNIS Alexa Fluor 647, biotin-PE, and anti-CD19-VioBlue antibody, which selectively marks $CD19^+$ NALM-6 target cells. Flow cytometric analysis was then performed by gating on the $CD19^-$ population, corresponding to Jurkat effector cells, to evaluate inducible receptor expression.

Anti-hNIS Alexa Fluor 647 and biotin-PE staining were used to assess inducible receptor expression at the surface of Jurkat cells. All assessments were performed exclusively on the floating Jurkat population to ensure selective analysis of effector cell responses.

In this co-culture experiment using CD19-positive NALM-6 target cells, synNotch-CD19-transduced Jurkat cells (SYN_NIS) showed no evidence of antigen-induced hNIS expression. Across all effector-to-target (E:T) ratios tested (1:1, 1:5, and 1:10), $hNIS^+$ cells remained consistently low, with values close to or even below background levels recorded in the respective unstained controls. Specifically, SYN_NIS Jurkat cells reached only 0.21% $hNIS^+$ at 1:1, 0.22% at 1:5, and 0.10% at 1:10, with corresponding background levels of 0.69%, 0.17%, and 0.13% (Figure 51). These results indicate that the observed fluorescence is likely due to assay noise or non-specific antibody binding, and not genuine inducible receptor expression via synNotch activation.

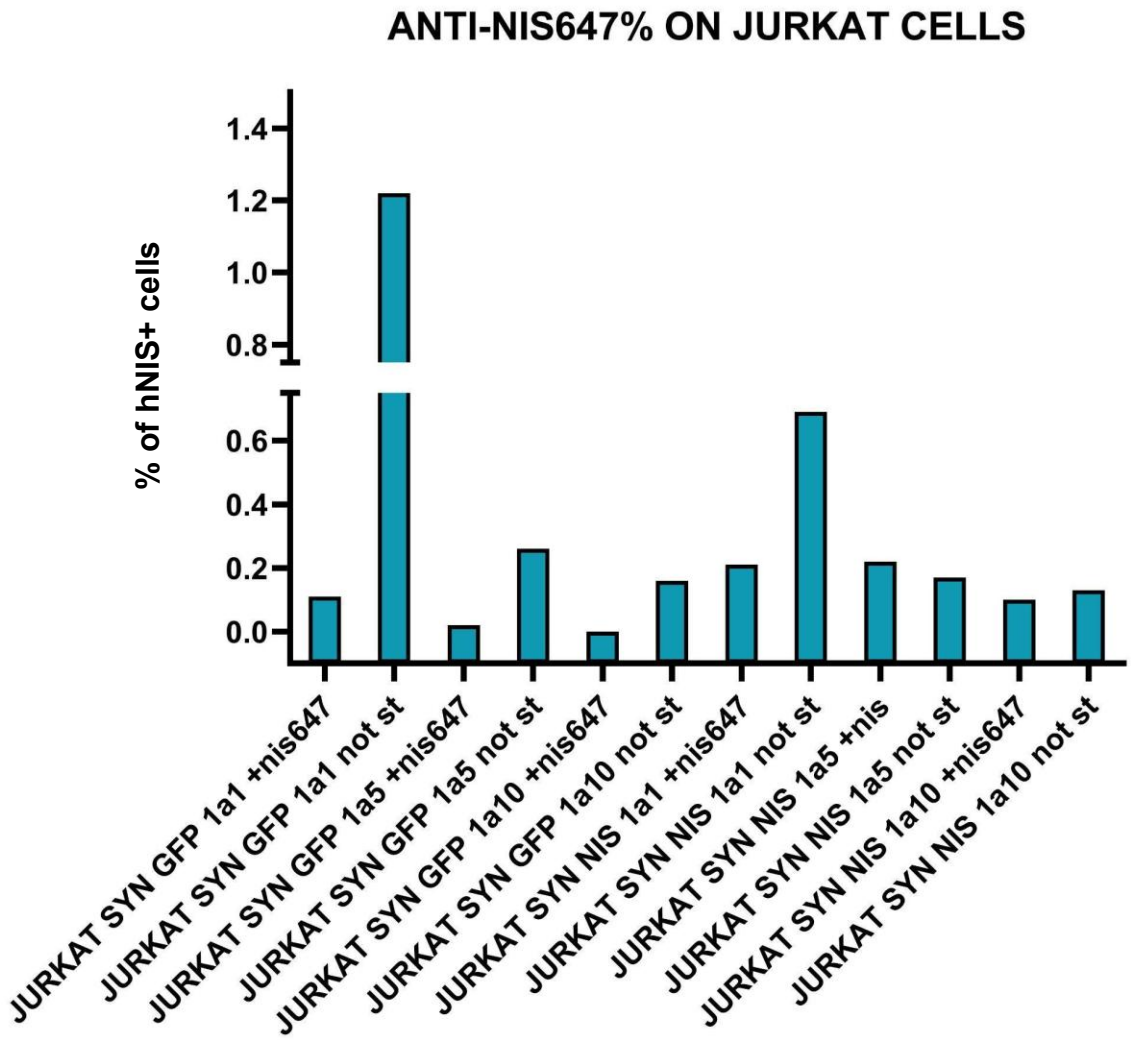

Figure 51. hNIS expression in SYN-transduced Jurkat cells co-cultured with NALM-6 cells. No clear antigen-dependent NIS induction was observed. Signal intensity remained close to or below background across all E:T conditions (1:1, 1:5, 1:10), indicating no functional synNotch activation. Data are shown as a representative experiment (n = 1).

Similarly, control groups transduced with the inducible vector alone (GAL4_NIS), which lack the synNotch receptor, did not show any appreciable hNIS upregulation. $hNIS^+$ percentages ranged from 0.04% to 0.07% across all E:T conditions, and in one case (1:1), the background of unstained cells even reached 1.47%, further underscoring the limited specificity of the anti-NIS staining in this setting (Figure 52).

Finally, both SYN_GFP (Figure 51) and GAL4_GFP (Figure 52) control populations, which do not carry the NIS gene, showed comparable or even higher signal than the test groups, reinforcing the conclusion that no true NIS induction occurred in this experimental context.

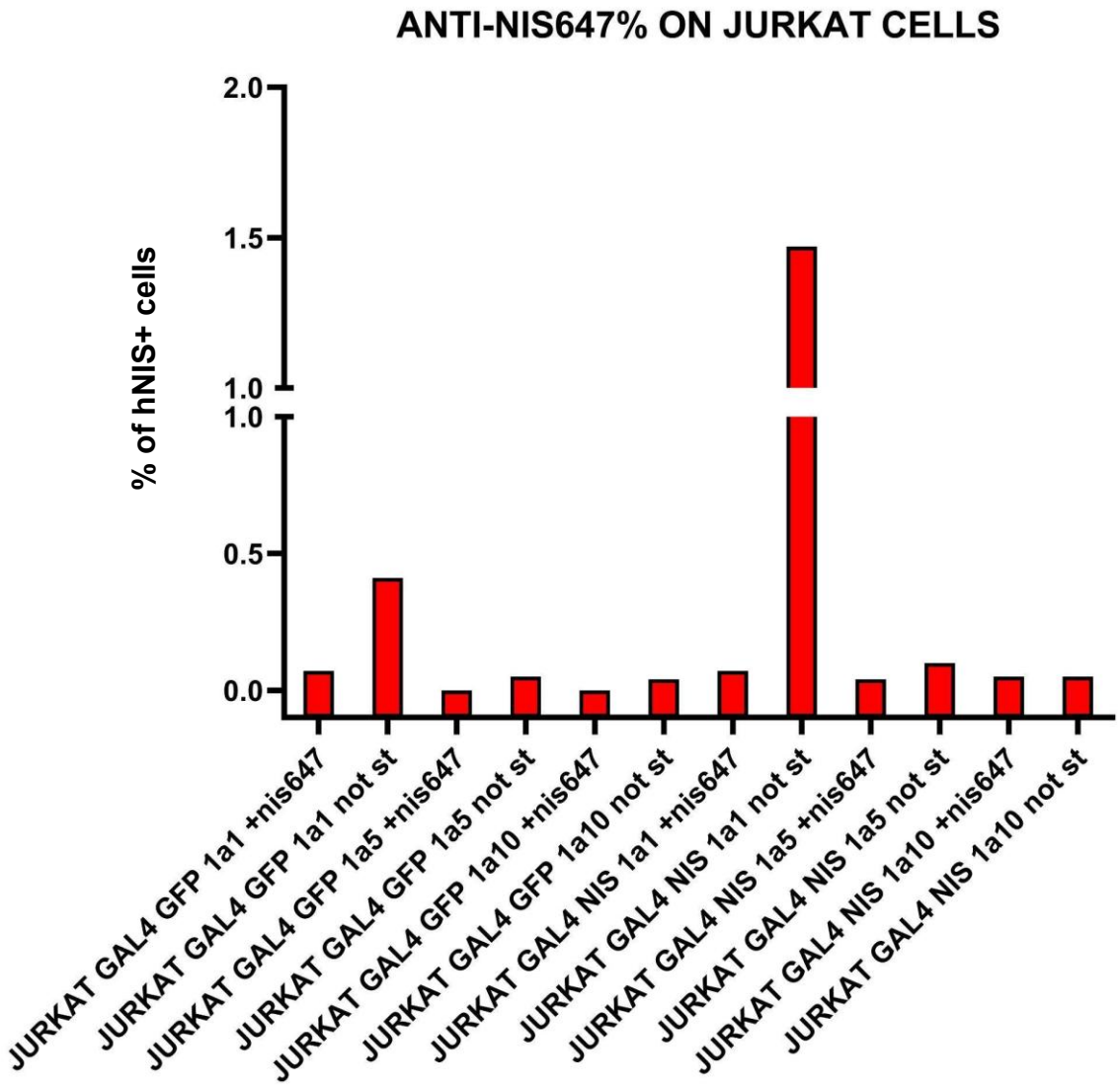

Figure 52. Assessment of anti-hNIS staining in GAL4_GFP and GAL4_NIS Jurkat cells after 72h co-culture with CD19^{+} NALM-6 target cells at E:T ratios of 1:1, 1:5, and 1:10. No specific NIS expression was detected in any condition; only in 1:1 GAL4_NIS the background of unstained cells reached 1.47%. Unstained controls showed comparable or even higher background levels. Data are shown as a representative experiment (n = 1).

Biotin-PE staining of Jurkat cells transduced with GAL4-avidin and GAL4-monodin vectors revealed a mild but measurable biotin$^+$ signal, particularly in the 1:5 E:T condition. Specifically, GAL4_Avidin cells reached 2.14% biotin$^+$ cells at 1:5, with lower levels at 1:1 (0.64%) and 1:10 (1.48%). GAL4_Monodin cells displayed a similar pattern, with a peak of 1.88% biotin$^+$ cells at 1:5, 0.99% at 1:1, and 1.40% at 1:10. However, these values must be interpreted with caution, as the GAL4_GFP control group, lacking any biotin-binding domain, also showed comparable levels of biotin$^+$ staining: 1.85% at 1:5, 0.93% at 1:10, and 0.80% at 1:1 (Figure 53).

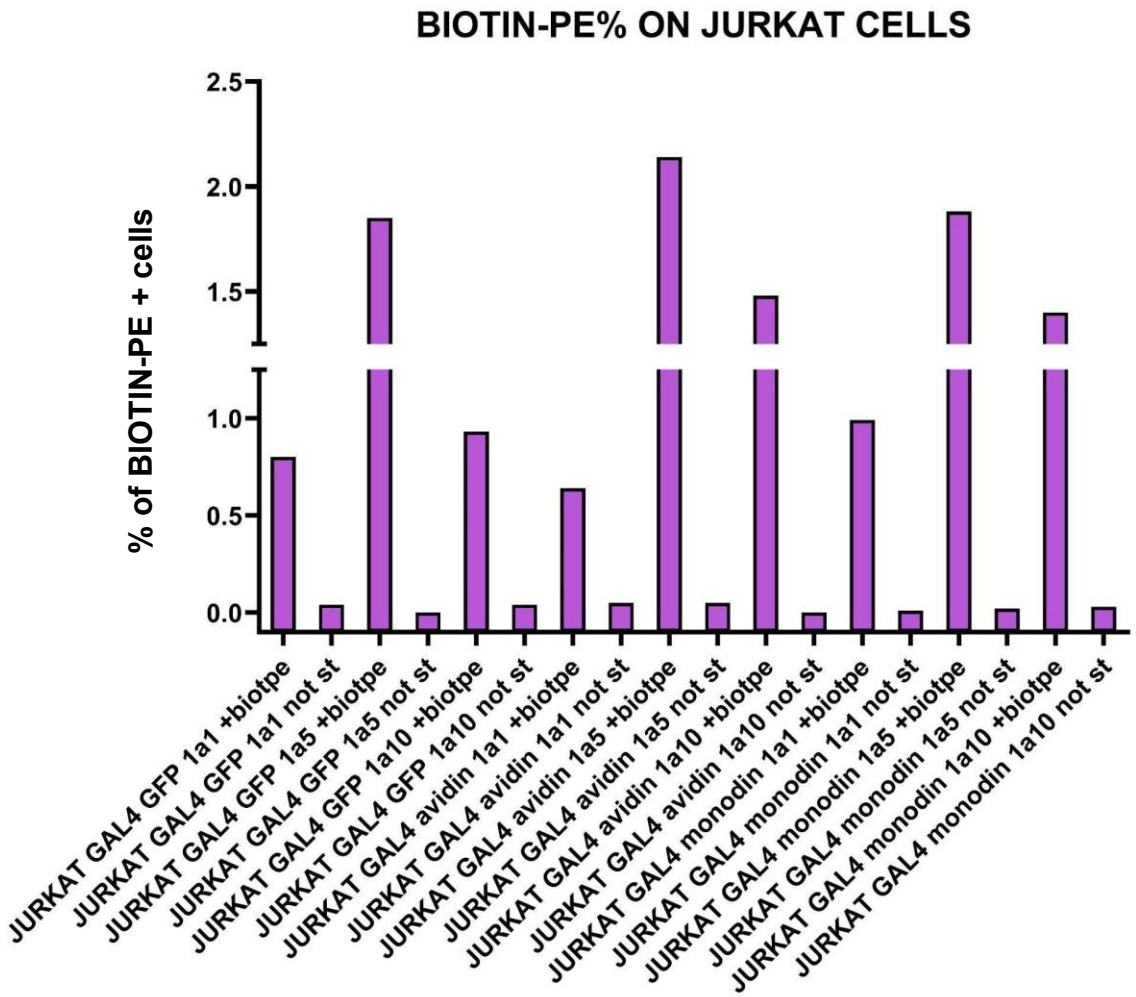

Figure 53. Biotin binding in GAL4-transduced Jurkat cells (avidin/monodin) after NALM-6 co-culture. Jurkat cells transduced with GAL4_Avidin or GAL4_Monodin vectors showed weak biotin-PE signal, with a modest increase at the 1:5 ratio (2.14% and 1.88%, respectively). However, similar levels were also detected in GAL4_GFP control cells, suggesting non-specific staining. Data are shown as a representative experiment (n = 1).

In SYN-transduced cells, no clear synNotch-dependent induction was observed. SYN_Avidin Jurkat cells showed 1.20% biotin^{+} signal at 1:5, 0.66% at 1:10, and 0.34% at 1:1. SYN_Monodin reached 0.81% at 1:5 and 0.89% at 1:10, with minimal background in the corresponding unstained controls. However, these values were nearly identical to those seen in SYN_GFP control cells, which displayed 0.85%, 0.68%, and 0.49% across the same E:T ratios, confirming the non-specific nature of the observed signal (Figure 54).

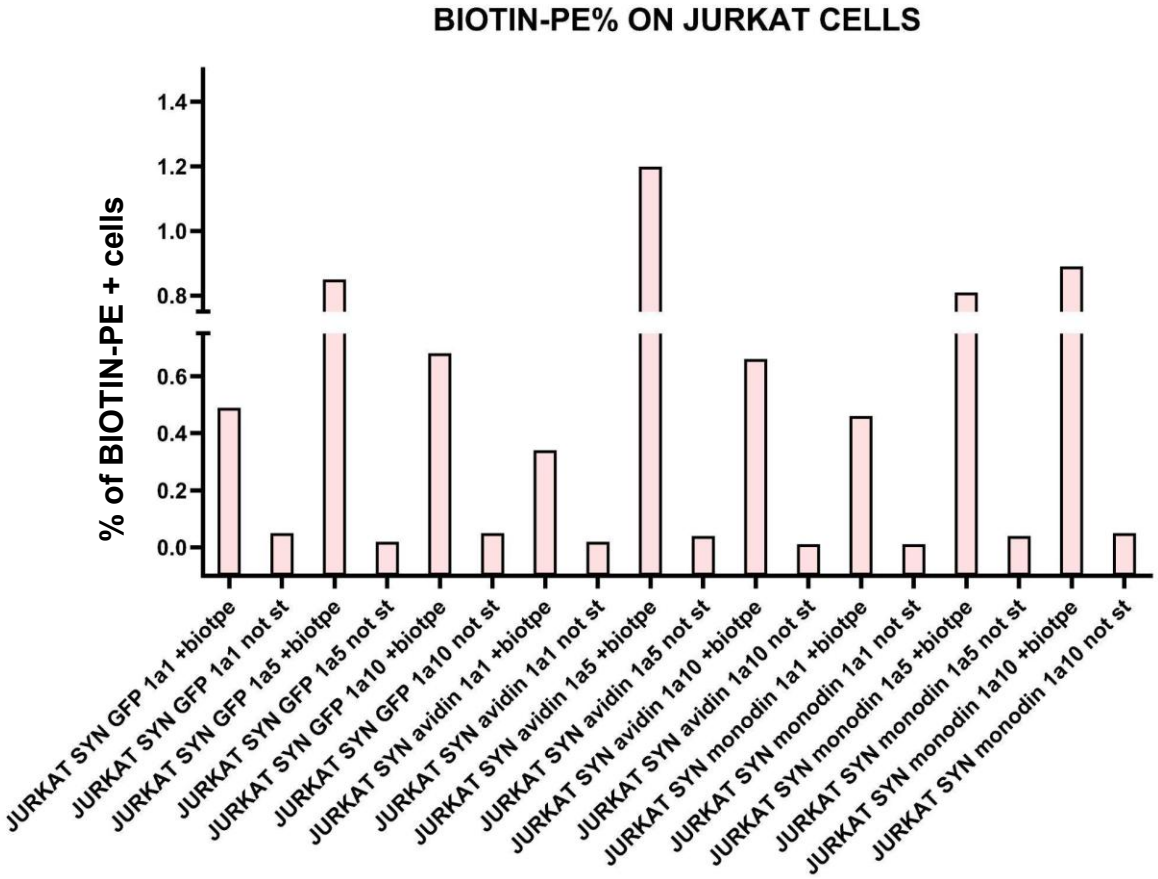

Figure 54. Biotin binding in SYN-transduced Jurkat cells (avidin/monodin) after NALM-6 co-culture. SYN_Avidin and SYN_Monodin Jurkat cells co-cultured with CD19^{+} targets showed no appreciable increase in biotin-PE staining compared to SYN_GFP controls. Maximum values remained below 1.2%, indicating a lack of synNotch-CD19-induced receptor expression. Data are shown as a representative experiment (n = 1).

Overall, these results demonstrate that, in the synNotch-CD19 setting, no inducible expression of either hNIS or biotin-binding receptors was observed, and most of the detected signal appears to stem from non-specific staining or background fluorescence rather than synNotch-mediated activation.

5. Discussion

The integration of diagnostic and therapeutic functionalities into a single engineered immune effector cell represents a real goal in the field of cancer immunotherapy and a desired tool which holds promise for fundamental advancements in therapy. The central goal of this thesis was to develop a modular, inducible theranostic system for adoptive cell therapies, particularly CAR-T and CAR-NK cells, capable of performing both real-time molecular imaging and localised delivery of therapeutic radionuclides. These dual-purpose systems are of increasing clinical interest, as they offer an unprecedented ability to monitor therapeutic cell fate in vivo while delivering precision treatment at the tumour site.

The motivation behind this work stems from the current limitations in cell-based therapies, especially in solid tumours, where poor trafficking, antigen heterogeneity, and an immunosuppressive tumour microenvironment often hinder efficacy. Furthermore, one of the major unmet needs in CAR-T cell therapy is the inability to monitor effector cells' distribution, activation, and persistence, non-invasively, once infused into patients. Molecular imaging strategies, such as those using human sodium iodide symporter, provide a valuable tool to address these challenges by enabling dynamic visualisation of engineered cells in vivo without disrupting their function or phenotype[112,147].

To tackle these obstacles, we designed and constructed a panel of twelve viral constructs, divided into constitutive and inducible expression systems, each tailored to express one of three effector modules: the hNIS, avidin, or monodin. These receptors were selected for their potential theranostic value: hNIS enables both SPECT/PET imaging and radionuclide therapy; avidin and monodin can allow pretargeted radiotherapy via biotinylated agents. The twelve constructs were built

using three viral backbones: pBULLET, a retroviral vector enabling NFAT-inducible expression; pCCL_EF1a, a lentiviral backbone to drive constitutive expression; pHR_5xGAL4 UAS, designed for transcriptional activation via the SynNotch-Gal4VP64 system.

The inducible systems are based on two well-characterised activation mechanisms: (i) the calcium/calcineurin-responsive NFAT promoter, which triggers transcription upon TCR or CAR engagement; and (ii) the synthetic SynNotch receptor, which provides modular, orthogonal control over gene expression based on extracellular ligand recognition.

The strategic goal was, in fact, to explore different configurations of controllable expression in engineered immune cells, comparing constitutive systems, which allow stable, continuous expression of the transgene, with inducible systems, in which expression is triggered only in response to immune activation. This would allow fine-tuned control over transgene activity, reducing systemic toxicity and enabling spatiotemporal regulation of therapeutic functions, and laying the ground for programmable, image-guided cell therapies capable of delivering localised therapy, while being non-invasively tracked in vivo, a critical advance for future clinical applications in oncology and beyond.

The functionality of these systems was assessed in both immortalised and primary immune cells, including Jurkat cells and human PBMC-derived T cells, using a combination of molecular, imaging, and cytometric assays. Functional readouts included radiotracer uptake (for hNIS), flow cytometry, and antigen-specific co-culture activation assays. Where relevant, we employed orthogonal experimental strategies (e.g., PHA/SynNotch ligand co-culture) to validate inducibility.

The first constitutive vector tested was the pCONTROL vector, a lentiviral construct encoding hNIS under a constitutive promoter. It also included additional functional elements: HSV-TK (herpes simplex virus thymidine kinase) as a suicide gene, and a hFGFR1 dimerizer-FLAG, which enables drug-inducible MAPK signalling. The three elements, HSV-TK, FGFR1-FKBP12-FLAG, and hNIS, were separated by self-cleaving peptides T2A and P2A to ensure stoichiometric expression from a single promoter. This early construct served to validate the proper expression, membrane

localisation, and functional activity of hNIS in Jurkat, HEK293T and other human cell lines. Western blot analysis confirmed successful expression of both hNIS and hFGFR1 dimerizer-FLAG, while flow cytometry using an anti-hNIS antibody (specific to an extracellular epitope) verified membrane localisation of the transporter in both cell types.

Functional assays, performed in collaboration with the CNR of Padua, demonstrated robust and specific uptake of [^{99m}Tc]pertechnetate (TcO_4^-) in hNIS-positive cells. Uptake was: time-dependent, peaking within 15–30 minutes and plateauing at 3 hours; temperature-sensitive, with significantly reduced uptake at 4 °C compared to 37 °C, consistent with active transport; blockable, as shown by complete inhibition following pre-incubation with $NaClO_4$ or $NaReO_4$, confirming that uptake was NIS-mediated and outcompeted by perchlorate and perrhenate[92,99].
Interestingly, uptake was roughly tenfold higher in HEK293T cells than in Jurkat cells, reflecting differences in transduction efficiency and hNIS surface expression levels.

To contextualise these results, two thyroid-derived cell lines (BCPAP and NTHY-ORI) were used to test uptake from human cells naturally expressing hNIS (more physiological expression). Both displayed limited uptake (<1%), attributable to low NIS expression at the membrane, a known feature of BCPAP due to its tumoral origin, and of NTHY-ORI due to minimal transporter trafficking[92]. These controls confirmed the specificity and dynamic range of the assay and provided a valuable benchmark for the performance of our engineered constructs.

Following functional validation of pCONTROL vector, we transitioned to the ARI-001 lentiviral platform, which uses an EF1α promoter to drive constitutive expression of transgenes. We engineered three ARI-001 constructs encoding hNIS, avidin, and monodin. Transfection of HEK293T cells demonstrated successful expression of all three transgenes, confirmed via flow cytometry: hNIS expression resulted in 85.8% NIS-positive cells with high fluorescence intensity; avidin and monodin constructs yielded 37.4% and 43.5% FLAG-positive cells, respectively, confirming robust receptor surface expression.
These results validated the generation of functional viral particles for downstream transduction in target cells. We then assessed the expression and functionality of these constructs after transduction in Jurkat cells and primary human Pan-T cells.

In Jurkat cells, monodin showed the highest surface expression, with 77.1% Biotin-PE$^+$ cells and strong GFP co-expression; avidin was detected in 33.2% of cells, while hNIS expression was present in 3.59% of cells, a lower percentage but distinct from background controls. The relatively low surface expression of hNIS compared with monodin and avidin is consistent with the complex structure and trafficking requirements of the sodium/iodide symporter. NIS is a 13-transmembrane domain glycoprotein (encoded by SLC5A5) whose correct folding, glycosylation, and transport to the plasma membrane are tightly regulated, and inefficient processing in non-thyroid cell types, such as Jurkat cells, has been reported to result in intracellular retention and reduced surface localisation. In addition, the larger size of the hNIS coding sequence compared with monodin and avidin may further contribute to reduced lentiviral packaging efficiency and transduction rates[100,148]. These results confirm successful membrane localisation of the receptors, highlight a superior surface display efficiency for monodin in Jurkat cells and the ability to recruit biotinylated payloads.

In Pan-T cells, which represent a more translationally relevant immune population, avidin outperformed monodin, with 3.7% Biotin-PE$^+$ cells, compared to 1.31% for monodin. Fold changes in Biotin-PE signal over controls were ~370× for avidin and ~131× for monodin, indicating both constructs maintained functionality in a primary T cell context, though with different efficiencies.

Interestingly, the trends were reversed between cell types: monodin expression was more efficient in Jurkat cells, whereas avidin showed better surface display in Pan-T cells. This inverse pattern suggests that the efficiency of membrane localisation, folding, and/or stability of these synthetic receptors may be significantly modulated by the host cell's internal environment. However, the efficiency of transduction was remarkably low in primary human T cells and, at present, the reason for this behaviour has not been fully elucidated.

Several factors could explain these observations:
1. Protein folding and ER processing/chaperone capacity
• T cells undergo significant protein synthesis during activation, invoking the unfolded protein response (UPR) and engaging ER chaperones like GRP78/CHOP. Jurkat cells respond differently to ER stress than primary T cells, indicating variation in folding capacity and ER stress sensitivity[149].

2. Glycosylation patterns and trafficking

• Glycosylation is cell-type specific and strongly influences membrane protein folding and localisation. Jurkat and primary T cells display distinct glycosylation profiles, as demonstrated by differential O-glycosylation of CD43/CD45, which impacts surface receptor expression[150].

3. Membrane composition and receptor internalisation/recycling

• Primary and transformed cells differ in endocytic trafficking dynamics. T cell receptor (TCR) endocytosis and recycling are tightly regulated in an activation-dependent manner, with fundamental differences between Jurkat and primary T cells that affect receptor surface residency[151,152].

4. Protein structure: monomeric vs tetrameric avidin/monodin

• Avidin is naturally tetrameric with high biotin affinity, while monomeric versions (like monodin) have different structural demands. Monomeric streptavidin is easier to express in certain contexts but requires different folding and stability conditions, which may impact efficiency in different cell types[125].

These findings emphasise the importance of testing engineered constructs across multiple cell types, especially when designing vectors for clinical translation. A construct that performs well in immortalised lines may behave differently in primary cells, with implications for both therapeutic efficacy and safety.

Together, these results confirm that hNIS is correctly expressed, membrane-localised, and functionally active, supporting its use as a reliable imaging and therapeutic gene[92,99,112] ; avidin and monodin can be efficiently displayed on immune cell surfaces, enabling potential ligand capture and pretargeted radiotherapy; the efficiency of expression is vector- and cell-type-dependent, with notable differences between Jurkat and Pan-T cells[153].

These findings lay a solid foundation for in vivo imaging and downstream theranostic applications and validate the ARI-001 platform as a robust backbone for constitutive gene delivery in adoptive cell therapy.

With the goal to restrain artificial receptor expression to the sites of antigen engagement and cell activation in the context of TCR and CAR-engineered ATMPs, we have also developed a viral vector harbouring inducible modules.

The inducible reporter construct based on the 8xNFAT promoter driving ZsGreen and hCD8 expression, originally developed by the Nakayama lab (Addgene #153417), demonstrated robust functionality and specificity in both immortalised (Jurkat) and primary (Pan-T) human T cell models. This system was designed to transcriptionally respond to activation of NFAT, a key transcription factor downstream of calcium-calcineurin signalling, itself triggered by TCR/CD3 or CAR activation[62].

Our experiments showed that in Jurkat cells, the reporter system was highly inducible and stimulus-responsive. When stimulated with PHA, a potent polyclonal T cell activator, up to 25.1% of transduced cells expressed ZsGreen, while stimulation via anti-CD3/CD28 beads induced 10.5% positivity. The stronger activation achieved with PHA is consistent with prior findings indicating that mitogenic agents can provoke more sustained intracellular calcium flux and NFAT nuclear translocation, compared to physiological bead-based TCR co-stimulation[154]. Importantly, non-transduced or unstimulated controls remained negative, confirming the absence of background signal and the tight inducibility of the system.

Moreover, we observed that virus concentration strongly impacted transduction efficiency and reporter output, with higher multiplicity of infections (MOIs) leading to greater proportions of NFAT-responsive cells. This aligns with established knowledge that reporters construct dosage influences both expression magnitude and sensitivity[155].

In primary Pan-T cells, PHA stimulation proved cytotoxic, as expected, since it has been shown that a high dose of PHA is cytotoxic to Chinese Hamster ovary (CHO) and other mammalian cells[156], and was therefore replaced by anti-CD3/CD28 Dynabeads, a more physiological and clinically relevant activation method[157]. Under these conditions, the reporter system was again clearly inducible, with GFP^+ cells reaching up to 11.3%. These results confirm that the 8xNFAT-ZsGreen-hCD8 construct is not only functional in immortalised cells but also in primary human T cells, an important step for translational applicability.

Of particular interest was the correlation between NFAT-ZsGreen activation and CD137 expression, a well-characterised T cell activation marker. CD137 (TNFRSF9, 4–1BB) is a costimulatory member of the tumour necrosis factor receptor (TNFR) superfamily, expressed by activated T cells and other cells[158]. The engagement of CD137 with its natural ligand CD137L (4–1BBL, TNFSF9) on activated dendritic cells (DCs) enhances T cell proliferation and cytokine secretion[159].

Dual staining revealed that CD3/CD28 co-stimulation led to a population of $GFP^+/CD137^+$ double-positive cells, with up to 22% of cells falling into this quadrant. This supports the construct's use as a faithful reporter of early TCR-induced signalling events and suggests its potential utility in dissecting activation kinetics or screening co-stimulatory ligands.

Perhaps the most biologically and translationally relevant observation emerged from the antigen-specific activation assay. Jurkat cells co-transduced with the anti-BCMA CAR and the NFAT-ZsGreen reporter showed robust NFAT activation (15% GFP^+) only upon co-culture with $BCMA^+$ ARP-1 multiple myeloma cells, while K562 $BCMA^-$ cells failed to induce reporter expression. This clearly demonstrates that the NFAT reporter is stringently dependent on CAR-antigen engagement, and not prone to ligand-independent tonic signalling, a frequent concern in CAR-T cell design[160]. These findings validate the system as a powerful tool for monitoring antigen-specific activation in engineered T cells, with high fidelity and minimal background.

Taken together, these results position the Nakayama 8xNFAT-ZsGreen-hCD8 vector as a reliable and highly sensitive inducible platform, suitable for preclinical models of CAR-T cell activation, and potentially adaptable for therapeutic use, such as inducible expression of cytokines, suicide switches, or logic gate elements. Its readout also facilitates sorting and tracking of activated subpopulations, expanding its utility in downstream assays.

Concerning pBULLET-based NFAT-inducible constructs, our results demonstrate that this system failed to achieve robust and specific surface expression of hNIS, avidin, or monodin in either Jurkat or primary Pan-T cells, despite confirmed transduction and measurable GFP reporter expression. These findings may reflect the multilayered regulation of NFAT-dependent transcription. As extensively described by Macián et

al., NFAT proteins regulate gene expression at two distinct levels. At accessible loci, such as the IL-2 promoter, NFAT binding is sufficient to rapidly initiate transcription; by contrast, at “closed” loci, such as those controlling lineage-specific genes, NFAT must cooperate with other transcription factors and chromatin-remodelling complexes to establish an open conformation before transcription can proceed. In T cells, this complexity is further amplified by the co-expression of multiple NFAT family members (NFAT1, NFAT2, NFAT4), whose functional redundancy masks individual contributions but also enables a dynamic, context-dependent regulation of gene expression[62].

This issue provides a plausible explanation for our data: in our system, GFP expression was efficiently achieved using the pBULLET vector, in which GFP is driven by the strong CMV promoter. This design provides a permissive transcriptional environment that readily supports the expression of simple reporter genes. However, this level of activation was not sufficient to drive robust expression of more complex membrane receptors through the NFAT reporter elements, such as hNIS or avidin, which require not only high transcriptional output, but also efficient processing, glycosylation, and membrane trafficking. A potential explanation for this difference may lie in the design of the NFAT-inducible vectors: for instance, the Nakayama vector contains eight tandem NFAT motif repeats, whereas pBULLET has fewer, possibly resulting in weaker transcriptional activation. Moreover, the Nakayama construct also co-expresses CD8, providing additional costimulatory signals that may enhance activation in TCR-stimulated cells and, indirectly, also in the CAR context. Altogether, these factors could explain the reduced ability of pBULLET to support high-level expression of complex membrane proteins compared to NFAT-enriched systems. Thus, our results highlight an important limitation of NFAT-only inducible systems when applied to complex, multi-step expression tasks[62].

Notably, we observed a progressive decline in GFP^+ cells over time across all Jurkat pBULLET-transduced populations, with a drop from initial peaks (e.g., ~54% in pBULLET_NIS at day 8 post transduction) to markedly lower levels by day 23 (~22%). This phenomenon may reflect selection against cells sustaining high levels of transgene expression under continuous culture conditions. Supporting this hypothesis, Triller et al. reported a similar decline in EGFP expression from retroviral vectors

containing an EGFP/Puromycin fusion cassette, which they attributed to a negative selection pressure against cells expressing these constructs. In their study, EGFP fluorescence intensity decreased significantly over 5 days of selection, despite sufficient residual expression for antibiotic resistance, suggesting that high transgene expression may impair cellular fitness and promote the outgrowth of low-expressing populations[161]. Analogously, our results imply that retroviral vectors like pBULLET may impose a selective disadvantage on highly expressing clones, leading to an enrichment of low-GFP subsets over time.

Again, in the study by Yukawa et al., NFAT alone is insufficient for establishing open chromatin states at inducible loci in T cells. Instead, cooperative activation with AP-1, induced via CD28 co-stimulation, is essential to recruit the BAF chromatin-remodelling complex and generate the accessible enhancer landscape necessary for robust gene transcription. In the absence of this cooperative AP-1 activity, loci under the control of NFAT-only promoters may remain in a closed chromatin conformation, limiting transcriptional output[162]. This mechanism is consistent with our observation that the minimal NFAT promoter was sufficient to drive detectable GFP expression, likely due to permissive integration events, yet failed to activate surface receptors encoded within the same backbone.

Additionally, Schlabach et al. systematically screened synthetic enhancer libraries in mammalian cells and showed that the number, type, and arrangement of transcription factor response elements upstream of a minimal promoter critically determine transcriptional output. In their retroviral luciferase-GFP system, single transcription factor response motifs often drove only weak transcription, whereas multimerized composite enhancers produced synergistic activation, approaching the levels of strong viral promoters[163]. They found that, while some enhancers could match the activity of the wild-type CMV enhancer, activity was highly cell-type dependent, and combining multiple response elements often yielded synergistic activation greater than single sites alone[163]. In addition, we cannot exclude that GFP is being silenced over time through CMV promoter methylation and histone acetylation, which is often observed in several cellular contexts. Incorporating multimerized NFAT sites or composite NFAT/AP-1 motifs, as shown by Schlabach, could substantially enhance inducible

expression strength while maintaining activation specificity and novel vector designs in this direction will be explored.

Collectively, our data indicate that pBULLET vectors in their current design are suboptimal for driving functional levels of complex surface receptors, emphasising the need for enhanced promoter designs and epigenetic stabilisers for reliable application in engineered T cell systems.

Regarding the second inducible system based on the SynNotch–GAL4 system, we observed that neither the HER2- nor the CD19-directed SynNotch receptors robustly induced expression of pHR_5xGAL4-driven elements (hNIS, avidin, monodin) in Jurkat cells. Moreover, in this case, we were unable to observe induction in transduced cells even after 72 hours in co-culture with $HER2^+$ SKBR3 or $CD19^+$ NALM-6 target cells. The level of signal at the membrane for the different receptors remained close to baseline, while unexpectedly high non-specific signals were detected in GFP-only controls. These findings suggest that the transcriptional output of the pHR_5xGAL4 construct is insufficient to drive robust receptor expression and that the synNotch system, as implemented here, may exhibit transgene expression leakiness in some conditions.

This is consistent with observations by Morsut et al., who demonstrated that, while many synthetic Notch receptors yield robust outputs, some extracellular domains lead to poor inducibility or high basal activation, as seen in their anti-mesothelin receptor. They reported that extending the core Notch regulatory region with additional EGF repeats significantly reduced basal leakiness without compromising ligand-induced activation, a strategy that could be applied to improve our constructs[50].

Besides, they also highlighted that synNotch activation is dose-dependent, with induction correlating with receptor expression levels and ligand density (graded dose–response). This may explain the slightly higher expression trends we observed at higher target densities (e.g., 1:10 E:T ratio in SYN_HER2_NIS), suggesting that ligand availability is a limiting factor for activation in our system[50].

Taken together, these insights suggest that the suboptimal performance of our synNotch constructs likely results from a combination of insufficient receptor tuning (e.g., extracellular domain geometry, linker design), low receptor expression levels,

and lack of structural modifications (such as EGF repeat extensions). Optimising these parameters, alongside improved payload detection strategies, may help reduce background activity and enhance antigen-dependent signalling, ultimately improving the specificity and robustness of the synNotch–GAL4 platform in T cells.

Additionally, to mention another relevant study, our findings of low inducibility and high background contrast sharply with the robust and precise antigen-dependent responses reported by Roybal et al. In their work, the authors implemented a two-step "AND-gate" synNotch circuit: T cells constitutively expressed a synNotch receptor recognising a priming antigen (e.g., CD19), which, upon engagement, released a transcriptional activator that drove expression of a CAR targeting a secondary antigen (e.g., mesothelin). This design ensured that CAR expression (and full T cell effector function) occurred only when both antigens were present, greatly enhancing tumour specificity while minimising off-target effects. Initially validated in Jurkat T cells, these circuits were later transitioned into primary human T cells, where they maintained strong inducibility with minimal basal activity, highlighting the robustness of the design[56].

By contrast, in our experiments, synNotch activation failed to consistently drive surface expression of inducible receptors such as hNIS, avidin, or monodin in Jurkat cells. This discrepancy may reflect key differences in payload type (our constructs rely on plasma membrane localisation, which is more prone to background and less functionally amplified than CAR-mediated cytotoxicity), receptor tuning (Roybal and colleagues optimized linker regions and regulatory domains to reduce basal activation, as also suggested by Morsut et al., 2016), and circuit architecture (AND-gate logic with potent effector outputs amplifies the functional readout)[50,136].

These observations suggest that adopting similar design strategies, such as incorporating high-impact payloads (e.g., CARs), optimising synNotch receptor geometry, or employing dual-antigen AND-gate circuits, may help bridge the gap between our current outcomes and the high performance in these dual-systems, improving the specificity and dynamic range of our inducible strategy.

6. Conclusions

My thesis presents a comprehensive effort to develop and evaluate theranostic gene circuits in engineered immune effector cells, with the ultimate goal of enabling both in vivo imaging and targeted radiotherapy in a controlled, antigen-dependent or independent manner, as for the constitutive expression vectors. By systematically designing, constructing, and functionally validating a library of viral vectors encoding the human sodium iodide symporter (hNIS), avidin, and monodin, we established a foundational platform for programmable, image-guided cellular therapies.

The results obtained from constitutive expression systems confirmed that all three receptors can be successfully delivered and expressed in both immortalised and primary T cells, with monodin showing superior surface display in Jurkat cells, and avidin performing better in primary Pan-T cells. These differences underscore the importance of host cell context in determining construct functionality and persistence.

Conversely, although inducible expression systems based on NFAT and SynNotch logic provided useful insights into stimulus-dependent gene control, their current configurations revealed notable limitations.

These findings suggest that promoter architecture, enhancer strength, and chromatin accessibility are critical parameters requiring further optimisation for high-performance inducible systems.

Taken together, the data generated in this work support several key conclusions:

1. Receptor feasibility in different cellular contexts: hNIS, avidin, and monodin can be stably expressed in both immortalised and primary T cells, but their functional performance is influenced by the host cell type.
2. Limitations of current inducible systems: whereas NFAT- and SynNotch-based architectures successfully mediated antigen-dependent control of reporter expression, both systems exhibited relatively suboptimal induction levels compared to expected responses.
3. Design priorities for next-generation circuits: achieving high inducibility with minimal basal (background) activity will require improved regulatory elements, possibly combining multiple promoter/enhancer modules, chromatin

accessibility tuning, and signal amplification strategies. Incorporating AND-gate logic, pharmacologic control elements, and fail-safe switches will be essential to translate these theranostic circuits toward clinically viable, safe, and precise cell therapies.

Ultimately, this work provides a solid proof-of-concept for dual-function immune cell platforms capable of combining diagnostic imaging with therapeutic delivery and highlights the major design considerations for advancing these tools toward clinical translation. Future directions include the *in vivo* validation of optimised constructs, the use of AND-gate logic for enhanced antigen specificity, and the integration of safety switches and pharmacologic control systems, moving toward a new generation of intelligent, programmable cell therapies.

ADDENDUM 1.

My thesis focuses on the development and optimisation of cell-based ATMPs. In this context, I had the chance to contribute to a side project aimed at characterising gene expression profiles of CARCIK-CD19 cells generated under different culturing conditions. Specifically, this research was carried out as part of a scientific collaboration between IRCCS IRST "Dino Amadori" and the Fondazione Tettamanti, focused on the optimisation and large-scale GMP production of non-viral engineered CARCIK-CD19 cells and the results were published in Journal of Translational Medicine[164]. This study presents a clinically applicable, scalable platform for generating CARCIK cells using the Sleeping Beauty transposon system and explores key variables such as serum-free media, bioreactor expansion, and immunophenotypic profiling. This work aligns with the general goals of this thesis, which include the development of innovative tools for improving the functionality, traceability, and translational readiness of engineered immune effector cells.

Background

Chimeric Antigen Receptor Cytokine-Induced Killer (CARCIK) cells represent a promising class of engineered immune effectors for adoptive cell therapies. Derived from peripheral blood mononuclear cells and engineered with the *Sleeping Beauty*

(SB) non-viral transposon system, CARCIK cells combine features of T lymphocytes and natural killer (NK)-like activity, with clinical potential particularly in the treatment of B-cell malignancies such as acute lymphoblastic leukaemia (ALL) and non-Hodgkin's lymphoma[164].

Goal

My task was to perform transcriptional profiling of CARCIK-CD19 cells expanded in different culture platforms (standard flasks versus G-Rex bioreactors). The analysis was designed to identify transcriptional signatures associated with T-cell activation, memory, metabolism, and exhaustion, and to correlate them with the immunophenotypic and functional data generated within this collaborative study. In this way, the transcriptional profiling provided molecular evidence to support the GMP scalability and translational readiness of CARCIK-CD19 cells.

Materials and Methods

CARCIK-CD19 cells were generated using the *Sleeping Beauty* transposon system, ensuring non-viral integration of the CAR construct. Following expansion under either flask or G-Rex conditions, RNA was extracted using the QIAamp RNA mini kit and stored at –80 °C. RNA quality and concentration were assessed with the Agilent 2100 Bioanalyzer. For gene expression analysis, the Nanostring nCounter® platform was used with the Immune Exhaustion Panel (XT-H-EXHAUST-12). For each sample, 50 ng of total RNA was hybridised at 65 °C for 22 hours according to the manufacturer's instructions and processed with the Nanostring Automated Prep Station (FLEX system). Data were analysed with nSolver Analysis Software 4.0, normalised against housekeeping genes and positive controls. Pathway scoring analysis was applied to evaluate biological pathway activation, while differential expression analysis was performed using culture condition (flask versus G-Rex) as a predictor. Multiple testing correction was applied with the Benjamini–Yekutieli procedure, and gene set enrichment analysis was used to highlight functional categories affected by culture conditions.

Results

Transcriptional analysis revealed a consistent molecular signature distinguishing G-Rex-expanded from flask-grown CARCIK cells. G-Rex CARCIK cells showed reduced expression of exhaustion-associated genes and upregulation of metabolic pathways linked to effector persistence. Gene signatures associated with T-cell memory formation and enhanced proliferative potential were more prominent in G-Rex cultures. These findings complemented immunophenotypic data, which showed higher frequencies of memory markers, lower levels of exhaustion markers, and preserved anti-CD19 cytotoxic activity in G-Rex-expanded CARCIK cells (Figure 1 Addendum 1).

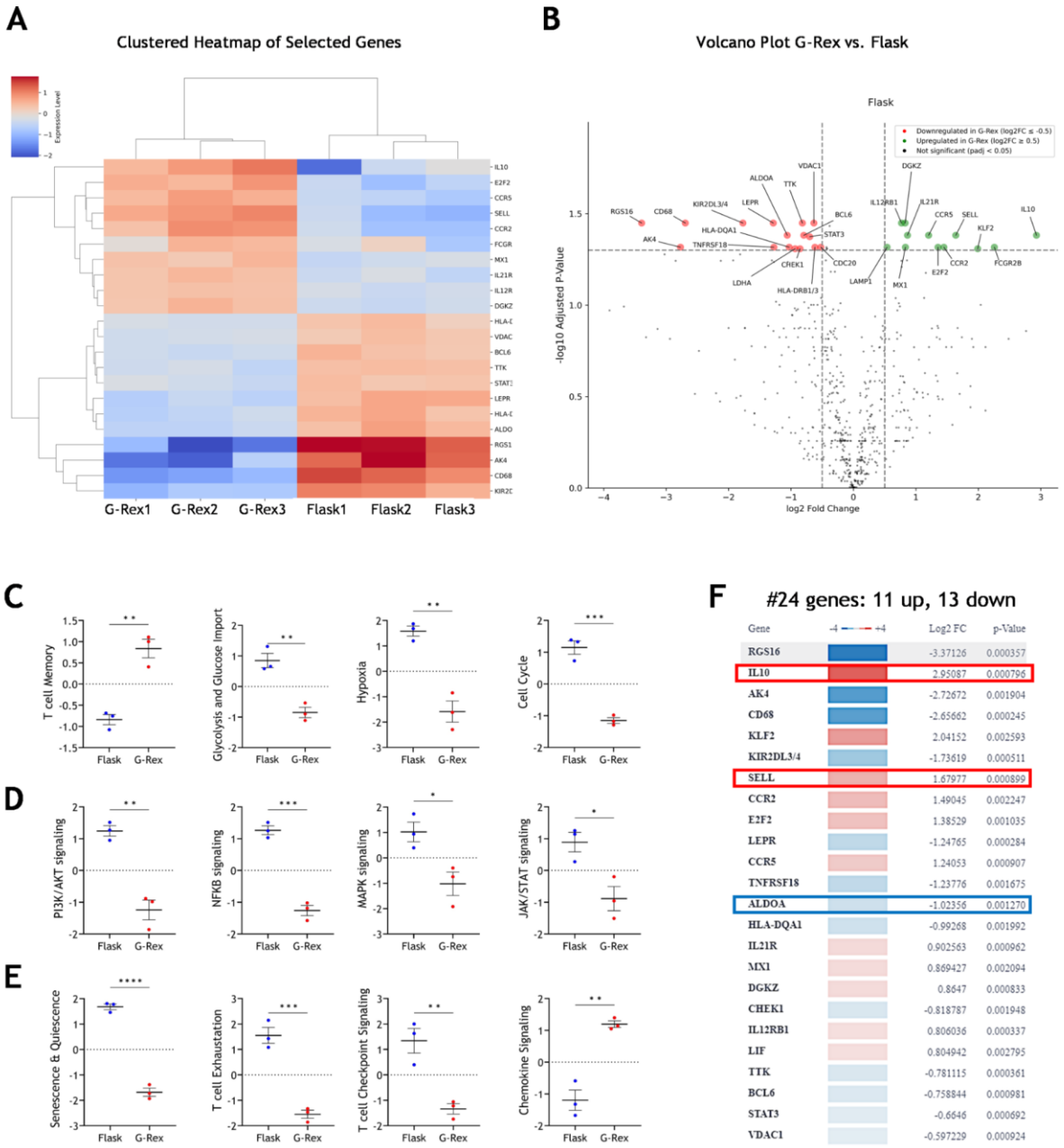

Figure 1 (Addendum 1). Gene expression characterisation of Flask- and G-Rex-derived CARCIK-CD19 cells. (A) Hierarchical clustering heatmap of Flask- and G-Rex- derived CARCIK-CD19 cells produced following Protocol 2. (B) Volcano plot of the differential gene expression analysis of Flask- and G-Rex- derived CARCIK-CD19. (C–E) Pathway analysis and (F) number of DEGs significantly up- and downregulated comparing Flask- and G-Rex-derived CARCIK-CD19 cells. From "*Optimized GMP-grade production of non-viral Sleeping Beauty-generated CARCIK cells for enhanced fitness and clinical scalability", Pisani et al*[164]*.*

Conclusions

The current study, recently published as *"Efficient non-viral GMP-compatible platform for generation and expansion of anti-CD19 CARCIK cells under feeder-free and serum-free conditions"* in the *Journal of Translational Medicine*, provides a clinically relevant and scalable platform for CARCIK cell manufacturing. My contribution, transcriptional profiling using Nanostring technology, added molecular depth to the phenotypic and functional characterisation, confirming that G-Rex expansion preserves functional fitness while limiting exhaustion. These findings further reinforce the idea that non-viral CAR platforms, such as the *Sleeping Beauty* transposon-based system, are suitable for clinical implementation and large-scale production of next-generation adoptive cell therapies.

ADDENDUM 2.

In March 2025, I had the opportunity to participate in the 3-Minute Thesis (3MT) competition organised by the University of Bologna. This international initiative challenges doctoral candidates to present the essence of their research in just three minutes, using clear and accessible language to engage a non-specialist audience.

My presentation focused on the central theme of this thesis: the development of innovative inducible effector cells capable of combining the precision of immunotherapy with the selectivity of targeted radionuclide uptake. To meet the spirit of the competition, I framed the project with a simple and compelling narrative, using the metaphor of "merging two superheroes into one unbeatable warrior against

cancer” to explain how cellular immunotherapy and radiotherapy could be combined into a single, more powerful therapeutic strategy. This communicative approach allowed me to make complex concepts, such as genetic engineering, inducible systems and radionuclide delivery, accessible while still conveying the novelty and potential impact of the research.

Among the numerous doctoral students who applied, my project was selected as one of the ten finalists. During the final event, I was awarded third place overall, a recognition that highlighted not only the scientific merit of the work but also the effectiveness of communicating biomedical innovation in an engaging and understandable way.

This experience represented a valuable complement to my doctoral journey. It strengthened my ability to explain advanced therapy medicinal products (ATMPs) and convey complex concepts beyond the boundaries of the laboratory, bridging the gap between cutting-edge science and public understanding. Ultimately, it reinforced the translational and societal relevance of my research and the importance of making innovative therapies comprehensible and inspiring for diverse audiences.

7. BIBLIOGRAPHY

1. Jeelani S, Reddy RCJ, Maheswaran T, Asokan GS, Dany A, Anand B. Theranostics: A treasured tailor for tomorrow. *J Pharm Bioallied Sci*. 2014;6(Suppl 1):S6-8. doi:10.4103/0975-7406.137249
2. Seidlin SM, Marinelli LD, Oshry E. Radioactive iodine therapy; effect on functioning metastases of adenocarcinoma of the thyroid. *J Am Med Assoc*. 1946;132(14):838-847. doi:10.1001/jama.1946.02870490016004
3. Maresca KP, Hillier SM, Femia FJ, et al. A series of halogenated heterodimeric inhibitors of prostate specific membrane antigen (PSMA) as radiolabeled probes for targeting prostate cancer. *J Med Chem*. 2009;52(2):347-357. doi:10.1021/jm800994j
4. Zechmann CM, Afshar-Oromieh A, Armor T, et al. Radiation dosimetry and first therapy results with a 124I/131I-labeled small molecule (MIP-1095) targeting PSMA for prostate cancer therapy. *Eur J Nucl Med Mol Imaging*. 2014;41(7):1280-1292. doi:10.1007/s00259-014-2713-y
5. Hofman MS, Violet J, Hicks RJ, et al. [177Lu]-PSMA-617 radionuclide treatment in patients with metastatic castration-resistant prostate cancer (LuPSMA trial): a single-centre, single-arm, phase 2 study. *Lancet Oncol*. 2018;19(6):825-833. doi:10.1016/S1470-2045(18)30198-0
6. Sneider A, VanDyke D, Paliwal S, Rai P. Remotely Triggered Nano-Theranostics For Cancer Applications. *Nanotheranostics*. 2017;1(1):1-22. doi:10.7150/ntno.17109
7. Shao F, Long Y, Ji H, Jiang D, Lei P, Lan X. Radionuclide-based molecular imaging allows CAR-T cellular visualization and therapeutic monitoring. *Theranostics*. 2021;11(14):6800-6817. doi:10.7150/thno.56989
8. Van Essen M, Krenning EP, De Jong M, Valkema R, Kwekkeboom DJ. Peptide Receptor Radionuclide Therapy with radiolabelled somatostatin analogues in patients with somatostatin receptor positive tumours. *Acta Oncol Stockh Swed*. 2007;46(6):723-734. doi:10.1080/02841860701441848
9. Strosberg J, El-Haddad G, Wolin E, et al. Phase 3 Trial of 177Lu-Dotatate for Midgut Neuroendocrine Tumors. *N Engl J Med*. 2017;376(2):125-135. doi:10.1056/NEJMoa1607427
10. Wolchok JD, Chiarion-Sileni V, Gonzalez R, et al. Overall Survival with Combined Nivolumab and Ipilimumab in Advanced Melanoma. *N Engl J Med*. 2017;377(14):1345-1356. doi:10.1056/NEJMoa1709684
11. Liu N, Zhang B, He J, Li S. Efficacy and safety of immune checkpoint inhibitors for advanced squamous non-small cell lung cancer: a systematic review and network meta-analysis. *Front Immunol*. 2025;16. doi:10.3389/fimmu.2025.1635757
12. Yin Q, Dai L, Sun R, Ke P, Liu L, Jiang B. Clinical Efficacy of Immune Checkpoint Inhibitors in Non-Small Cell Lung Cancer Patients with Liver Metastases: A Network Meta-Analysis of Nine Randomized Controlled Trials. *Cancer Res Treat*. 2022;54(3):803-816. doi:10.4143/crt.2021.764
13. Bergman PJ. Cancer Immunotherapy. *Vet Clin North Am Small Anim Pract*. 2024;54(3):441-468. doi:10.1016/j.cvsm.2023.12.002
14. Smyth MJ, Godfrey DI, Trapani JA. A fresh look at tumor immunosurveillance and immunotherapy. *Nat Immunol*. 2001;2(4):293-299. doi:10.1038/86297
15. Wallace ME, Smyth MJ. The role of natural killer cells in tumor control—effectors and regulators of adaptive immunity. *Springer Semin Immunopathol*. 2005;27(1):49-64. doi:10.1007/s00281-004-0195-x

16. Itoh H, Horiuchi Y, Nagasaki T, et al. Evaluation of immunological status in tumor-bearing dogs. *Vet Immunol Immunopathol*. 2009;132(2):85-90. doi:10.1016/j.vetimm.2009.04.020
17. Schmiedt CW, Grimes JA, Holzman G, McAnulty JF. Incidence and risk factors for development of malignant neoplasia after feline renal transplantation and cyclosporine-based immunosuppression. *Vet Comp Oncol*. 2009;7(1):45-53. doi:10.1111/j.1476-5829.2008.00172.x
18. Catchpole B, Gould SM, Kellett-Gregory LM, Dobson JM. Immunosuppressive cytokines in the regional lymph node of a dog suffering from oral malignant melanoma. *J Small Anim Pract*. 2002;43(10):464-467. doi:10.1111/j.1748-5827.2002.tb00015.x
19. Zagury D, Gallo RC. Anti-cytokine Ab immune therapy: present status and perspectives. *Drug Discov Today*. 2004;9(2):72-81. doi:10.1016/S1359-6446(03)02955-6
20. Morse MA, Mosca ,Paul J, Clay ,Timothy M, and Lyerly HK. Dendritic cell maturation in active immunotherapy strategies. *Expert Opin Biol Ther*. 2002;2(1):35-43. doi:10.1517/14712598.2.1.35
21. Johnson SB, Park HS, Gross CP, Yu JB. Use of Alternative Medicine for Cancer and Its Impact on Survival. *JNCI J Natl Cancer Inst*. 2018;110(1):121-124. doi:10.1093/jnci/djx145
22. Sambi M, Bagheri L, Szewczuk MR. Current Challenges in Cancer Immunotherapy: Multimodal Approaches to Improve Efficacy and Patient Response Rates. *J Oncol*. 2019;2019:1-12. doi:10.1155/2019/4508794
23. Robbins PF, Lu YC, El-Gamil M, et al. Mining Exomic Sequencing Data to Identify Mutated Antigens Recognized by Adoptively Transferred Tumor-reactive T cells. *Nat Med*. 2013;19(6):747-752. doi:10.1038/nm.3161
24. Pearce A, Haas M, Viney R, et al. Incidence and severity of self-reported chemotherapy side effects in routine care: A prospective cohort study. *PloS One*. 2017;12(10):e0184360. doi:10.1371/journal.pone.0184360
25. Di Maio M, Basch E, Bryce J, Perrone F. Patient-reported outcomes in the evaluation of toxicity of anticancer treatments. *Nat Rev Clin Oncol*. 2016;13(5):319-325. doi:10.1038/nrclinonc.2015.222
26. Chung H, Jung H, Noh JY. Emerging Approaches for Solid Tumor Treatment Using CAR-T Cell Therapy. *Int J Mol Sci*. 2021;22(22):12126. doi:10.3390/ijms222212126
27. McCune JS. Rapid Advances in Immunotherapy to Treat Cancer. *Clin Pharmacol Ther*. 2018;103(4):540-544. doi:10.1002/cpt.985
28. Pietrobon V, Todd LA, Goswami A, Stefanson O, Yang Z, Marincola F. Improving CAR T-Cell Persistence. *Int J Mol Sci*. 2021;22(19):10828. doi:10.3390/ijms221910828
29. Elahi R, Khosh E, Tahmasebi S, Esmaeilzadeh A. Immune Cell Hacking: Challenges and Clinical Approaches to Create Smarter Generations of Chimeric Antigen Receptor T Cells. *Front Immunol*. 2018;9:1717. doi:10.3389/fimmu.2018.01717
30. Larson RC, Maus MV. Recent advances and discoveries on the mechanisms and functions of CAR T cells. *Nat Rev Cancer*. 2021;21(3):145-161. doi:10.1038/s41568-020-00323-z
31. Neelapu SS, Locke FL, Bartlett NL, et al. Axicabtagene Ciloleucel CAR T-Cell Therapy in Refractory Large B-Cell Lymphoma. *N Engl J Med*. 2017;377(26):2531-2544. doi:10.1056/NEJMoa1707447
32. Sermer D, Brentjens R. CAR T-cell therapy: Full speed ahead. *Hematol Oncol*. 2019;37(S1):95-100. doi:10.1002/hon.2591

33. Prommersberger S, Reiser M, Beckmann J, et al. CARAMBA: a first-in-human clinical trial with SLAMF7 CAR-T cells prepared by virus-free Sleeping Beauty gene transfer to treat multiple myeloma. *Gene Ther*. 2021;28(9):560-571. doi:10.1038/s41434-021-00254-w
34. Micklethwaite KP, Gowrishankar K, Gloss BS, et al. Investigation of product-derived lymphoma following infusion of piggyBac-modified CD19 chimeric antigen receptor T cells. *Blood*. 2021;138(16):1391-1405. doi:10.1182/blood.2021010858
35. Gaimari A, De Lucia A, Nicolini F, et al. Significant Advancements and Evolutions in Chimeric Antigen Receptor Design. *Int J Mol Sci*. 2024;25(22):12201. doi:10.3390/ijms252212201
36. Noh JY, Seo H, Lee J, Jung H. Immunotherapy in Hematologic Malignancies: Emerging Therapies and Novel Approaches. *Int J Mol Sci*. 2020;21(21):E8000. doi:10.3390/ijms21218000
37. Fang J, Zhou F. BCMA-targeting chimeric antigen receptor T cell therapy for relapsed and/or refractory multiple myeloma. *Ann Hematol*. 2024;103(4):1069-1083. doi:10.1007/s00277-023-05444-7
38. Chekol Abebe E, Yibeltal Shiferaw M, Tadele Admasu F, Asmamaw Dejenie T. Ciltacabtagene autoleucel: The second anti-BCMA CAR T-cell therapeutic armamentarium of relapsed or refractory multiple myeloma. *Front Immunol*. 2022;13. doi:10.3389/fimmu.2022.991092
39. Zhao WH, Liu J, Wang BY, et al. A phase 1, open-label study of LCAR-B38M, a chimeric antigen receptor T cell therapy directed against B cell maturation antigen, in patients with relapsed or refractory multiple myeloma. *J Hematol OncolJ Hematol Oncol*. 2018;11(1):141. doi:10.1186/s13045-018-0681-6
40. Au R. Immunooncology: Can the Right Chimeric Antigen Receptors T-Cell Design Be Made to Cure All Types of Cancers and Will It Be Covered? *J Pharm*. 2017;2017:e7513687. doi:10.1155/2017/7513687
41. Tahmasebi S, Elahi R, Khosh E, Esmaeilzadeh A. Programmable and multi-targeted CARs: a new breakthrough in cancer CAR-T cell therapy. *Clin Transl Oncol*. 2021;23(6):1003-1019. doi:10.1007/s12094-020-02490-9
42. Escobar G, Berger TR, Maus MV. CAR-T cells in solid tumors: Challenges and breakthroughs. *Cell Rep Med*. Published online September 12, 2025:102353. doi:10.1016/j.xcrm.2025.102353
43. Ramos CA, Rouce R, Robertson CS, et al. In Vivo Fate and Activity of Second- versus Third-Generation CD19-Specific CAR-T Cells in B Cell Non-Hodgkin's Lymphomas. *Mol Ther J Am Soc Gene Ther*. 2018;26(12):2727-2737. doi:10.1016/j.ymthe.2018.09.009
44. Miao L, Zhang J, Huang B, et al. Special Chimeric Antigen Receptor (CAR) Modifications of T Cells: A Review. *Front Oncol*. 2022;12:832765. doi:10.3389/fonc.2022.832765
45. Figueroa JA, Reidy A, Mirandola L, et al. Chimeric antigen receptor engineering: a right step in the evolution of adoptive cellular immunotherapy. *Int Rev Immunol*. 2015;34(2):154-187. doi:10.3109/08830185.2015.1018419
46. Hoyos V, Savoldo B, Quintarelli C, et al. Engineering CD19-specific T lymphocytes with interleukin-15 and a suicide gene to enhance their anti-lymphoma/leukemia effects and safety. *Leukemia*. 2010;24(6):1160-1170. doi:10.1038/leu.2010.75
47. Asmamaw Dejenie T, Tiruneh G/Medhin M, Dessie Terefe G, Tadele Admasu F, Wale Tesega W, Chekol Abebe E. Current updates on generations, approvals, and clinical

trials of CAR T-cell therapy. *Hum Vaccines Immunother*. 2022;18(6):2114254. doi:10.1080/21645515.2022.2114254
48. Tousley AM, Rotiroti MC, Labanieh L, et al. Co-opting signalling molecules enables logic-gated control of CAR T cells. *Nature*. 2023;615(7952):507-516. doi:10.1038/s41586-023-05778-2
49. Kopan R, Ilagan MXG. The canonical Notch signaling pathway: unfolding the activation mechanism. *Cell*. 2009;137(2):216-233. doi:10.1016/j.cell.2009.03.045
50. Morsut L, Roybal KT, Xiong X, et al. Engineering Customized Cell Sensing and Response Behaviors Using Synthetic Notch Receptors. *Cell*. 2016;164(4):780-791. doi:10.1016/j.cell.2016.01.012
51. Gordon WR, Vardar-Ulu D, Histen G, Sanchez-Irizarry C, Aster JC, Blacklow SC. Structural basis for autoinhibition of Notch. *Nat Struct Mol Biol*. 2007;14(4):295-300. doi:10.1038/nsmb1227
52. Gordon WR, Zimmerman B, He L, et al. Mechanical Allostery: Evidence for a Force Requirement in the Proteolytic Activation of Notch. *Dev Cell*. 2015;33(6):729-736. doi:10.1016/j.devcel.2015.05.004
53. Cortese M, Torchiaro E, D'Andrea A, et al. Preclinical efficacy of a HER2 synNotch/CEA-CAR combinatorial immunotherapy against colorectal cancer with HER2 amplification. *Mol Ther*. 2024;32(8):2741-2761. doi:10.1016/j.ymthe.2024.06.023
54. Wang T, Lau CH, Wang N, et al. SynNotch-Programmed Macrophages for Cancerous Cell Detection and Sensing. *ACS Sens*. 2024;9(11):6136-6147. doi:10.1021/acssensors.4c01997
55. Li H, Zhao Y. Increasing the safety and efficacy of chimeric antigen receptor T cell therapy. *Protein Cell*. 2017;8(8):573-589. doi:10.1007/s13238-017-0411-9
56. Roybal KT, Rupp LJ, Morsut L, et al. Precision Tumor Recognition by T Cells With Combinatorial Antigen-Sensing Circuits. *Cell*. 2016;164(4):770-779. doi:10.1016/j.cell.2016.01.011
57. Srivastava S, Salter AI, Liggitt D, et al. Logic-Gated ROR1 Chimeric Antigen Receptor Expression Rescues T Cell-Mediated Toxicity to Normal Tissues and Enables Selective Tumor Targeting. *Cancer Cell*. 2019;35(3):489-503.e8. doi:10.1016/j.ccell.2019.02.003
58. Williams JZ, Allen GM, Shah D, et al. Precise T cell recognition programs designed by transcriptionally linking multiple receptors. *Science*. 2020;370(6520):1099-1104. doi:10.1126/science.abc6270
59. Hyrenius-Wittsten A, Su Y, Park M, et al. SynNotch CAR circuits enhance solid tumor recognition and promote persistent antitumor activity in mouse models. *Sci Transl Med*. 2021;13(591):eabd8836. doi:10.1126/scitranslmed.abd8836
60. Choe JH, Watchmaker PB, Simic MS, et al. SynNotch-CAR T cells overcome challenges of specificity, heterogeneity, and persistence in treating glioblastoma. *Sci Transl Med*. 2021;13(591):eabe7378. doi:10.1126/scitranslmed.abe7378
61. Chmielewski M, Abken H. CAR T Cells Releasing IL-18 Convert to T-Bethigh FoxO1low Effectors that Exhibit Augmented Activity against Advanced Solid Tumors. *Cell Rep*. 2017;21(11):3205-3219. doi:10.1016/j.celrep.2017.11.063
62. Macian F. NFAT proteins: key regulators of T-cell development and function. *Nat Rev Immunol*. 2005;5(6):472-484. doi:10.1038/nri1632
63. Müller MR, Rao A. NFAT, immunity and cancer: a transcription factor comes of age. *Nat Rev Immunol*. 2010;10(9):645-656. doi:10.1038/nri2818

64. Maakaron JE, Hu M, Jurdi NE. Chimeric antigen receptor T cell therapy for cancer: clinical applications and practical considerations. *BMJ*. 2022;378:e068956. doi:10.1136/bmj-2021-068956
65. Hou AJ, Chen LC, Chen YY. Navigating CAR-T cells through the solid-tumour microenvironment. *Nat Rev Drug Discov*. 2021;20(7):531-550. doi:10.1038/s41573-021-00189-2
66. Valkenburg KC, de Groot AE, Pienta KJ. Targeting the tumour stroma to improve cancer therapy. *Nat Rev Clin Oncol*. 2018;15(6):366-381. doi:10.1038/s41571-018-0007-1
67. Rodriguez-Garcia A, Palazon A, Noguera-Ortega E, Powell DJ, Guedan S. CAR-T Cells Hit the Tumor Microenvironment: Strategies to Overcome Tumor Escape. *Front Immunol*. 2020;11:1109. doi:10.3389/fimmu.2020.01109
68. Nagarsheth N, Wicha MS, Zou W. Chemokines in the cancer microenvironment and their relevance in cancer immunotherapy. *Nat Rev Immunol*. 2017;17(9):559-572. doi:10.1038/nri.2017.49
69. Lanitis E, Irving M, Coukos G. Targeting the tumor vasculature to enhance T cell activity. *Curr Opin Immunol*. 2015;33:55-63. doi:10.1016/j.coi.2015.01.011
70. Huang Y, Kim BYS, Chan CK, Hahn SM, Weissman IL, Jiang W. Improving immune-vascular crosstalkfor cancer immunotherapy. *Nat Rev Immunol*. 2018;18(3):195-203. doi:10.1038/nri.2017.145
71. Tahmasebi S, Elahi R, Esmaeilzadeh A. Solid Tumors Challenges and New Insights of CAR T Cell Engineering. *Stem Cell Rev Rep*. 2019;15(5):619-636. doi:10.1007/s12015-019-09901-7
72. Krenciute G, Prinzing BL, Yi Z, et al. Transgenic Expression of IL15 Improves Antiglioma Activity of IL13Rα2-CAR T Cells but Results in Antigen Loss Variants. *Cancer Immunol Res*. 2017;5(7):571-581. doi:10.1158/2326-6066.CIR-16-0376
73. Mu-Mosley H, Ostermann L, Muftuoglu M, et al. Transgenic Expression of IL15 Retains CD123-Redirected T Cells in a Less Differentiated State Resulting in Improved Anti-AML Activity in Autologous AML PDX Models. *Front Immunol*. 2022;13:880108. doi:10.3389/fimmu.2022.880108
74. Labanieh L, Mackall CL. CAR immune cells: design principles, resistance and the next generation. *Nature*. 2023;614(7949):635-648. doi:10.1038/s41586-023-05707-3
75. Depil S, Duchateau P, Grupp SA, Mufti G, Poirot L. “Off-the-shelf” allogeneic CAR T cells: development and challenges. *Nat Rev Drug Discov*. 2020;19(3):185-199. doi:10.1038/s41573-019-0051-2
76. Themeli M, Rivière I, Sadelain M. New cell sources for T cell engineering and adoptive immunotherapy. *Cell Stem Cell*. 2015;16(4):357-366. doi:10.1016/j.stem.2015.03.011
77. Wu X, Schmidt-Wolf IGH. An Alternative Source for Allogeneic CAR T Cells With a High Safety Profile. *Front Immunol*. 2022;13:913123. doi:10.3389/fimmu.2022.913123
78. Zhang Y, Schmidt-Wolf IGH. Ten-year update of the international registry on cytokine-induced killer cells in cancer immunotherapy. *J Cell Physiol*. 2020;235(12):9291-9303. doi:10.1002/jcp.29827
79. Magnani CF, Gaipa G, Lussana F, et al. Sleeping Beauty-engineered CAR T cells achieve antileukemic activity without severe toxicities. *J Clin Invest*. 2020;130(11):6021-6033. doi:10.1172/JCI138473
80. Merker M, Salzmann-Manrique E, Katzki V, et al. Clearance of Hematologic Malignancies by Allogeneic Cytokine-Induced Killer Cell or Donor Lymphocyte Infusions. *Biol*

Blood Marrow Transplant J Am Soc Blood Marrow Transplant. 2019;25(7):1281-1292. doi:10.1016/j.bbmt.2019.03.004
81. Sharma A, Ren X, Rosato A, et al. Cytokine-induced killer (CIK) cells, successes and challenges: report on the first international conference dedicated to the clinical translation of this unique adoptive cell immunotherapy. *Cancer Immunol Immunother CII*. 2024;73(2):21. doi:10.1007/s00262-023-03605-1
82. Bendelac A, Rivera MN, Park SH, Roark JH. Mouse CD1-specific NK1 T cells: development, specificity, and function. *Annu Rev Immunol*. 1997;15:535-562. doi:10.1146/annurev.immunol.15.1.535
83. Imai K, Kanno M, Kimoto H, Shigemoto K, Yamamoto S, Taniguchi M. Sequence and expression of transcripts of the T-cell antigen receptor alpha-chain gene in a functional, antigen-specific suppressor-T-cell hybridoma. *Proc Natl Acad Sci U S A*. 1986;83(22):8708-8712. doi:10.1073/pnas.83.22.8708
84. Shin S, El-Diwany R, Schaffert S, et al. Antigen recognition determinants of gammadelta T cell receptors. *Science*. 2005;308(5719):252-255. doi:10.1126/science.1106480
85. Nörenberg J, Jaksó P, Barakonyi A. Gamma/Delta T Cells in the Course of Healthy Human Pregnancy: Cytotoxic Potential and the Tendency of CD8 Expression Make CD56+ γδT Cells a Unique Lymphocyte Subset. *Front Immunol*. 2020;11:596489. doi:10.3389/fimmu.2020.596489
86. Franceschetti M, Pievani A, Borleri G, et al. Cytokine-induced killer cells are terminally differentiated activated CD8 cytotoxic T-EMRA lymphocytes. *Exp Hematol*. 2009;37(5):616-628.e2. doi:10.1016/j.exphem.2009.01.010
87. Liang G, Feng G, Chen H, et al. Changes in the TCR repertoire of T-cell subsets during culture of cytokine-induced killer cells. *FEBS Lett*. 2022;596(20):2696-2705. doi:10.1002/1873-3468.14501
88. Schmidt-Wolf IG, Negrin RS, Kiem HP, Blume KG, Weissman IL. Use of a SCID mouse/human lymphoma model to evaluate cytokine-induced killer cells with potent antitumor cell activity. *J Exp Med*. 1991;174(1):139-149. doi:10.1084/jem.174.1.139
89. Pievani A, Borleri G, Pende D, et al. Dual-functional capability of CD3+CD56+ CIK cells, a T-cell subset that acquires NK function and retains TCR-mediated specific cytotoxicity. *Blood*. 2011;118(12):3301-3310. doi:10.1182/blood-2011-02-336321
90. Yoon SH, Lee JM, Woo SJ, et al. Transfer of Her-2/neu specificity into cytokine-induced killer (CIK) cells with RNA encoding chimeric immune receptor (CIR). *J Clin Immunol*. 2009;29(6):806-814. doi:10.1007/s10875-009-9308-6
91. Emami-Shahri N, Papa S. Dynamic imaging for CAR-T-cell therapy. *Biochem Soc Trans*. 2016;44(2):386-390. doi:10.1042/BST20150257
92. De la Vieja A, Dohan O, Levy O, Carrasco N. Molecular Analysis of the Sodium/Iodide Symporter: Impact on Thyroid and Extrathyroid Pathophysiology. *Physiol Rev*. 2000;80(3):1083-1105. doi:10.1152/physrev.2000.80.3.1083
93. Jung H. The sodium/substrate symporter family: structural and functional features. *FEBS Lett*. 2002;529(1):73-77. doi:10.1016/S0014-5793(02)03184-8
94. Darrouzet E, Lindenthal S, Marcellin D, Pellequer JL, Pourcher T. The sodium/iodide symporter: State of the art of its molecular characterization. *Biochim Biophys Acta BBA - Biomembr*. 2014;1838(1, Part B):244-253. doi:10.1016/j.bbamem.2013.08.013
95. Kogai T, Brent GA. The sodium iodide symporter (NIS): Regulation and approaches to targeting for cancer therapeutics. *Pharmacol Ther*. 2012;135(3):355-370. doi:10.1016/j.pharmthera.2012.06.007

96. Schlumberger M, Lacroix L, Russo D, Filetti S, Bidart JM. Defects in iodide metabolism in thyroid cancer and implications for the follow-up and treatment of patients. *Nat Clin Pract Endocrinol Metab*. 2007;3(3):260-269. doi:10.1038/ncpendmet0449
97. Hingorani M, Spitzweg C, Vassaux G, et al. The Biology of the Sodium Iodide Symporter and its Potential for Targeted Gene Delivery. *Curr Cancer Drug Targets*. 10(2):242-267. doi:10.2174/156800910791054194
98. Dai G, Levy O, Carrasco N. Cloning and characterization of the thyroid iodide transporter. *Nature*. 1996;379(6564):458-460. doi:10.1038/379458a0
99. Spitzweg C, Nelson PJ, Wagner E, et al. The sodium iodide symporter (NIS): novel applications for radionuclide imaging and treatment. Published online October 1, 2021. doi:10.1530/ERC-21-0177
100. Ravera S, Reyna-Neyra A, Ferrandino G, Amzel LM, Carrasco N. The Sodium/Iodide Symporter (NIS): Molecular Physiology and Preclinical and Clinical Applications. *Annu Rev Physiol*. 2017;79:261-289. doi:10.1146/annurev-physiol-022516-034125
101. Jiang H, DeGrado TR. [^{18}F]Tetrafluoroborate ([^{18}F]TFB) and its analogs for PET imaging of the sodium/iodide symporter. *Theranostics*. 2018;8(14):3918-3931. doi:10.7150/thno.24997
102. Samnick S, Al-Momani E, Schmid JS, Mottok A, Buck AK, Lapa C. Initial Clinical Investigation of [18F]Tetrafluoroborate PET/CT in Comparison to [124I]Iodine PET/CT for Imaging Thyroid Cancer. *Clin Nucl Med*. 2018;43(3):162-167. doi:10.1097/RLU.0000000000001977
103. Portulano C, Paroder-Belenitsky M, Carrasco N. The Na+/I− Symporter (NIS): Mechanism and Medical Impact. *Endocr Rev*. 2014;35(1):106-149. doi:10.1210/er.2012-1036
104. Dittmann M, Gonzalez Carvalho JM, Rahbar K, et al. Incremental diagnostic value of [18F]tetrafluoroborate PET-CT compared to [131I]iodine scintigraphy in recurrent differentiated thyroid cancer. *Eur J Nucl Med Mol Imaging*. 2020;47(11):2639-2646. doi:10.1007/s00259-020-04727-9
105. Jauregui-Osoro M, Sunassee K, Weeks AJ, et al. Synthesis and biological evaluation of [18F]tetrafluoroborate: a PET imaging agent for thyroid disease and reporter gene imaging of the sodium/iodide symporter. *Eur J Nucl Med Mol Imaging*. 2010;37(11):2108-2116. doi:10.1007/s00259-010-1523-0
106. Khoshnevisan A, Jauregui-Osoro M, Shaw K, et al. [18F]tetrafluoroborate as a PET tracer for the sodium/iodide symporter: the importance of specific activity. *EJNMMI Res*. 2016;6:34. doi:10.1186/s13550-016-0188-5
107. O' Doherty J, Jauregui-Osoro M, Brothwood T, et al. 18F--tetrafluoroborate (18F--TFB), a PET probe for imaging sodium-iodide symporter expression: Whole-body biodistribution, safety and radiation dosimetry in thyroid cancer patients. *J Nucl Med Off Publ Soc Nucl Med*. 2017;58(10):1666-1671. doi:10.2967/jnumed.117.192252
108. Diocou S, Volpe A, Jauregui-Osoro M, et al. [18F]tetrafluoroborate-PET/CT enables sensitive tumor and metastasis in vivo imaging in a sodium iodide symporter-expressing tumor model. *Sci Rep*. 2017;7:946. doi:10.1038/s41598-017-01044-4
109. Verburg FA, Giovanella L, Hoffmann M, et al. New! F-18-based PET/CT for sodium-iodine-symporter-targeted imaging! *Eur J Nucl Med Mol Imaging*. 2020;47(11):2484-2486. doi:10.1007/s00259-020-04763-5
110. Klutz K, Schaffert D, Willhauck MJ, et al. Epidermal Growth Factor Receptor-targeted 131I-therapy of Liver Cancer Following Systemic Delivery of the Sodium Iodide Symporter Gene. *Mol Ther*. 2011;19(4):676-685. doi:10.1038/mt.2010.296

111. Kitzberger C, Spellerberg R, Morath V, et al. The sodium iodide symporter (NIS) as theranostic gene: its emerging role in new imaging modalities and non-viral gene therapy. *EJNMMI Res*. 2022;12:25. doi:10.1186/s13550-022-00888-w
112. Volpe A, Lang C, Lim L, et al. Spatiotemporal PET Imaging Reveals Differences in CAR-T Tumor Retention in Triple-Negative Breast Cancer Models. *Mol Ther*. 2020;28(10):2271-2285. doi:10.1016/j.ymthe.2020.06.028
113. Paganelli G, Ferrari M, Cremonesi M, et al. IART: intraoperative avidination for radionuclide treatment. A new way of partial breast irradiation. *Breast Edinb Scotl*. 2007;16(1):17-26. doi:10.1016/j.breast.2006.10.003
114. Paganelli G, De Cicco C, Ferrari ME, et al. Intraoperative avidination for radionuclide treatment as a radiotherapy boost in breast cancer: results of a phase II study with (90)Y-labeled biotin. *Eur J Nucl Med Mol Imaging*. 2010;37(2):203-211. doi:10.1007/s00259-009-1260-4
115. Chinol M, De Cobelli O, Trifirò G, et al. Localization of avidin in superficial bladder cancer: a potentially new approach for radionuclide therapy. *Eur Urol*. 2003;44(5):556-559. doi:10.1016/s0302-2838(03)00369-5
116. Paganelli G, Belloni C, Magnani P, et al. Two-step tumour targetting in ovarian cancer patients using biotinylated monoclonal antibodies and radioactive streptavidin. *Eur J Nucl Med*. 1992;19(5):322-329. doi:10.1007/BF00177053
117. Paganelli G, Magnani P, Zito F, et al. Three-Step Monoclonal Antibody Tumor Targeting in Carcinoembryonic Antigen- positive Patients'.
118. Cremonesi M, Ferrari M, Chinol M, et al. Three-step radioimmunotherapy with yttrium-90 biotin: dosimetry and pharmacokinetics in cancer patients. *Eur J Nucl Med*. 1999;26(2):110-120. doi:10.1007/s002590050366
119. Paganelli G, Grana C, Chinol M, et al. Antibody-guided three-step therapy for high grade glioma with yttrium-90 biotin. *Eur J Nucl Med*. 1999;26(4):348-357. doi:10.1007/s002590050397
120. Grana C, Chinol M, Robertson C, et al. Pretargeted adjuvant radioimmunotherapy with Yttrium-90-biotin in malignant glioma patients: A pilot study. *Br J Cancer*. 2002;86(2):207-212. doi:10.1038/sj.bjc.6600047
121. Paganelli G, Bartolomei M, Ferrari M, et al. Pre-targeted locoregional radioimmunotherapy with 90Y-biotin in glioma patients: phase I study and preliminary therapeutic results. *Cancer Biother Radiopharm*. 2001;16(3):227-235. doi:10.1089/10849780152389410
122. Paganelli G, Ferrari M, Ravasi L, et al. Intraoperative avidination for radionuclide therapy: a prospective new development to accelerate radiotherapy in breast cancer. *Clin Cancer Res Off J Am Assoc Cancer Res*. 2007;13(18 Pt 2):5646s-5651s. doi:10.1158/1078-0432.CCR-07-1058
123. Lim KH, Huang H, Pralle A, Park S. Stable, high-affinity streptavidin monomer for protein labeling and monovalent biotin detection. *Biotechnol Bioeng*. 2013;110(1):57-67. doi:10.1002/bit.24605
124. Aslan FM, Yu Y, Mohr SC, Cantor CR. Engineered single-chain dimeric streptavidins with an unexpected strong preference for biotin-4-fluorescein. *Proc Natl Acad Sci U S A*. 2005;102(24):8507-8512. doi:10.1073/pnas.0503112102
125. Laitinen OH, Nordlund HR, Hytönen VP, et al. Rational design of an active avidin monomer. *J Biol Chem*. 2003;278(6):4010-4014. doi:10.1074/jbc.M205844200

126. Sano T, Cantor CR. Intersubunit contacts made by tryptophan 120 with biotin are essential for both strong biotin binding and biotin-induced tighter subunit association of streptavidin. *Proc Natl Acad Sci U S A*. 1995;92(8):3180-3184. doi:10.1073/pnas.92.8.3180
127. Wu SC, Wong SL. Engineering soluble monomeric streptavidin with reversible biotin binding capability. *J Biol Chem*. 2005;280(24):23225-23231. doi:10.1074/jbc.M501733200
128. Chilkoti A, Tan PH, Stayton PS. Site-directed mutagenesis studies of the high-affinity streptavidin-biotin complex: contributions of tryptophan residues 79, 108, and 120. *Proc Natl Acad Sci U S A*. 1995;92(5):1754-1758. doi:10.1073/pnas.92.5.1754
129. Hendrickson WA, Pähler A, Smith JL, Satow Y, Merritt EA, Phizackerley RP. Crystal structure of core streptavidin determined from multiwavelength anomalous diffraction of synchrotron radiation. *Proc Natl Acad Sci U S A*. 1989;86(7):2190-2194. doi:10.1073/pnas.86.7.2190
130. Weber PC, Ohlendorf DH, Wendoloski JJ, Salemme FR. Structural origins of high-affinity biotin binding to streptavidin. *Science*. 1989;243(4887):85-88. doi:10.1126/science.2911722
131. Lim KH, Huang H, Pralle A, Park S. Engineered streptavidin monomer and dimer with improved stability and function. *Biochemistry*. 2011;50(40):8682-8691. doi:10.1021/bi2010366
132. Helppolainen SH, Nurminen KP, Määttä JAE, et al. Rhizavidin from Rhizobium etli: the first natural dimer in the avidin protein family. *Biochem J*. 2007;405(3):397-405. doi:10.1042/BJ20070076
133. Nagy L, Mezősi-Csaplár M, Rebenku I, Vereb G, Szöőr Á. Universal CAR T cells targeted to HER2 with a biotin-trastuzumab soluble linker penetrate spheroids and large tumor xenografts that are inherently resistant to trastuzumab mediated ADCC. *Front Immunol*. 2024;15. doi:10.3389/fimmu.2024.1365172
134. Sabahi M, Jabbari P, Alizadeh Haghighi M, et al. Proposing a tandem AND-gate CAR T cell targeting glioblastoma multiforme. *Med Hypotheses*. 2020;137:109559. doi:10.1016/j.mehy.2020.109559
135. Nakayama M. Multiplex T Cell Stimulation Assay Utilizing a T Cell Activation Reporter-Based Detection System. *Front Immunol*. 2020;11:17.
136. Roybal KT, Williams JZ, Morsut L, et al. Engineering T Cells with Customized Therapeutic Response Programs Using Synthetic Notch Receptors. *Cell*. 2016;167(2):419-432.e16. doi:10.1016/j.cell.2016.09.011
137. Goldenberg DM, Rossi EA, Sharkey RM, McBride WJ, Chang CH. Multifunctional antibodies by the Dock-and-Lock method for improved cancer imaging and therapy by pretargeting. *J Nucl Med Off Publ Soc Nucl Med*. 2008;49(1):158-163. doi:10.2967/jnumed.107.046185
138. Kurebayashi Y, Choyke PL, Sato N. Imaging of cell-based therapy using ^{89}Zr-oxine *ex vivo* cell labeling for positron emission tomography. *Nanotheranostics*. 2021;5(1):27-35. doi:10.7150/ntno.51391
139. Lee SH, Soh H, Chung JH, et al. Feasibility of real-time in vivo 89Zr-DFO-labeled CAR T-cell trafficking using PET imaging. *PLOS ONE*. 2020;15(1):e0223814. doi:10.1371/journal.pone.0223814
140. Day IL, Tamboline M, Lipshutz GS, Xu S. Recent developments in translational imaging of in vivo gene therapy outcomes. *Mol Ther*. 2025;33(6):2548-2564. doi:10.1016/j.ymthe.2024.12.049

141. Semenova AV, Викторовна CA, Sivolobova GF, et al. Reporter Transgenes for Monitoring the Antitumor Efficacy of Recombinant Oncolytic Viruses. *Acta Naturae*. 2022;14(3):46-56. doi:10.32607/actanaturae.11719
142. Helfer BM, Ponomarev V, Patrick PS, et al. Options for imaging cellular therapeutics in vivo: a multi-stakeholder perspective. *Cytotherapy*. 2021;23(9):757-773. doi:10.1016/j.jcyt.2021.02.005
143. Sellmyer MA, Richman SA, Lohith K, et al. Imaging CAR T Cell Trafficking with eDHFR as a PET Reporter Gene. *Mol Ther J Am Soc Gene Ther*. 2020;28(1):42-51. doi:10.1016/j.ymthe.2019.10.007
144. Urbanska K, Lanitis E, Poussin M, et al. A universal strategy for adoptive immunotherapy of cancer through use of a novel T-cell antigen receptor. *Cancer Res*. 2012;72(7):1844-1852. doi:10.1158/0008-5472.CAN-11-3890
145. Lohmueller JJ, Ham JD, Kvorjak M, Finn OJ. mSA2 affinity-enhanced biotin-binding CAR T cells for universal tumor targeting. *Oncoimmunology*. 2017;7(1):e1368604. doi:10.1080/2162402X.2017.1368604
146. Perez-Amill L, Suñe G, Antoñana-Vildosola A, et al. Preclinical development of a humanized chimeric antigen receptor against B cell maturation antigen for multiple myeloma. *Haematologica*. 2021;106(1):173-184. doi:10.3324/haematol.2019.228577
147. Emami-Shahri N, Foster J, Kashani R, et al. Clinically compliant spatial and temporal imaging of chimeric antigen receptor T-cells. *Nat Commun*. 2018;9(1):1081. doi:10.1038/s41467-018-03524-1
148. Martín M, Geysels RC, Peyret V, Bernal Barquero CE, Masini-Repiso AM, Nicola JP. Implications of Na+/I- Symporter Transport to the Plasma Membrane for Thyroid Hormonogenesis and Radioiodide Therapy. *J Endocr Soc*. 2019;3(1):222-234. doi:10.1210/js.2018-00100
149. Kemp K, Poe C. Stressed: The Unfolded Protein Response in T Cell Development, Activation, and Function. *Int J Mol Sci*. 2019;20(7):1792. doi:10.3390/ijms20071792
150. Mazurov D, Ilinskaya A, Heidecker G, Filatov A. Role of O-Glycosylation and Expression of CD43 and CD45 on the Surfaces of Effector T Cells in Human T Cell Leukemia Virus Type 1 Cell-to-Cell Infection. *J Virol*. 2012;86(5):2447-2458. doi:10.1128/JVI.06993-11
151. Charpentier JC, King PD. Mechanisms and functions of endocytosis in T cells. *Cell Commun Signal*. 2021;19(1):92. doi:10.1186/s12964-021-00766-3
152. van der Donk LEH, Ates LS, van der Spek J, Tukker LM, Geijtenbeek TBH, van Heijst JWJ. Separate signaling events control TCR downregulation and T cell activation in primary human T cells. *Immun Inflamm Dis*. 2021;9(1):223-238. doi:10.1002/iid3.383
153. Minutolo NG, Hollander EE, Powell DJ. The Emergence of Universal Immune Receptor T Cell Therapy for Cancer. *Front Oncol*. 2019;9. doi:10.3389/fonc.2019.00176
154. Jiao J, Zhao X, Hou R, et al. Comparison of two commonly used methods for stimulating T cells. *Biotechnol Lett*. 2019;41(12):1361-1371. doi:10.1007/s10529-019-02743-w
155. Wang N, Rajasekaran N, Hou T, Lisowski L, Mellins ED. Comparison of transduction efficiency among various lentiviruses containing GFP reporter in bone marrow hematopoietic stem cell transplantation. *Exp Hematol*. 2013;41(11):934-943. doi:10.1016/j.exphem.2013.07.002
156. Ren J, Shi J, Kakuda Y, et al. Phytohemagglutinin isolectins extracted and purified from red kidney beans and its cytotoxicity on human H9 lymphoma cell line. *Sep Purif Technol*. 2008;63(1):122-128. doi:10.1016/j.seppur.2008.04.004

157. Sommermeyer D, Hudecek M, Kosasih PL, et al. Chimeric antigen receptor-modified T cells derived from defined CD8+ and CD4+ subsets confer superior antitumor reactivity in vivo. *Leukemia*. 2016;30(2):492-500. doi:10.1038/leu.2015.247
158. Melero I, Hirschhorn-Cymerman D, Morales-Kastresana A, Sanmamed MF, Wolchok JD. Agonist Antibodies to TNFR Molecules That Costimulate T and NK Cells. *Clin Cancer Res*. 2013;19(5):1044-1053. doi:10.1158/1078-0432.CCR-12-2065
159. Pichler AC, Carrié N, Cuisinier M, et al. TCR-independent CD137 (4-1BB) signaling promotes CD8+-exhausted T cell proliferation and terminal differentiation. *Immunity*. 2023;56(7):1631-1648.e10. doi:10.1016/j.immuni.2023.06.007
160. Long AH, Haso WM, Shern JF, et al. 4-1BB costimulation ameliorates T cell exhaustion induced by tonic signaling of chimeric antigen receptors. *Nat Med*. 2015;21(6):581-590. doi:10.1038/nm.3838
161. Triller J, Prots I, Jäck HM, Wittmann J. An Enhanced Retroviral Vector for Efficient Genetic Manipulation and Selection in Mammalian Cells. *Biomolecules*. 2024;14(9):1131. doi:10.3390/biom14091131
162. Yukawa M, Jagannathan S, Vallabh S, et al. AP-1 activity induced by co-stimulation is required for chromatin opening during T cell activation. *J Exp Med*. 2020;217(1):e20182009. doi:10.1084/jem.20182009
163. Schlabach MR, Hu JK, Li M, Elledge SJ. Synthetic design of strong promoters. *Proc Natl Acad Sci*. 2010;107(6):2538-2543. doi:10.1073/pnas.0914803107
164. Pisani I, Melita G, de Souza PB, et al. Optimized GMP-grade production of non-viral Sleeping Beauty-generated CARCIK cells for enhanced fitness and clinical scalability. *J Transl Med*. 2025;23(1):559. doi:10.1186/s12967-025-06416-3